Modelling Hysteresis in Magnetically Ordered Materials

By Tiancheng Song

Advisor: Dr. R. M. Roshko

Department of Physics and Astronomy
University of Manitoba

Doctor of Philosophy

Abstract

This thesis presents a generalized version of the Preisach model of hysteresis which is designed to describe the temperature dependence and field dependence of the irreversible response of magnetically ordered materials everywhere below their critical temperature T_c. The model decomposes the magnetizing process into a sequence of Barkhausen events, each of which is represented by a double well potential with moment μ, two states $\phi = \pm\mu$, a dissipation energy $W_d = \mu h_c$ and a stored energy $W_s = 2\mu h_i$. A given magnetic material is characterized by an ensemble of Barkhausen elements with a distribution of characteristic fields $p(h_c, h_i)$. The distribution is allowed to vary with temperature in order to reflect intrinsic variations with temperature of the anisotropy and pinning mechanisms, in such a way that the coercive field distribution collapses into a δ-function $\delta(h_c)$ as T approaches T_c from below. Thermal fluctuations are represented by a thermal viscosity field $h_T^* = (k_B T/\mu) ln(t_{exp}/\tau_0)$.

The model was used to simulate numerically various standard experimental response functions, including the temperature dependence of the zero field cooled moment in a fixed applied field h_a, the temperature dependence of the field cooled moment in a fixed applied field, initial magnetizing and major hysteresis loop isotherms, and remanences, and the influence of each model parameter on the magnetic response functions was studied systematically. The model simulations identified the ratio η of the mean zero temperature dissipation barrier $\bar{W}_d(0)$ to the critical thermal fluctuation energy $W_c = k_B T_c ln(t_{exp}/\tau_0)$ as an important parameter which influences the principal structural characteristics of the response, and which can be used to classify materials as fluctuation-dominated or anisotropy-dominated.

The model was applied to the analysis of the measured response functions five systems, two nanoparticulate systems, Fe/SiO_2 and $NiFe_2O_4$, which were

fluctuation-dominated, and three ferromagnetic perovskites $SrRuO_3$, $La_{0.5}Sr_{0.5}-CoO_3$, and $La_{0.7}Sr_{0.3}MnO_3$, which were anisotropy-dominated. The analysis yielded the spectrum of Barkhausen characteristic fields $p(h_c, h_i, T)$ and the Barkhausen moment $\mu(T)$, from which it is possible to reconstruct a physical picture of the evolution of the Barkhausen free energy barriers with temperature, as well as some description of the reversible component of the response.

Acknowledgements

I am very grateful to my advisor, Professor R.M.Roshko for his encouragement and guidance throughout this research project. Without his helpful suggestions, working on this thesis would have been more difficult. I am very much in debt to him for many hours of interesting discussions which occupied a lot of his time.

I greatly appreciate the financial support from Professor R. M. Roshko and the fellowships from the Graduate Studies, University of Manitoba, which made my work and thesis possible.

Lastly, I wish to thank my family for their infinite encouragement to me.

Contents

List of Figures

List of Tables

Chapter 1

Hysteresis in Magnetic Materials

1.1 Hysteresis

Hysteresis is one of the most recognizable and important characteristics of ferromagnetic materials, and forms the basis for a wide variety of technologies, from permanent magnets to magnetic recording media, from energy conversion devices to electronic devices. Hysteresis refers to the non-unique, history-dependent and time-delayed response of magnetic materials to changes in an external applied magnetic field. Essentially, hysteresis originates from the existence of metastable minima in the free energy, which result from a complex and delicate balance of several competing energy terms, which include exchange energy, anisotropy energy (crystalline, shape, stress, etc), magnetostatic energy, and applied field energy.

1.2 Types of Hysteresis

1.2.1 Hysteresis: Delay

When we apply a time-varying magnetic field $H_a = H_a(\omega t)$, the output response of the material is $M = M(\omega t - \delta)$, where the response depends on the frequency ω. There is a delay δ which represents the lag in the response behind the applied field. Here M is magnetization. This kind of response can be expressed by a

complex susceptibility. Assume the external field is

$$H_a = H_0 e^{i\omega t} \tag{1.1}$$

Also assume that the response M is linear:

$$M = M_0 e^{i(\omega t - \delta)} \tag{1.2}$$

Then the complex susceptibility is

$$\tilde{\chi} = \frac{M}{H_a} = \frac{M_0}{H_0} e^{-i\delta} = \chi' - i\chi'' \tag{1.3}$$

When the response is non-linear, the susceptibility is much more complicated, and it is a function of frequency.

$$\tilde{\chi}(\omega) = \chi'(\omega) - i\chi''(\omega)$$

In the discussion in this thesis, we assume all processes are quasi-static, so that the input changes are arbitrarily slow, and the rate-dependence of hysteresis is negligible.

1.2.2 Hysteresis: History or Memory

The future evolution of a magnetic system depends not only the present stimulus but also the past history. There are two kinds of such memory, local memory and nonlocal memory, according to the subdivision of Giorgio Bertotti [1].

Local memory. In figure (1.1), which shows a system with local memory, the values of the external field H_a and the total moment M are sufficient to specify the system. Each point in the $M - H_a$ plane uniquely specifies one state. If the state is at point (H_1, M_1), the subsequent evolution will be either (H_2, M_2) or (H_3, M_3). There are only two possible curves originating from the point (H_1, M_1), which depend on whether the stimulus H_2 or H_3 is smaller or greater than H_1.

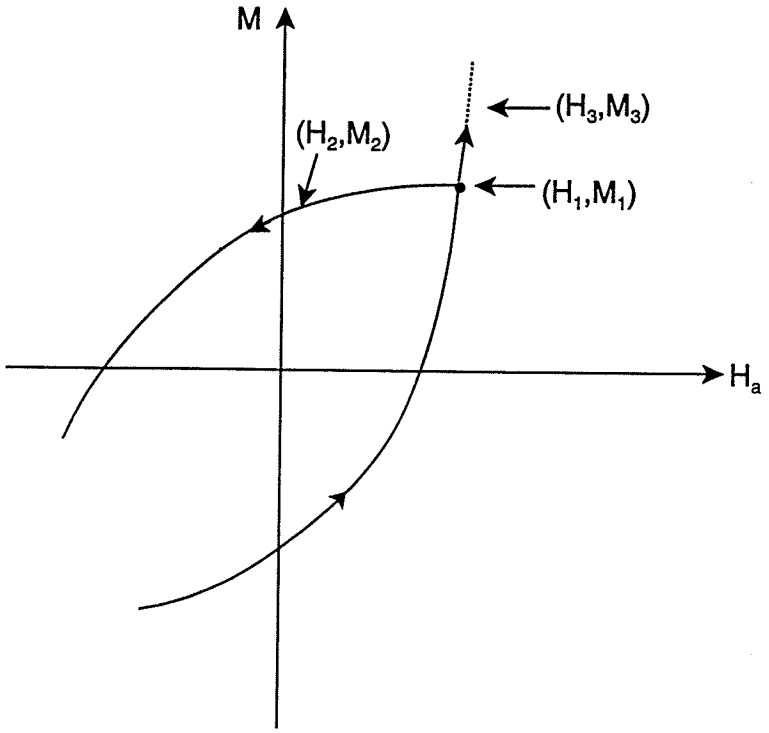

Figure 1.1: *History-dependent hysteresis*

All the past history before the point (H_1, M_1) is wiped out.

Nonlocal memory. In a system with nonlocal memory, H_a and M do not give a complete characterization of the system. In figure (1.1), if the present state is at point (H_1, M_1), after a new stimulus H_2, we cannot specify the next state of the system unless the past history is provided. In such a case, the curves originating from the point (H_1, M_1) will form a family of curves, with more than just two possible branches. This kind of behaviour is typical of real magnetic materials.

1.3 Characterization of Hysteresis

1.3.1 Hysteresis Loop

The hysteresis loop is the most obvious manifestation of the history-dependent behaviour of magnetic systems, according to which, the present state depends on both the applied field and the history. If the magnetic system is in a demagnetized

state, then after an external field is applied, the component of the magnetization along the direction of the field will evolve along $O \rightarrow E \rightarrow A$ as shown in figure (1.2), until the field is sufficiently large that no further gain of magnetization can be achieved. At this stage, the magnetic system is uniformly magnetized, and the system has reached the *saturation* state. The curve OEA is called the *initial magnetizing curve.* When the field is reduced after saturation, the magnetization follows another branch $A \rightarrow B \rightarrow C$. The residual magnetization when the applied field reaches zero is referred to as the *saturation remanence* M_r. To reverse the magnetization, an oppositely directed field is needed to demagnetize the material, until the magnetization is zero. The field at this stage is called the *coercivity* H_c. Continuing to increase the field in the reverse direction, will eventually produce saturation in the negative direction at the state C. Changing the direction of the field, and gradually increasing it will generate the branch $C \rightarrow D \rightarrow A$. The whole sequence $A \rightarrow B \rightarrow C \rightarrow D \rightarrow A$ constitutes a so-called *major hysteresis loop.* On the other hand, if the magnetic system is magnetized along the initial magnetization curve up to E where the material is not saturated magnetically, and the field is then reversed to state G where the field value is equal in magnitude to that at state E, then a loop $E \rightarrow F \rightarrow G \rightarrow H \rightarrow E$ is formed, called the *minor loop.* Obviously, there are an infinity of such minor loops.

There are many different shapes of hysteresis loops. These can be classified into six kinds as shown in figure (1.3).

(1). Tall and narrow: the saturation magnetization is high, while the coercivity is low.

(2). Wide (pot-bellied): both the saturation magnetization and the coercivity are high.

(3). Rectangular: the loop is approximately a rectangle.

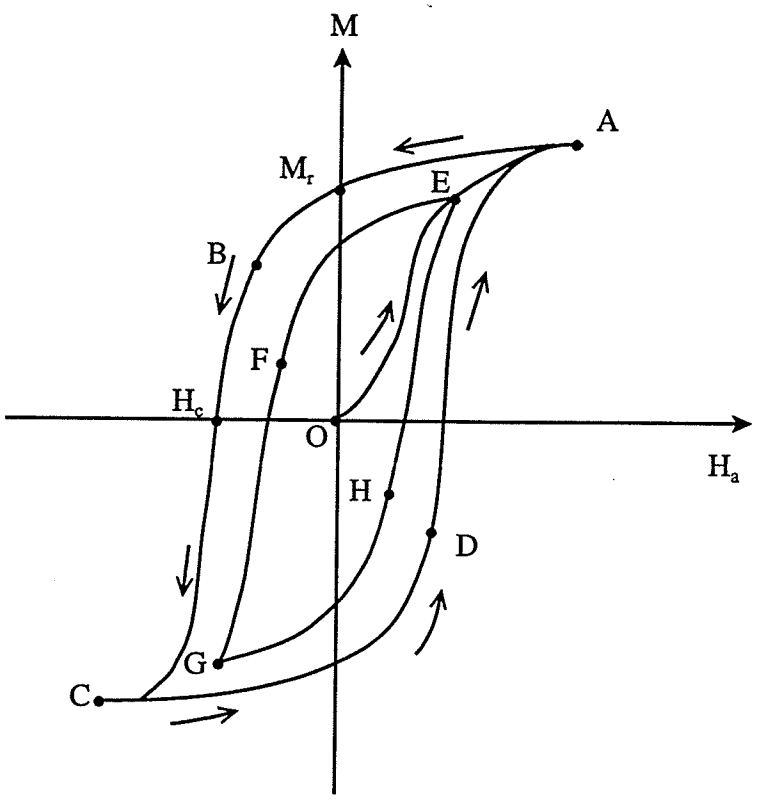

Figure 1.2: *Hysteresis loop*

(4). Skewed rectangular: a parallel polygon.

(5). Wasp-waisted: the width of the loop is narrower in the middle than in the other parts. This thesis will provide one possible explanation for such a shape.

(6). Asymmetric: the ascending branch and the descending branch are not symmetric with respect to the origin.

So, the shapes of hysteresis loops are very complicated. It is possible to calculate hysteresis loops of materials theoretically using various models. The Preisach model discussed in this thesis is an elegant tool for calculating and interpreting hysteresis loops.

1.3.2 Magnetizing Remanence and Demagnetizing Remanence

If, along the initial magnetization curve, before the saturation state is reached, and after each increment of the magnetic field, the field is removed, then there

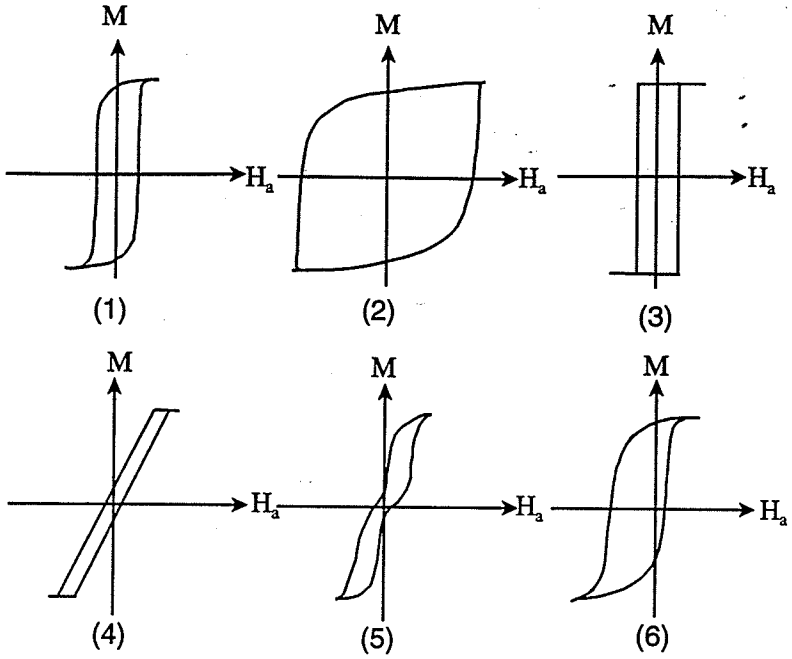

Figure 1.3: *Different shapes of hysteresis loops*

will be a remanence, M_{r1}, M_{r2}, M_{r2}, ... M_r, as shown in figure (1.4). When these remanences are plotted with respect to the external field, they will form a curve called the *magnetizing remanence curve* (dashed line OA in figure (1.4)).

Correspondingly, when we demagnetize the system, and, after each step of decrement of the reversed field, we remove the field, then the response of the system is called the *demagnetizing remanence.* When the demagnetizing remanence is equal to zero, the corresponding field is called the *remanent coercivity*, denoted by H_{cr}. As long as hysteresis is present, H_{cr} is larger than H_c.

1.3.3 Anhysteretic Curve

Are there ways to reach a magnetization state which is independent of the history of the magnetic system? In fact there are two ways to generate such a history-independent or anhysteretic curve. One way is to superimpose a constant field H_0 onto an oscillating field of slowly decreasing amplitude, as shown in figure (1.5). If the static biasing field is changed to another value, and the same sequence is repeated, the states for all different H_0 will form the *anhysteretic curve.* This curve

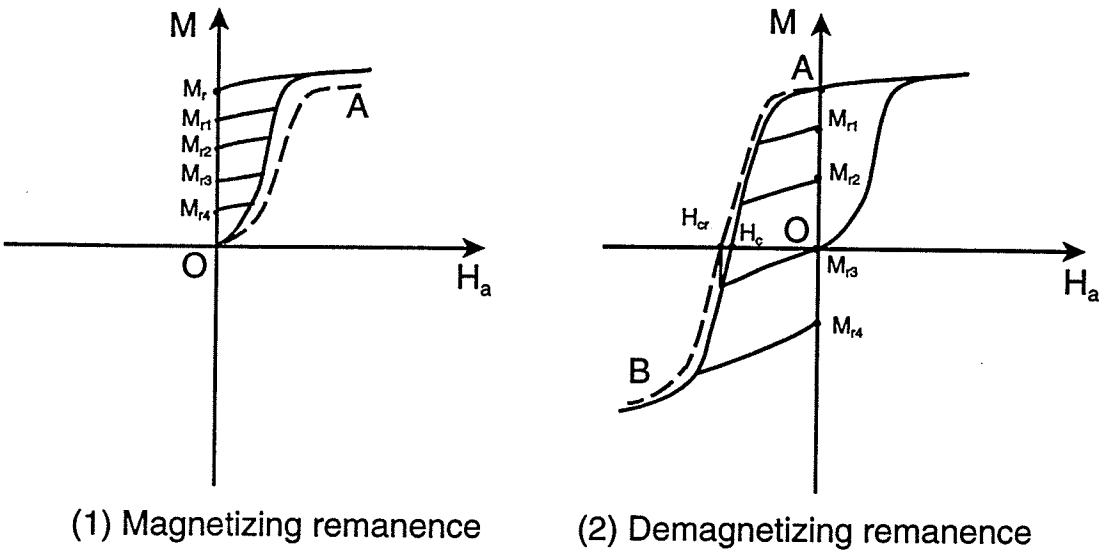

Figure 1.4: *Magnetizing remanence and demagnetizing remanence*

is independent of history. The oscillating field erases any memory of previous states possibly occupied by the system before demagnetization.

Another way to generate a history-independent curve is to heat the magnetic system above the Curie temperature, and then slowly cool it down to the final temperature under a constant field H_0. The states after thermal demagnetization and ac-demagnetization are slightly different, but the two sequences bring the system quickly to thermodynamic equilibrium under the given field([1],p19), while hysteresis prevents the system from reaching the equilibrium state.

Ac-demagnetization and thermal demagnetization will be discussed in depth in the following sections.

1.4 Theoretical Basis Hysteresis

1.4.1 Spontaneous Magnetization

Even when ferromagnetic materials are in their demagnetized state, they are subdivided into small magnetically saturated regions called *domains*. In each domain the atomic magnetic moments are aligned in some specific pattern by the

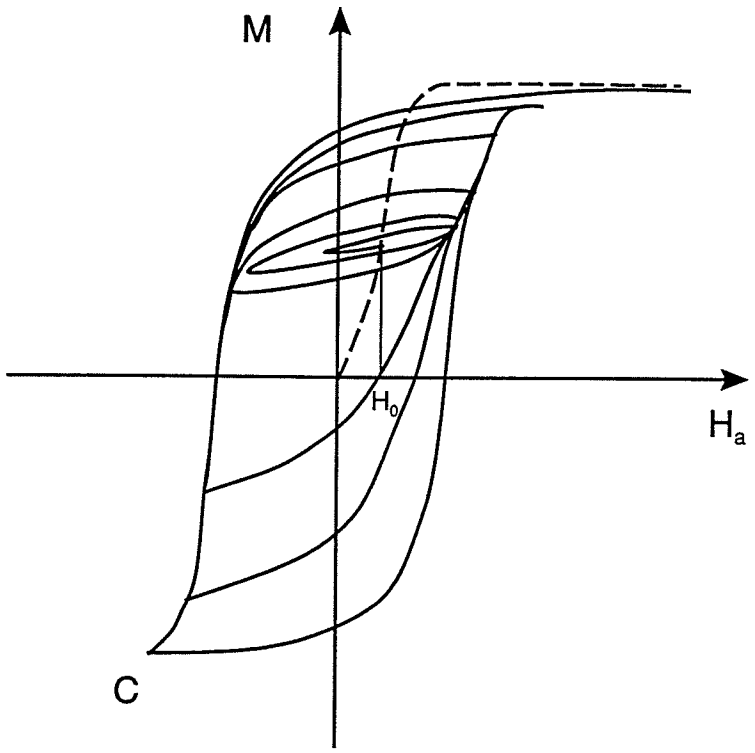

Figure 1.5: *Generating sequence for the anhysteretic curve(dashed lines)*

exchange interaction. This interaction leads to a *spontaneous magnetization.*

Exchange interaction

Assume that in one domain we have many atoms. The exchange interaction between atom i and atom j depends on their magnetic moments, which are related to the total spin of the electrons on that atom by $\vec{\mu} = g\mu_B\vec{S}$, where g is spin splitting factor, μ_B is Bohr magneton. The exchange energy is then:

$$E_{ex} = -\sum_{i<j} 2A_{ij}\vec{S}_i \cdot \vec{S}_j \tag{1.4}$$

where A_{ij} is the exchange integral between atom i and atom j. If only the closest z neighbours of atom i are taken into account, and if we make the assumption that all atoms have same number of neighbours, then the interaction between

atom i and all of its neighbours is:

$$E_{ex,i} = -2A\vec{S}_i \cdot \sum_{j=1}^{z} \vec{S}_j \tag{1.5}$$

Equation (1.5) can be written:

$$E_{ex,i} = -g\mu_B \vec{S}_i \cdot \vec{H}_e \tag{1.6}$$

where $\vec{H}_e$ is the effective magnetic field experienced by the i-th atom:

$$\vec{H}_e = \frac{2A}{g\mu_B} \sum_{j=1}^{z} \vec{S}_j \tag{1.7}$$

If spin $\vec{S}_j$ is replaced by its average value $< \vec{S}_j >$, the total moment is:

$$\vec{M} = Ng\mu_B < \vec{S}_j > \tag{1.8}$$

and the effective magnetic field in equation (1.7) can then be rewritten as:

$$\vec{H}_e = \frac{2zA}{Ng^2\mu_B^2}\vec{M} = \lambda\vec{M} \tag{1.9}$$

where

$$\lambda = \frac{2zA}{Ng^2\mu_B^2} \tag{1.10}$$

where z is the number of nearest neighbour atoms, N is the total number of atoms, and A is the exchange integral assumed to be constant.

Equation (1.9) provides the physical origin for the spontaneous alignment of the atomic magnetic moments into specific patterns. According to Weiss *molecular field* theory, $\vec{H}_e$ in equation (1.9) is also called the *molecular field.*

Spontaneous magnetization

For ferromagnetic systems, if we have n atoms per volume in the molecular field H_e, we can calculate the magnetic moment at temperature T as follows.

First, each atom has a magnetic moment related to the total angular momentum of the atom:

$$\mu_J = g_J\sqrt{J(J+1)}\mu_B \tag{1.11}$$

where J is a quantum number which comes from the spin and orbital momenta, g is the *spectroscopic splitting factor*, or *g factor*, and μ_B is the *Bohr magneton* [2].

The possible values of μ_J along the direction of the molecular field H_e can only take on discrete values:

$$\mu_H = g\mu_B M_J \tag{1.12}$$

where M_J is the magnetic quantum number. The possible values of M_J can only be:

$$M_J = J, J-1, J-2, ..., -(J-2), -(J-1), -J$$

The potential energy of each moment in the field H_e is:

$$E_p = -gM_J\mu_B H_e \tag{1.13}$$

According to Boltzmann statistics, the probability of an atom having energy E_p is proportional to

$$e^{-E_P/k_BT} = e^{g\mu_B M_J H_e/k_BT}$$

where k_B is Boltzmann's constant. The magnetization M is:

$$M(T) = n\frac{\sum_{M_J=-J}^{J} g\mu_B M_J e^{g\mu_B M_J H_e/k_BT}}{\sum_{M_J=-J}^{J} e^{g\mu_B M_J H_e/k_BT}} \tag{1.14}$$

Performing the sum in equation (1.14) results in the function:

$$M(T) = ng\mu_B JB(J,\alpha) \tag{1.15}$$

where $B(J,\alpha) = \frac{2J+1}{2J}coth\frac{2J+1}{2J}\alpha - \frac{1}{2J}coth\frac{\alpha}{2J}$ is called the *Brillouin function* [3],

and $\alpha = gJ\mu_B H_e/k_B T$. The factor $ngJ\mu_B$ is the product of the number of atoms per unit volume and the maximum moment of each atom in the direction of the field, and is in fact the saturation magnetization M_0.

So the magnetization is:

$$M(T)/M_0 = B(J, \alpha) \tag{1.16}$$

Equation (1.16) is a self-consistent expression for M(T). Its solution can be obtained as follows.

From equation (1.9)

$$\alpha = gJ\mu_B H_e/k_B T = gJ\mu_B \lambda M(T)/k_B T \tag{1.17}$$

With $M_0 = ngJ\mu_B$, equation (1.17) becomes:

$$\frac{M(T)}{M_0} = \frac{k_B T}{n\lambda(gJ\mu_B)^2}\alpha \tag{1.18}$$

Equation (1.16) and equation (1.18) are functions of (J, α). Given a temperature T, these two equations can be solved simultaneously to uniquely specify the value of M(T).

Curie Temperature

If we draw the curve of Equation (1.16) and the straight line of equation (1.18) versus α at various temperatures, then when the slope of the curve is equal to the slope of the straight line at the origin $\alpha = 0$, the spontaneous magnetization will be zero. The corresponding temperature is the Curie Temperature T_c. This procedure yields:

$$T_c = ng^2\mu_B^2 J(J+1)\lambda/3k_B \tag{1.19}$$

Paramagnetism

Above the Curie temperature, the spontaneous magnetization disappears, but each atom still has a permanent moment, so that when an external magnetic field is applied, there will be an induced magnetization along the direction of the field:

$$M' = ng\mu_B JB(J,\alpha) \tag{1.20}$$

As long as there is a magnetization, there will be a molecular field, so α in this case contains two fields:

$$\alpha = gJ\mu_B(H_a + \lambda M')/k_B T \tag{1.21}$$

When $T \gg T_c$, $\alpha \ll 1$, so equation (1.20) can be expanded as:

$$M' \approx ngJ\mu_B \frac{J+1}{3J}\alpha \tag{1.22}$$

Substituting equation (1.21) into equation (1.22) yields, after some manipulation, the susceptibility:

$$\chi = \frac{M'}{H_a} = \frac{n(J+1)Jg^2\mu_B^2}{3k_B} \frac{1}{T - (\frac{nJ(J+1)g^2\mu_B^2\lambda}{3k_B})} \tag{1.23}$$

If we define: $C = \frac{n(J+1)Jg^2\mu_B^2}{3k_B}$ and $\Delta = \frac{nJ(J+1)g^2\mu_B^2\lambda}{3k_B}$, then equation(1.23) is the Curie-Weiss law:

$$\chi = \frac{C}{T - \Delta} \tag{1.24}$$

Approximation of the Temperature Dependence of the Spontaneous Magnetization

At low temperatures, $T \to 0$, the Brillouin function becomes:

$$B(J,\alpha) \approx 1 - \frac{1}{J}e^{-\alpha/J} \tag{1.25}$$

From equation (1.16) and equation (1.18), the spontaneous magnetization can be obtained:

$$\frac{M(T)}{M_0} = 1 - \frac{1}{J} e^{-\frac{3}{J+1}\frac{T_c}{T}} \tag{1.26}$$

This is not consistent with experimental data.

Another theory, called *spin wave theory*, gives a better result:

$$\frac{M(T)}{M_0} = 1 - aT^{3/2} \tag{1.27}$$

where $a = \frac{0.1174}{z}(\frac{k_B}{A})^{3/2}$, A is the exchange integral, and z is the number of atoms in one primitive cell.

At high temperatures, $\alpha \to 0$, the Brillouin function becomes

$$B(J,\alpha) \approx \frac{J+1}{3J}\alpha - \frac{(J+1)}{3J} \cdot \frac{(2J^2+2J+1)}{30J^2}\alpha^2 \tag{1.28}$$

After some manipulation, the spontaneous magnetization is given by:

$$[\frac{M(T)}{M_0}]^2 = \frac{10}{3} \cdot \frac{(J+1)^2}{J^2+(J+1)^2}(\frac{T_c}{T} - 1) \qquad (T \to T_c) \tag{1.29}$$

More generally, equation (1.29) can be rewritten in the form:

$$\frac{M(T)}{M_0} = [\frac{10}{3} \cdot \frac{(J+1)^2}{J^2+(J+1)^2}]^{\frac{1}{2}}(\frac{T_c}{T} - 1)^{\beta} \tag{1.30}$$

In molecular field theory, $\beta = 1/2$. But many experimental results show that $\beta \approx 1/3$. Further improvement of the theory yields $\beta \approx 1/3$ as well[2].

1.4.2 Free Energy

Anisotropy Energy

(1). *Magnetocrystalline Anisotropy*

Crystal structures with different symmetries have different forms of anisotropy energy. Uniaxial and cubic forms are the most common. For uniaxial symmetry,

the anisotropy energy is given by

$$E_k = V(K_0 + K_1 sin^2\theta + K_2 sin^4\theta + ...) \tag{1.31}$$

where the K_0, K_1, K_2... are crystalline anisotropy constants, θ is the angle between the easy axis and the direction of the magnetization, and V is the volume of the material. For cubic symmetry, the anisotropy energy has the form:

$$E_k = V[K_0 + \frac{K_1}{4}(sin^2 2\theta + sin^4\theta sin^2 2\varphi) + \frac{K_2}{16} sin^2\theta sin^2 2\theta sin^2 2\varphi + ...] \tag{1.32}$$

where (θ,φ) are the orientation angles of the magnetization vector in a spherical coordinate system.

(2). *Shape Anisotropy Energy*

This energy is caused by discontinuities in the magnetization at the surface of the material, which generate a demagnetizing field. Usually an approximation can be written as:

$$E_s = \frac{1}{2V}(N_x m_x^2 + N_y m_y^2 + N_z m_z^2) \tag{1.33}$$

where m_x, m_y,m_z are the components of the magnetic moment along three axes, and N_x, N_y, N_z are the demagnetizing factors.

(3). *Other Anisotropy Energies* Other anisotropy energies include the *surface anisotropy energy* [17], when the magnetic system is composed of single-domain fine particles, and the magnetoelastic anisotropy energy which is caused by the stress inside materials. In the special case when the magnetostriction is isotropic, then for a cubic crystal the magneto-elastic energy takes the form:

$$E_{me} = -\frac{3}{2}\lambda\sigma cos^2\theta \tag{1.34}$$

where λ is the strain, σ is the stress, and θ is the angle between M and σ.

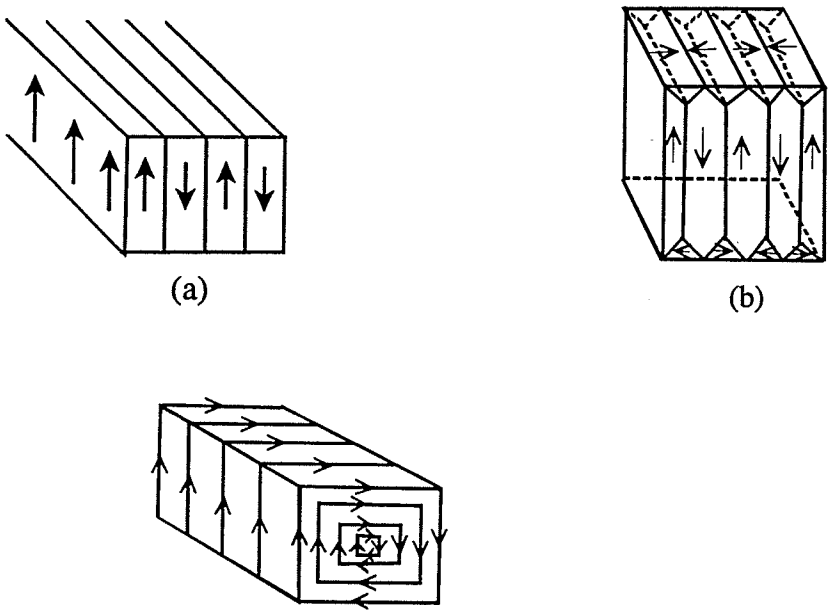

Figure 1.6: *Three domain shapes*

1.4.3 Domain Structure

The existence of domains in magnetic materials is essentially the result of minimizing the free energy. The relevant energies are exchange energy, magnetostatic energy (demagnetizing energy), external magnetic field energy, magnetocrystalline anisotropy energy, and magnetoelastic energy. If a bulk material were not subdivided into domains, the demagnetizing energy would be very large. Usually the demagnetizing energy is the principal impetus for the formation of domains.

Once a bulk material is partitioned into domains, the domain configurations can assume various forms, but the following principal types are observed: (a) open flux, (b) closed flux, (c) rotating flux [5], as shown in figure (1.6).

In part (a) of figure (1.6), the demagnetizing energy still exists, because there is a magnetization discontinuity on the surfaces, but it is much smaller than if there were no subdivision into domains. The free energy contains mag-

netostatic energy, domain wall energy, no magnetocrystalline energy (since the magnetization is along the easy axis), no magnetoelastic energy (strain), and no intra-domain exchange energy(since the neighbouring atomic moments are aligned parallel).

In part (b) of figure (1.6), there is no demagnetizing energy, because the magnetic flux is closed inside the sample. If the material has cubic symmetry, the moments are along the easy axes, so there is no crystalline anisotropy energy. The main energies are domain wall energy and magnetoelastic energy which is due to the fact that the closure domains are unable to deform freely under the spontaneous stress exerted by the principal domains (the bigger domains). When the material has uniaxial symmetry, magnetocrystalline anisotropy energy must be included.

In part(c) of figure (1.6), the atomic moments gradually rotate in a continuous manner, and the magnetic flux is closed inside, so there is no demagnetizing energy, no domain wall energy, but exchange energy must be considered. This type of domain structure is not common.

1.4.4 Single Domain Particles

Generally speaking, in magnetic systems, all forms of energy contribute to the final structure, which corresponds to a local minimum in the total free energy. Multidomain structure is one possible final state. From the discussion above, we can see that many of the energy terms depend on the dimensions of the specific magnetic sample. When the dimensions reach some lower critical value, the particle can assume a single domain structure. This can be seen from the following simple model [6].

For a spherically shaped particle, there are two kinds of energy to consider:

exchange energy and magnetostatic energy. The magnetostatic energy is

$$E_s = \frac{V}{2}NM^2 = \frac{1}{2}(\frac{4\pi}{3}R^3)(\frac{4\pi}{3})M^2 \tag{1.35}$$

where R is the radius of the sphere, $\frac{4\pi}{3}$ is the demagnetizing factor in CGS units, and M is the magnetization. To calculate the exchange energy for a configuration in which the atomic moments point along closed rings about a common axis, the sphere is divided into small cylinders, each cylinder being composed of many rings. This simple model gives the following expression for the exchange energy:

$$E_{ex} = \frac{4\pi AR}{a}[ln\frac{2R}{a} - 1] \tag{1.36}$$

where a is the interatomic distance, A is the exchange constant, and R is the radius. When the energy in equation (1.35) and the energy in equation (1.36) reach a balance, we obtain a critical radius for the sphere. When the particle is smaller than this value, the whole particle is a single domain. Otherwise the magnetostatic energy turns out to be bigger, and as a result the particle must be multidomain in order to decrease the total energy.

1.5 Magnetizing and Magnetization Reversal Processes

1.5.1 The Magnetizing Process

The magnetizing process is a mixture of domain wall motion and magnetic moment rotation. Roughly speaking, there are four stages in the magnetizing process as shown in figure (1.7):

(1). Reversible domain wall motion:

When the external applied field is small, domains which are oriented in the same direction as the field will expand by domain wall motion. After the field is re-

moved, the domain walls resume their original positions, so that the initial part of the magnetization curve is reversible.

(2). Irreversible Domain Wall Motion and Barkhausen Jumps:

With a further increase in the applied field, the magnetization will experience sudden and discontinuous changes, which are caused by the sudden motion of domain walls or a sudden change in the domain configuration. The former effect is called the *Barkhausen effect* (figure (1.8); the latter is a sudden change in the topological structure of the domains. Both mechanisms are irreversible.

(3). Rotation of Magnetic Moments within Domains:

Here, the increase of magnetization is mainly caused by the rotation (reversible and irreversible) of domain moments as they reorient along the direction of the external field.

(4). Approach to Saturation:

A rather large increase in H_a produces only a relatively small increase in M.

The above subdivision is somewhat arbitrary, because wall motion and rotation are not sharply divisible processes.

1.5.2 Magnetization Reversal

The process of demagnetizing a magnetic material from the saturation state to the zero magnetization state by applying a reverse field is called the magnetization reversal process. It includes domain wall motion and nucleation, and moment rotation (reversible or irreversible). The coercivity in this process is associated only with the irreversible processes.

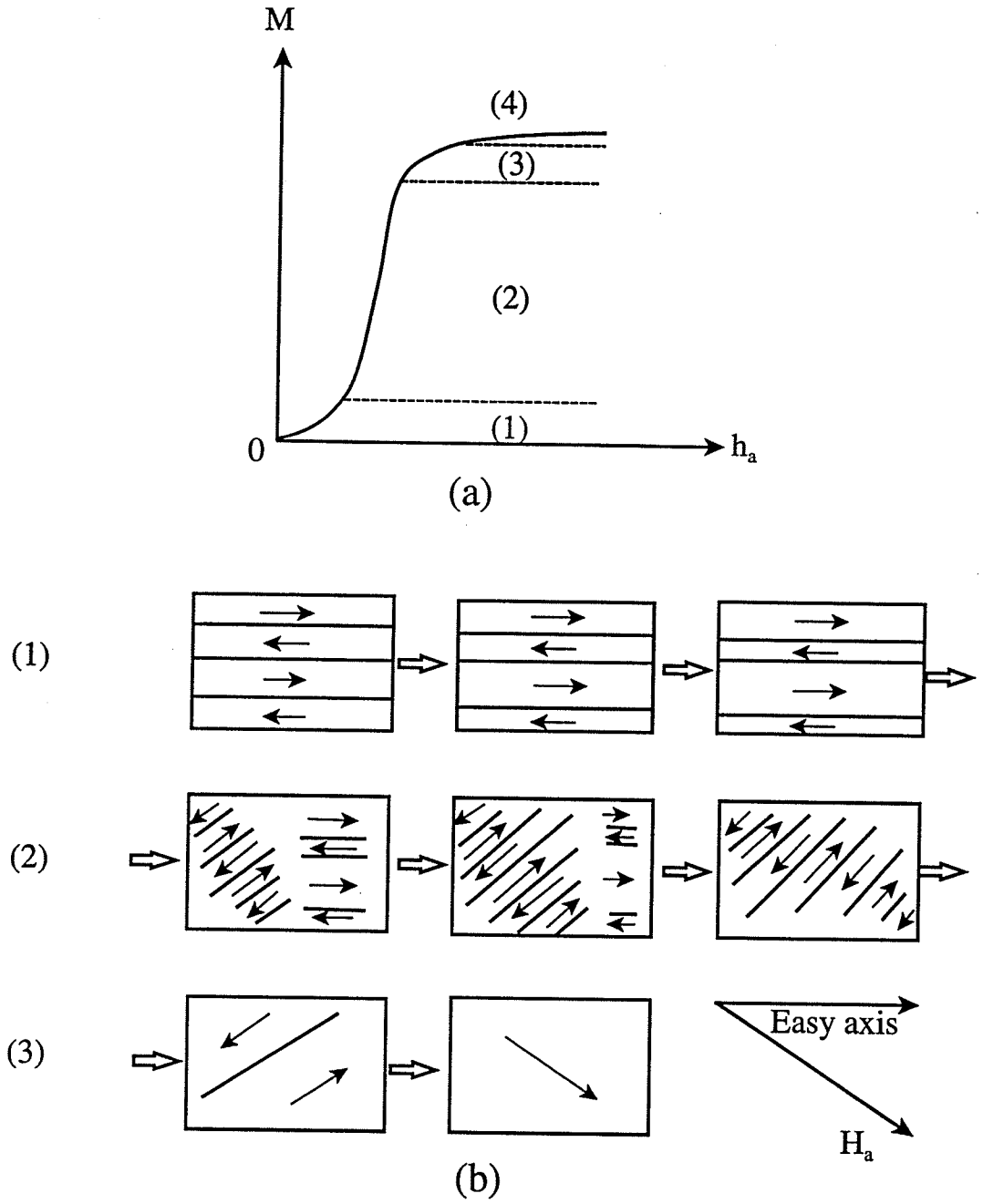

Figure 1.7: *Magnetization process: the regions (1), (2) and (3) in part (a) correspond to the magnetic domain structures of pictures (1), (2) and (3) in part (b).*

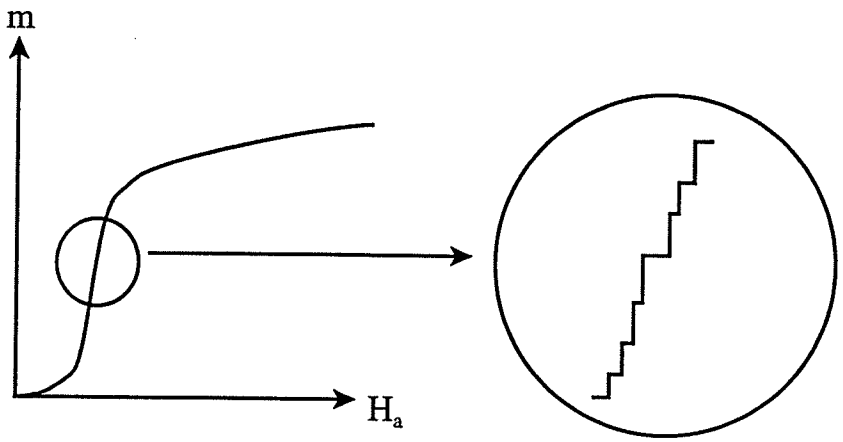

Figure 1.8: *Barkhausen jumps*

(1). Coercivity Dominated by Irreversible Domain Wall Motion:

If the material has a multidomain structure, then when the external magnetic field is reduced from its saturation value, domains which favour minimization of the system free energy will nucleate and grow. At the same time, hindrances try to prevent the wall motion. If the field is sufficient big, the magnetization will experience a series of Barkhausen jumps. Since wall motion through a distance x is equivalent to a change in magnetization, the critical field is proportional to the maximum gradient of the system free energy:

$$H_0 \propto \frac{\partial E}{\partial x} \tag{1.37}$$

where the free energy E includes the domain wall energy and its adjoining domain energy. The hindrance to the domain wall motion may come from different sources, such as inclusions, micro-stress, and so on.

Consider an example of a 180^0 domain wall, shown in figure (1.9)([2], p333). Part (a) represents the system free energy E as a function of domain wall position x. The gradient of the energy with respect to x is shown in part (b). At $H_a = 0$, the wall is at position 1, in an energy minimum. As H_a is increased from zero, the

wall moves reversibly to 2. If the field is removed, the wall returns to 1. Position 2 is a point of maximum energy gradient; if the field is sufficient to move the wall to 2, it is sufficient to cause the wall to make an irreversible jump to 3, which is the only point ahead of the wall with an equally strong restoring force. This is a Barkhausen jump. If the field is reduced to zero, the wall will go back, not to point 1, but to point 4, which is the nearest zero field energy minimum, thus exhibiting the phenomenon of hysteresis and remanence. A reverse field will then drive the wall reversibly from 4 to 5, and by another Barkhausen jump from 5 to 6. If the diagram in (b) is rotated through 90^0, it takes the form of the elementary hysteresis loop in (c).

The hysteresis loop of a real specimen is a sum of a large number of elementary loops which represent the response from all domain wall motions, summed over the whole volume of the specimen. The coercivity of the specimen is the average of all the critical fields of the different domain growth instabilities. The argument here is the background underlying the Preisach model, which divides a magnetic system into small, elementary bistable subsystems.

When stress is important, the coercivity due to domain wall motion is given by the model in [5](p324):

$$H_0 = \frac{3}{2}\frac{\lambda_s \Delta\sigma}{\mu_0 M_s cos\theta}\frac{\delta}{l} \tag{1.38}$$

where λ_s is the magnetostriction, σ is the stress, δ is the width of the domain wall, and l is the wavelength of the stress distribution. Thus, the coercivity is proportional to the product of the stress and the magnetostriction.

When *inclusions* are important, the model yields the coercivity :

$$H_0 \approx p^{'}\frac{K_1}{\mu_0 M_s}\beta^{3/2} \tag{1.39}$$

where $p^{'} = \delta/d$, d is the diameter of the inclusion, $\delta = \gamma/K_1$, γ is the domain

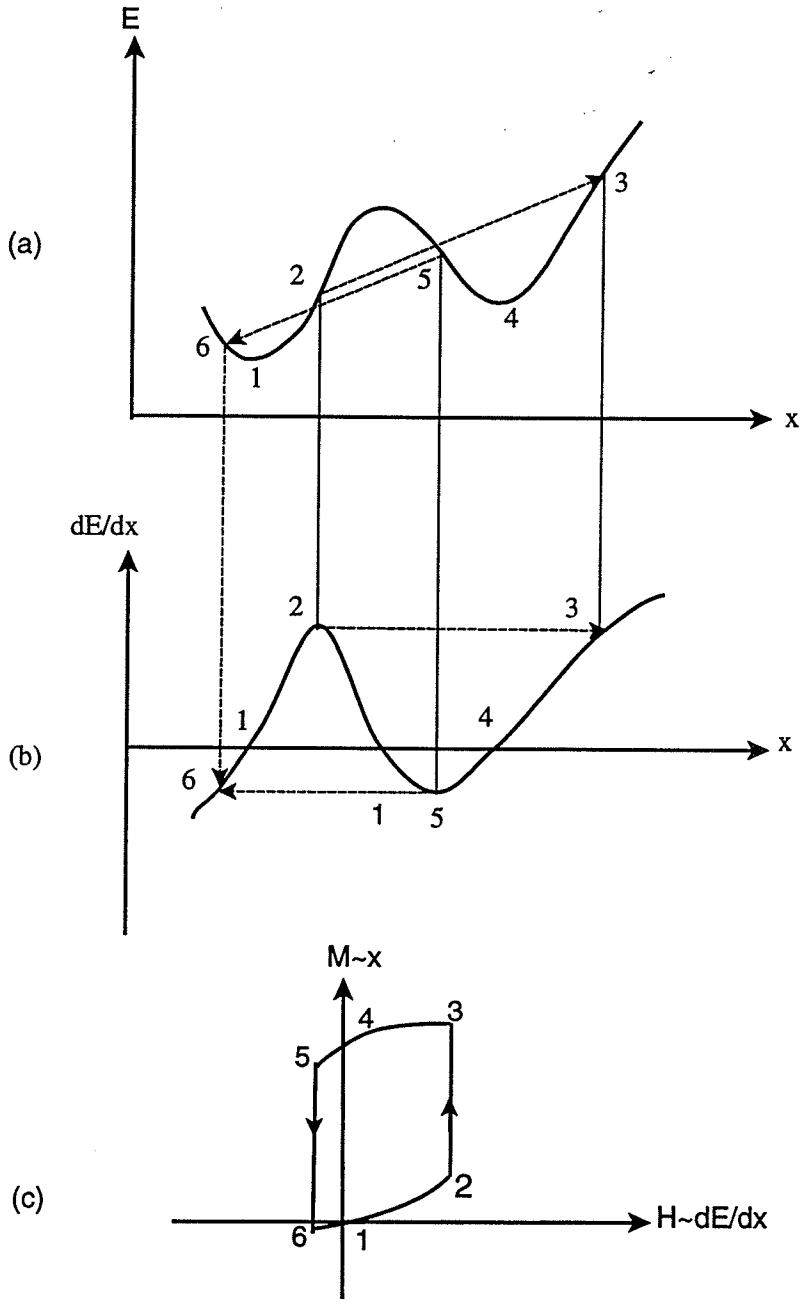

Figure 1.9: *Reversible and irreversible domain wall motion*

wall energy per unit area, and K_1 is the anisotropy constant. Thus, the critical field is proportional to the density of inclusions and to the anisotropy constant.

(2). Coercivity Dominated by Magnetic Moment Rotation in Single Domain Particles:

The coercivity and the magnetization reversal mechanism in bulk materials composed of fine particles depends on many factors; the size, the anisotropy,and the packing density of particles play important roles. First we discuss here the coercivity of a single particle, and later the reversal mechanism of bulk materials.

Coercivity of a Single Particle

(a). Coherent Rotation:

The coherent rotation mode was proposed by Stoner and Wohlfarth [7]. In this mode, the spins of all the atoms in the particle remain parallel to one another throughout the rotation. Assume a single-domain particle with a prolate spheroidal shape and with uniaxial crystal anisotropy, as shown in figure (1.10). The spontaneous magnetization is M_s, and all the spins in the particle rotate coherently in response to the applied field. The total energy has two terms, anisotropy energy and magnetostatic energy:

$$E = K_u sin^2\theta + H_a M_s cos(\alpha - \theta) \tag{1.40}$$

Minimizing E with respect to θ for a fixed α, which is the direction of the external field with respect to the easy axis, yields a series of hysteresis loops (figure (1.10)). When the applied field is along the direction of the easy axis($\alpha = 0$), the hysteresis loop is a rectangle with critical field (in C.G.S units) :

$$H_0 = 2K_u/M_s. \tag{1.41}$$

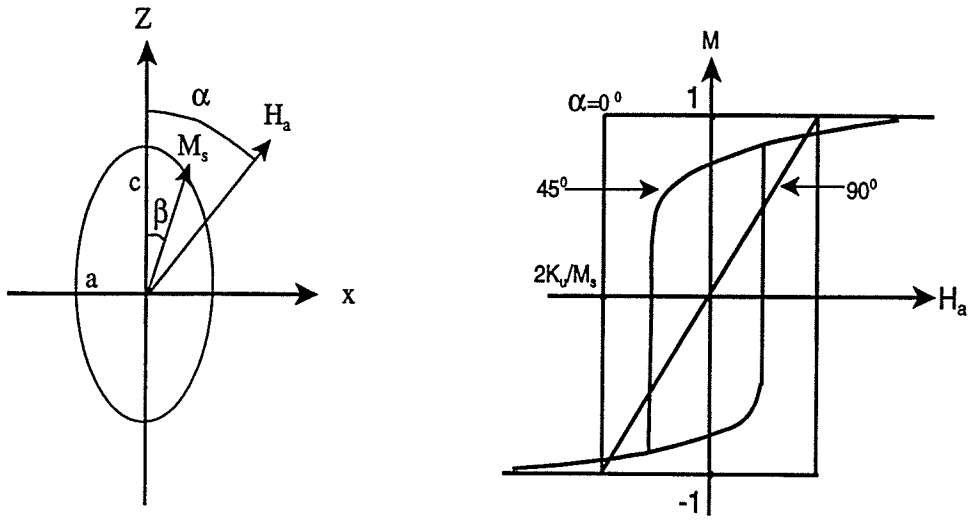

Figure 1.10: *Coherent rotation of the magnetization in an ellipsoidal particle, and hysteresis loops*

When the field is perpendicular to the easy axis ($\alpha = 90^o$), there is no hysteresis at all. At all other angles α, the loops lie between these two extremes. K_u in equation (1.41) has different forms depending on the source of the anisotropy.

When the applied field is along the easy axis of a single domain particle, and if the anisotropy is shape-dominated, the critical field has the form:

$$H_0 = 2(N_a - N_c)/M_s \tag{1.42}$$

where N_a and N_b are the demagnetizing coefficients parallel to the a and c axes. If the anisotropy is stress-dominated, the critical field is:

$$H_0 = 2\frac{3\lambda_{si}\sigma}{M_s} \tag{1.43}$$

where λ_{si} is the saturation magnetostriction for isotropic materials, and σ is the stress. If the anisotropy is crystalline anisotropy-dominated, the critical field is:

$$H_0 = \frac{2K_1}{M_s} \tag{1.44}$$

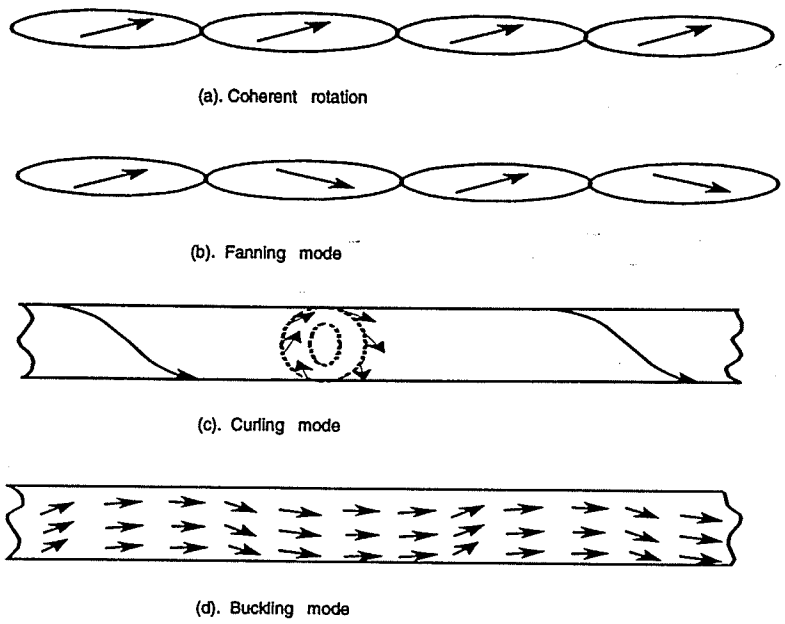

Figure 1.11: *Spin reversal modes in single domain particles*

where K_1 is the crystal anisotropy constant.

(b). Incoherent Rotation

The coherent rotation mode cannot explain the coercivity of a chain of Fe particles prepared by electro-deposition. Other spin rotation modes such as the *fanning mode*, the *curling mode*, and the *buckling mode* were developed, as shown in figure (1.11).

Fanning mode: In part (b) of figure (1.11), a long particle is modelled as a chain of ellipsoids. The spontaneous moments M_s of successive ellipsoids in the chain fan out in a plane by rotating in opposite directions in alternate ellipsoids. In this mode, some exchange energy is introduced, but exchange energy is essentially short ranged, so that the spins contributing to this energy form only a small fraction of the total. Thus the total exchange energy is considered to be small.

Curling mode: In part (c) of figure (1.11), a long particle is modeled as a cylinder. During the reversal process, the spins are always parallel to the surface, so that no free poles are formed and no magnetostatic energy is involved.

Buckling mode: In part (d) of figure (1.11), the spin rotation forms a "wave" along the cylinder.

Among all these spin rotation modes, the one which dominates depends on the diameter of the particle, and coherent rotation always gives the largest coercivity.

Coercivity of an assembly of single-domain particles

When magnetic particles are packed in a non-magnetic binder, the coercivity of the assembly is independent of packing factor p (the volume fraction of magnetic particles) only when the anisotropy of each individual particle is not shape anisotropy-dominated. When shape anisotropy is important, the coercivity of the assembly is related to the single particle coercivity by

$$H_{ci}(p) = H_{ci}(0)(1-p) \tag{1.45}$$

where H_{ci} is the coercivity of an isolated particle.

1.6 Thermal Relaxation

1.6.1 Superparamagnetism of Fine Particles

Up to now, we have not taken into account the thermal fluctuation energy. If the size of the fine particles is sufficiently small, thermal energy will be large enough to overcome the anisotropy barrier, and thus reverse the magnetic state freely. When a field is applied, the moments tend to align along the direction of the field, so the system will behave like a paramagnet. This phenomenon is called *superparamagnetism*. The only difference between *paramagnetism* and *superparamagnetism* is that the moment per atom or ion in a paramagnet is only a few μ_B, but the moment per particle in superparamagnetic assemblies is much bigger. The various regions of magnetic behaviour with respect to the size of fine particles

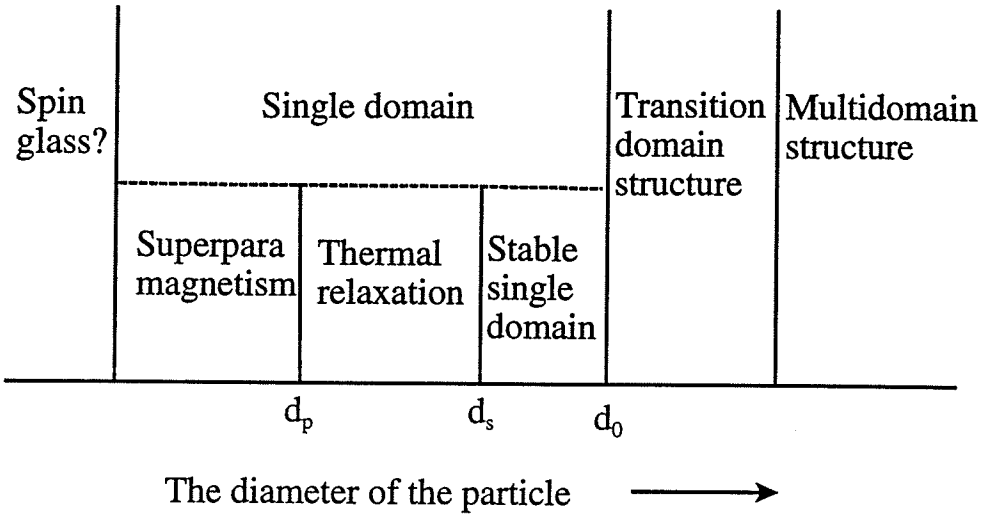

Figure 1.12: *Response of magnetic behaviour as a function of particle size*

is shown in figure (1.12), where d_p is critical size for superparamagnetism, d_s is the critical size separating the thermally activated regime and the stable single domain structure, and d_0 is the critical size separating the multidomain structure and single domain structure. The following simple model yields a picture of the behaviour of superparamagnetic particles. Consider n particles with uniaxial anisotropy, each with a moment μ, and ignore interactions between the particles. All the easy axes of the particles are aligned in the same direction. Then the magnetization of the system at equilibrium at temperature T is

$$M(T) = n\frac{\mu e^{\frac{-\mu H_a}{k_B T}} - \mu e^{\frac{\mu H_a}{k_B T}}}{e^{\frac{-\mu H_a}{k_B T}} + e^{\frac{\mu H_a}{k_B T}}} = n\mu * tanh(\frac{\mu H_a}{k_B T}) \tag{1.46}$$

where k_B is Boltzmann constant, and there is no hysteresis.

1.6.2 Thermal Relaxation and Blocking

Hysteresis will appear when particles of a certain size are cooled to a particular temperature. Suppose an assembly of uniaxial particles has been brought to some

initial state of magnetization M_i by an applied field, and the field is turned off at $t = 0$. Some particles in the assembly will immediately reverse their magnetization, and the magnetization of the assembly will begin to decrease. The rate of decrease is proportional to the magnetization at that time and to the Boltzmann probability $e^{-\frac{KV}{k_BT}}$.

$$\frac{dM}{dt} = f_0 M e^{-\frac{KV}{k_BT}} = \frac{M}{\tau} \tag{1.47}$$

where f_0 is a frequency factor and has a value of about $10^9 sec^{-1}$, and τ is the relaxation time defined by:

$$\tau = \frac{1}{f_0} e^{\frac{KV}{k_BT}} \tag{1.48}$$

Integrating equation (1.47) gives the magnetization at time $t > 0$:

$$M(t) = M_i e^{-\frac{t}{\tau}} \tag{1.49}$$

Here, the meaning of τ becomes apparent. It is in fact the time when the magnetization drops to $\frac{1}{e}$ of the initial value. Suppose that the observation time in an experiment is typically 100 seconds. Then the corresponding critical volume V_p and the related anisotropy barrier of the particle can be obtained from equation (1.48):

$$KV_p = \ln(\tau f_0) k_B T = ln(10^2 * 10^9) k_B T \simeq 25 k_B T \tag{1.50}$$

The *effective thermal field* can be obtained from $H_T^* M(T) = 25 k_B T$ so

$$H_T^* = 25 k_B T / M(T) \tag{1.51}$$

If the particles have a unique size, there will be a unique temperature T_B, called the *blocking temperature*, below which the magnetization will be stable. From (1.50):

$$T_B = \frac{KV_p}{25 k_B} \tag{1.52}$$

1.6.3 The Effect of Thermal Relaxation on the Coercivity

Thermal energy effectively lowers the height of the energy barrier between two energy minima. When a field is applied in an attempt to activate the moment from one state to another, thermal activation will help, and the coercivity will be less than the intrinsic one. Consider an assembly of uniaxial particles with their easy axes parallel to each other. A field is applied to try to reverse the magnetization. The total energy is:

$$E = V(Ksin^2\theta + HM_scos\theta) \tag{1.53}$$

where K is the anisotropy constant, V is the volume of the particle, M_s is the spontaneous moment of each particle, H_a is applied field, and θ is the angle between the applied field and the moment. The energy maximum and energy minimum are given by $\frac{\partial E}{\partial \theta} = 0$. When $sin\theta = 0$, the minimum energy is:

$$E_{min} = VHM_s \tag{1.54}$$

The maximum energy occurs when $cos\theta = \frac{HM_s}{2K}$:

$$E_{max} = KV[1 + (\frac{HM_s}{2K})^2] \tag{1.55}$$

The energy barrier is

$$\Delta E = E_{max} - E_{min} = KV(1 - \frac{HM_s}{2K})^2 \tag{1.56}$$

Now consider the effect of thermal activation. For a time constant of 100 seconds, at a temperature T, the thermal activation energy will be $25k_BT$. If this energy is big enough to overcome the barrier, the moment will be reversed, and the applied field at this critical value will be the coercivity. i.e.:

$$\Delta E = KV(1 - \frac{H_cM_s}{2K})^2 = 25k_BT \tag{1.57}$$

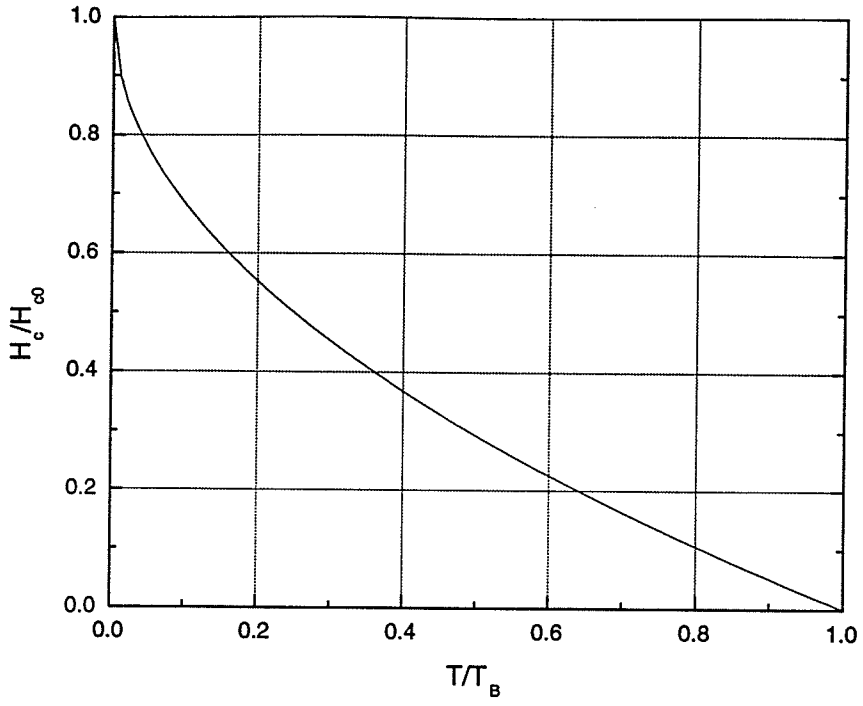

Figure 1.13: *Temperature dependence of the coercivity of single-domain fine particles*

The coercivity is thus

$$H_c = \frac{2K}{M_s}[1 - (\frac{25k_BT}{KV})^{1/2}] \tag{1.58}$$

When V is very large or when T approaches zero, H_c approaches $2K/M_s$. If we define $H_{c0} \equiv 2K/M_s$, substitute equation (1.52) into equation (1.58), and remember that particles of the critical size V_p have zero coercivity at their blocking temperature, the coercivity is then:

$$H_c = H_{c0}[1 - (\frac{T}{T_B})^{1/2}] \tag{1.59}$$

If we ignore the temperature dependence of the anisotropy constant K, the dependence of the coercivity on temperature is shown in figure (1.13). Once we include the temperature dependence of K, or a distribution of orientations, or mixed anisotropies, the result is difficult to calculate, but the thermal contribution to the evolution of the coercivity continues to have two parts: the temperature

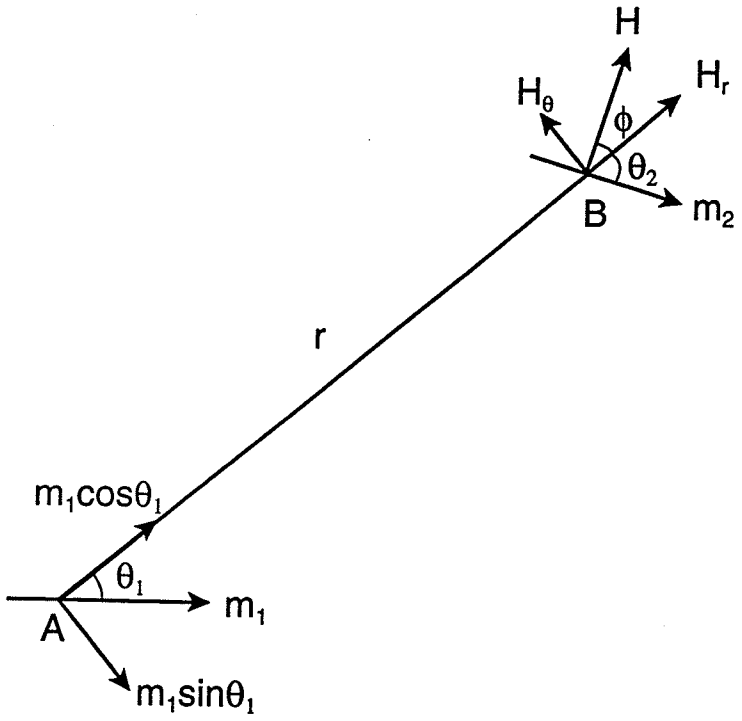

Figure 1.14: *Dipole-dipole interaction*

dependence of the intrinsic anisotropy barrier and thermal activation.

1.7 Inter-particle Interactions

In an assembly of fine particles, there are different kinds of interactions between the particles. The principal interactions are the dipole-dipole interaction, the exchange interaction, the superexchange interaction, and the RKKY interaction.

1.7.1 Dipole-dipole Interactions

A magnetic particle can be approximately treated as a magnetic dipole with a magnetic moment m. Consider two such dipoles m_1 and m_2 separated by a distance r. The magnetic field generated by the dipole m_1 at position B has two components (refer to figure (1.14)).

The component parallel to r is

$$H_r = \frac{2m_1 \cdot cos\theta_1}{r^3} \tag{1.60}$$

The component perpendicular to r is:

$$H_{\theta_1} = \frac{m_1 \cdot sin\theta_1}{r^3} \tag{1.61}$$

The total field H is

$$H = (H_{\theta_1}^2 + H_r^2)^{1/2} = \frac{m_1}{r^3}(3cos^2\theta_1 + 1)^{1/2} \tag{1.62}$$

The potential energy of another dipole m_2 in such a field H is

$$E_p = \frac{m_1 m_2}{r^3}[cos(\theta_1 - \theta_2) - 3cos\theta_1 cos\theta_2] \tag{1.63}$$

The potential energy of dipole m_1 in the field generated by dipole m_2 has the same form. So equation (1.63) is the mutual interaction energy of the two dipoles.

1.7.2 Direct Exchange Interactions and Superexchange Interactions

Direct exchange operates between atomic moments which are close enough to have sufficient overlap of their atomic wave functions. If two atoms i and j have spin angular momenta $\vec{S}_i h/2\pi$ and $\vec{S}_j h/2\pi$, respectively, then the exchange energy is

$$E_{ex} = -2J_{ex}\vec{S}_i \cdot \vec{S}_j = -2J_{ex}S_i S_j cos\phi \tag{1.64}$$

where J_{ex} is an exchange integral, which occurs in the calculation of the exchange effect, and ϕ is the angle between the spins. If J_{ex} is positive, E_{ex} is a minimum when the spins are parallel ($cos\phi = 1$) and a maximum when they are anti-parallel ($cos\phi = -1$) . A positive value of the exchange integral is therefore a necessary condition for ferromagnetism to occur.

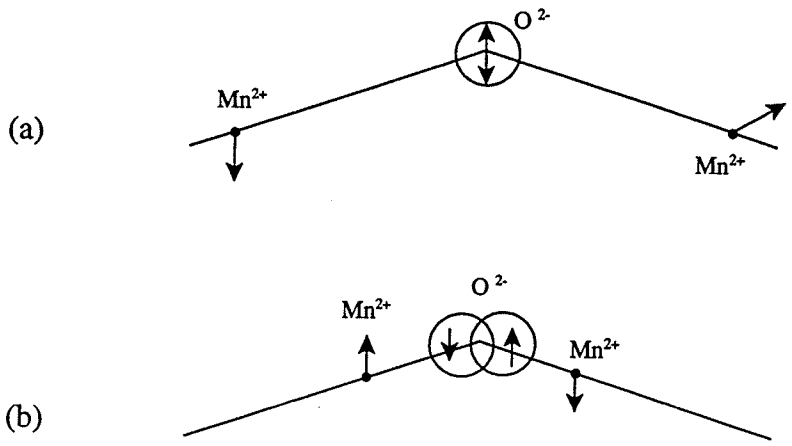

Figure 1.15: *Superexchange interaction*

Superexchange describes the interaction between moments on ions which are too far apart to be connected by direct exchange, but which are coupled over a relatively long distance through a non-magnetic medium. Consider, for example, two ions Mn^{2+}, which are randomly oriented, being brought up to an O^{2-} ion from a large distance, as in figure (1.15)(a). The O^{2-} has no net moment, because it has a neon-like structure of filled shells. But imagine that the outer electrons of the oxygen ion constitute two superposed orbits, one with a net spin up, the other with a net spin down, as in figure (1.15)(a). When a manganese ion with spin up is brought close to the oxygen ion, the spin up part of the oxygen ion will be displaced as in figure (1.15)(b), because parallel spins repel one another. If now another manganese ion is brought up from the right it is forced to have spin down when it comes close to the spin up side of the "unbalanced" oxygen ion. As an result, the spins of the two manganese ions turn out to be oriented antiparallel oriented[2].

1.7.3 The RKKY Interaction

The RKKY interaction is essentially a kind of indirect exchange interaction which couples moments over relatively large distances. It is the dominant exchange interaction in metals where there is little or no direct overlap between neighbouring magnetic electrons. It therefore acts through an intermediary, which in metals is the conduction electron gas (the itinerant electrons). The RKKY interaction was named after Ruderman, Kittel, Kasuya and Yoshida and is given by

$$H_{RKKY} \equiv -2J(R_{12})\vec{S}_1 \cdot \vec{S}_2 \tag{1.65}$$

where R_{12} is the distance between two magnetic ions, $J(R_{12}) \sim \frac{cos(k_F R_{12}+\delta)}{R_{12}}$ is the exchange integral, $\vec{S}_1$ and $\vec{S}_2$ are the spins of the localized electrons, k_F is the Fermi wave vector of the conduction electrons, and δ is a phase factor. It can be seen that $J(R_{12})$ oscillates from positive to negative as the separation of the ions changes, and has a damped oscillatory shape. Therefore, depending on the separation between a pair of ions, their magnetic coupling can be ferromagnetic or antiferromagnetic. A magnetic ion induces a spin polarization in the conduction electrons in its neighbourhood. This spin polarization in the itinerant electrons is communicated to other magnetic ions far away, leading to an indirect coupling.

Chapter 2

A Preisach Model for Interpreting Hysteresis

This thesis describes the analysis of the irreversible response of several different magnetic materials. The theoretical basis for the analysis is the Preisach model of hysteresis. The model was first formulated in 1935[8], and the basic properties of both the scalar and vector versions have been described in the literature in considerable detail[9][10][11][12].

In this chapter we describe a generalized version of the Preisach model which we have been developing over the past few years, for the purpose of interpreting the irreversible response of magnetically ordered materials, and studying its relationship to the critical component of the response, over a wide range of temperatures which extend from $T = 0K$ up to the critical ordering temperature $T = T_c$.

2.1 Basic Philosophy and Justification

The vast majority of magnetic materials which form the subject of current investigation, whether for fundamental or technological reasons, are *magnetically ordered*, in the sense that they possess a characteristic critical temperature T_c at which the permanent atomic moments undergo a sudden, spontaneous, coop-

erative alignment, driven by the exchange interaction. Below T_c. the material consists of uniformly magnetized regions, which may be either discrete particles or magnetic domains, or some mixture of these. In general, the state of a magnetic system in a given field h_a at a given temperature T cannot be completely specified by global response functions such as the total system moment m, since each value of m can be realized by a multiplicity of distinct configurations of uniformly magnetized regions. Each of these configurations is metastable in the sense that it corresponds to a local minimum in the free energy landscape in a multidimensional configuration space. These metastable minima are separated by energy barriers, due to anisotropy and domain wall pinning effects which trap the system temporarily in a particular configuration and prevent it from exploring all of its configuration space ergodically, and thus from reaching thermal equilibrium within the time scale t_{exp} of a given experiment. Each energy barrier W is characterized by a *blocking temperature* $T_B < T_c$, below which thermal fluctuations are insufficient to excite an overbarrier transition. Furthermore, the free energy landscape itself depends explicitly on temperature, and all of the free energy barriers must collapse along with the spontaneous moment of the domains or particles as the critical temperature is approached from below. Thus, in response to changes in field or temperature, the system evolves from one configuration to another along a very complex path in a multivalleyed configuration space, driven in part by field-induced distortions of the free energy landscape which extinguish local transition barriers, and in part by thermal overbarrier activation events. This path is highly sensitive to the precise sequence of application of the external stimuli, as well as to the time scale t_{exp} of the experiment, and this situation is reflected in the multivaluedness of experimental response functions such as the total system moment $m(h_a, T)$, a phenomenon known as *hysteresis*.

Micromagnetics represents an attempt to "map out" this free energy land-

scape explicitly in some appropriate multi-dimensional configuration space. The material is subdivided into many elementary volumes, each large compared to the interatomic spacing but small on the scale over which the magnetization vector changes significantly. A given elementary volume ΔV around point $\vec{r}$ is assigned a local anisotropy axis $\hat{n}(\vec{r})$, and a local magnetization vector $\vec{m}(\vec{r})$ which has the same magnitude for all volume elements, but variable orientation. The free energy $\Delta G(\vec{m}(\vec{r}), h_a, T)$ of each element includes contributions from anisotropy, magnetostatic energy, applied free energy, and exchange energy between neighbouring elements, and the free energy G of the entire material is minimized, with respect to orientation changes in all the local magnetization vectors $\vec{m}(\vec{r})$. A local minimum in the G hypersurface represents an allowed metastable configuration of the system, represented by specifying the entire vector field $\vec{M}_{ms}(\vec{r})$ at all points $\vec{r}$ in the material.

In the Preisach approach to hysteresis, the focus is still on the free energy landscape, but the emphasis is placed almost entirely on the sudden discontinuous transitions between metastable states, usually termed Barkhausen events, which occur whenever an occupied local minimum in the energy landscape is extinguished, since this is where the characteristics of the measured irreversible response of a material are most directly encoded. Furthermore, macroscopic hysteresis is not a local property of a material, but rather is a characteristic of the entire specimen under investigation, which necessarily involves a spatial average over volumes containing many uniformly magnetized elements(domains or particles). As a consequence, many of the details of specific microscopic mechanisms and specific microstructural features tend to be "washed out" in the averaging process, leaving only a few dominant physical ingredients which are best characterized by their statistical properties. Thus, the basic idea is to describe a single elementary Barkhausen instability associated with, say, the irreversible motion of

a certain segment of a domain wall, by a single degree of freedom, and then to assemble the overall behaviour by superposing the contributions from very many such independent elements, whose properties are given by a probability distribution which, by hypothesis, is an inherent property of the system, prescribable in advance, and independent of the specific magnetization trajectory. While a description based on an ensemble of bistable elements is clearly incapable of yielding a point-by-point configuration vector field $\vec{M}(\vec{r})$ of the micromagnetic type, it nevertheless embodies many subtle and complex features observed in real magnetic materials (like nonlocal memory–the existence of many microscopic configurations for each macroscopic state, defined by the applied h_a , and the total moment m). It may thus offer a fruitful avenue to explore in the pursuit of fundamental principles on which to found a general description of hysteresis.

2.2 The Preisach Model

2.2.1 The Decomposition

As mentioned above, the Preisach model decomposes all magnetic systems into an ensemble of bistable subsystems, each characterized by a moment μ, two states $\phi = \pm\mu$, and a double well free energy profile with two zero field transition barriers W_+ and W_-, as shown in figure (2.1).

The barriers can be represented either by their equivalent fields:

$$\alpha = W_-/\mu \tag{2.1}$$

and

$$\beta = -W_+/\mu \tag{2.2}$$

or by a coercive field

$$h_c = (W_+ + W_-)/2\mu \tag{2.3}$$

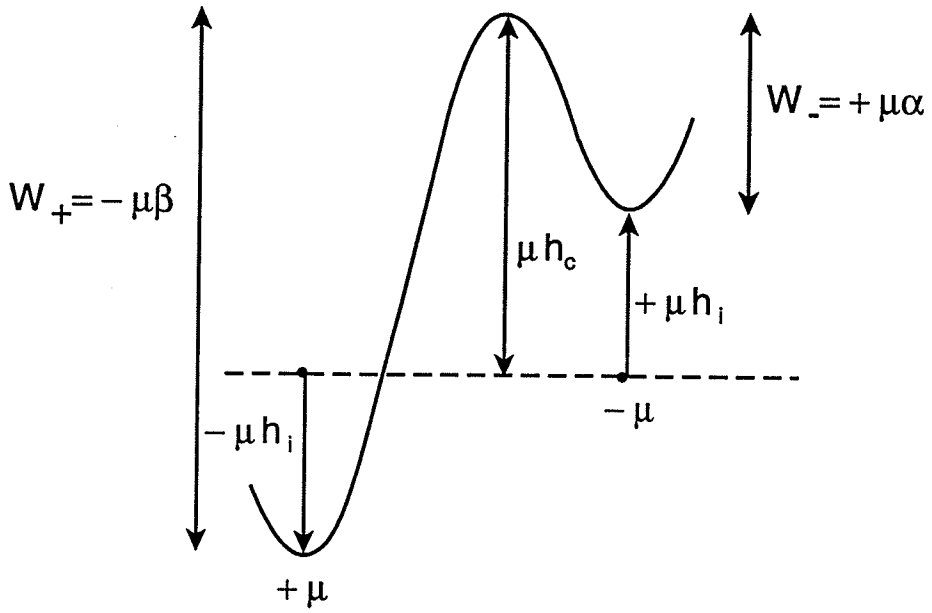

Figure 2.1: *The free energy profile in zero applied field for an elementary Barkhausen subsystem, with two states* $\phi = \pm\mu$ *separated by energy barriers* $W_- = \mu\alpha = \mu(h_c - h_i)$ *and* $W_+ = -\mu\beta = \mu(h_c + h_i)$.

and an asymmetry field

$$h_i = (W_+ - W_-)/2\mu \tag{2.4}$$

In essence, the model reduces the magnetizing process to a sequence of elementary Barkhausen instabilities of magnitude μ. The coercive field h_c functions like an *intrinsic anisotropy field*, which stabilizes the two moment orientations $\phi = \pm\mu$, and measures the energy *dissipated* as heat in a Barkhausen transition[1], while the asymmetry field h_i behaves like a *local interaction field* due to neighbouring subsystems, which lifts the degeneracy of the two valleys, and measures the *energy stored* in a transition[1]. A given magnetic material is identified by a particular *distribution* $f(W_+, W_-)$ of free energy barriers,or equivalently by a distribution of the characteristic fields, either $p(\alpha, \beta)$ or $p(h_c, h_i)$.

2.2.2 Inter-State Transitions

Transitions between the two states of a subsystem require excitation over the barriers $W_{\pm}$ by some combination of *field energy* and *thermal energy*. In particular, the application of an external field h_a shifts the energy of the $\phi = +\mu$ state by $-\mu h_a$, and the energy of $\phi = -\mu$ state by $+\mu h_a$, and thus modifies all the subsystem energy barriers from $W_{\pm}$ to

$$W'_{+} = -\mu(\beta - h_a) \tag{2.5}$$

and

$$W'_{-} = \mu(\alpha - h_a) \tag{2.6}$$

For subsystems with $\beta > h_a$, $W'_{+} < 0$, and only the $\phi = -\mu$ state is accessible. Similarly, for subsystems with $\alpha < h_a$, $W'_{-} < 0$, and only the $\phi = +\mu$ state is accessible. All subsystems with ($h_a < \alpha < \infty$, $-\infty < \beta < h_a$) are *bistable* in the sense that they have *two* accessible states and *two* positive energy barriers $W'_{\pm} > 0$. For the bistable subsystems, transitions may also be induced thermally if the system is at finite temperature T. For an experiment with a characteristic time constant t_{exp} , thermal transitions at temperature T are limited to those barriers which are less than or equal to the *effective thermal fluctuation energy*, defined by

$$W^*(T) = k_B T ln(t_{exp}/\tau_0) \tag{2.7}$$

These thermal transitions may also be described by an *equivalent thermal viscosity field* h^*_T:

$$h^*_T = W^*(T)/\mu = (k_B T/\mu) ln(t_{exp}/\tau_0) \tag{2.8}$$

which defines the maximum equivalent *field barrier* which can be activated at temperature T. Since each bistable subsystem has two energy barriers, a large

barrier:

$$W_L = \mu(h_c+ \mid h_i + h_a \mid) \tag{2.9}$$

and a small barrier:

$$W_S = \mu(h_c- \mid h_i + h_a \mid) \tag{2.10}$$

there are two thermal excitation conditions, $W^* = W_L$, which yields:

$$h^*_{TL} = h_c+ \mid h_i + h_a \mid \tag{2.11}$$

and $W^* = W_S$, which yields:

$$h^*_{TS} = h_c- \mid h_i + h_a \mid \tag{2.12}$$

Both the field and thermal excitation conditions can be represented graphically in the Preisach plane[1][8], in which each subsystem is located with respect to orthogonal coordinate axes by either its characteristic fields (h_c, h_i) or by the equivalent fields (α, β) which reduce the barriers $W'_{\pm}$ to zero. Figure (2.2) shows the Preisach plane in a positive field $h_a > 0$, at a finite temperature T. The quadrant enclosed between the boundaries $\alpha = h_a$ and $\beta = h_a$ contains the bistable subsystems, which can potentially occupy either state $\phi = \pm\mu$. For a given temperature T, there are two thermal excitation boundaries, the dashed boundaries h^*_{TS}, which identify those subsystems whose lower energy barrier matches $W^*(T)$, and the solid boundaries h^*_{TL}, which are the locus of subsystems whose higher barrier matches $W^*(T)$. Subsystems which lie to the left or above the h^*_{TS} boundaries have a thermally active lower barrier and a thermally inactive higher barrier, and consequently occupy their lower energy state exclusively, while those subsystems within the shaded region have two thermally active barriers, *equilibrium* Boltz-

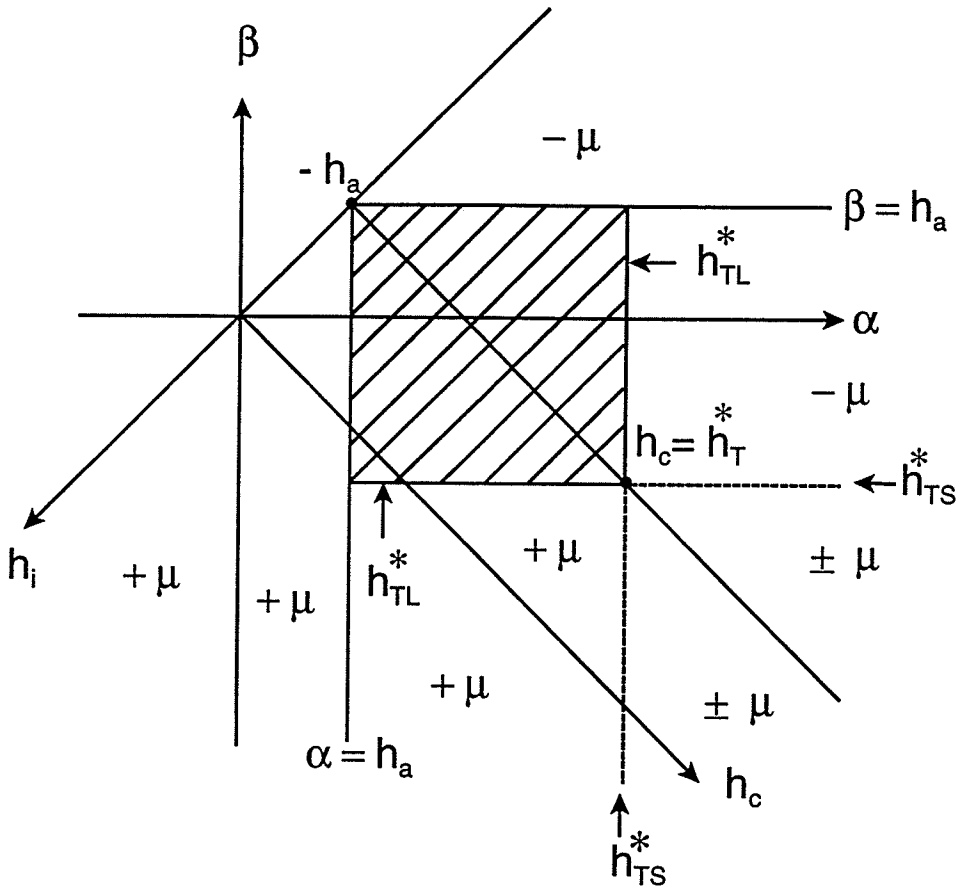

Figure 2.2: *The Preisach plane in a positive applied field h_a. The quadrant defined by $(h_a < \alpha < \infty, -\infty < \beta < h_a)$ consists of bistable subsystems with two positive energy barriers. The two sets of thermal boundaries labelled h^*_{TL} and h^*_{TS} are the loci of subsystems whose larger and smaller energy barriers, respectively, match the thermal fluctuation energy $W^*(T) = \mu h^*_T$ at temperature T. The shaded area identifies those subsystems which are in thermal equilibrium at temperature T.*

mann level populations and a superparamagnetic response function:

$$\phi_{sp} = \mu(T) tanh[\mu(T)(h_a + h_i)/k_B T] \tag{2.13}$$

2.2.3 Description of Standard Experimental Protocols in the Preisach Plane

The Preisach diagram in figure (2.2) provides the basis for a description of common experimental protocols, such as field cooling(FC), zero field cooling (ZFC)

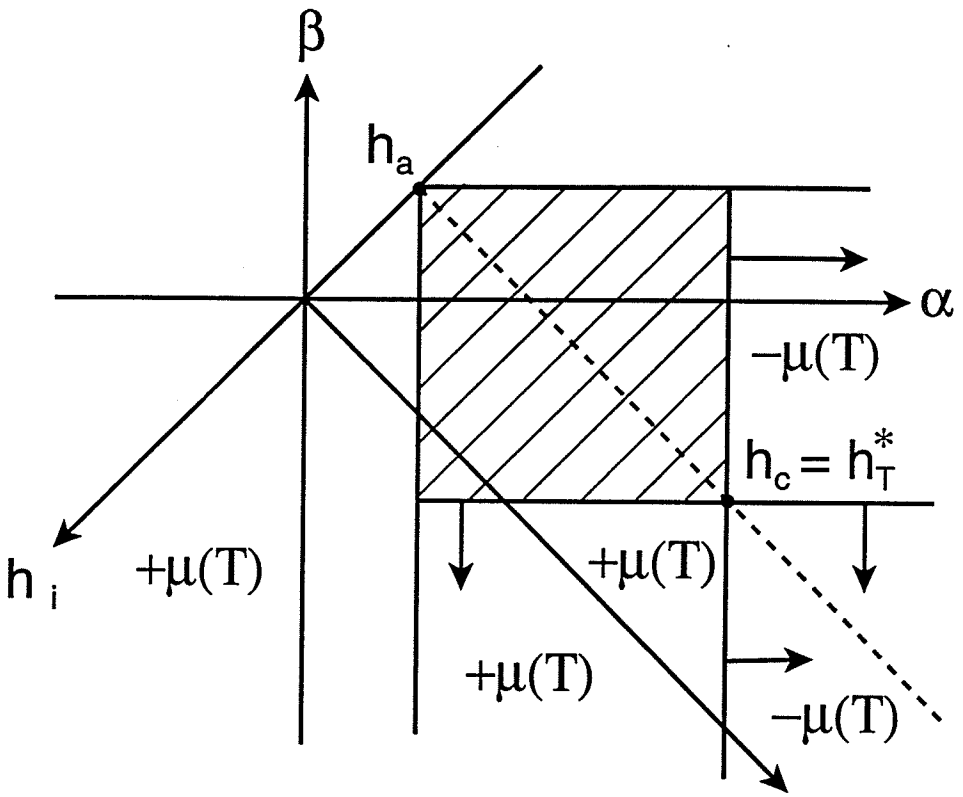

Figure 2.3: *Subsystem states at temperature T after cooling to T=0 in zero field* $h_a = 0$ *and then warming in an applied field* $h_a > 0$. *The shaded region is superparamagnetic.*

and moment-versus-field isotherms.

The system response upon warming in a field $h_a > 0$, after first cooling to $T = 0$ in zero field, is replicated by simply translating the vertex $h_c = h_T^*$ in figure (2.2) outward along the dotted diagonal $h_i = -h_a$ in the direction of increasing h_c, starting from $h_c = h_T^* = 0$. Figure (2.3) shows the motion of the thermal boundaries under ZFC conditions. The subsystems behind the thermal instability boundaries are activated into their appropriate states as shown, while those in the region of double occupancy ($\phi = \pm\mu$) in front of the dashed boundaries retain their zero field cooled configuration.

To simulate field cooling(FC) from a high temperature, the vertex $h_c = h_T^*$ is translated *inward* starting from $h_c = h_T^* = \infty$, where the entire bistable

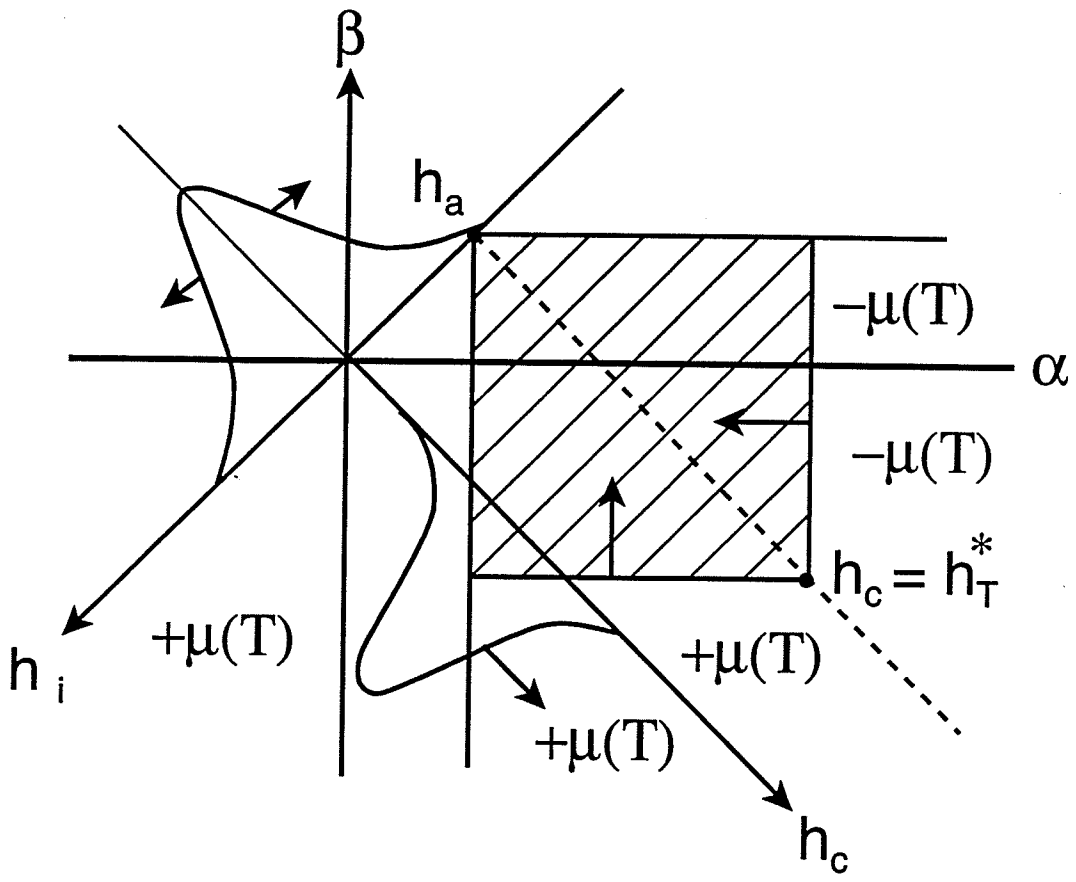

Figure 2.4: *Subsystem states at temperature T after cooling in an applied field h_a. The shaded region is superparamagnetic.*

quadrant is superparamagnetic. Figure (2.4) shows the Preisach plane under FC conditions. The FC protocol eliminates the possibility of double occupancy ($\phi = \pm\mu$) in front of the dashed thermal boundaries and, with the exception of the superparamagnetic region, forces all subsystems below the diagonal $h_i = -h_a$ into their $\phi = +\mu$ state, and all subsystems above the diagonal into their $\phi = -\mu$ state.

To generate the magnetic response at a fixed temperature T to any sequence of field applications and reversals, including the initial magnetizing curve, major and minor hysteresis loops and remanences, the vertex $h_i = -h_a$ in figure (2.4) and figure (2.3) is shifted in the appropriate direction along the $h_i - axis$, keeping

h_T^* fixed. This process has a *directional dependence*, in the sense that under ZFC conditions the configuration of the Preisach plane in a given field h_a in the region of double occupancy ($\phi = \pm\mu$) is not unique, but rather depends upon whether the field was approached from above or below. For all of these protocols, the system response is obtained by weighting the state $\phi(h_c, h_i, h_a, T)$ of each subsystem by the Preisach distribution $p(h_c, h_i)$ and integrating over the entire Preisach plane:

$$m = \int_0^{\infty} dh_c \int_{-\infty}^{+\infty} dh_i \phi(h_c, h_i, h_a, T) p(h_c, h_i) \tag{2.14}$$

2.2.4 Intrinsic Thermal Effects in the Preisach Model

Thermal effects are not limited to overbarrier fluctuations alone. In fact, both the spontaneous moment μ of the subsystems, and the subsystem free energy barriers $W_{\pm}$, are expected to depend explicitly on temperature. The variation of the spontaneous moment is related to the existence of the critical temperature T_c, and is assumed to obey a power law of the form:

$$\mu(T) = \mu_0 (1 - T/T_c)^{\Gamma} \tag{2.15}$$

where $\Gamma \sim 1/3$ for magnetic systems. If we assume, in keeping with standard practice[1], that the Preisach distribution is a product of Gaussian coercive and interaction field distributions:

$$p(h_c, h_i) = \frac{1}{2\pi\sigma_c\sigma_i} exp(-\frac{(h_c - \bar{h}_c)^2}{2\sigma_c^2}) exp(-\frac{(h_i - km)^2}{2\sigma_i^2}) \tag{2.16}$$

which includes the long range mean-field-like interactions $\bar{h}_i = km$ proportional to the total induced moment m[14], then the temperature dependence of the free energy barriers $W_{\pm}(T)$ is described by introducing similar power law temperature

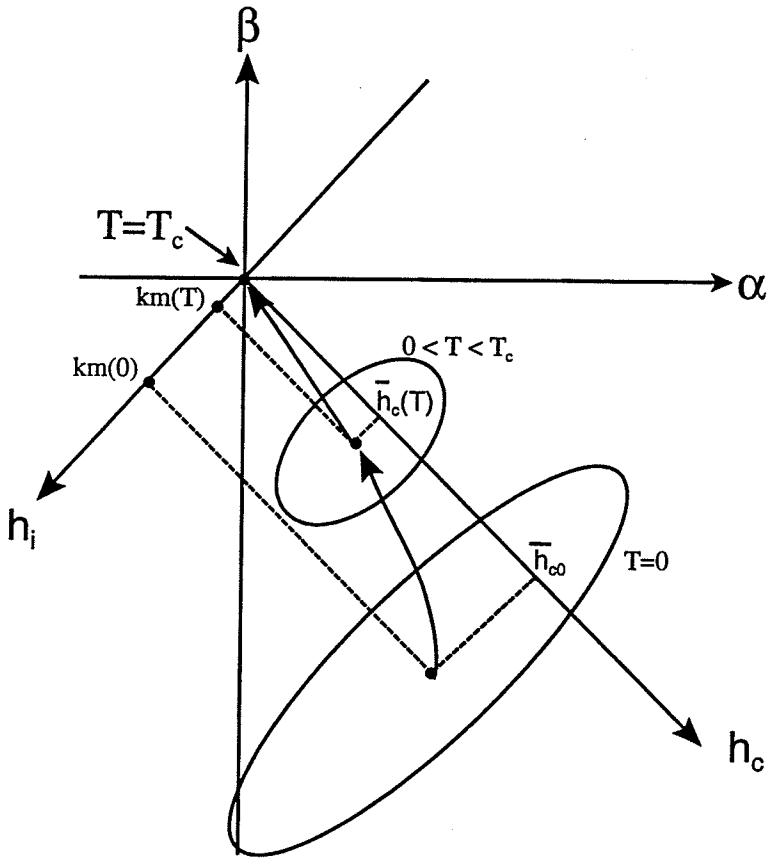

Figure 2.5: *A schematic representation of the collapse of the Preisach distribution* $p(h_c, h_i)$ *as the temperature* T *approaches the critical temperature* T_c *from below. Both the mean coercive field* $\bar{h}_c(T)$ *and the mean interaction field* $\bar{h}_i(T) = km(T)$ *vanish as* $T \to T_c$*, as do the dispersions* $\sigma_c(T)$ *and* $\sigma_i(T)$*.*

dependences into the Preisach distribution parameters:

$$\bar{h}_c = \bar{h}_{c0}(1 - T/T_c)^{\Gamma_c}$$

$$\sigma_c = \sigma_{c0}(1 - T/T_c)^{\Gamma_c'}$$

$$\sigma_i = \sigma_{i0}(1 - T/T_c)^{\Gamma_i} \tag{2.17}$$

Thus both distributions collapse into δ-functions as $T \to T_c$ from below, as expected on physical grounds. This is illustrated schematically in figure (2.5). The thermal viscosity field h_T^*, which describes the effects of thermal fluctuations, is related to the thermal fluctuation energy $W^*(T)$ through $h_T^* = W^*(T)/\mu(T) =$

$(k_B T/\mu(T))ln(t_{exp}/\tau_0)$. Similarly, the temperature dependence of the free energy barriers $W_{\pm}(T)$ is defined by the temperature dependence of the characteristic fields $h_c(T)$ and $h_i(T)$ through the relation $W_{\pm}(T) = \mu(T)[h_c(T) \pm h_i(T)]$.

Chapter 3

Preisach Model Predictions

3.1 Fundamental Characteristic Energies

According to the generalized Preisach model discussed in the previous chapter, the temperature dependence of the magnetic response below the critical temperature T_c has two sources:

(a) The variation with temperature of properties which are intrinsic to the system, such as the spontaneous moment $\mu(T)$ and the free energy barriers $W_{\pm}(T)$.

(b) Thermal fluctuations, which effectively reduce all of the subsystem energy barriers by $W^*(T)$ and which are extrinsic to the system.

The model contains two fundamental characteristic energies, which form a natural basis for a quantitative comparison of the two thermal processes and their effects on the magnetic response functions. One of these characteristic energies is the *critical thermal fluctuation energy* W_c:

$$W_c \equiv k_B T_c ln(t_{exp}/\tau_0) \tag{3.1}$$

which measures the highest energy barrier which can be thermally activated for a system with a critical temperature T_c. The other is the *mean zero temperature*

anisotropy barrier $\bar{W}_a(0)$:

$$\bar{W}_a(0) = \mu_0 \bar{h}_{c0} \tag{3.2}$$

which places an upper limit on the height to which the barriers of a given system can grow, and thus measures, in some sense, the ability of a system to resist the equilibrating effects of thermal fluctuations. The relative strength of the two characteristic energies is measured by the dimensionless parameter η:

$$\eta \equiv \bar{W}_a(0)/W_c \tag{3.3}$$

3.2 Anisotropy-Dominated Systems and Thermal Fluctuation-Dominated Systems

In order to appreciate the physical significance of these two characteristic energies, it is necessary to compare the temperature dependence of the two competing thermal processes.

Figure (3.1) shows the temperature dependence, on a dimensionless temperature scale, T/T_c, of the spontaneous $\mu(T) = \mu_0(1 - T/T_c)^{\Gamma}$, and of the band of anisotropy barriers which lie between the two boundary curves:

$$W_a^{\pm}(T) = [\bar{W}_a(0) \pm 0.4\bar{W}_a(0)](1 - T/T_c)^{1/3} \tag{3.4}$$

where we have assumed that $\sigma_c = 0.4$, and $\Gamma + \Gamma_c = 1/3$. The figure also shows the effective thermal fluctuation energy:

$$W^*(T) = k_B T ln(t_{exp}/\tau_0) = [\bar{W}_a(0)/\eta](T/T_c) \tag{3.5}$$

for two extreme situations, $\eta = 0.2$, $\eta = 4.0$, plotted as a function of T/T_c, and represented by the two straight lines in figure (3.1). If we temporarily neglect the effect of interaction fields h_i, and the applied field h_a, neither of which are fundamental to the present discussion, then the intersection of $W^*(T)$ with the two

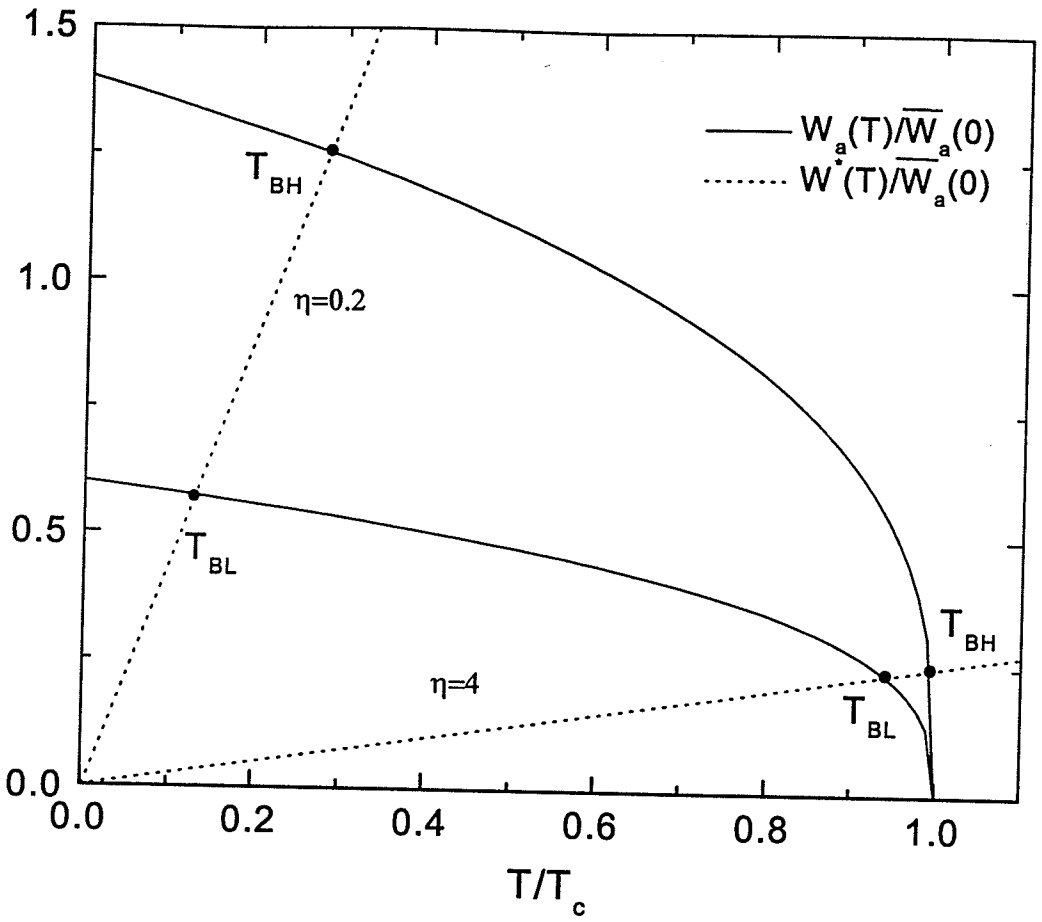

Figure 3.1: *The temperature dependence of a band of anisotropy barriers between* $W_a^{\pm}(T) = \bar{W}_a(0)(1 \pm 0.4)(1 - T/T_c)^{1/3}$ *(solid curves), and the temperature dependence of the effective thermal fluctuation energy* $W^*(T) = k_B T ln(t_{exp}/\tau_0) = [\bar{W}_a(0)/\eta](T/T_c)$, *for two limiting situations where* $\eta = \bar{W}_a(0)/W_c = 0.2$ *and* $\eta = 4.0$.

boundary curves $W_a^{\pm}(T)$ defines the range of excitation or blocking temperatures T_B for the system, which lie roughly between the two limits T_{BL} and T_{BH}.

For the system with $\eta = 0.2$, the critical growth of the spontaneous moment and of the free energy landscape occurs almost entirely above the highest blocking temperature T_{BH}, where $W^*(T) > W_a^+(T)$ and hence where thermal energy is sufficient to activate all of the free energy barriers, so that this system will be in thermal equilibrium and will exhibit a reversible superparamagnetic response through the landscape development phase. Below T_{BH}, where the system exhibits hysteresis, the free energy barriers evolve very slowly with temperature in

comparison with the thermal fluctuation energy $W^*(T)$, as shown in figure (3.1). Consequently, the temperature dependence of the magnetic response functions (FC moment, ZFC moment, hysteresis loop and so on) originates almost exclusively from the thermal-fluctuation-assisted reduction in the $effective$ barrier heights:

$$W_{eff}(T) = W_a(T) - W^*(T) \tag{3.6}$$

rather than from changes in the intrinsic properties of the subsystems with temperature. We refer to systems like this as $fluctuation - dominated$ systems. As figure (3.1) suggests, when the system is cooled through T_c in zero applied field $h_a = 0$, blocking will proceed 'sequentially' , with the highest barriers blocking first at T_{BH} and the smallest barriers blocking last at T_{BL}. Once the highest-barrier subsystems freeze, they are capable of generating *static* local interaction fields, which will lift the degeneracy of the energy levels of neighbouring smaller-barrier subsystems, causing them to freeze with unequal Boltzmann populations. Thus the structure of the ground state for this system may be characterized by highly *asymmetric* level populations close to (1,0) or (0,1), and this is the configuration which we have adopted for the purpose of these simulations.

By contrast, for the system with $\eta = 4.0$, the thermal fluctuation energy $W^*(T)$ intersects the barrier distribution $W_a^{\pm}(T)$ very close to T_c, during the early stages of the development process. For the case considered here, the temperature T at which the average energy barrier reaches the critical height W_c is given by:

$$\bar{W}_a(T) = \mu(T)\bar{h}_c(T) = \bar{W}_a(0)(1 - T/T_c)^{1/3} = W_c = \frac{1}{4}\bar{W}_a(0) \tag{3.7}$$

which yields $1 - T/T_c = (1/4)^3 \approx 0.016$, that is, very close to T_c. As before, blocking occurs over a range of temperatures between T_{BL} and T_{BH}. However, in this case, the superparamagnetic regime ($T_{BH} \leq T \leq T_c$) is very narrow, and

blocking is complete not far below T_c, so that the temperature dependence of the magnetic response throughout the hysteretic regime($T < T_{BH}$) is expected to be dominated by the evolution of the free energy barriers $W_a(T)$, that is, by changes in the *intrinsic* properties of the subsystems themselves with temperature, with only a minor contribution from thermal fluctuations $W^*(T)$, as a comparison of the changes in $W_a(T)$ and $W^*(T)$ with temperature in figure (3.1) clearly shows. We refer to the systems like this as *anisotropy – dominated* systems. Although blocking is expected to proceed 'sequentially' as before, the structure of the ground state in this type of system is much more difficult to predict, since rapid changes in the size of the spontaneous moment $\mu(T)$ throughout the blocking regime can potentially lead to considerable variation in the strength of the interaction fields produced by the blocked subsystems, and hence in the ability of a blocked subsystem to split the levels of neighbouring unblocked subsystems. Thus, the ground state level populations may vary from nearly random $(\frac{1}{2}, \frac{1}{2})$ if the interaction fields are weak, to highly asymmetric (1,0) or (0,1) if the interaction fields are strong. For reasons of simplicity, we adopt the latter configuration throughout.

3.3 Preisach Predictions of the FC and ZFC Response

While the model clearly admits a broad spectrum of behaviour, depending upon the specific values of the barrier distribution parameters and on the slope of the thermal fluctuation line $W^*(T)$ in figure (3.1), we will continue to focus on the two limiting situations described above, since these are of particular interest from an experimental perspective. All systems are assumed to share a certain basic set of parameters:

$$\bar{h}_{c0} = 1.0$$

$$\sigma_{c0} = 0.4$$

$$\sigma_{i0} = 0.02 \tag{3.8}$$

which are all normalized to the real zero-temperature coercive field, a critical temperature T_c such that

$$k_B T_c = 0.01 \tag{3.9}$$

which is normalized to the real critical thermal energy, distribution exponents

$$\Gamma = \Gamma_c = \Gamma_c' = \Gamma_i = \frac{1}{3} \tag{3.10}$$

and an experimental time parameter $\Omega \equiv ln(t_{exp}/\tau_0) = 25$, typical of static measurements. Variations in the ratio $\eta = \bar{W}_a(0)/W_c$ are accomplished by manipulating the spontaneous subsystem moment μ_0, so that the ratios $\eta = 0.2$ and $\eta = 4.0$ correspond to $\mu_0 = 0.05$ and $\mu_0 = 1.0$, respectively. Other parameters from the basic set are then varied as necessary in order to illustrate specific systematic effects. In discussing the behaviour of the ZFC and FC response, we will tend to focus on the low-field limit $h_a \ll \bar{h}_{c0}$, where thermally-induced effects dominate field-induced effects.

Figure (3.2) shows a comparison of the temperature dependence of the FC and ZFC response of the fluctuation-dominated ($\eta = 0.2$) and anisotropy dominated ($\eta = 4.0$) systems in an applied field $h_a = 0.04$. In both cases, the magnetic response is characterized by a *bifurcation temperature*, below which the FC and ZFC moments follow different branches, with the FC moment always lying above the ZFC moment, and above which the two branches merge into a single long superparamagnetic tail which extends up to T_c. The ZFC branch always exhibits a peak as a function of temperature. The physical origin of this peak is ultimately thermally activated overbarrier relaxation. The mo-

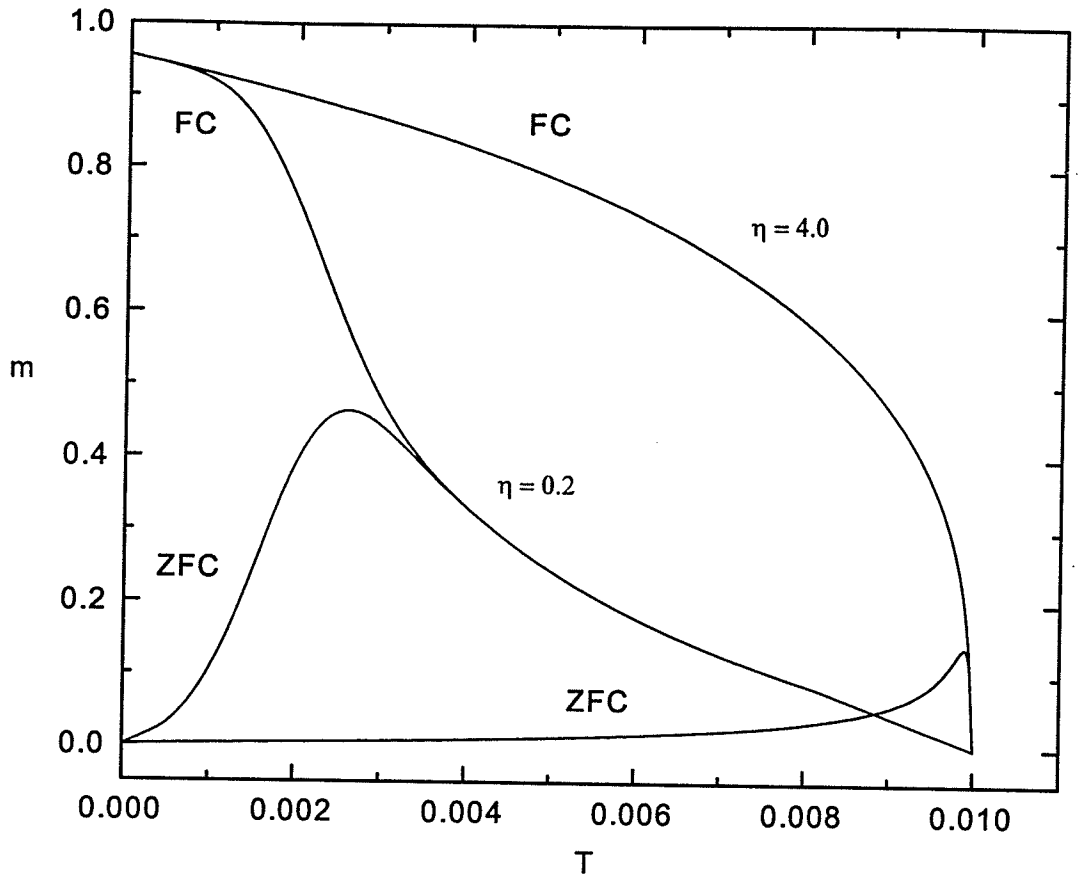

Figure 3.2: *The temperature dependence of the ZFC and FC response functions in an applied field* $h_a = 0.04$ *for a fluctuation-dominated system with* $\eta = 0.2$ *and an anisotropy-dominated system with* $\eta = 4.0$.

ment initially increases with temperature, as subsystems with interaction fields $-h_a \leq h_i \leq 0$ in figure (2.3) are activated from the $-\mu(T)$ state to the $+\mu(T)$ state through the thermal boundary h^*_{TS}, either by the motion of the boundary itself or by the collapse of the Preisach distribution. Eventually, however, the total system moment must decrease as the subsystem spontaneous moment $\mu(T)$ weakens and also as progressively more of the subsystems reach equilibrium and respond superparamagnetically as $\phi_{sp} = \mu(T)tanh[\mu(T)(h_a + h_i)/k_BT]$. However, in $fluctuation - dominated$ systems, the *temperature dependence* of this structure is determined by sources *extrinsic* to the system, that is, by changes in the thermal fluctuation energy $W^*(T)$ with temperature, and hence by the *motion*

of the thermal boundaries in figure (2.2). By contrast, in anisotropy-dominated systems, the characteristics of the peak are determined almost entirely by changes in the *intrinsic properties of the subsystems* [$\mu(T)$ and $\bar{h}_c(T)$ and $\sigma_c(T)$] with temperature, and thus by the power law dependences in equation (2.17), although some fluctuation-assisted reduction of the barrier heights is unavoidably present. In order to illustrate this point, we show in figure (3.3) a comparison of the ZFC response of both systems in two applied fields $h_a = 0.04$ and $h_a = 0.4$, with the usual power law temperature dependences for the subsystem parameters $\Gamma_c = \Gamma_c' = \Gamma_i = 1/3$ (solid curves), and with these intrinsic temperature dependences removed entirely, $\Gamma_c = \Gamma_c' = \Gamma_i = 0$(dotted curves). Clearly, the effect on the fluctuation-dominated system is negligible, while, for the anisotropy-dominated system, 'freezing' the distribution essentially eliminates the peak.

The mean zero-temperature anisotropy barrier $\bar{W}_a(0) = \mu_0 \bar{h}_{c0}$ plays an important role in defining the location of the peak in the ZFC response. This is illustrated in figure (3.4), which shows the FC and ZFC response in both the fluctuation-dominated and anisotropy-dominated regimes, for various values of the spontaneous moment μ_0. For the fluctuation-dominated systems in figure (3.4)(a), where the barrier distribution evolves very slowly with temperature, the temperature of the peak corresponds closely to the temperature at which $W^*(T)$ matches the mean zero-temperature anisotropy barrier $\bar{W}_a(0)$, that is

$$W^*(T_{peak}) = k_B T_{peak} ln(t_{exp}/\tau_0) \cong \bar{W}_a(0) \tag{3.11}$$

which yields an immediate estimate for the mean zero-temperature Barkhausen moment

$$\mu_0 \cong (k_B T_{peak}/\bar{h}_{c0}) ln(t_{exp}/\tau_0) \tag{3.12}$$

For the anisotropy-dominated systems in figure (3.4)(b), the collapse of the

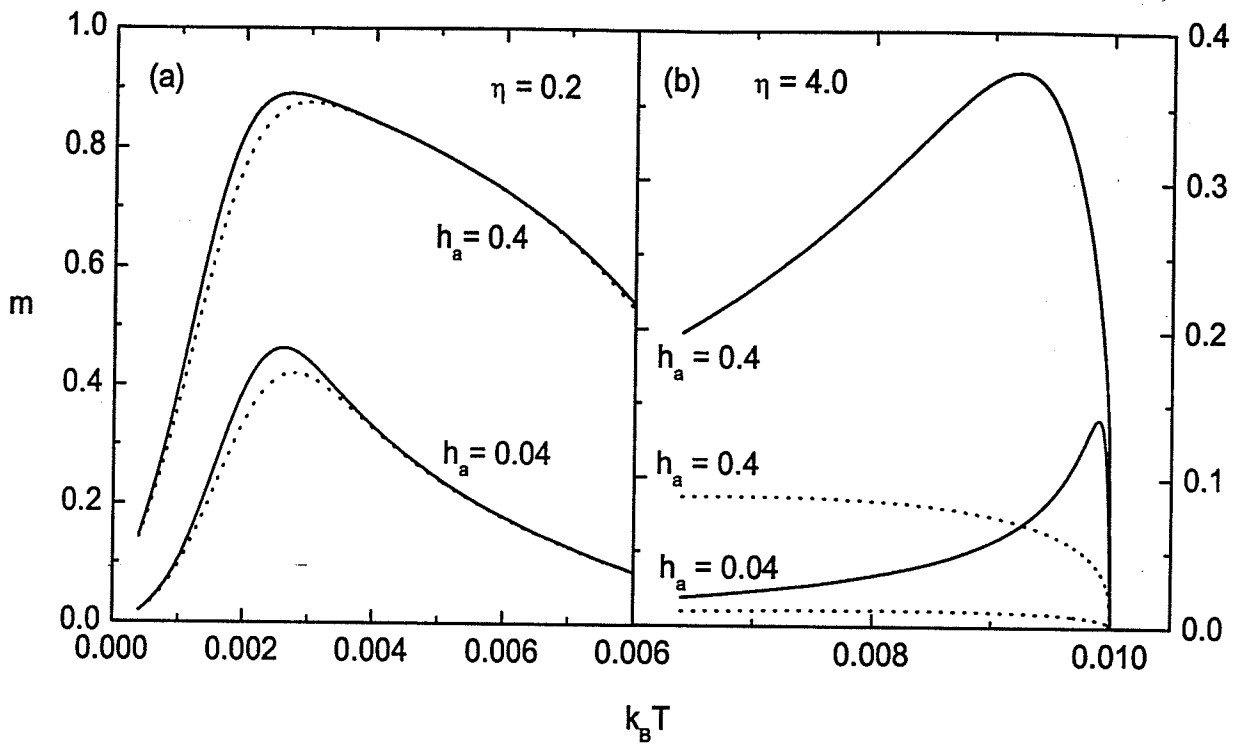

Figure 3.3: *A comparison of the behaviour of the ZFC moment for the fluctuation-dominated and anisotropy-dominated systems in two applied fields* $h_a = 0.04$ *and* $h_a = 0.4$*, with the usual subsystem exponents* $\Gamma_c = \Gamma_c' = \Gamma_i = 1/3$*(solid curves) and with the intrinsic temperature dependence removed entirely,* $\Gamma_c = \Gamma_c' = \Gamma_i = 0$*(dotted curves).*

free energy landscape and the spontaneous moment complicates this relationship considerably, and estimates of μ_0 depend on much more subtle structural features, such as the temperature dependence of the ZFC response *below* the peak.

3.4 The Effect of the Dispersion of Interaction Fields on the FC and ZFC Response

Interaction fields play a particularly important role in shaping the temperature dependence of the magnetic response, particular the FC branch. Figure (3.5) shows the effect of varying the dispersion σ_{i0} of interaction fields for both fluctuation-dominated and anisotropy-dominated systems, in an applied field $h_a = 0.04$. When $\sigma_{i0} \ll h_a \ll \bar{h}_{c0}$, cooling from a high temperature blocks virtually all of the

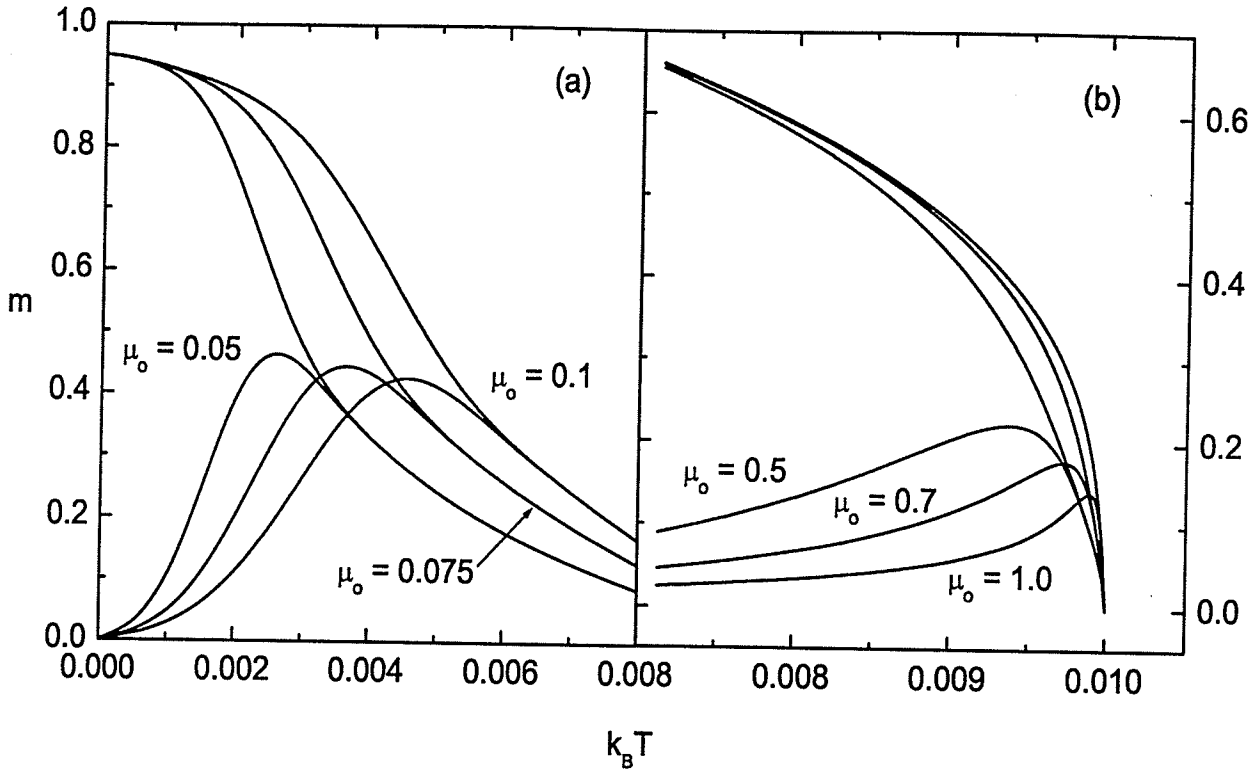

Figure 3.4: *The dependence of the FC and ZFC response on the spontaneous subsystem moment μ_0 for (a) fluctuation-dominated systems (b) anisotropy-dominated systems, in an applied field $h_a = 0.04$*

subsystems in figure (2.4) into their $+\mu(T)$ state, and the temperature dependence of the FC branch is determined either by the superparamagnetic response function $tanh(a/T)$ if the system is fluctuation dominated(figure (3.5) (a)), or by the critical temperature dependence of the spontaneous moment $\mu(T)$ if the system is anisotropy dominated (figure (3.5) (b)). As σ_{i0} increases, the fraction of subsystems which are blocked into the $-\mu(T)$ state grows progressively larger, and the cancellation of the positive and negative moments causes the FC branch to deviate progressively further below the limiting curves for weak interactions($\sigma_{i0} \ll h_a$). Figure (3.5) also shows that, by comparison with the FC response, interactions have a relatively minor influence on the characteristics of the ZFC branch, which tends out to be dominated by anisotropy effects, as discussed earlier.

Systematics like those predicted in figure (3.5)(a) are familiar from a num-

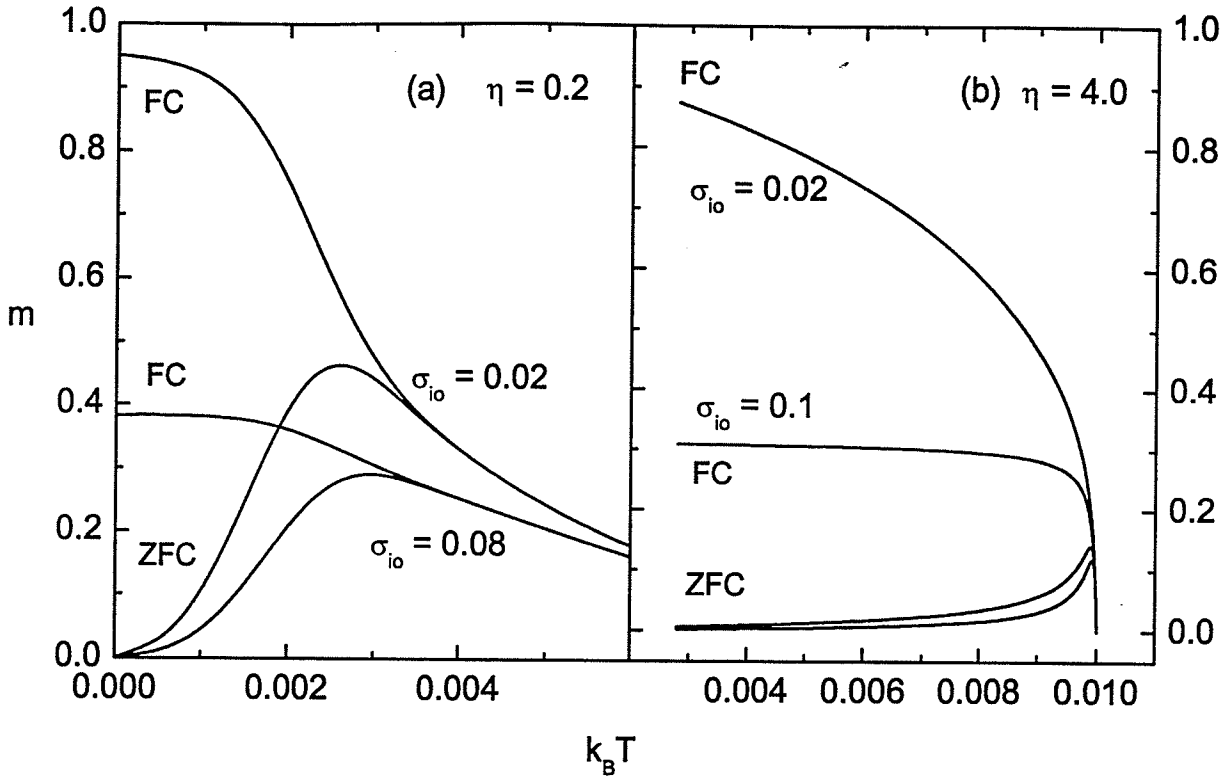

Figure 3.5: *The dependence of the FC and ZFC response on the dispersion σ_{i0} of the interaction fields for (a) a fluctuation-dominated system and (b) an anisotropy dominated system. The applied field is $h_a = 0.04$*

ber of experimental studies of fine particle assemblies which manipulate the level of particle clustering[17] [18]. A detailed comparison of these experimental and theoretical systematics will be presented in a later section, using an extreme limit of the model where the temperature dependence of the spontaneous moment and of the barrier distribution are neglected. Similarly the systematic trends in figure (3.5)(b) have been recently observed in several ferromagnetic perovskites[38], with $SrRuO_3$ representing the limit of weak interactions($\sigma_{i0} \ll h_a$) and $Ni_{0.8}Zn_{0.2}Fe_2O_4$ representing the opposite limit of a strongly interacting system($\sigma_{i0} \gg h_a$)

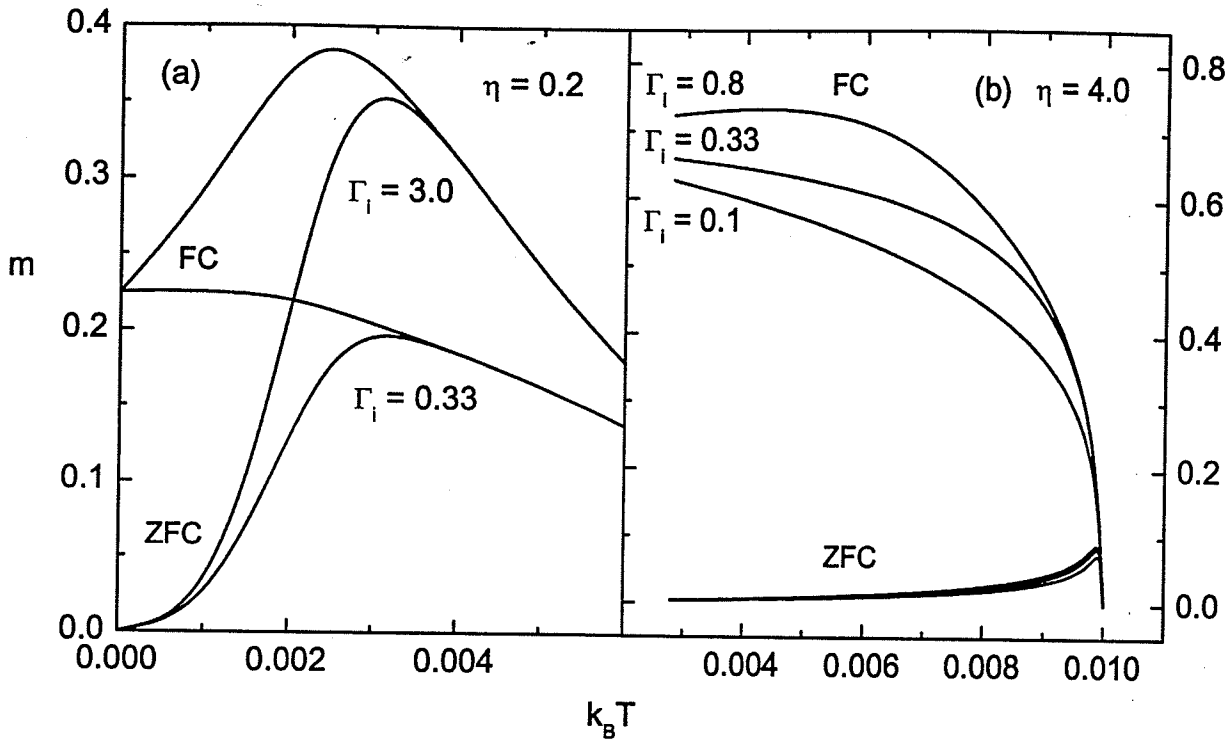

Figure 3.6: *The dependence of the FC and ZFC response on the interaction field exponent* Γ_i *for (a) a fluctuation-dominated system with* $\sigma_{i0} = 0.14$ *in an applied field* $h_a = 0.04$ *and (b) an anisotropy-dominated system with* $\sigma_{i0} = 0.02$ *in an applied field* $h_a = 0.02$.

3.5 The Effect of the Temperature Dependence of the Interaction Fields on the FC and ZFC Response

The temperature dependence of the interaction field distribution also has a profound effect on the shape of the FC and ZFC response functions, and figure (3.6) shows how the response functions of both fluctuation-dominated and anisotropy dominated systems vary with the interaction field exponent Γ_i which controls the dispersion $\sigma_i(T) = \sigma_{i0}(1 - T/T_c)^{\Gamma_i}$. For values of $\Gamma_i < 1$, the curvature of $\sigma_i(T)$ is negative($d^2\sigma_i/dT^2 < 0$), so that the interaction fields vary relatively slowly with temperature, except in the immediate vicinity of T_c, where $\mid d\sigma_i/dT \mid \rightarrow \infty$, and the FC moment changes monotonically with temperature. However, for $\Gamma_i > 1$, the curvature $d^2\sigma_i/dT^2$ is positive, so the temperature dependence of the in-

teraction fields is strong at low temperatures and the interaction fields become negligible well below T_c. Under these conditions the FC moment may exhibit a peak as a function of temperature if the collapse of the interaction field distribution, which increases the moment by increasing the number of subsystems in figure (2.3) with interaction fields $h_i \geq -h_a$ and hence with positive moments, is sufficiently rapid to counteract either the superparamagnetic response $tanh(a/T)$ from the shaded region in figure (2.3), or the critical collapse of the spontaneous moment $\mu(T)$. While, in principle, this effect is observable in both fluctuation-dominated and anisotropy-dominated systems, as shown in figure (3.6), rapid changes in the strength of the interaction fields *well below* T_c are difficult to justify on physical grounds for anisotropy-dominated systems, since in these systems it must ultimately originate from rapid changes in the spontaneous moment $\mu(T)$. However in the fluctuation-dominated systems, the crossover to superparamagnetism tends to occur well below T_c and provides a physically plausible source for a rapid weakening of the interaction fields.

3.6 Preisach Predictions of Hysteresis Loop Isotherms

Figure (3.7) shows the temperature dependence of the major hysteresis loop for both fluctuation-dominated and anisotropy-dominated systems. For the fluctuation dominated system($\eta = 0.2$) the collapse of the hysteresis loop is driven almost exclusively by extrinsic thermal fluctuation effects, while for the anisotropy-dominated systems($\eta = 4.0$), the collapse is defined by the intrinsic temperature dependences in equation (2.17). The Preisach simulations also reveal an interesting structural anomaly in the major hysteresis loops at 'high' temperatures, which is particularly apparent in the hysteresis isotherms of the fluctuation-dominated system in figure (3.7(a)). When the system is warmed close to the reversible super-

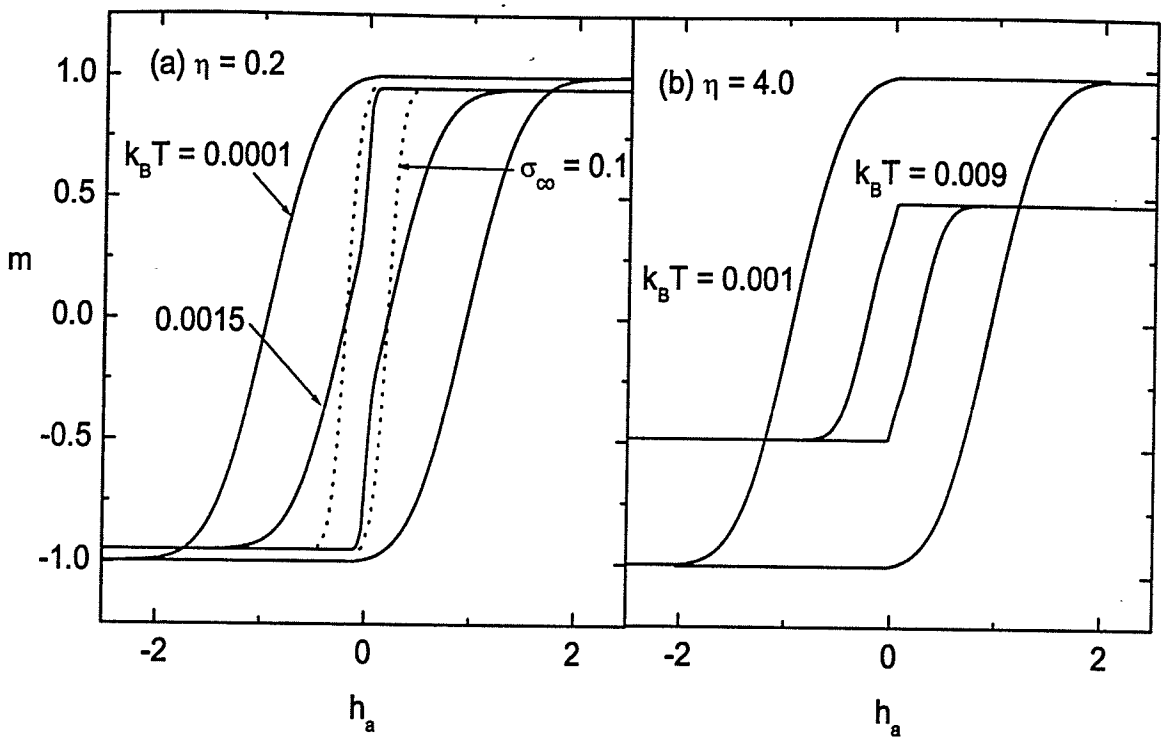

Figure 3.7: *The temperature dependence of the major hysteresis loop for (a) fluctuation-dominated and (b) an anisotropy-dominated system. The solid curves correspond to* $\sigma_{c0} = 0.4$, *the dotted curve in (a) shows the change in the* $k_BT = 0.0015$ *hysteresis isotherm when the coercive field dispersion is reduced to* $\sigma_{c0} = 0.1$

paramagnetic regime, the hysteresis loop develops a *constriction* in the vicinity of the origin. This type of distortion is referred to in the literature as 'wasp-waisting' [26] or 'pinching' [27]. Such distortions of the major hysteresis loop from "text-book" behaviour are frequently encountered in geological materials, which tend to be heterogeneous mixtures of various minerals, grain sizes, and domain configurations. Similar distortions have also been observed in a number of weakly interacting frozen ferrofluids[20][21][27][28], where they have been attributed to resonant tunneling[29]. Wasp-waisted loops have been modelled theoretically[26] by superposing the magnetic response from two or more subpopulations of particles, which are distinguished from each other either on the basis of vastly difference coercive fields, or by superparamagnetic versus single-domain response. The Preisach model offers a uniquely integrated approach to hysteresis, in which com-

petitions like these are treated within a *single unified* theoretical framework. As a consequence, the model offers a unique insight into the physical origins of loop asymmetries. For the systems investigated here, wasp-waisting originates entirely from *thermal relaxation.* In terms of the Preisach diagram in figure (2.2), when the system recoils from positive saturation to the saturated remanence state, the switching boundary $\beta = h_a$ sweeps downward through the Preisach plane from $\beta = \infty$ to $\beta = 0$, forcing all particles with $\beta > 0$ into the $\varphi = -\mu$ state, and leaving a saturation remanence at $T = 0$ equal to the sum of all the particle moments within the fourth quadrant of the plane. This remanence differs only slightly from the saturation moment, since the Preisach distribution tends to be concentrated within the fourth quadrant. When $T \neq 0$, the two dashed thermal activation boundaries h^*_{TS} in figure (2.2) partition the fourth quadrant into a thermally relaxed *demagnetized* component, and a thermally blocked, remanent component. When h^*_T is comparable to the mean coercive field $\bar{h}_c(T)$, thermal relaxation demagnetizes a significant portion of the fourth quadrant, and the moment drops precipitously when h_a approaches zero from above. The approach to negative saturation along the negative half branch of the major loop is more gradual, since the activation boundary $h^*_{TS} = h_c - \mid h_i + h_a \mid$ must now invert roughly half of the Preisach distribution, which requires negative fields:

$$h_a \cong h^*_T - \bar{h}_c - \sigma_c - \sigma_i \cong -\sigma_c - \sigma_i \tag{3.13}$$

The steepness of the major loop for $h_a < 0$ is thus directly dependent on the dispersions σ_c and σ_i of coercive fields and interaction fields. A broad distribution will tend to delay the approach to negative saturation and 're-open' the loop, producing the 'wasp-waisted' or 'pinched' appearance. The dotted curve in figure (3.7(a)) illustrates the effect of varying the dispersion of coercive fields σ_{c0} on the hysteresis isotherm $k_BT = 0.0015$ for the fluctuation-dominated system, and

clearly shows that when the distribution of coercive fields becomes sufficiently narrow, the 'wasp-waisting' becomes unobservable.

3.7 Preisach Predictions for the Field Dependence of the Maximum in the ZFC Moment in Fluctuation-Dominated Systems

3.7.1 Field Dependence of T_{max}

The maximum in the temperature dependence of the ZFC moment is an archetypal characteristic of "superparamagnetic" assemblies of fine magnetic particles. As described earlier, it originates from a competition between unidirectional thermal transitions and bidirectional transitions which produce thermal equilibrium. Experiments on a variety of "superparamagnetic" systems have shown that the temperature T_{max} of the ZFC maximum varies with the applied field h_a, and that the magnitude and the sign of this variation depends on the degree of aggregation and hence on the strength of the interparticle coupling. To be specific, in a frozen suspension of amorphous iron-carbon particles ($Fe_{1-x}C_x$ and $x \simeq 0.25$) , for which interparticle interactions have been characterized as "negligible", $\Delta T_{max}/\Delta h_a$ is positive, and T_{max} changes by about 20% as h_a is varied from zero to values near the system coercive field[28]. In homogeneous rigid films of $\gamma - Fe_2O_3$ particles, with varying degree of particle aggregation, the peak temperature T_{max}, measured in a fixed low field h_a, is observed to increase with the level of particle aggregation [17][18][31]. In the limit of extreme dilution, there appears to be some inconsistency in the sign of the field dependence of T_{max}, and both positive and negative values of $\Delta T_{max}/\Delta h_a$ have been reported[18]. However for higher levels of aggregation, $\Delta T_{max}/\Delta h_a$ is consistently negative.

In figure (3.8), we show numerically calculations of T_{max} as a function of h_a for six model "systems" with identical moments $\mu_0 = 1.0$, and identical coercive

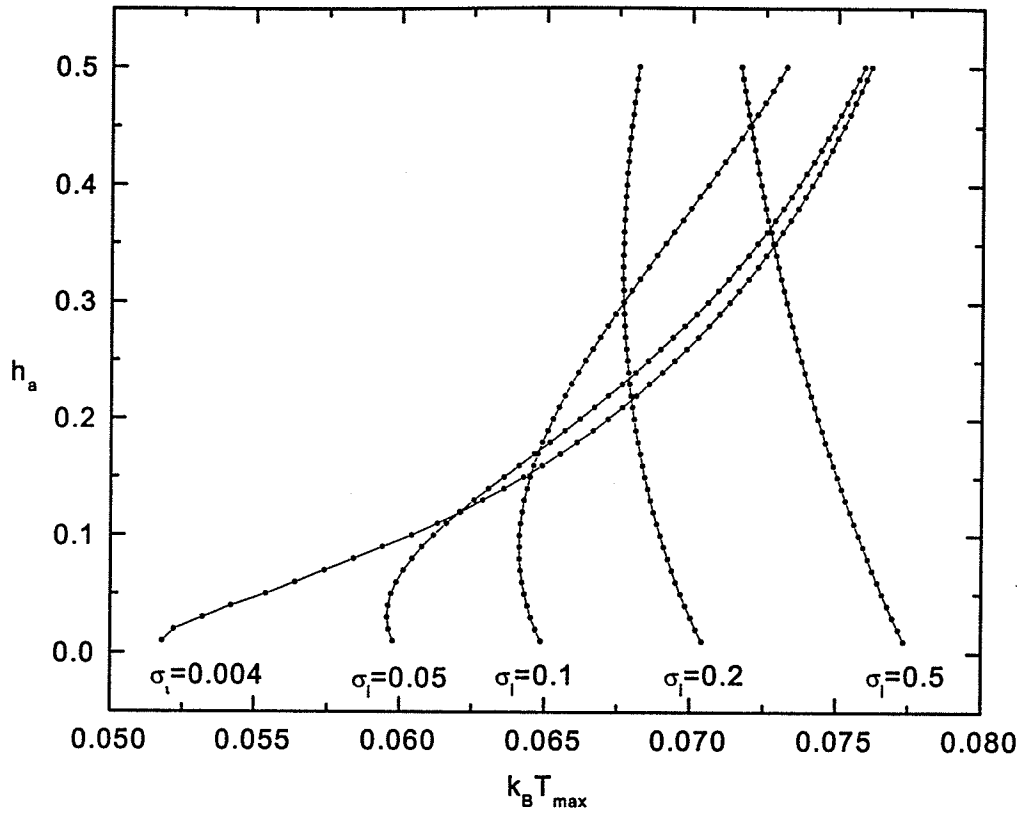

Figure 3.8: *The field dependence of the temperature T_{max} of the maximum in the ZFC response for six model "systems" with $\bar{h}_c = 1$ and $\sigma_c = 0.3$, but with different values of σ_i=0.004, 0.05, 0.1, 0.2 and 0.5*

field parameters $\bar{h}_c = 1$ and $\sigma_c = 0.3$, but with different values of σ_i. For all systems, T_c is assumed to be infinite, so that the Preisach free energy landscape and the spontaneous moment are temperature independent.

Figure (3.9) shows the initial slope $(\Delta T_{max}/\Delta h_a)_{h_a=0.02}$ of the curves in figure (3.8), calculated between the two lowest fields $h_a = 0.02$ and $h_a = 0.04$, plotted as a function of σ_i. An inspection of these figures shows the model reproduces all of the systematics observed experimentally. Specifically:

1. At low fields $h_a < 0.05$, T_{max} increases monotonically with σ_i and hence with the degree of particle clustering;

2. In the limit of very low interactions $\sigma_i < 0.04$, corresponding experimentally to a highly dispersed system of particles with large interparticle sep-

arations, T_{max} varies monotonically with h_a and the slope of dT_{max}/dh_a is positive, which is consistent with the behaviour of the "noninteracting" FeC system[28];

3. For values of σ_i between $0.04 < \sigma_i < 0.3$, the functional dependence of T_{max} on h_a becomes much more complex and the sign of the slope dT_{max}/dh_a depends on the magnitude of the applied field. In the low field limit $h_a \ll \bar{h}_c$, the slope of dT_{max}/dh_a is always *negative* and increases in magnitude with increasing σ_i, as shown in figure (3.9), which is precisely the trend reported for the $\gamma - Fe_2O_3$ suspensions with increasing aggregation[18]. For values of σ_i near the lower end of this range($\sigma_i \sim 0.04$), the slope dT_{max}/dh_a is small, and minor variations in σ_i can easily change the sign of the slope at low fields(see figure (3.9)). This suggests that the inconsistencies in the sign of ΔT_{max} observed in dilute suspensions of $\gamma - Fe_2O_3$ which have nominally the same concentration[18], may be due to slight variations in the degree of particle clustering.

4. For values of $\sigma_i > 0.3$, T_{max} decreases monotonically with increasing h_a over the entire field range $0 \leq h_a \leq \bar{h}_c$.

As before, the unique visual representation of the ZFC response afforded by the Preisach construction in figure (2.4) allows us to establish the physical basis for some of the systematic trends in figure (3.8) and figure (3.9). For example, the tendency for T_{max} to increase monotonically with σ_i at low reduced fields $h_a < 0.05$ is directly related to the changes in the imbalance between the populations of SP particles with positive and negative moments in the two halves of the shaded area in figure (2.3), caused by the changes in the shape of interaction field distribution. For small σ_i this imbalance(which always favours the positive moments)is appreciable, the SP temperature dependence is strong, and the crossover from

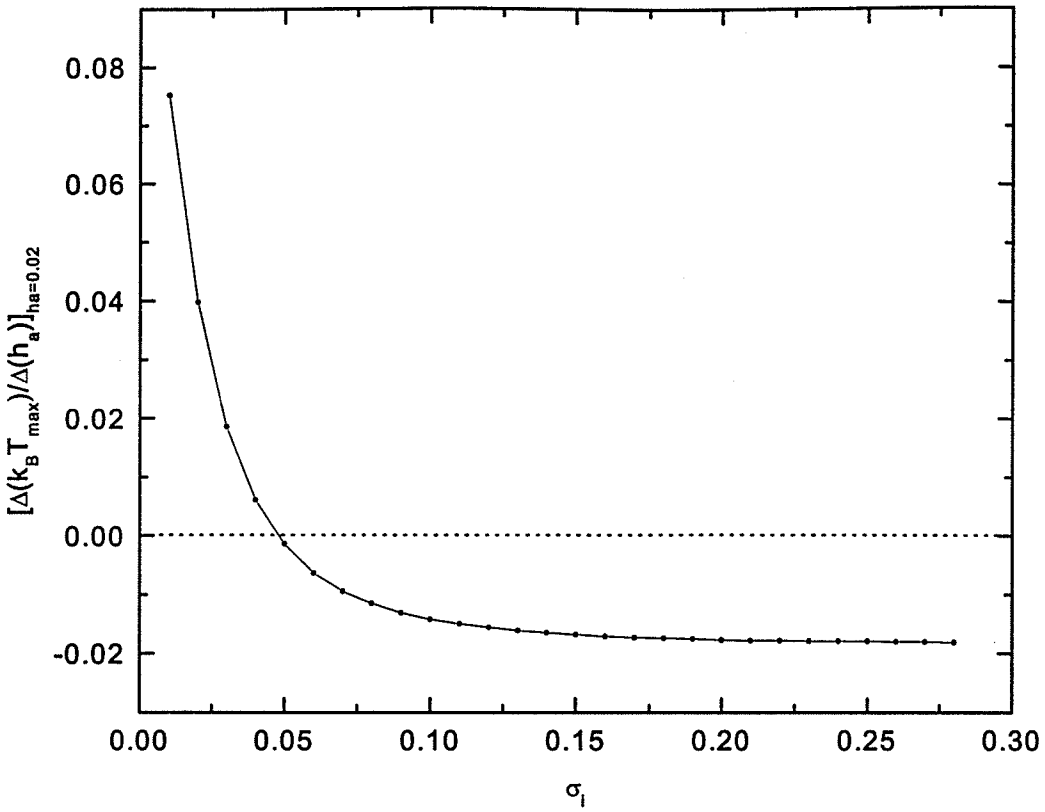

Figure 3.9: *The "initial" slope* $(\Delta T_{max}/\Delta h_a)_{h_a=0.02}$ *of the curves in figure (3.8) calculated between the two lowest applied fields* h_a *=0.02 and* h_a*=0.04, plotted as a function of* σ_i.

the regime of unidirectional thermal transitions to the equilibrium(SP) regime occurs at "low" temperatures. As σ_i increases, and the distribution broadens, the two populations tend to equalize, the SP temperature dependence weakens, and the crossover is delayed to higher temperatures. (The restrictions to low applied fields $h_a \leq \bar{h}_c$ is necessary in order to limit the contribution from the unidirectional transitions, and thus ensure that the contribution from SP particles dominates the response.) This imbalance also accounts for the tendency for T_{max} to decrease monotonically with h_a for large reduced values of $\sigma_i > 0.3$. As h_a increases and the shaded area propagates along the h_i axis, the imbalance between the two SP populations becomes progressively more severe, enhancing the SP temperature dependence and depressing the crossover temperature T_{max}. At the other extreme, when the interaction field distribution is very narrow ($\sigma_i \ll 1$) and

the particles are crowded along the h_c axis, only that portion of the shaded region in figure (2.3) which actually *intersects* with the h_c axis makes any significant SP contribution, and this intersection is clearly delayed to progressively larger values of h_T^* as h_a is increased. Thus the crossover temperature T_{max} increases monotonically with h_a. (The more complex systematics at intermediate values of σ_i ,such as the tendency for T_{max} to first decrease and then increase with h_a , are probably a consequence of a competition between the latter two effects described above.)

It should be pointed out that the temperature of the peak in the ZFC moment is not *coincident* with the mean blocking temperature $\bar{T}_B$ of the subsystems. According to the model, in zero applied field, blocking occurs on average when the effective thermal activation energy $W^* = k_B T \cdot \Omega$ matches the mean barrier height $\bar{W}_a \cong \bar{h}_c$, which yields $k_B \bar{T}_B \cong \bar{h}_c/\Omega \approx 0.04$. An inspection of the low field response function in figure (3.5) shows that the ZFC peak lies well above the mean blocking temperature(between one and two standard deviations away, $(\bar{h}_c + \sigma_c)/\Omega < T_{max} < (\bar{h}_c + 2\sigma_c)/\Omega$), towards the upper end of the blocking temperature distribution, which explains the consistent proximity of the peak to the ZFC-FC bifurcation temperature, where hysteresis vanishes and all the subsystems are superparamagnetic. In fact, the structural feature of these response functions which is most closely correlated with the mean blocking temperature is the *inflection point* in the ZFC moment, where the rate of change of the moment dm_{ZFC}/dT is a maximum, and the reasons are obvious from a consideration of the Preisach diagram in figure (2.3). As mentioned earlier, the initial growth of the ZFC moment with temperature is dominated by the unidirectional thermal transitions from $\phi = -\mu$ to $\phi = +\mu$ induced by the motion of the instability boundary $\alpha = h_a + h_T^*$ in figure (2.4) through the Preisach distribution. The rate at which these transitions accumulate with temperature will be largest when

the instability line passes through the center of the distribution $h_c = \bar{h}_c$. Thus dm_{ZFC}/dT will exhibit a maximum when $h_a + h_T^* = \bar{h}_c$ which, for small applied field $h_a \ll \bar{h}_c$, is identical to the blocking condition $k_B \bar{T}_B \cong \bar{h}_c/\Omega$. This analysis suggests that efforts to quantify the blocking process experimentally should probably focus on the inflection point in the ZFC moment $m_{ZFC}(T)$, in preference to the maximum.

Our numerical calculations show that the numerical ZFC and FC data obey a $Curie - Weiss$ law at high temperature. Figure (3.10) shows the inverse ZFC moment m_{ZFC}^{-1} plotted as a function of temperature for three model "systems" with parameters $\mu = 1.0$, $\bar{h}_c = 1.0$, $\sigma_c = 0.3$, and three different dispersions of interaction fields $\sigma_i = 0.004, 0.04$ and 0.08. In each case, the high temperature data obey a Curie-Weiss law of the form $m_{ZFC} = C/(T - \theta_{SP})$, with a negative superparamagnetic Curie-Weiss temperature θ_{SP}. The magnitude of θ_{SP} increases with the dispersion σ_i of interaction fields, which is precise by the same trend as that observed experimentally when the degree of particle aggregation is increased[18] [31]. This indicates that the experimental behaviour is probably a consequence of the changes in the fluctuations of the random local interaction field, rather than a long range mean field effect, such as a shape-dependent demagnetizing factor (except, perhaps, in exceptional circumstances such as thin film geometry). Notice that θ_{SP} rigorously vanishes only in the limit $\sigma_i = 0$ where the interaction field distribution collapses into a δ function, so that finite experimental values of θ_{SP} are synonymous with interactions, according to the model.

3.7.2 The Field Dependence of the Anisotropy Barrier

One further refinement should be considered which is neglected in the standard formulation of the Preisach model, but which is an explicit component of other Preisach-based approaches to superparamagnetism[32][33]. According

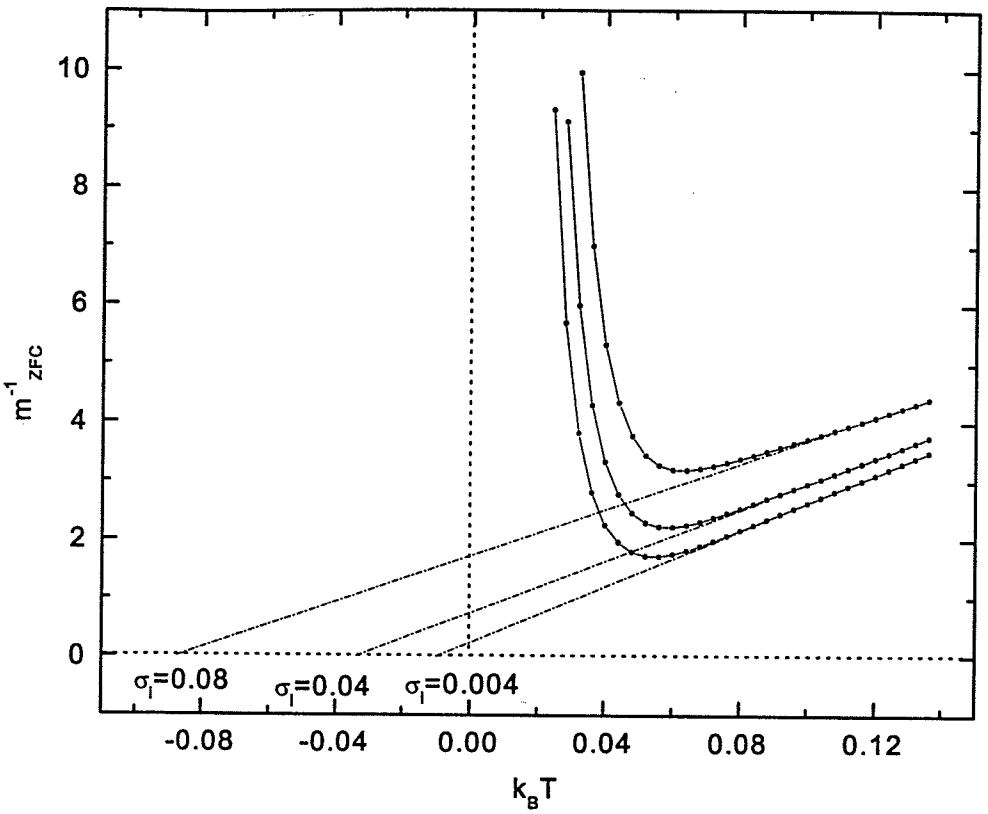

Figure 3.10: *The inverse ZFC moment plotted as a function temperature for three model "systems" with identical parameters* $\bar{h}_c = 1$ *and* $\sigma_c = 0.3$, *but different values of* $\sigma_i = 0.004, 0.04$ *and* 0.08. *The dashed lines show the high temperature Curie-Weiss law, extrapolated to* $m_{ZFC}^{-1} = 0$

to the Stoner-Wohlfarth theory of coherent rotation in uniaxial single domain particles[7], when the applied field h_a is aligned with the easy axis, the intrinsic energy barrier due to anisotropy varies with h_a as:

$$E_a = \mu(h_c/2)[1 + (h_a/h_c)^2] \tag{3.14}$$

and grows from a minimum value $E_a = \mu h_c/2$ when $h_a = 0$ to a maximum value of $E_a = \mu h_c$ when $h_a = h_c$. By contrast, the Preisach decomposition, which characterizes the subsystems by their two critical instability fields (α, β), yields an energy level diagram like that in figure (2.1) in which the anisotropy barrier is fixed at the coercive field $h_c = (\alpha - \beta)/2$. which is the maximum value allowed by the Stoner-Wohlfarth theory. The Preisach model thus exaggerates the

height of the thermal activation barrier when h_a is subcritical, so that the instability criteria based on the energy profile in figure (2.1) actually *underestimate* the effectiveness of thermal fluctuations in producing transitions. Based on the Stoner-Wohlfarth theory, the "correct" condition for thermal activation in the absence of interactions is:

$$0 \leq (h_c/2)[1 + (h_a/h_c)^2] - h_a \leq h_T^* \tag{3.15}$$

which is satisfied by all the subsystems whose coercive fields h_c lie between

$$h_a \leq h_c \leq (h_a + h_T^*) + \sqrt{(h_a + h_T^*)^2 - h_a^2} \tag{3.16}$$

Thus for noninteracting systems(σ_i=0), the effect of a field-dependent anisotropy barrier is formally identical to replacing h_T^* in the original thermal instability criteria by

$$\tilde{h}_T^* = h_T^* + \sqrt{(h_a + h_T^*)^2 - h_a^2} \tag{3.17}$$

If interaction fields are present, the analysis becomes considerably more complicated. Nevertheless, it is possible to show that the replacement of h_T^* by $\tilde{h}_T^*$ is approximately valid for interacting systems as well, provided that the interaction fields are weak in comparison with h_a. (A comparison of this approximate expression with the exact version of the instability boundary[32][33] derived for interacting Stoner-Wohlfarth particles with easy axes aligned with the applied field shows that they are actually very similar, particularly when it is remembered that only a small fraction of particles in the Preisach plane have moments which differ significantly from $\pm\mu$).

This allowed us to perform some limited comparisons of the model predictions with and without a field-dependent anisotropy barrier, and to explore the principal consequences of introducing this extra field dependence into the formal-

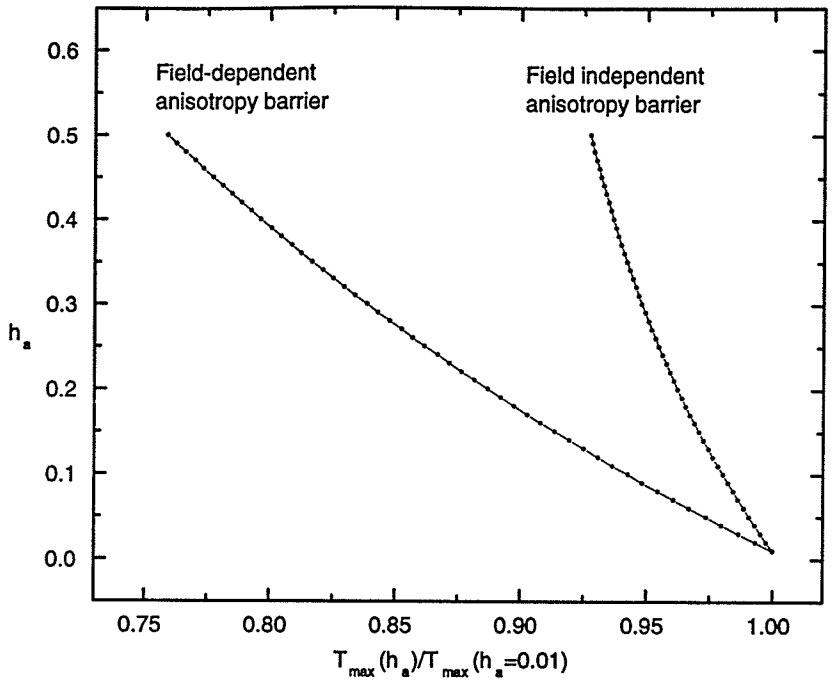

Figure 3.11: *A comparison of the field dependence of T_{max} calculated using the standard Preisach formalism with a field-independent anisotropy barrier, and the modified version of the Preisach model which incorporates the variable Stoner-Wohlfarth barrier for coherent rotation.*

ism. Generally speaking, the various systematic trends described in the previous sections appear to be essentially unaltered. The principal effect of incorporating a field dependence into the anisotropy barrier is to *exaggerate* these systematics, so that, for example, the curvature of the various data sets in figure (3.8) which describe the variation of T_{max} with h_a becomes more pronounced. As an illustration, figure (3.11) compares the field dependence of T_{max} for a model "system" with $h_c = 1$, $\sigma_c = 0.3$, and $\sigma_i = 0.3$, using the the standard Preisach formalism and the modified version with the variable Stoner-Wohlfarth barrier for coherent rotation. The enhancement of the field-dependence of T_{max}, which is clearly apparent in this figure, is of particular interest from the perspective of comparisons with experiment data, since the relative changes $\Delta T_{max}/T_{max}$ predicted by the standard Preisach approach(that is, with a linearly field-independent barrier) tend to be much smaller than those which characterize real systems like $\gamma - Fe_2O_3$.

(This is also a feature of other models of "superparamagnetics" assemblies[17].) While our analysis suggests that it may be possible to resolve such discrepancies by manipulating the details of the barrier growth, it is nevertheless important to emphasize that the standard formulation of the Preisach model contains the essential physical ingredients which are needed to replicate and interpret the principal systematic trends observed experimentally.

Similar comments apply, perhaps even more pointedly, to another physical mechanism, which appears to play a prominent role in the Stoner-Wohlfarth-based models of superparamagnetism[32][33]. In order to simulate experimental effects related to variations in the degree of particle aggregation, such as the motion of the peak in the ZFC moment, these models introduce a very specific physical process whereby "dynamic interactions" induce a $mean\ field-like\ shift$ in the distribution of particle coercive fields. While this mechanism may very well be present in real superparamagnetic assemblies, our numerical simulations clearly show that it is unnecessary to supplement the Preisach formalism in this rather artificial manner and that, contrary to the conclusions reached by these authors in [33], the *physical basis* for essentially the entire spectrum of experimental systematics can be traced directly to the characteristics of the distribution of static interaction fields (and hence to the parameter σ_i).

Chapter 4

Experimental Instrumentation, Sample Preparation, and Preisach Simulation Procedure

4.1 Measuring the Moment - Physical Property Measurement System(PPMS Model 6000)

4.1.1 PPMS

A Physical Property Measurement System(PPMS Model 6000), manufactured by Quantum Design, was used to measure the magnetic moment as a function of temperature T and applied field h_a. The *PPMS Model* 6000 has the following basic functional components:

- **Dewar:** The aluminum PPMS dewar contains the liquid helium bath in which the PPMS probe is immersed. The outer layer of the dewar contains reflective super insulation to help minimize helium consumption. This region is evacuated and contains activated charcoal(on the cold surface) to help maintain the vacuum.

- **Probe:** The probe (figure 4.1) is the critical part of the PPMS. The probe is the hardware component that sits within the liquid helium bath inside the dewar. It incorporates all of the elemental temperature control hardware,

the superconducting magnet, the helium level meter, electrical connectors, gas lines, and sample puck connectors. The probe is composed of several concentric stainless steel tubes, along with other important elements including the outer and inner vacuum tubes, the sample tube, the impedance assembly, the magnet, the baffled rods, the helium level meter, the protective cap and the probe head.

- **Pump**: A direct drive pump pumps continuously on the system to control the pressure in the sample tube and to aid thermal control.
- **Model 6000 controller**: The controller is composed of motherboard(system integration), system bridge board, gas valves and gas lines(temperature control) and magnet power supply.
- **Magnet controller and magnet power supply**: The magnet power supply is the current source for the magnet.
- **Magnet characteristics** The maximum magnetic field can reach 9 T with a stability of 0.05 G.

4.1.2 ACMS

In addition to the components described above, the ACMS insert, an optional component which houses the system's drive and detection coils, is used to perform the DC magnetization and AC susceptibility measurements. The insert fits directly into the PPMS sample chamber and contains a sample space that lies within the uniform field region of the host PPMS, allowing DC field and temperature control using conventional methods.

The sample is held within the insert's coil set on the end of a thin, rigid sample rod. The sample holder is translated longitudinally by a DC servo motor

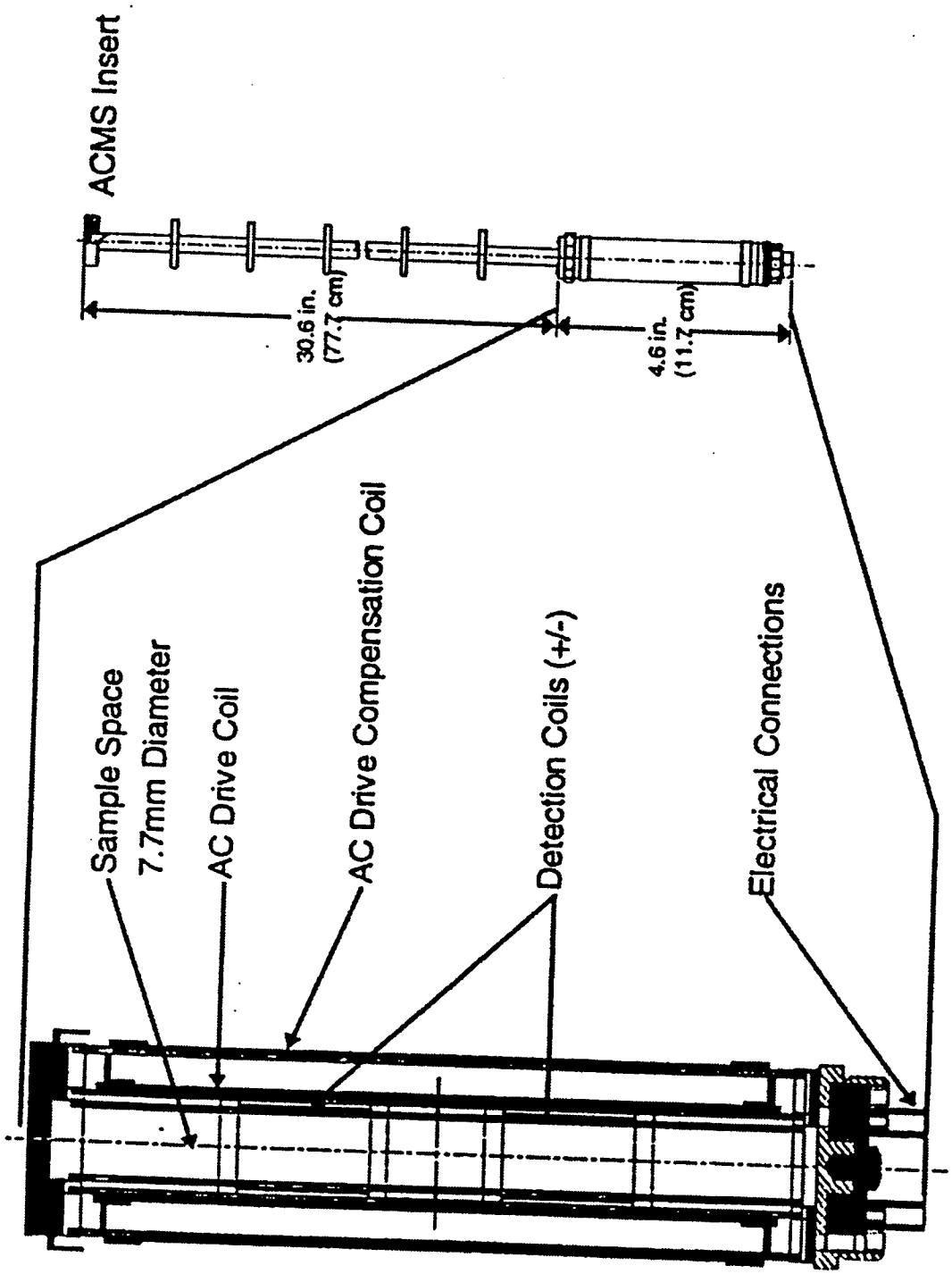

Figure 4.1: *The PPMS probe*

in the sample transport assembly, which mounts to the top of the PPMS probe. The DC servo motor provides rapid and very smooth longitudinal sample motion.

The ACMS contains an AC drive coil set that provides an alternating excitation field and a detection coil set that inductively responds to the combined sample moment and excitation field. The copper drive and detection coils are situated within the ACMS insert, concentric with the PPMS superconducting DC magnet as shown in figure 4.2.

The drive coil is wound longitudinally around the detection coil set. It can generate alternating fields of up to $\pm 10Oe$ in a frequency range of 10Hz to 10KHz at any temperature.

The detection coils are arranged in a first-order gradiometer configuration to help isolate the sample's signal from uniform background sources. This configuration utilizes two sets of counterwound copper coils connected in series and separated by several centimeters. During DC measurements a constant field is applied to the measurement region and the sample is moved quickly through both sets of coils, inducing a signal in them according to Faraday's Law. This measurement is commonly called the *extraction method.*

A compensation coil is situated outside the AC drive coil. The drive coil and compensation coil are counterwound and connected in series so that they receive the same excitation signal. The compensation coil actually reduces dipole fields to quadrupole fields.

Each detection coil also contains a low-inductance calibration coil to increase the accuracy of the phase and amplitude during AC measurements.

During DC measurements, the amplitude of the detection coil signal is dependent upon both the extraction speed and the sample's magnetic moment. The DC servo motor employed by the ACMS extracts the sample at speeds of approximately 100cm/sec, thus increasing the signal strength over a conventional DC

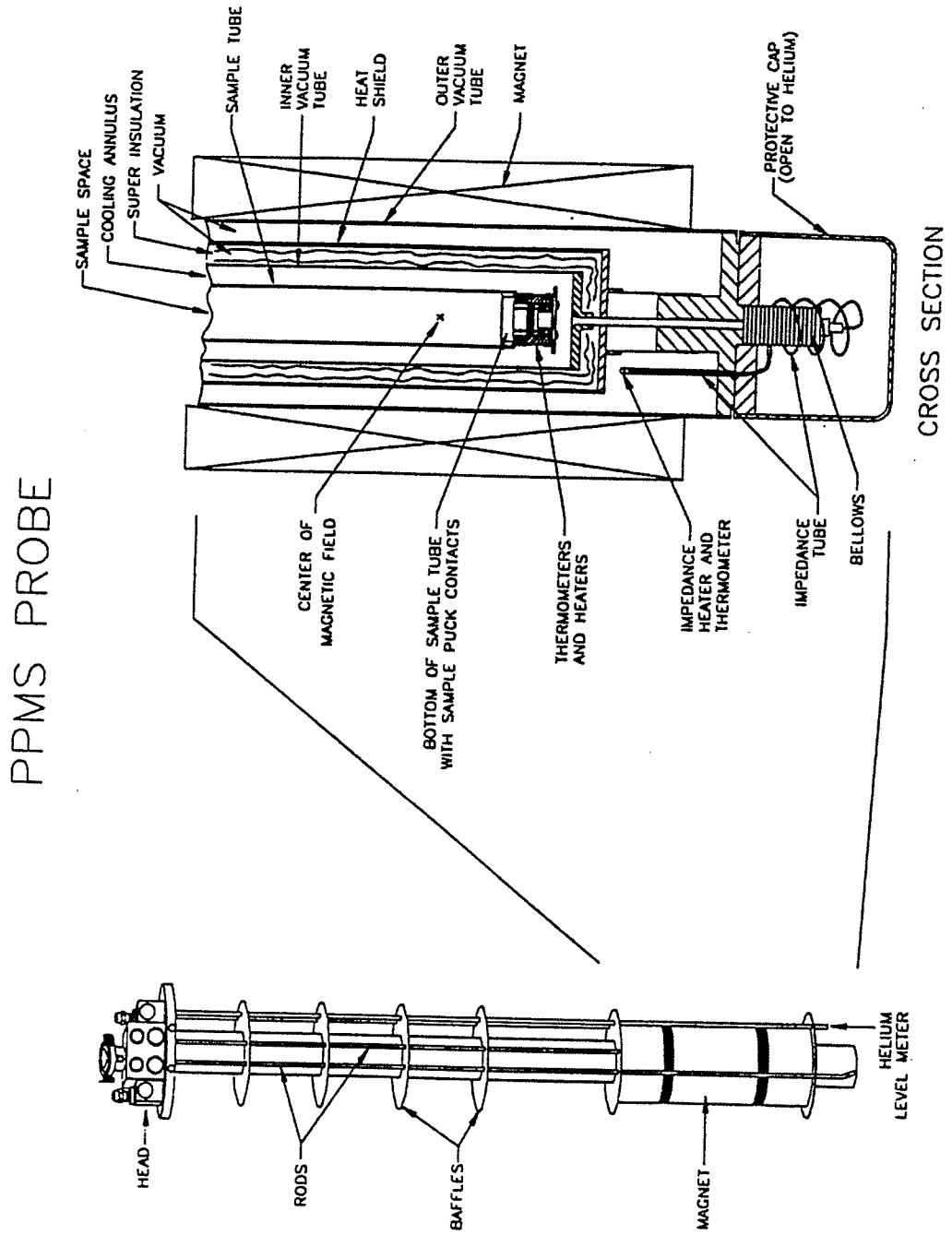

Figure 4.2: *The ACMS insert and coil set*

extraction system. The short scan time also allows the averaging of several scans for each measurement, further reducing the contributions to random error. These advantages result in greater measurement accuracy and sensitivity compared to systems with slower sample extraction speeds.

The ACMS coils are connected to the PPMS electronics of the Model 6000 controller which communicates with a host computer to write measurement sequences in variable magnetic field and temperature environments thus simplifying the data gathering process.

4.1.3 DC measurements

During a DC measurement, the PPMS applies a constant magnetic field to the sample space and the sample transport servo motor translates the sample through the entire detection coil set in approximately 0.05sec. To synchronize sample translation with data acquisition, the servo motor sends a handshake signal to the DSP(Digital Signal Processing) that triggers data acquisition. The ACMS takes 4096 voltage readings during sample translation and creates a voltage profile curve for the translation. The detection coils register a voltage proportional to the rate of change of magnetic flux through them, so the voltage profile is the time derivative of the net flux through the coils. The actual sample moment is obtained by numerically integrating the voltage profile and fitting the known waveform for a dipole moving through the detection coils to the resulting data using a regression algorithm. Alternatively, the integrated data can be used to calculate the sample's centre position.

4.1.4 Features of the PPMS 6000

Some features of PPMS Model 6000 are:

- Sensitivity of DC measurement: $2.5 \times 10^{-5} emu$

- Capability to maintain temperature below 4.2 K for indefinite periods of time and smooth temperature transitions when warming and cooling through 4.2 K.
- Temperature range: 1.8K-400K
- Maximum magnetic field: 9 $Tesla$
- sample volume: a cylindar with a diameter of 3mm and a length of 8mm.

4.2 Experimental Protocols

4.2.1 Hysteresis Loops

Numerical simulations of hysteresis loops, and fits of these simulations to measured hysteresis loops constitute one of the primary sources of information on the Preisach distribution parameters $\bar{h}_c(T)$, $\sigma_c(T)$, $\sigma_i(T)$ and $\mu(T)$, which together define the spectrum of Barkhausen free energy barriers for a given magnetic material. However, fits to a single hysteresis loop measured at a single temperature are far from sufficient to provide an unambiguous identification of the Barkhausen spectrum, and offer no insight whatsoever into the thermal processes which are responsible for the temperature dependence of important macroscopic characteristic parameters like the coercive field H_c or the saturation remanence $M_{r,sat}$.

In the current investigation, each hysteresis isotherm measurement was preceded by a thermal demagnetization at a temperature either above the critical temperature T_c or above the highest blocking temperature $T_{B,max}$. The initial magnetization curve and the major hysteresis loop were then measured at a fixed temperature T. Hysteresis isotherms were measured over a wide range of temperatures which were chosen to representatively sample the entire irreversible regime($0 \leq T < T_c$ or $0 \leq T < T_{B,max}$).

4.2.2 FC and ZFC Moment

While hysteresis and magnetizing isotherms provide a direct probe of the excitation fields(and hence the excitation barriers) which characterize the Barkhausen spectrum, measurements of the field cooled(FC) and zero field cooled(ZFC) moment provide a similarly direct probe of the temperature dependence of the excitation barriers. Measurements of the FC and ZFC moment as a function of temperature, performed over a wide range of applied fields, thus provide an important complement to the measurements of magnetizing and hysteresis isotherms, for purposes of reconstructing the Barkhausen free energy profile of a material. In the zero field cooling(ZFC) protocol, the sample is cooled in zero applied field from a reference temperature T_{ref} above either the magnetic ordering temperature T_c, or above the highest blocking temperature $T_{B,max}$ where the system is in the superparamagnetic state, to the lowest measuring temperature, typically, $T = 5K$. Then a static external field h_a is applied, and the moment is measured as the sample is warmed in a fixed field to T_{ref}. To acquire the corresponding field cooled(FC) curve, the magnetic system is cooled in the external field h_a from the reference temperature T_{ref}, to the lowest experimental temperature, and the moment is measured on warming as before, in a fixed field.

4.3 Preisach Simulations and the Analytical Procedure

4.3.1 Fitting Parameters

In the Preisach approach, the goal is to determine the parameters defined in equations 2.15, 2.16, and 2.17 by fitting numerical simulations of the response functions(FC moment, ZFC moment, initial magnetizing curve, major hysteresis loop) to the experimentally measured response functions. These parameters can

be grouped roughly into two categories: the parameters that are essentially fixed by certain physical constraints, and the parameters that are more or less freely varied in the fitting process.

4.3.2 Parameters Specified by Physical Constraints

The following parameters have values which are essentially fixed by the experimental data, and hence are relatively inflexible. For ferromagnetically ordered materials, the critical ordering temperature T_c coincides with a rapid decrease in both the FC and ZFC moment with increasing temperature, over a relatively narrow temperature interval , as the system is warmed from the ordered phase into the weakly magnetic paramagnetic phase. Measurements of the field and temperature dependence of critical peaks observed in the ac susceptibility [24] can be used to refine preliminary estimates based on the FC and ZFC moment, although a very precise knowledge of T_c is seldom required for an analysis of irreversible phenomena. For fluctuation-dominated materials, no such direct evidence is available since T_c typically lies well within the superparamagnetic regime. The mean zero temperature coercive field $\bar{h}_{c0}$ can be estimated from the measured coercivity H_c at the lowest experimental measuring temperature, typically between $2K \leq T \leq 5K$. Similarly, the saturation moment m_{sat} of the system is fixed by the saturation value of the lowest temperature hysteresis isotherm measured in applied fields $h_a \gg H_c$. As for the parameter $\alpha = ln(t_{exp}/\tau_0)$, our experimental measuring time constant is typically $t_{exp} \approx 100s$, so $\alpha \sim 25$, assuming $\tau_0 \sim 10^{-9}$ to $10^{-10}s$.

4.3.3 Flexible Parameters

While the remaining parameters are comparatively flexible, the influence of several of these parameters tends to be confined primarily to specific structural features

of the response functions. These relationships have been discussed in some depth in chapter 3, and here we content ourselves with only a briefly summary of the correlations established by the numerical simulations:

- **Distribution of coercive fields**: The parameters $\bar{h}_{c0}$, σ_{c0}, Γ_c and Γ_c' affect the temperature dependence of the ZFC moment and the field dependence of the major hysteresis loop, but have a negligible impact on the temperature dependence of the FC moment.

- **Distribution of interaction (asymmetry) fields**: The parameters σ_{i0} and Γ_i affect the temperature dependence and amplitude of the FC moment, and the squareness of the major loop(that is, the ratio $m_{r,sat}/m_{sat}$), but have only a weak influence on the ZFC moment. Large values of Γ_i correspond to a rapid decrease in the strength of the interaction fields with increasing temperature, and generate a maximum on the temperature dependence of the FC moment.

- **The width of the interaction field distribution** σ_{i0} : The magnitude of σ_{i0} is closely related to the field dependence of the FC moment at $T = 0$. For very small $\sigma_{i0} \ll \bar{h}_{c0}$, the field dependence is weak, while for $\sigma_{i0} \geq \bar{h}_{c0}$, the field dependence is strong.

- **The width of of the coercive field distribution** σ_{c0} : The parameter σ_{c0} defines the shape of the major hysteresis loop and the initial magnetizing curve at $T = 0$, primarily by defining the slope in the vicinity of $\bar{h}_{c0}$.

- **Zero temperature spontaneous moment** μ_0: The parameter μ_0 affects the location and the shape of the maximum in the ZFC moment, and also affects the temperature dependence of the coercive field $\bar{h}_c(T)$ through its influence on the thermal viscosity field h_T^*.

- **Reversible component of the response.** This is generally the most difficult contribution to define reliably, since the parameters f and λ may both, in principle, be temperature dependent, and also since reversibility is not necessarily an independent additive contribution the magnetic response, but is often an "intrinsic" component of hysteresis loops(for instance, the Stoner-Wohlfarth loops for coherent rotation). As a first approximation, the factor f is roughly defined by $f \cong 1 - m_{r,sat}/m_{sat}$ and is assumed to be temperature independent unless the fits demand otherwise.

- **Mean coercive field $\bar{h}_c(T)$.** For anisotropy-dominated systems, with FC and ZFC response functions resembling those in figure (3.2) with $\eta = 4.0$, the functional dependence of $\bar{h}_c(T)$ is initially assumed to be closely related to the temperature dependence of the measured coercive field $H_c(T)$, and varied as necessary to improve the fits. For fluctuation-dominated systems with FC and ZFC response functions like those in figure (3.2)with $\eta = 0.2$, the functional dependence of $\bar{h}_c(T)$ is chosen to be roughly constant throughout the hysteretic regime, and thermal fluctuations h_T^* are allowed to define the temperature dependence of the response functions, at least as a first approximation.

- **Spontaneous Barkhausen moment $\mu(T)$.** According to the simulations, the temperature dependence of the FC moment in high fields $h_a \gg \bar{h}_{c0}$ is determined almost exclusively by the temperature dependence of $\mu(T)$. Thus, as a starting point, the functional dependence of $\mu(T)$ is approximately defined by the shape of $m_{FC}(T)$ measured in the highest field h_a.

4.3.4 Fitting Procedure

An iterative fitting procedure is followed, guided by the systematic trends that we observed in the numerical simulations in chapter 3 and summarized above. Starting from an initial set of parameters chosen in accordance with the assumptions outlined above, the Preisach model is used to simulate numerical response functions which are compared with the experimental response functions. The parameters are then varied individually and manually in order to improve the fits. This procedure allows us to develop a a clear picture of the systematic trends induced by varying each parameter, and hence to isolate the dominant physical mechanism responsible for each of the principal structural features and systematic trends which characterize the experimental data.

Our goal is to simulate the entire set of major hysteresis loops, and ZFC and FC moments using a common set of parameters so that the quality of the fits are often sacrificed in preference to obtaining a set of parameters which describe the widest spectrum of experimental behaviour.

4.4 Sample Preparation

All of the magnetic materials investigated in this thesis were fabricated by collaborators either at the University of Manitoba or at the University of Lanzhou, with whom we are currently involved in a CIDA (Canadian International Development Agency) project. Consequently, we present here only a brief summary of the fabrication procedures.

4.4.1 Thin Film $Fe_{60}(SiO_2)_{40}$

Nanometer-sized Fe particles dispersed in a matrix of amorphous SiO_2 are currently the subject of extensive research. Although bulk Fe is magnetically very

soft, systems of nanodimensional Fe particles dispersed in SiO_2, Al_2O_3 and Cu, have a high coercivity, making such materials potential candidates for magnetic recording media[34][35].

There are conventionally two kinds of $Fe_x(SiO_2)_{1-x}$ media, distinguished by different fabrication techniques. One uses magnetron sputtering to deposit Fe and SiO_2 onto a glass substrate which is kept at a constant temperature. By adjusting the deposition time, films with different widths can be obtained. Another way is the conventional ceramic technique. The sample is prepared by high energy ball-milling using stainless steel balls, starting from Fe powders and sol-gel derived silica in properly weighted proportion[34].

The microstructure of $Fe_x(SiO_2)_{1-x}$ is composition dependent for sputtered granular thin films. Mössbauer spectroscopy shows the presence of α-Fe, at low SiO_2 content, and the presence of isolated superparamagnetic Fe particles at high SiO_2 content[36] . A small amount of Fe oxide was also observed which tends to soften the film[37].

The system analyzed here was a thin film of $Fe_{60}(SiO_2)_{40}$ with 33% Fe, $1\mu m$ in thickness, fabricated by RF sputtering at room temperature onto a Kapton substrate. The average particle diameter determined by transmission electron microscopy was $2.4nm$.

4.4.2 $Ni_{1-x}Zn_xFe_2O_4$

Ni, Zn and Fe nitrates were dissolved together in a minimum amount of deionized water to produce a clear solution. Polyvinyl alcohol(PVA) was used to make a gel. The aqueous PVA solution was added to the nitrate solution and dehydrated at $60 - 80^oC$. The gelation proceeded step by step and a slightly red gel-type precursor was obtained. The precursor was calcined at different temperatures to obtain $Ni_{1-x}Zn_xFe_2O_4(0 \leq x \leq 1.0)$ fine powder with particle sizes ranging from

6-90nm.

4.4.3 $SrRuO_3$

Strontium ruthenate $SrRuO_3$, has a distorted perovskite structure, and is a ferromagnetic oxide containing a single kind of magnetic ion Ru^{4+}. Polycrystalline $SrRuO_3$ was prepared by mixing $SrCO_3$ and nanocrystalline RuO_2 taken in the stoichiometric ratio and heating initially at 900^oC for 72 hours with 6 intermediate grindings. Formation of single-phase compounds was established by powder x-ray-diffractions(XRD) measurements. The compound so obtained was then ground well and annealed in air at various temperatures from 950 to 1300^oC for 12 hours.

4.4.4 $La_{0.5}Sr_{0.5}CoO_3$

Samples of nominal composition $La_{0.5}Sr_{0.5}CoO_3$ were prepared using standard ceramic techniques. Stoichiometric quantities of La_2O_3 (ultrapure), $SrCO_3$ and Co_3O_4 were thoroughly mixed and ground for 24 hours by ball milling in acetone. The dried powder was subsequently pressed into pellet form and fired at 900^oC for 24 hours. The pellet was then reground, mixed with a binder, and then refired in oxygen for 24 hours at 1000^oC followed by 96 hours at 1050^oC.

4.4.5 $La_{0.7}Sr_{0.3}MnO_3$

Polycrystalline $La_{0.7}Sr_{0.3}MnO_3$ bulk samples were prepared by the sol-gel process. Stoichiometric amounts of $La(NO_3)_3 \cdot 6H_2O$, $Mn(NO_3)_2$ and $Sr(NO_3)_2$ were dissolved initially in ion-free water, and then added to an aqueous polyvinyl alcohol solution heated to $60 - 80^oC$. The solution was stirred for one hour. The final sol-gel material, obtained by a gelation procedure, was then decomposed at 520 K and presintered at 800 K in air. The powder was pressed into a rectangu-

lar shape at a pressure of 250 MPa, and then sintered again in air at 973 K. A single phase perovskite structure resulted, as confirmed by x-ray diffraction using Cu K_α radiation. The broad diffraction peaks indicate a fine grain structure in this sample, estimated at about 15 nm diameter using Scheller's formula [25] applied to the full width at half maximum of the (110) peak, and confirmed by transmission microscopy.

Chapter 5

Analysis of Fluctuation-Dominated Magnetic Systems

5.1 Granular $Fe_x(SiO_2)_{1-x}$

The principal features of the field and temperature dependence of the magnetic response of the particulate Fe/SiO_2 thin film are summarized in figures (5.1) and (5.2), which show respectively measurements of the field cooled (FC) and zero field cooled (ZFC) moment as a function of temperature T, performed over a wide range of applied fields h_a, and of the initial magnetizing curve and major hysteresis loop as a function of h_a, performed over a wide range of temperatures. The ZFC moment exhibits a well defined maximum, which becomes progressively broader and shifts to lower temperatures with increasing applied field. The FC moment also exhibits a maximum in this system, which is essentially coincident with the ZFC maximum, and the two branches bifurcate very close to the maximum, with $m_{FC} > m_{ZFC}$ for all temperatures $T < T_{max}$. Above T_{max}, both the FC and ZFC moment exhibit a long superparamagnetic tail. As figure (5.2) shows, this system exhibits hysteresis at all temperatures $T < 90K$. With increasing temperature both the coercivity and the saturation remanence decrease, and the loop becomes progressively steeper, but the saturation moment remains essentially constant.

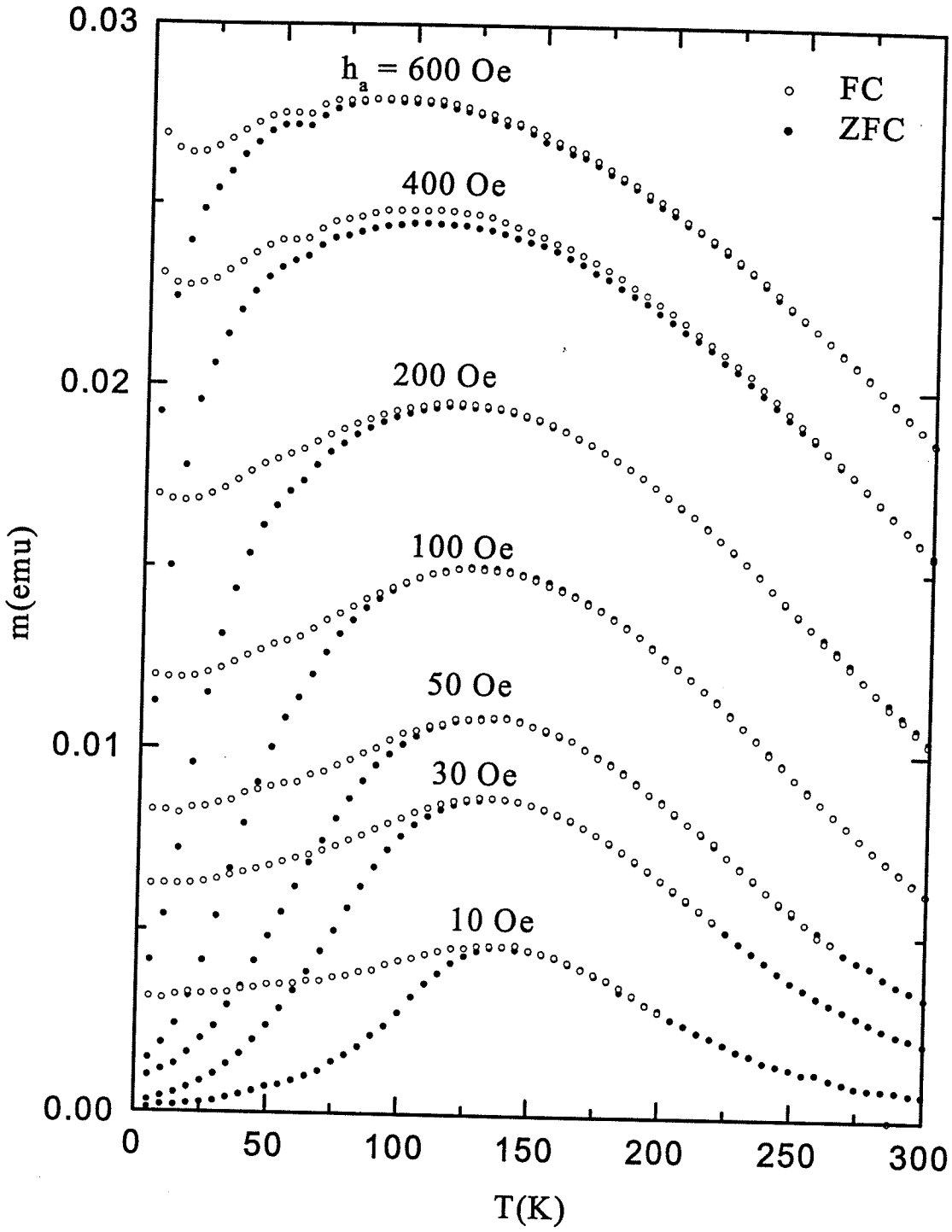

Figure 5.1: *The FC and ZFC moment of $Fe - SiO_2$ as a function of temperature T, over a wide range of applied fields h_a.*

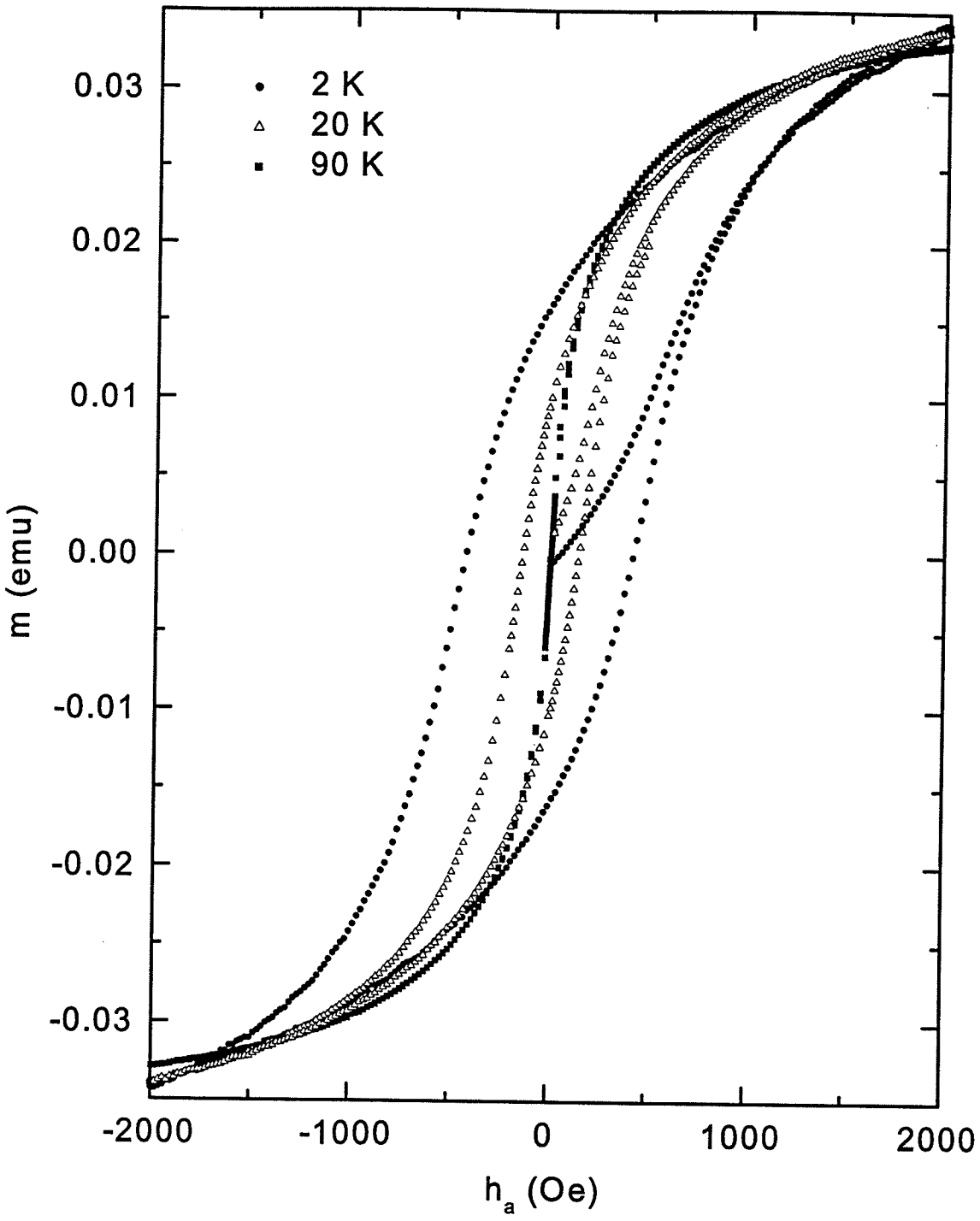

Figure 5.2: *The initial magnetization curves and major hysteresis loops for $Fe - SiO_2$ for T= 2 K, 20 K, 90K.*

If figures (5.1) and (5.2) are compared with figures (3.2) and (3.7), which show Preisach simulations of the FC and ZFC moment and hysteresis loops of fluctuation-dominated and anisotropy-dominated systems, respectively, it is clear that the principal structural features and systematics of the measured response functions closely resemble those in figures (3.2)(a) and (3.7)(a). This allows us to identify the Fe/SiO_2 medium as a fluctuation-dominated system, for which the temperature dependence of the magnetic response is determined primarily by thermal activation over energy barriers which are essentially temperature independent over most of the hysteretic regime, and for which critical effects are not explicit to play a role. This behaviour is not a trivial consequence of the particulate microstructure. To emphasize this point, we show in figures (5.3) and (5.4), similar measurements performed on a system of particulate aligned CrO_2 recording particles, which exhibits behaviour much closer to that expected for an anisotropy-dominated system, as shown in figures (3.2)(b) and (3.7)(b). In fact, the fundamental difference between the two systems lies entirely in the height of the anisotropy barriers, which are much smaller in $Fe - SiO_2$ than in CrO_2. (The latter material is a ferromagnet with a critical temperature $T_c \approx 398K$, and anisotropy effects are dominant because the easy axes of the CrO_2 particles are aligned with each other, and with the applied field.)

The data in figures (5.1) and (5.2), allow us to obtain preliminary estimates for several of the important Preisach fitting parameters. From the lowest temperature hysteresis loop at $T = 2K$, we obtain an estimate of the zero temperature coercivity $\bar{h}_{c0} \cong 600\ Oe$. From the inflection point in the temperature dependence of the ZFC moment measured in the lowest field $h_a = 10\ Oe$, we obtain an estimate for the zero temperature spontaneous Barkhausen moment μ_0 since $\mu_0 \bar{h}_{c0} \cong k_B T_{infl} ln(t_{exp}/\tau_0) \cong 25 k_B T_{infl}$, which yields $\mu_0 \cong 5 \times 10^{-16}$emu. From the ratio of the saturation remanence to the saturation moment for the $T = 2K$

hysteresis loop, we obtain an estimate for the reversible fraction $f \cong 0.5$. From the existence of the maximum in the FC moment, we infer that the dispersion of interaction fields $\sigma_i(T)$ must decrease rapidly with increasing temperature as $T \rightarrow T_{max}$, so that if $\sigma_i(T) = \sigma_{i0}(1 - T/T_b)^{\Gamma_i}$, with $T_b \cong T_{max}$, it follows from a comparison with figure (3.6)(a) that $\Gamma_i > 1$. In fact, the numerical calculations to be discussed shortly confirm all of the these initial estimates. Of the remaining fitting parameters, σ_{c0} is determined by the shape of the initial magnetizing curve and the major hysteresis loop at $T = 2K$, while σ_{i0} is determined by the field dependence of the FC moment at $T = 2K$ in figure (5.1).

The numerical Preisach simulations were performed assuming the following product of two Gaussian functions for the Preisach distribution:

$$p(h_c, h_i) = (2\pi\sigma_c^2)^{-\frac{1}{2}} exp[-(h_c - \bar{h}_c)^2/2\sigma_c^2] \cdot (2\pi\sigma_i^2)^{-\frac{1}{2}} exp[-h_i^2/2\sigma_c^2] \qquad (5.1)$$

Intrinsic temperature dependences were described by allowing the Preisach fitting parameters to vary with temperature as follows:

$$\left\{ \begin{array}{lcl} \mu(T) & = & \mu_0(1 - T/T_c)^{\Gamma} \\ \bar{h}_c(T) & = & \bar{h}_{c0}(1 - T/T_c)^{\Gamma_c} \\ \sigma_c(T) & = & \sigma_{c0}(1 - T/T_c)^{\Gamma_c'} \\ \sigma_i(T) & = & \sigma_{i0}(1 - T/T_b)^{\Gamma_i} \end{array} \right\} \qquad (5.2)$$

Although the ideal goal was to describe all of the experimental data using a single set of fitting parameters, fits were in fact performed individually to each pair of FC and ZFC moments and to each hysteresis isotherm, in order to better identify any systematic variations in the Preisach parameters. Tables (5.1) and (5.2) summarize all the values of the fitting parameters, and figures (5.5) through (5.12) show the numerical simulations as solid curves. A comparison of figure (5.1) with figure (5.5) shows that the numerical simulations replicate all the principal structure features and systematic trends observed in the measured FC and ZFC

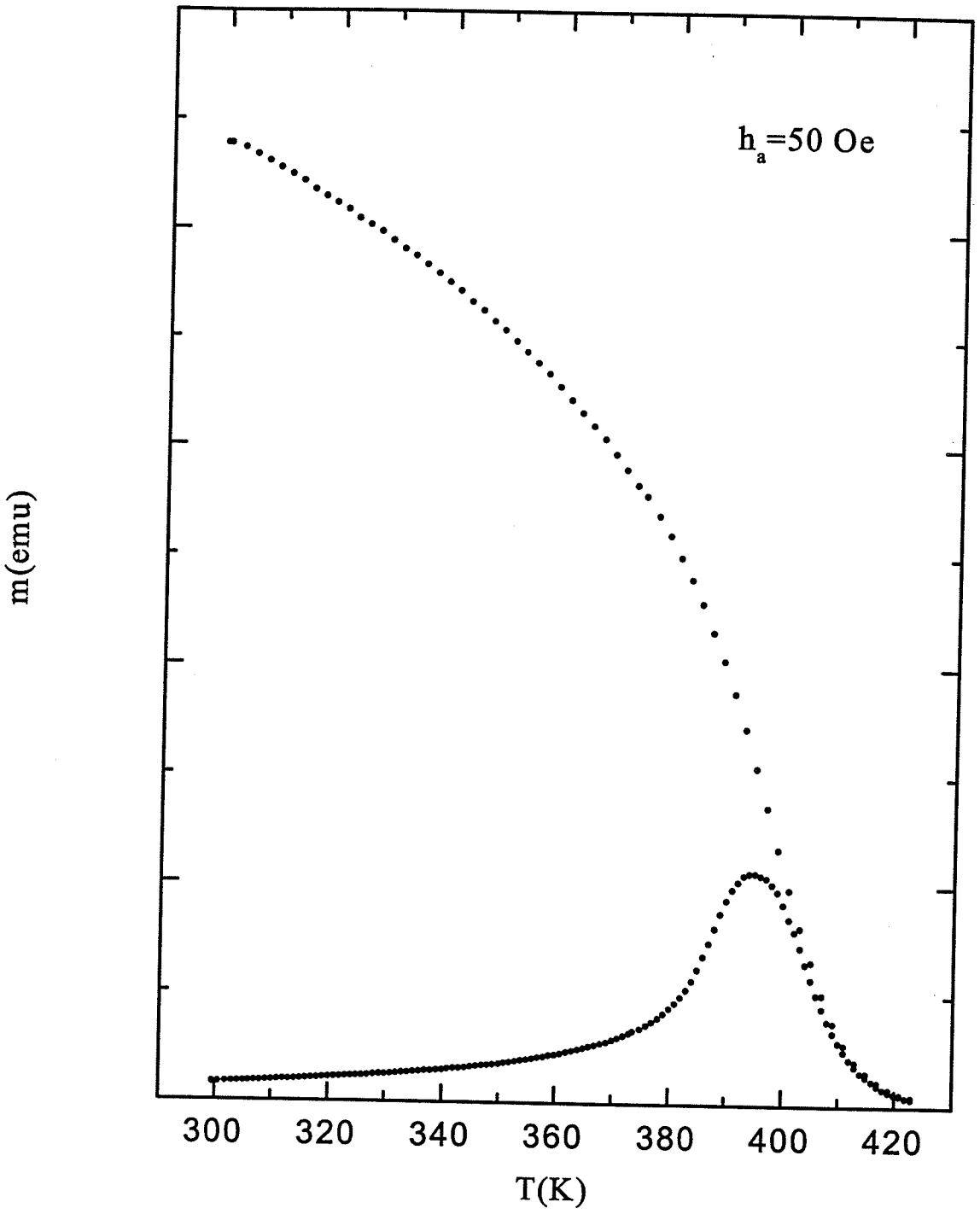

Figure 5.3: *The FC and ZFC moment of CrO_2 ($T_c = 398K$) as a function of temperature T in an applied field $h_a = 50$ Oe.*

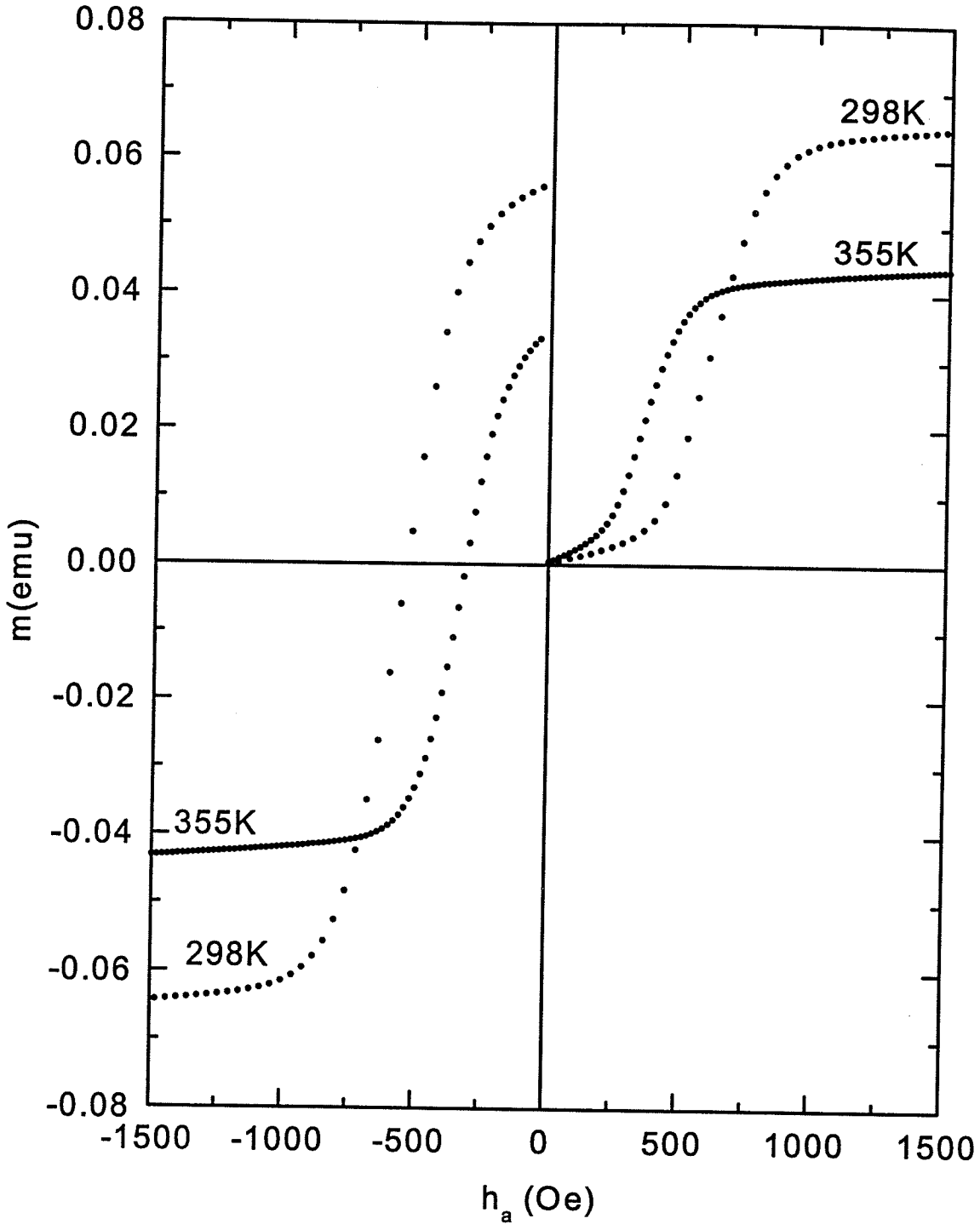

Figure 5.4: *The initial magnetization curve and the descending branch of the major hysteresis loop of CrO_2 ($T_c = 398K$) for T= 298 K, 355K.*

Table 5.1: Fitting parameters from ZFC and FC moment of $Fe - SiO_2$ ($T_c = 500K$)

h_a(Oe)	14	32	55	100	200	400	600
$\mu_0(10^{-16}$emu)	5	4	3	2.5	2	2	2
h_{c0}(Oe)	600	600	600	600	600	600	600
σ_{c0} (Oe)	240	240	240	240	240	240	240
σ_{i0} (Oe)	72	84	108	138	168	240	360
Γ	1/3	1/3	1/3	1/3	1/3	1/3	1/3
Γ_c	1/3	1/3	1/3	1/3	1/3	1/3	1/3
Γ'_c	1/3	1/3	1/3	1/3	1/3	1/3	1/3
Γ_i	2.5	2.5	2.5	2.5	2.5	2.5	2.5
λ(1/Oe)	0.0006	0.0006	0.0006	0.0006	0.0006	0.0006	0.0006
f	0.5	0.5	0.5	0.5	0.5	0.5	0.5
m_{sat}(emu)	0.04	0.04	0.04	0.04	0.04	0.04	0.04
$T_b(K)$	130	120	120	120	120	115	115

moment, and figures (5.6), (5.7) and (5.8) illustrate the typical quality of the individual fits. Figures (5.9) through (5.12) compare the numerical simulations of the hysteresis isotherms with the measured isotherms, and figure (5.13) compares the measured and model coercive fields, H_c and $\bar{h}_c$, respectively.

An inspection of tables (5.1) and (5.2) shows that the free energy dissipation barriers, as defined by $\mu\bar{h}_c = \mu_0\bar{h}_{c0}(1 - T/T_c)^{\Gamma_c+\Gamma}$ and $\mu\sigma_c = \mu_0\sigma_{c0}(1 - T/T_c)^{\Gamma'_c+\Gamma}$, are very weakly dependent on temperature throughout the entire hysteretic regime ($T < 90K$) and, in fact, over the entire experimental temperature range $T \leq 300K$, confirming that thermal fluctuations (through h^*_T) are primarily responsible for the temperature dependences observed in the FC and ZFC moments and in the hysteresis isotherms, and that the critical temperature T_c has very little effect on the measured response. In particular, the temperature dependence of the measured coercive field in figure (5.13) is replicated very well by this approach, and is clearly a consequence of an effective reduction in the barrier heights by the thermal fluctuation energy $W^* = k_B T ln(t_{exp}/\tau_0)$, rather

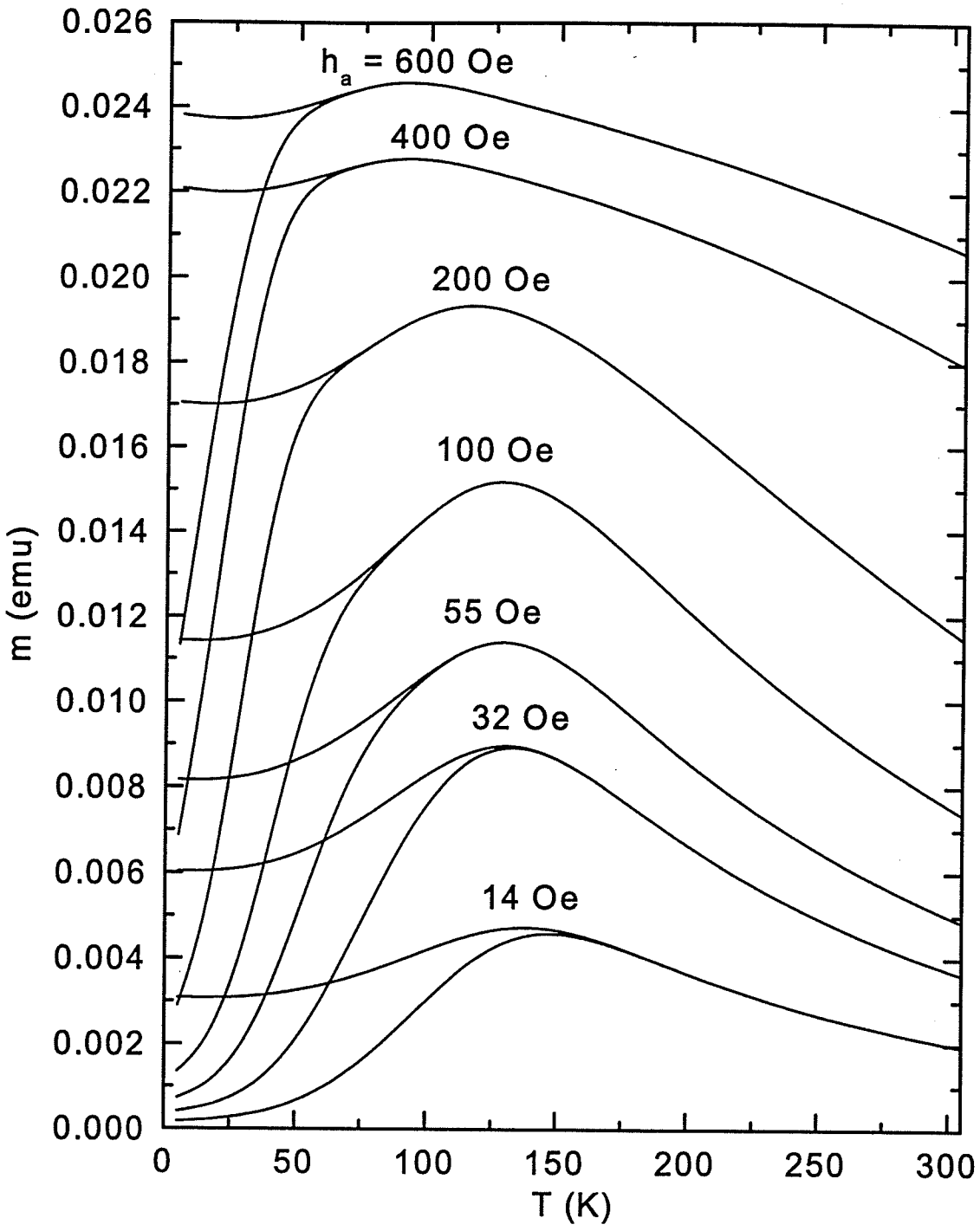

Figure 5.5: *Preisach numerical simulations of FC and ZFC moments for* $Fe - SiO_2$.

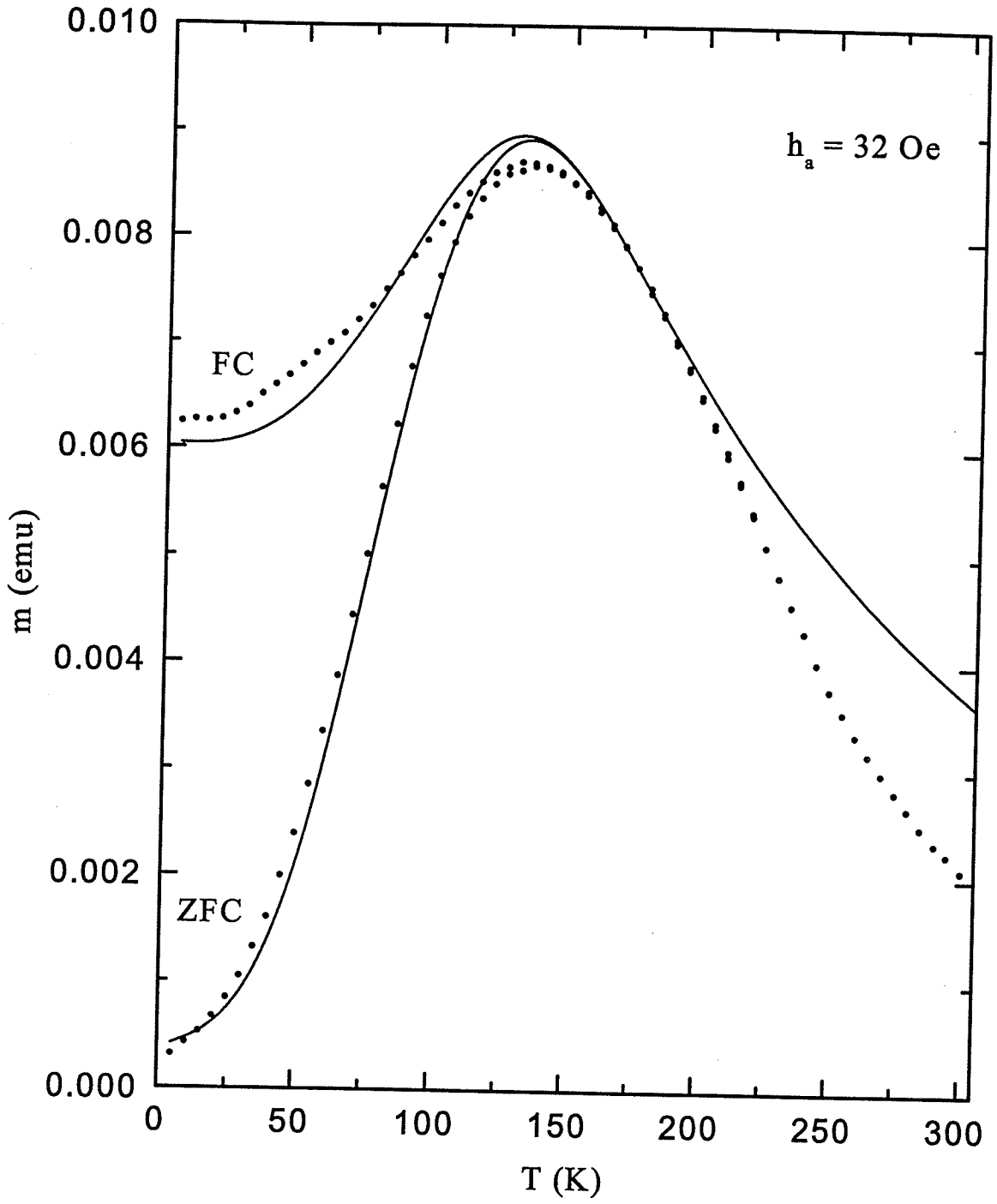

Figure 5.6: *A comparison of the Preisach numerical simulations with the measured FC and ZFC moment of* $Fe - SiO_2$ *for* $h_a = 32Oe$.

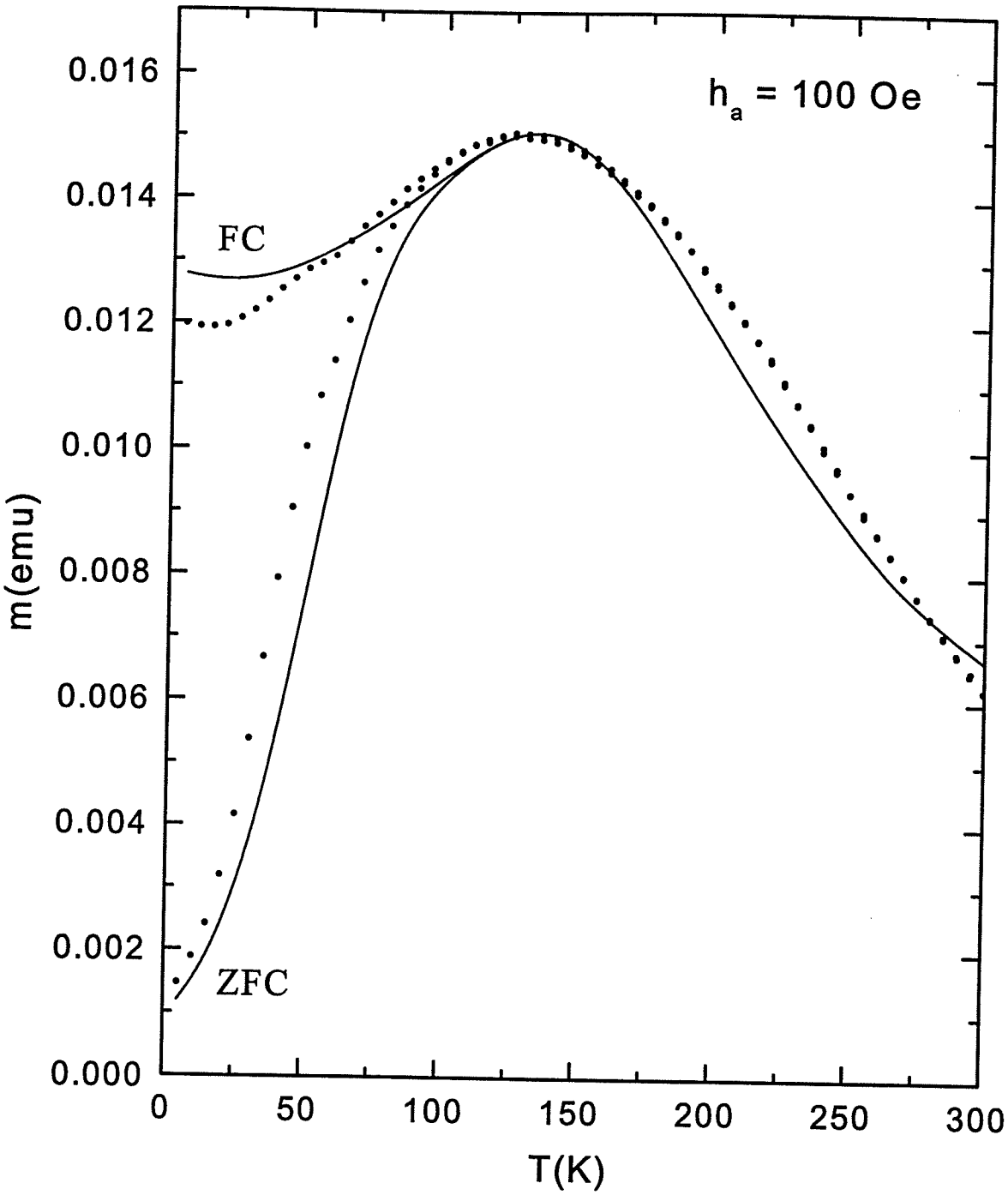

Figure 5.7: *A comparison of the Preisach numerical simulations with the measured FC and ZFC moment of* $Fe - SiO_2$ *for* $h_a = 100Oe$.

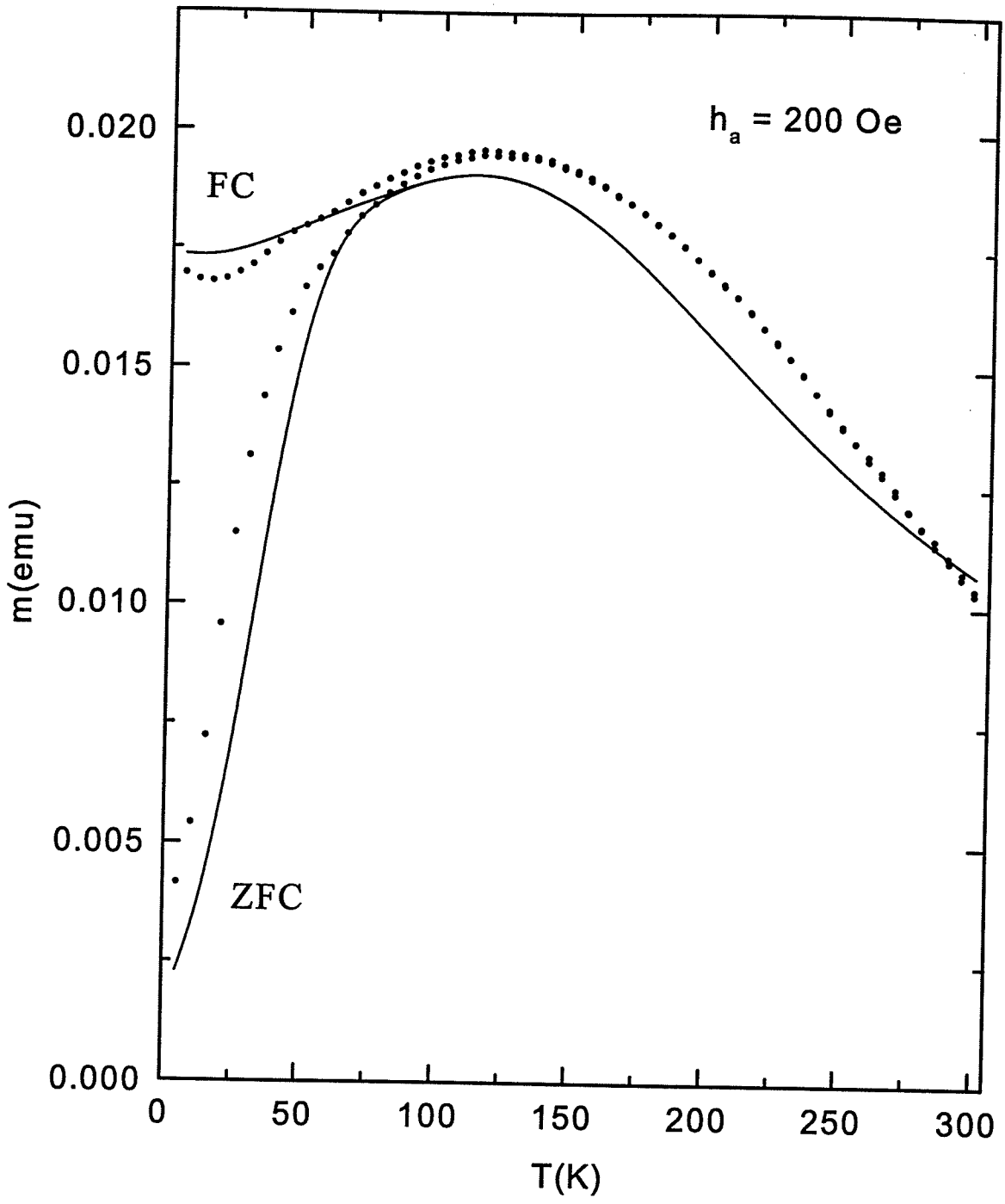

Figure 5.8: *A comparison of the Preisach numerical simulations with the measured FC and ZFC moment of* $Fe - SiO_2$ *for* $h_a = 200Oe$.

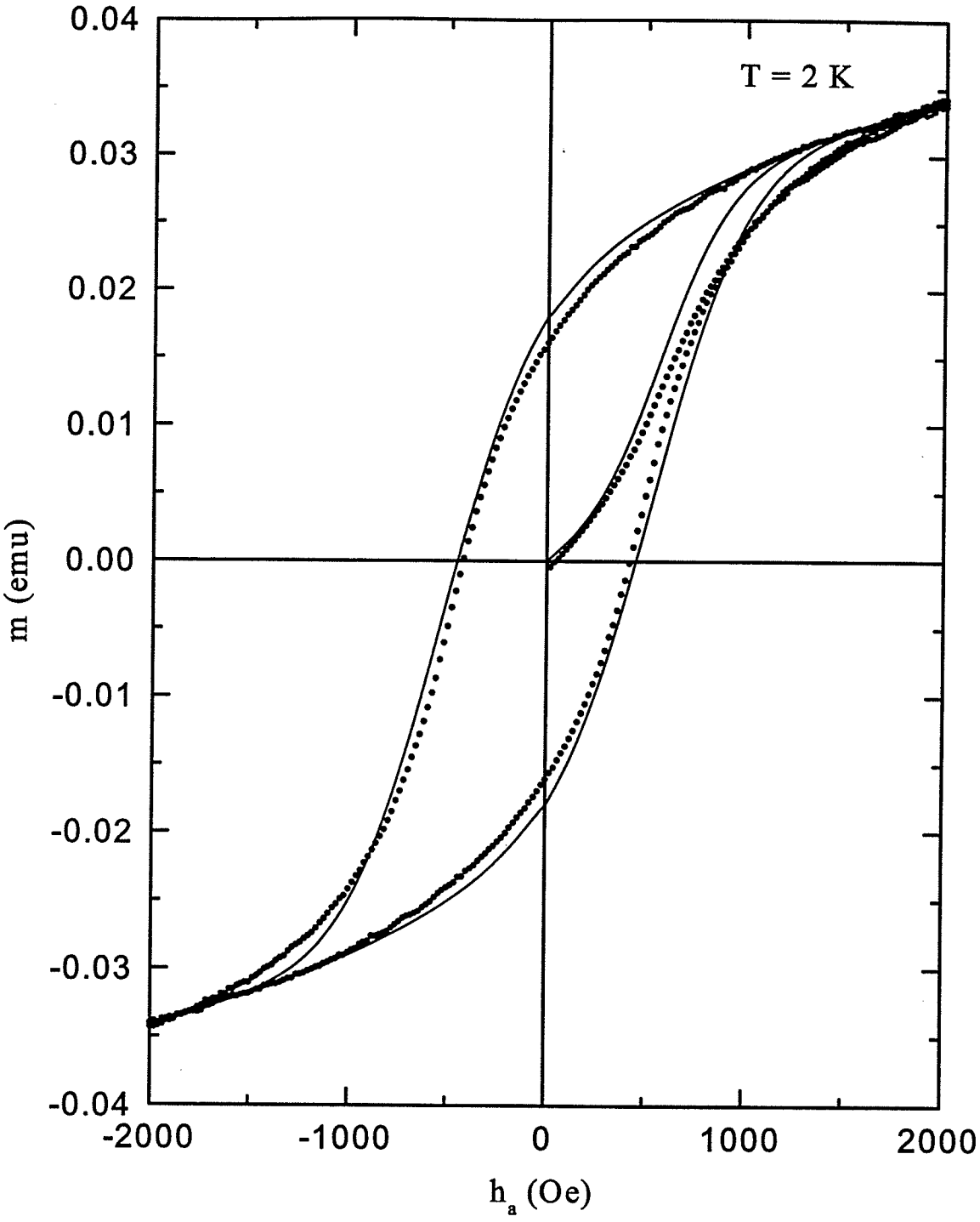

Figure 5.9: *A comparison of the Preisach simulations with the measured initial magnetizing curve and major hysteresis loop of* $Fe - SiO_2$ *for* $T = 2K$.

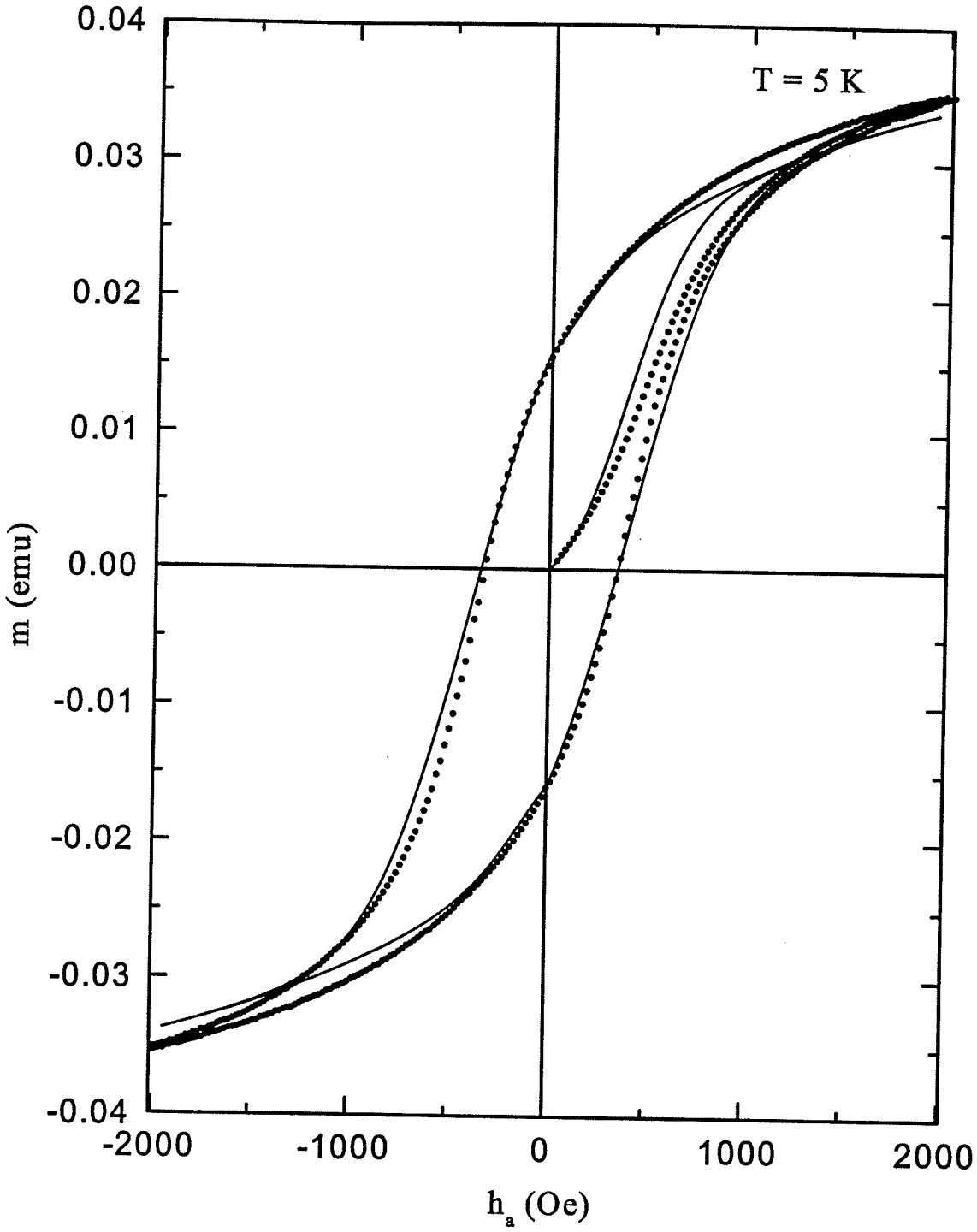

Figure 5.10: *A comparison of the Preisach simulations with the measured initial magnetizing curve and major hysteresis loop of* $Fe - SiO_2$ *for* $T = 5K$.

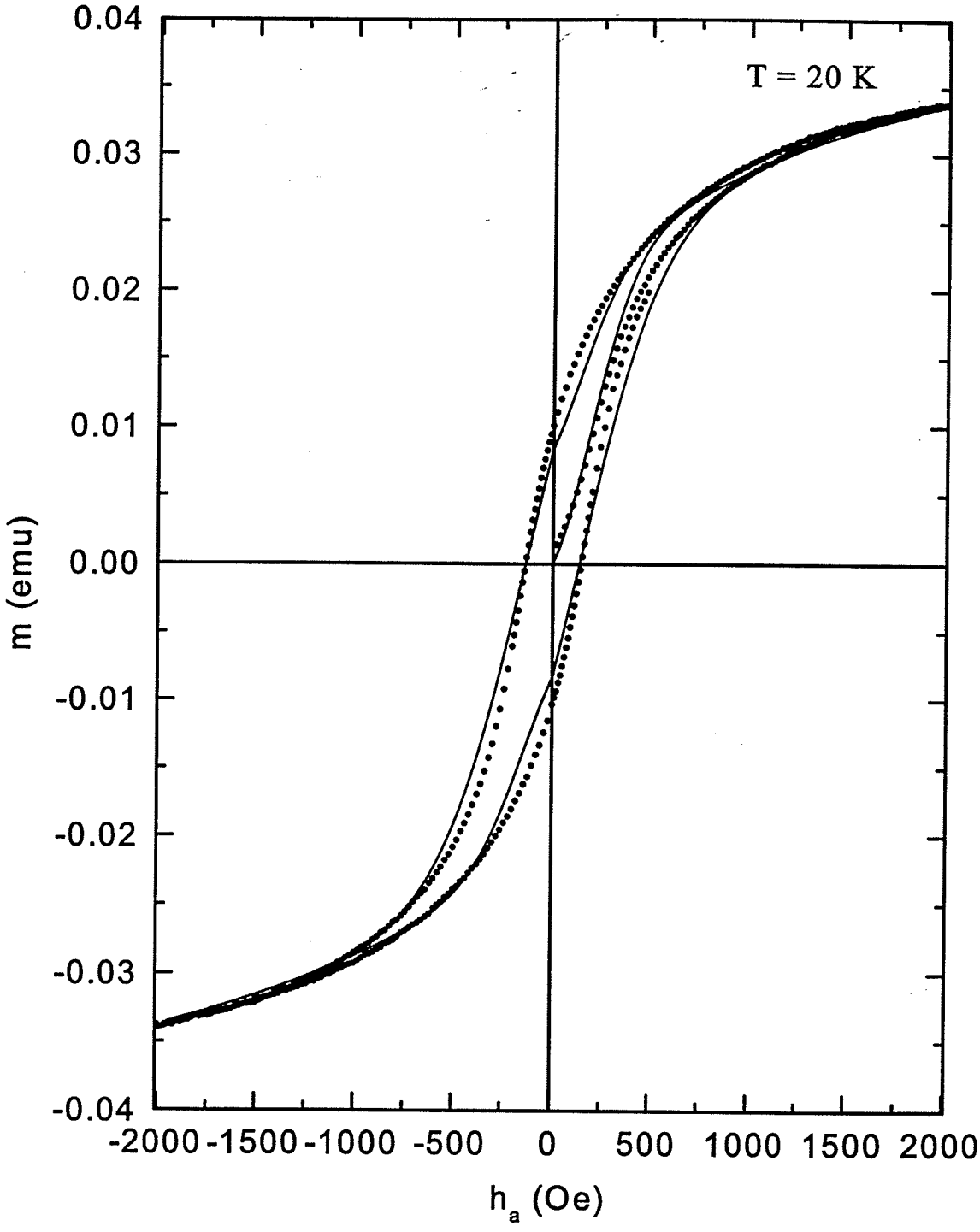

Figure 5.11: *A comparison of the Preisach simulations with the measured initial magnetizing curve and major hysteresis loop of* $Fe - SiO_2$ *for* $T = 20K$.

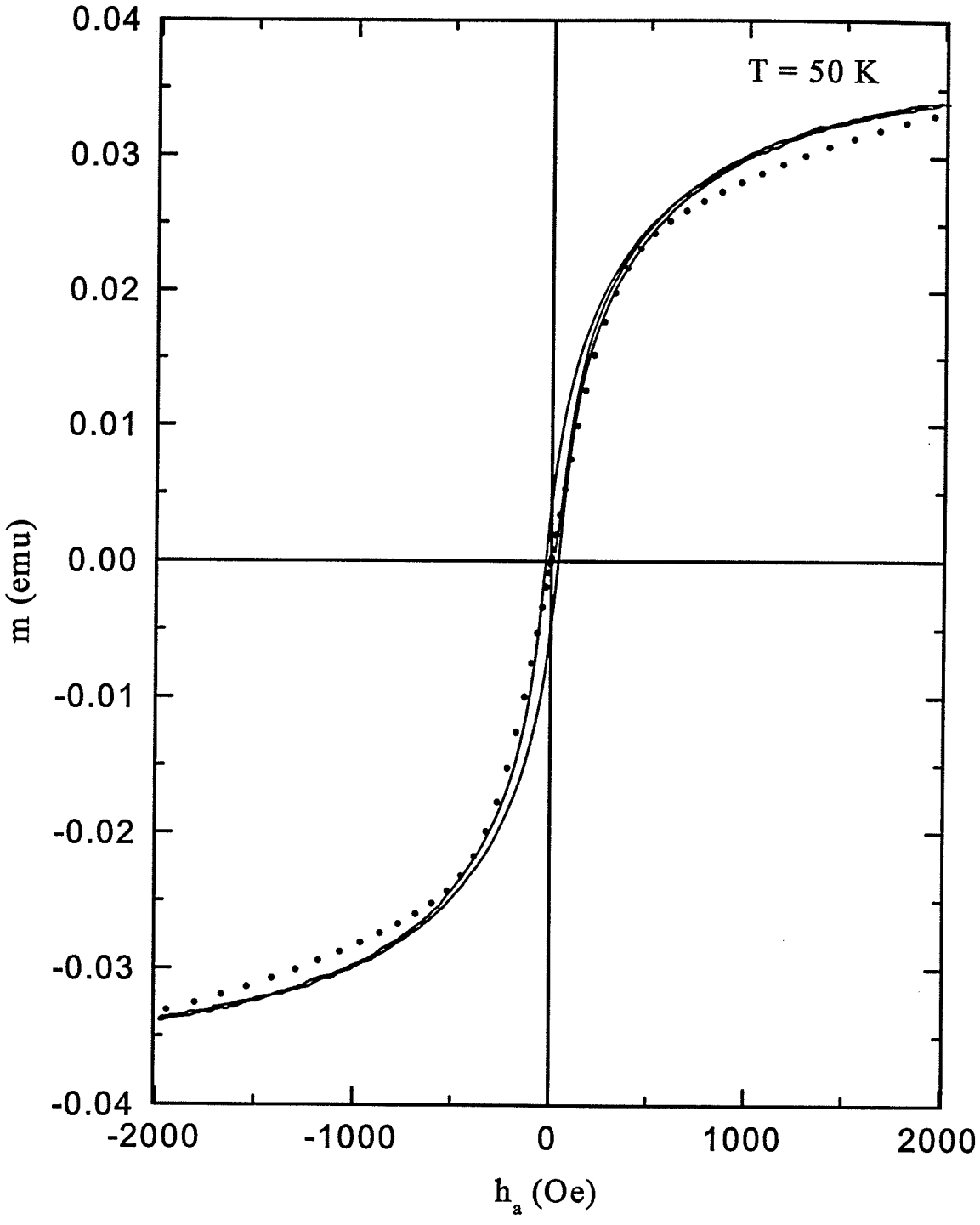

Figure 5.12: *A comparison of the Preisach simulations with the measured initial magnetizing curve and major hysteresis loop of* $Fe - SiO_2$ *for* $T = 50K$.

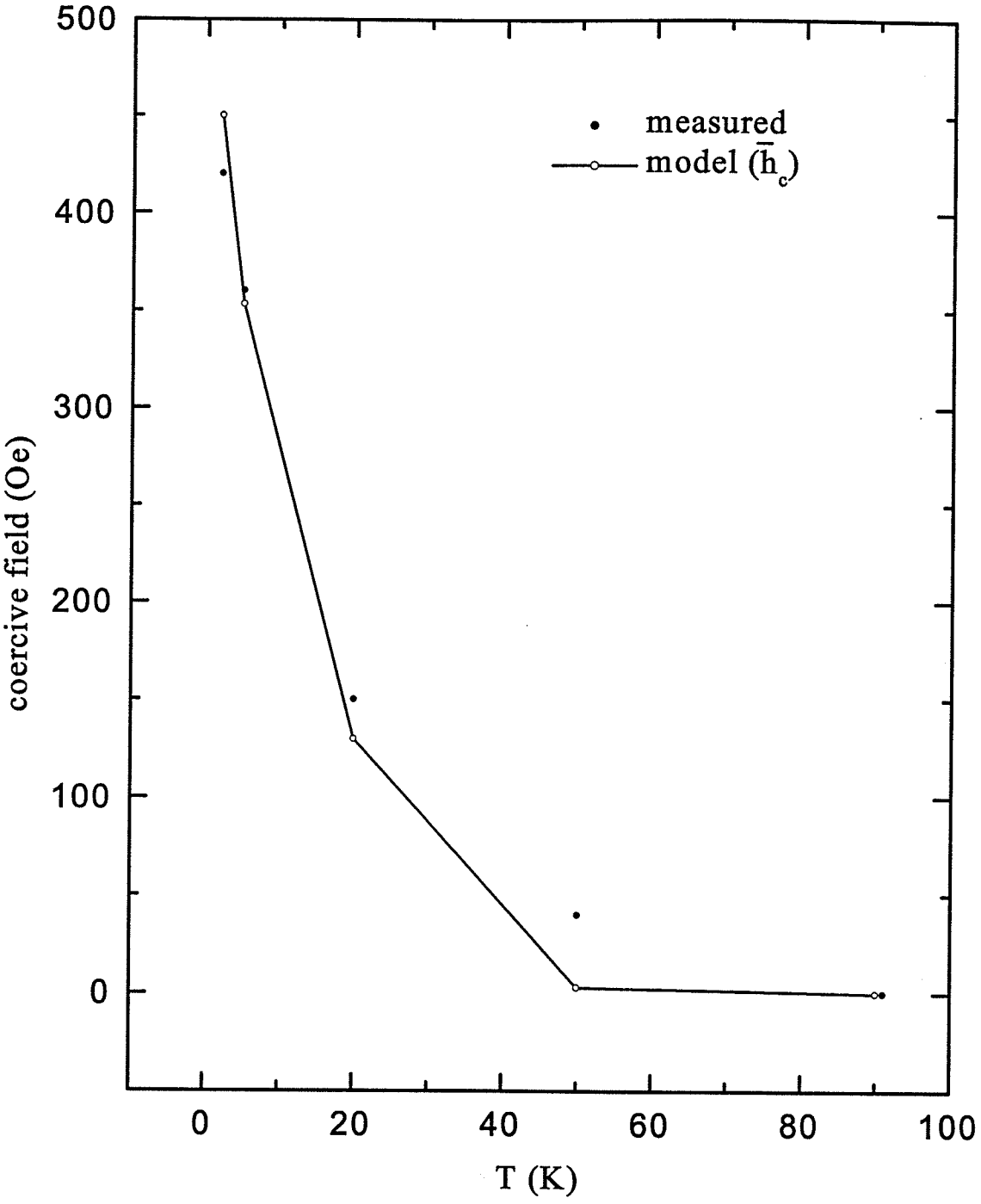

Figure 5.13: *Temperature dependence of the measured and model coercive fields for* $Fe - SiO_2$.

Table 5.2: Fitting parameters from hysteresis loops of $Fe - SiO_2$ ($T_c = 500K$)

T (K)	2	5	20	50
$\mu_0(10^{-16}\text{emu})$	3	3	3	2
h_{c0}(Oe)	600	600	600	600
σ_{c0} (Oe)	240	240	240	240
σ_{i0} (Oe)	240	240	180	240
Γ	1/3	1/3	1/3	1/3
Γ_c	1/3	1/3	1/3	1/3
Γ_c'	1/3	1/3	1/3	1/3
Γ_i	2.5	2.5	2.5	2.5
λ(1/Oe)	0.0006	0.0007	0.0006	0.00071
f	0.5	0.5	0.5	0.5
m_{sat}(emu)	0.04	0.04	0.04	0.04
$T_b(K)$	130	130	130	130

than of explicit variations in the dissipation mechanisms ($\bar{h}_c$ and σ_c) with temperature. The numerical simulations also replicate the maximum observed in the temperature dependence of the FC moment, and show that the physical origin of this structure is directly related to the temperature dependence of the interaction fields h_i, which decrease rapidly as $\sigma_i(T) = \sigma_{i0}(1 - T/T_b)^{2.5}$ with increasing temperature and vanish in the vicinity of the low field FC and ZFC maximum ($T_b \sim 115 - 130K$). From a physical point of view, this behaviour is a reasonable consequence of the gradual unblocking of the particles by thermal fluctuations as $T \to T_{max}$, since an unblocked particle is a much weaker source of static interaction fields than a blocked particle.

In order to obtain a good description of the reversible superparamagnetic tail for temperatures $T > T_{max}$ in the FC and ZFC response, it was necessary to employ a critical temperature $T_c \cong 500K$ which is much less than the critical temperature $T_c \cong 1000K$ for bulk iron. At this stage, it is unclear whether this is a real effect related to the small particle size, or whether it simply reflects some inadequacy in the model treatment of superparamagnetism, perhaps related to

the use of the *tanh* function rather than a Langevin function.

In conclusion, we show in figure (5.14) plots of the temperature dependence of the mean anisotropy barrier $\bar{W}_a(T) = \mu(T)\bar{h}_c(T) = \mu_0\bar{h}_{c0}(1 - T/T_c)^{\Gamma+\Gamma_c}$, the anisotropy barriers $W_a^{\pm}(T)$, one standard deviation higher and lower than $\bar{W}_a(T)$, $W_a^{\pm}(T) = \mu_0\bar{h}_{c0}(1 \pm \sigma_{c0})(1 - T/T_c)^{\Gamma_c+\Gamma_c'}$, and the thermal fluctuation energy $W^* = k_B T \cdot ln(t_{exp}/\tau_0)$, all normalized to $\bar{W}_a(0) = \mu_0\bar{h}_{c0}$. The figure emphasizes the fluctuation-dominated nature of the Fe/SiO_2 system, since the temperature dependence of W^* clearly dominates that of the free energy landscape throughout the irreversible regime $T < 100K$.

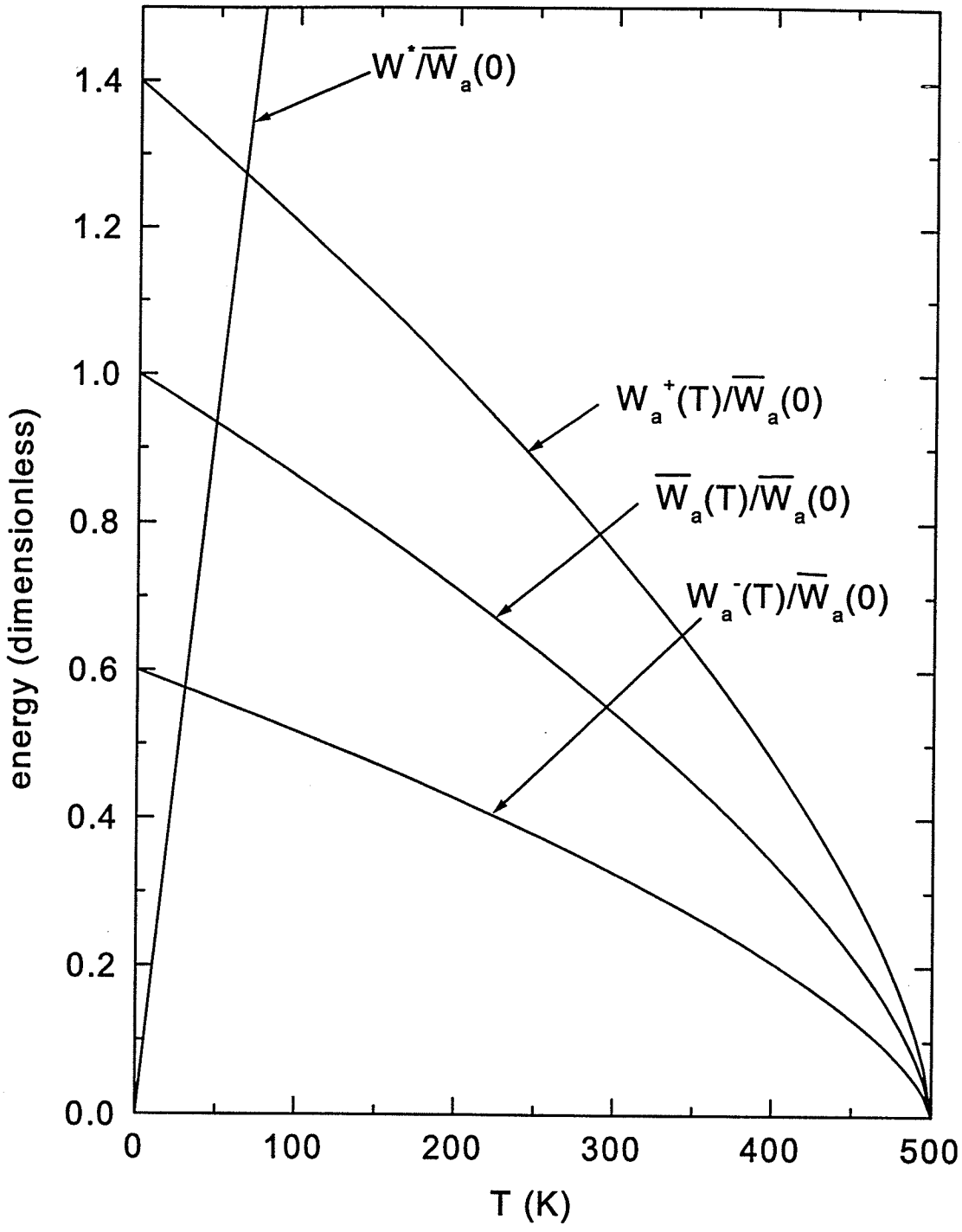

Figure 5.14: *The temperature dependence of the dissipation barriers and the thermal fluctuation energy for* $Fe - SiO_2$.

5.2 Analysis of particulate $NiFe_2O_4$

The analysis of the particulate $NiFe_2O_4$ material proceeded in a very similar fashion to that for the $Fe - SiO_2$. Figures (5.15) and (5.16) summarize the principal characteristics of the FC and ZFC response and of the major hysteresis isotherms for $NiFe_2O_4$, respectively. As with $Fe - SiO_2$, the principal structural features of the response in figures (5.15) and (5.16) are typical of a fluctuation-dominated system. This material exhibits a low temperature hysteretic regime for $T < 40K$ in which the collapse of the major hysteresis loop with increasing temperature is confined almost entirely to the width of the loop (that is, to the coercive field) and to the saturation remanence, with virtually no change in the saturation moment. This low temperature irreversible regime is succeeded by a reversible regime which appears as a long superparamagnetic tail in the FC and ZFC moments extending from $T = 50K$ up to room temperature $T = 300K$. As before, the data permit preliminary estimates of several of the key Preisach fitting parameters to be established. Thus, the mean zero temperature coercive field is $\bar{h}_{c0} \cong 1000$ Oe, the zero temperature spontaneous Barkhausen moment is $\mu_0 \cong 7.0 \times 10^{-17}$ emu, and the reversible fraction is $f \cong 0.6$. Furthermore, the maximum in the temperature dependence of the FC moment is a strong indication of a rapid collapse of the interaction fields h_i with increasing temperature which, as before, is physically very reasonable for a system in which thermal fluctuations are gradually destabilizing (or unblocking) the Barkhausen moments and thus lessening their effectiveness as sources of static internal interaction fields.

The fits to the $NiFe_2O_4$ data were performed assuming the same product function for the Preisach distribution in equation (5.2) used for the $Fe - SiO_2$ analysis. Figures (5.17) through (5.23) show comparisons of the numerical simulations of the FC and ZFC moments and major hysteresis isotherms with the

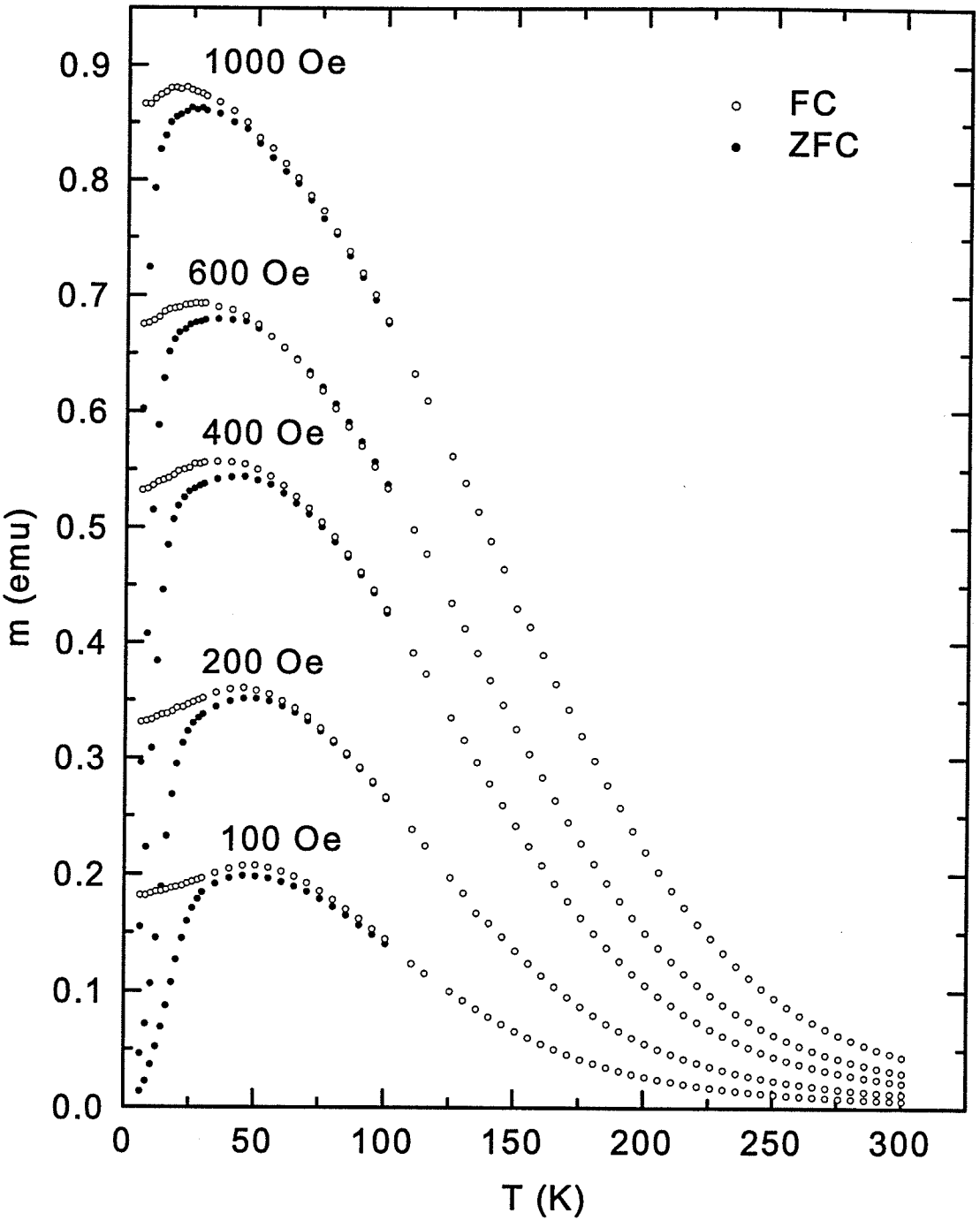

Figure 5.15: *The measured FC and ZFC moment of $NiFe_2O_4$ as a function of temperature T, over a wide range of applied fields h_a.*

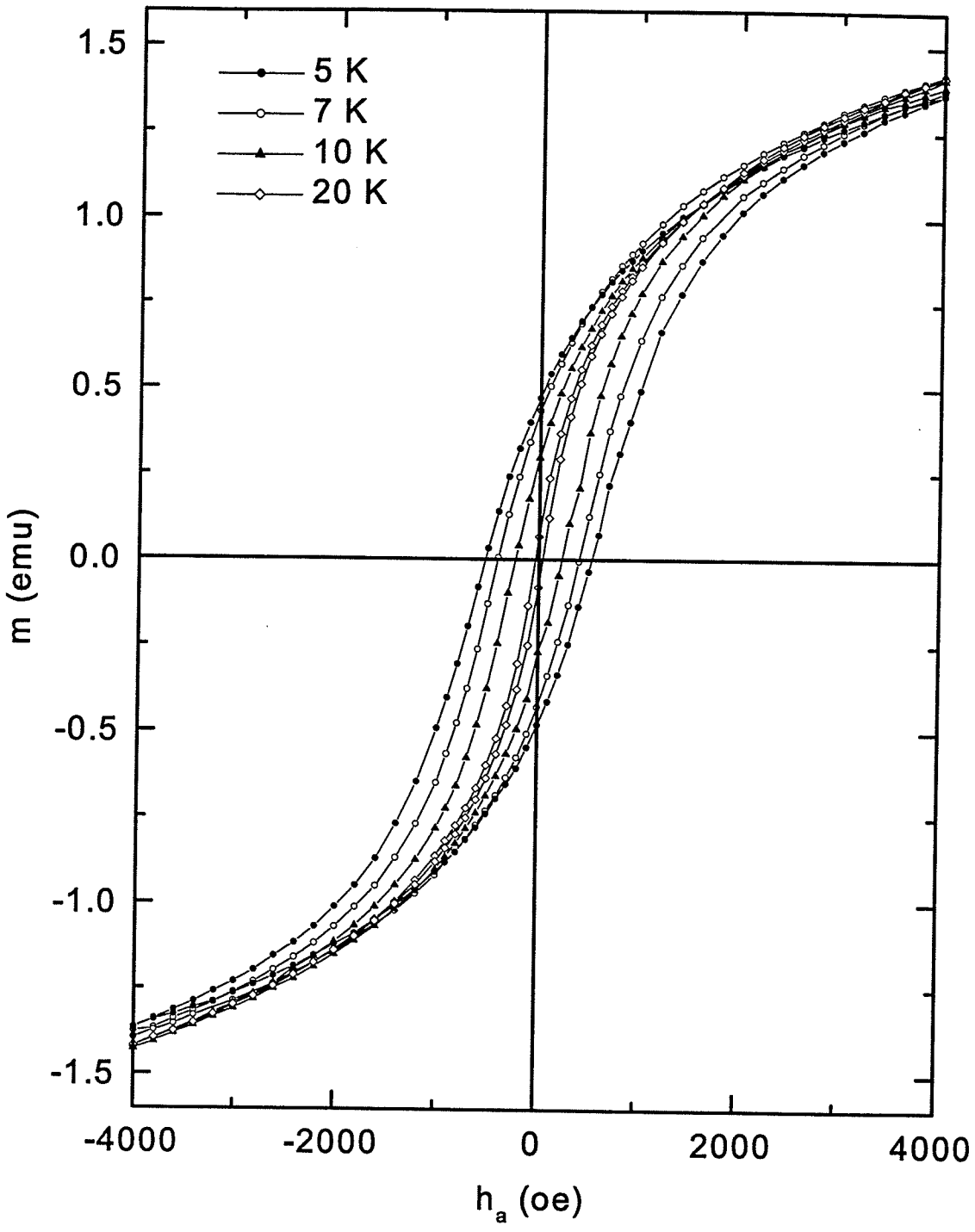

Figure 5.16: *The measured major hysteresis loops of $NiFeO_4$ at temperatures T = 5 K, 7 K, 10 K, 20 K*

experimental data, and tables (5.3) and (5.4) summarize the values of the best fit parameters, which are remarkably consistent across the entire data set. For this material, the dispersion of interaction fields was found to obey the functional form $\sigma_i(T) = exp[-(T/T_b)^{\Gamma_i}]$ with characteristic temperature $T_b = 120$ K and exponent $\Gamma_i = 1.0$. Furthermore, the model was unable to replicate the strong curvature of the superparamagnetic tail observed in figure (5.15) for any reasonable choice for the critical temperature T_c unless the spontaneous moment $\mu(T)$ was also allowed to vary rapidly with temperature through the superparamagnetic regime. For the current analysis, a functional form $\mu(T) = exp[-(T/T_m)^{\Gamma_m}]$ with $\Gamma_m = 2.0$ and $T_m = 200$ K provided a reasonable description of the superparamagnetic behaviour. The form of this function suggests that the Barkhausen elements are relatively constant in size throughout the hysteretic regime ($T < 40K$), but *fracture* into progressively smaller entities as T increases through the superparamagnetic phase. This is consistent with a Curie-Weiss law analysis of the superparamagnetic tail, which yields a similar tendency for the effective Curie-Weiss moment to decrease dramatically and systematically with increasing temperature. In this particular case, the fracturing may represent a break up of large scale clusters of $NiFe_2O_4$ particles which are internally strongly correlated magnetically. This interpretation is consistent with the large value of μ_0, which exceeds by orders of magnitude the moment expected for a single $NiFe_2O_4$ particle. It is also possible, of course, that the strong temperature dependence of $\mu(T)$ is a critical effect related to the collapse of the spontaneous moment as $T \rightarrow T_c$, but this is unlikely to be the case since it would require a critical temperature T_c on the order of 200K or less, which seems physically unreasonable.

In order to obtain the best fit to the FC and ZFC data, it was necessary to allow two of the parameters, μ_0 and σ_{i0}, to vary systematically with applied field h_a. Inspection of table (5.3) shows that μ_0 decreases monotonically with

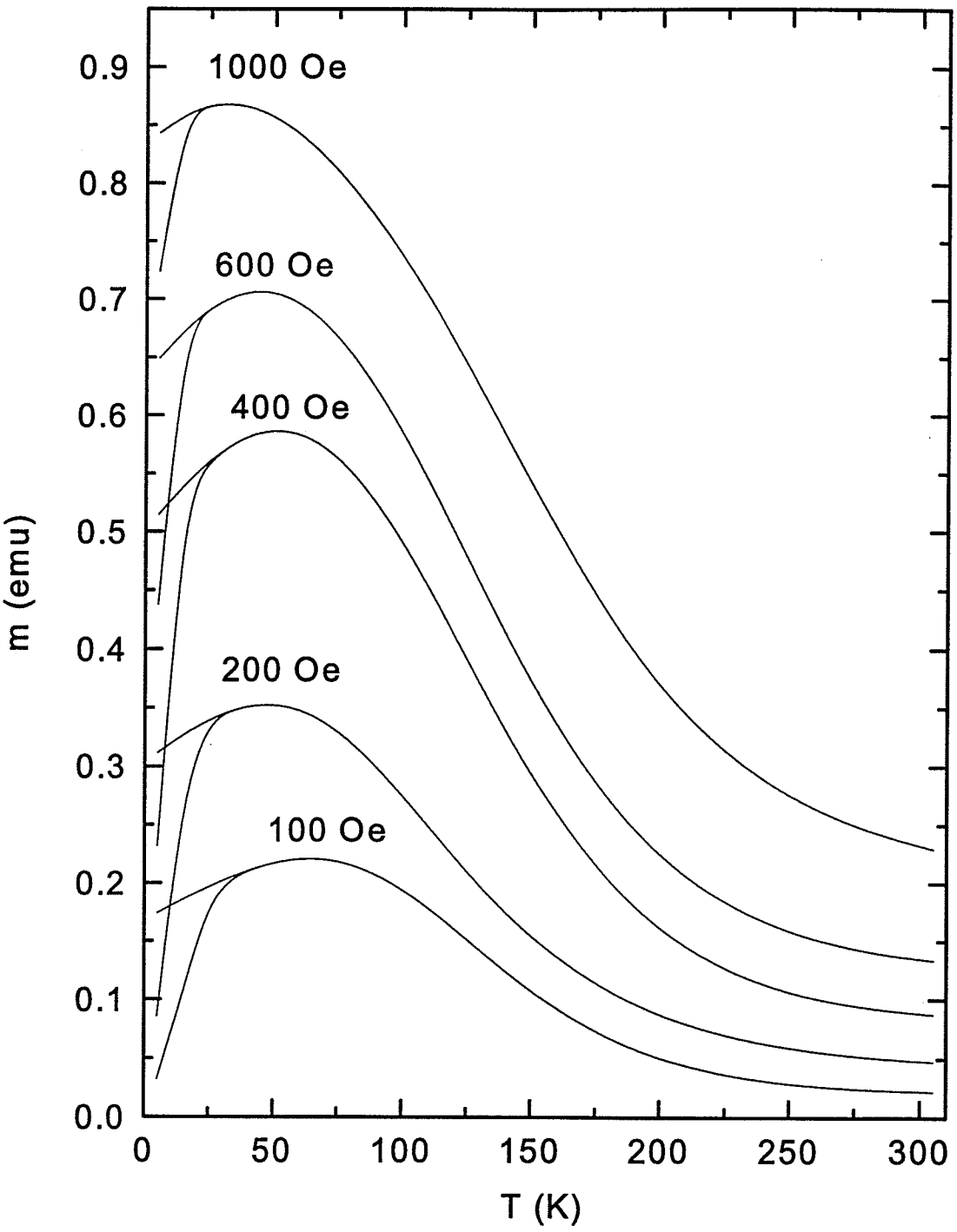

Figure 5.17: *The Preisach simulations of the FC and ZFC moments of* $NiFe_2O_4$ *in figure (5.15).*

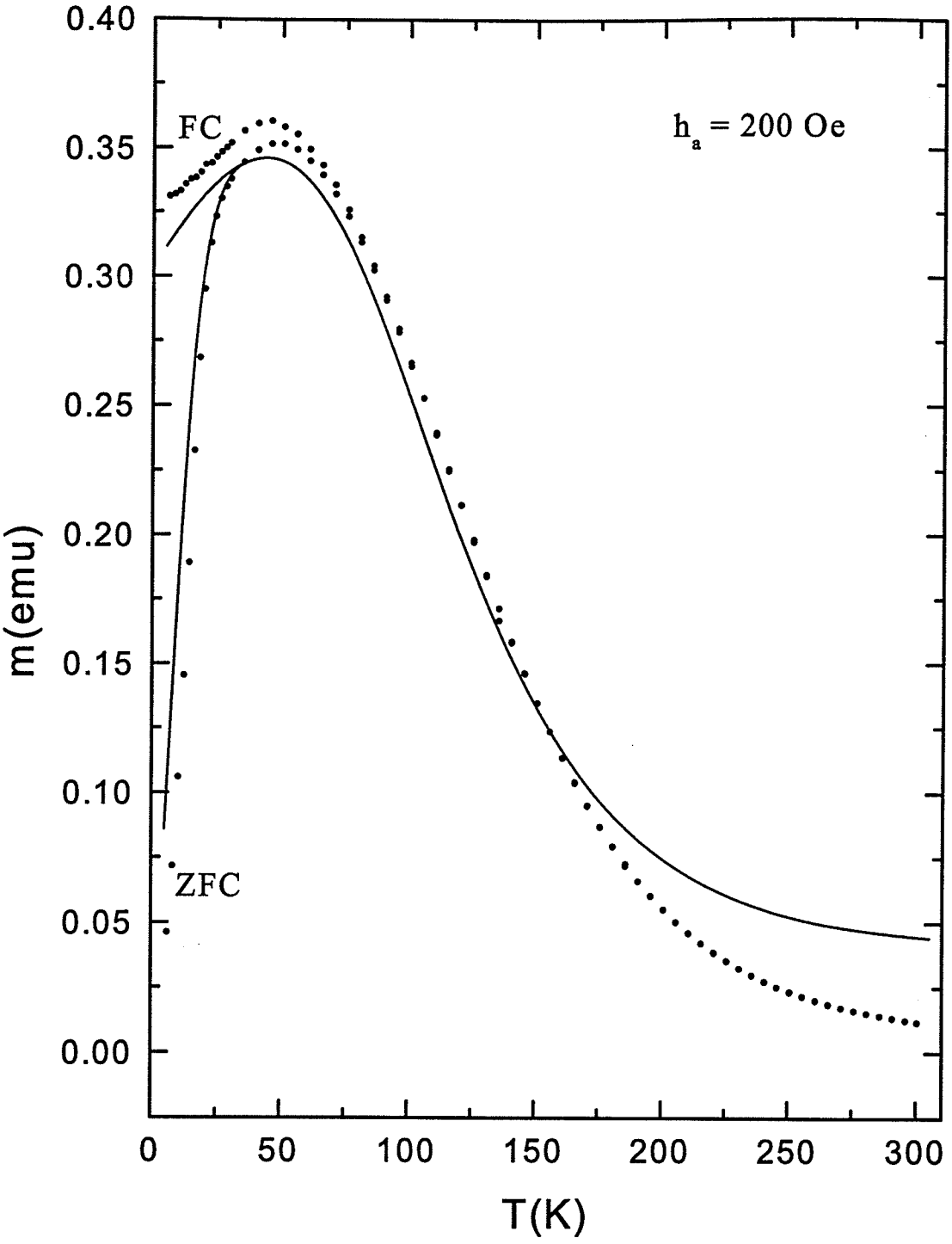

Figure 5.18: *Comparison of Preisach simulations (solid curves) with the measured FC and ZFC response of $NiFe_2O_4$ (discrete points) for $h_a = 200Oe$.*

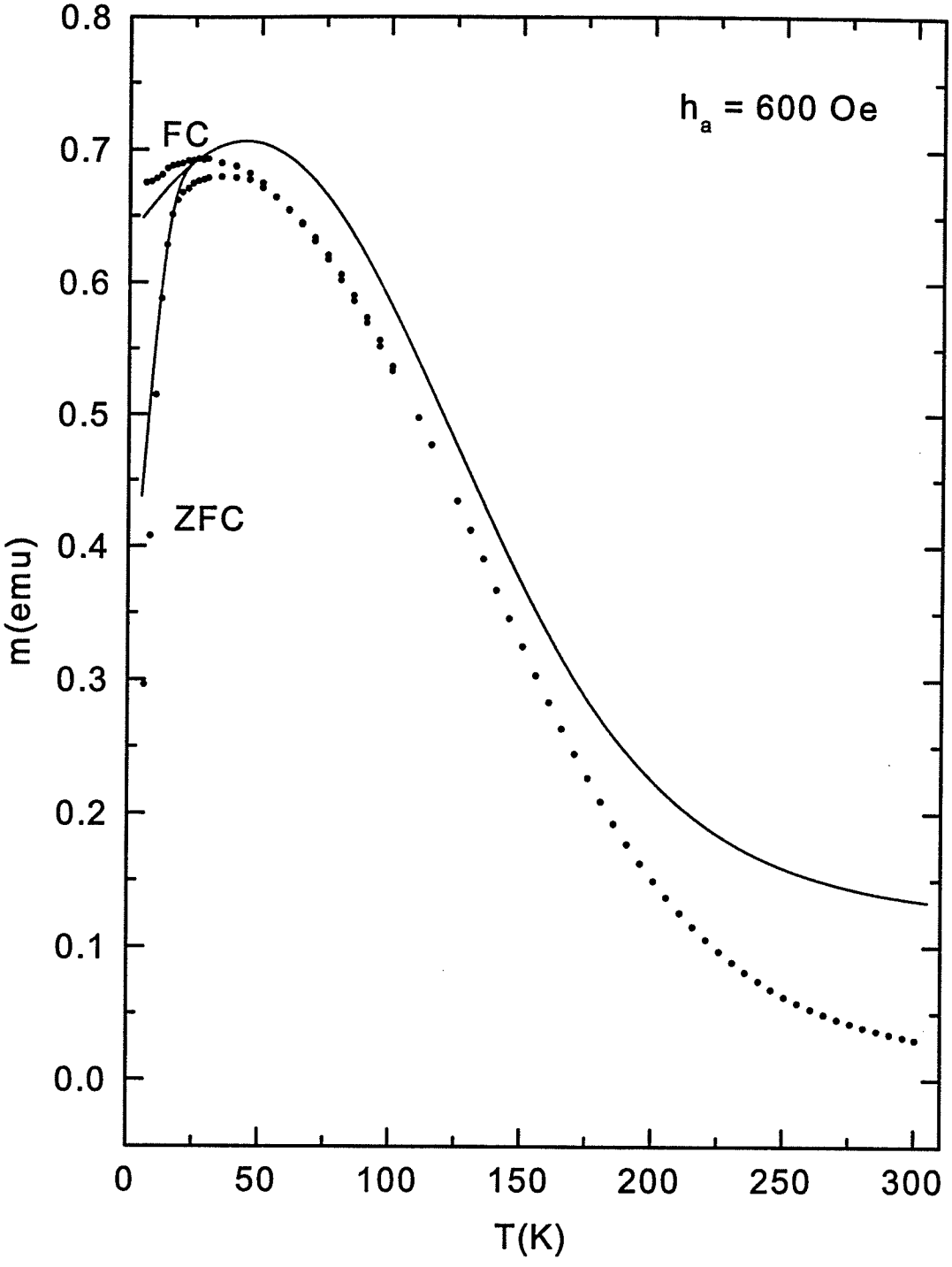

Figure 5.19: *Comparison of Preisach simulations (solid curves) with the measured FC and ZFC response of $NiFe_2O_4$ (discrete points) for $h_a = 600Oe$.*

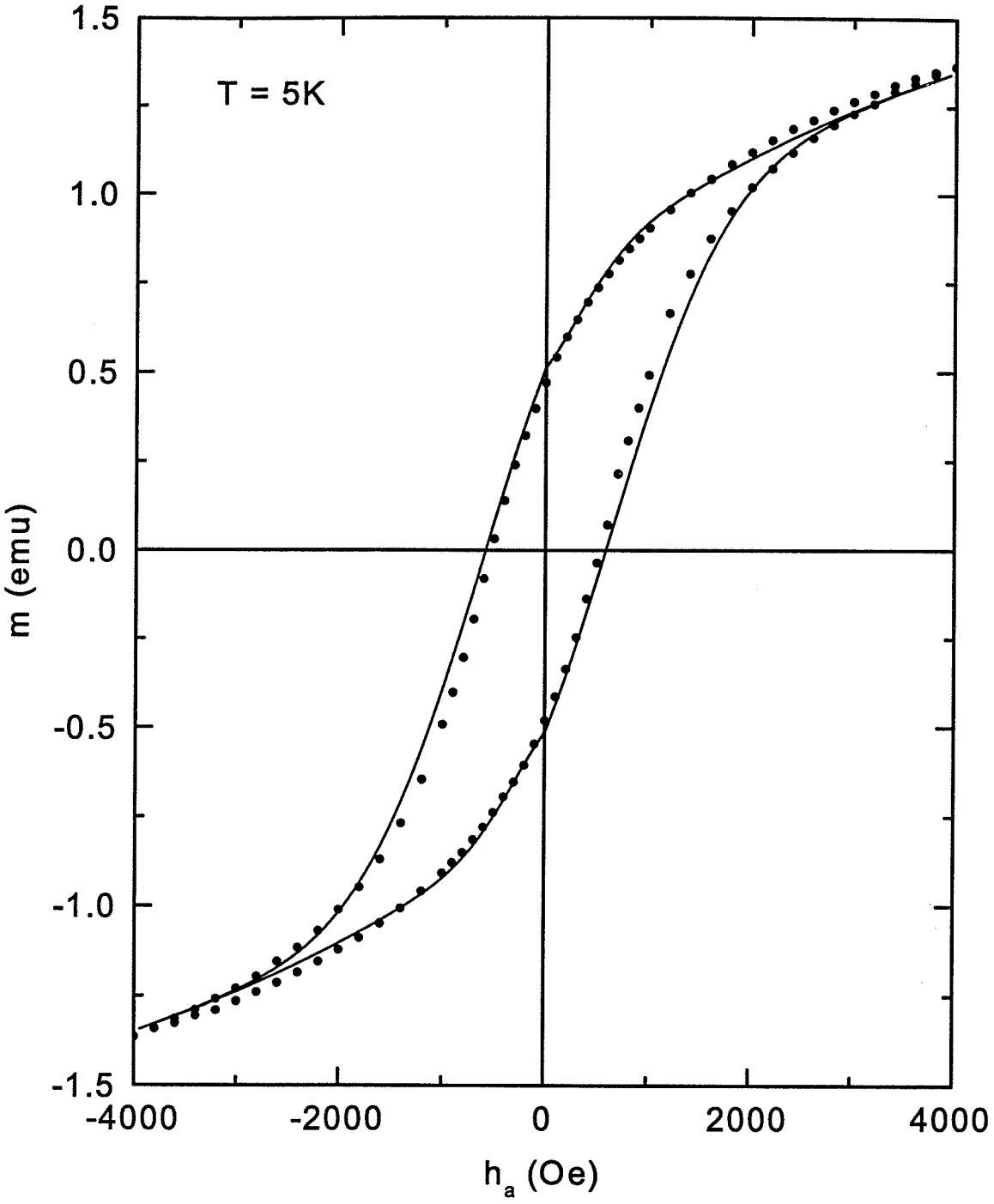

Figure 5.20: *Comparison of Preisach simulations of the major hysteresis loop (solid curves) with the measured major loop of $NiFe_2O_4$ (discrete points) at $T = 5K$.*

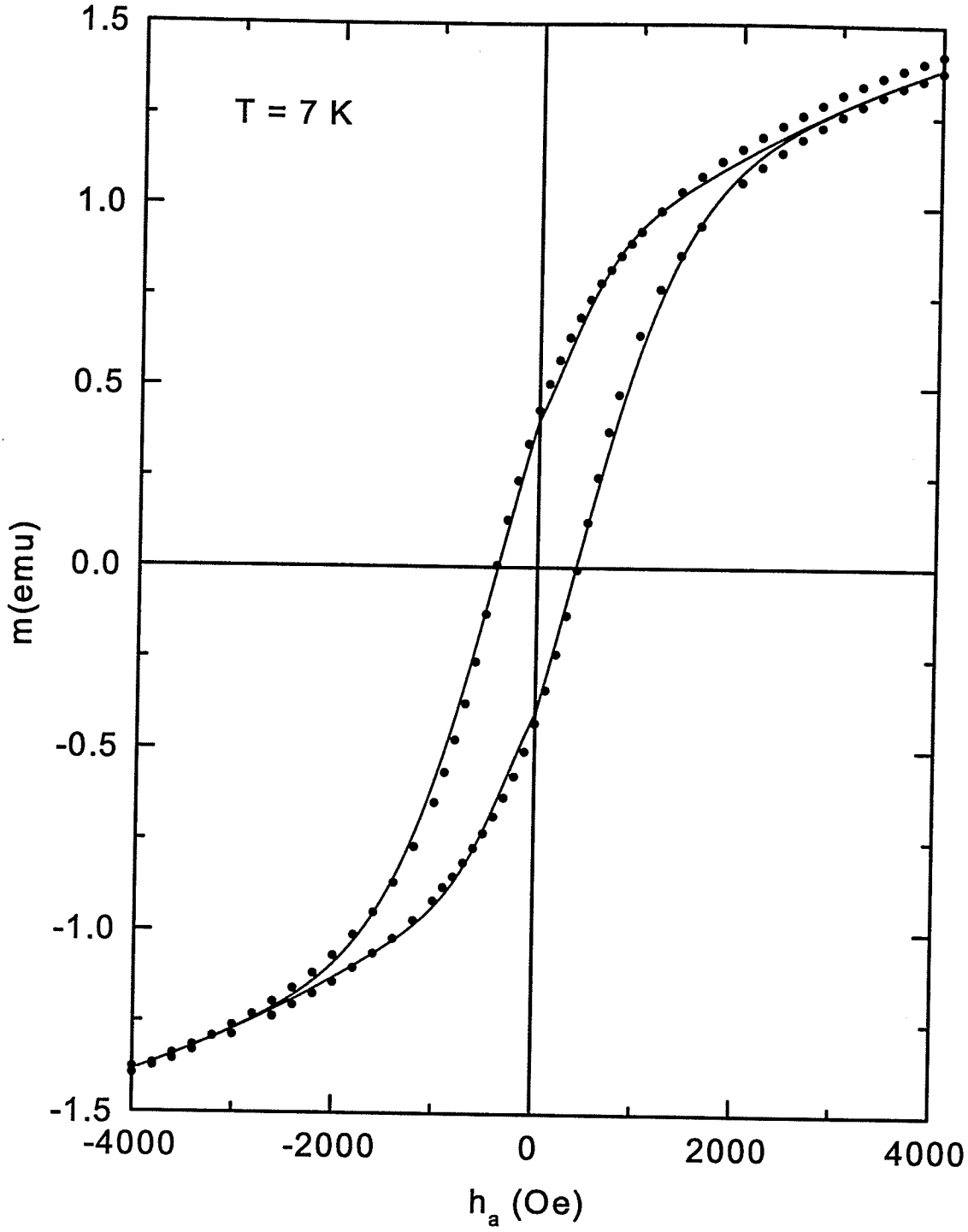

Figure 5.21: *Comparison of Preisach simulations of the major hysteresis loop (solid curves) with the measured major loop of $NiFe_2O_4$ (discrete points) at $T = 7K$.*

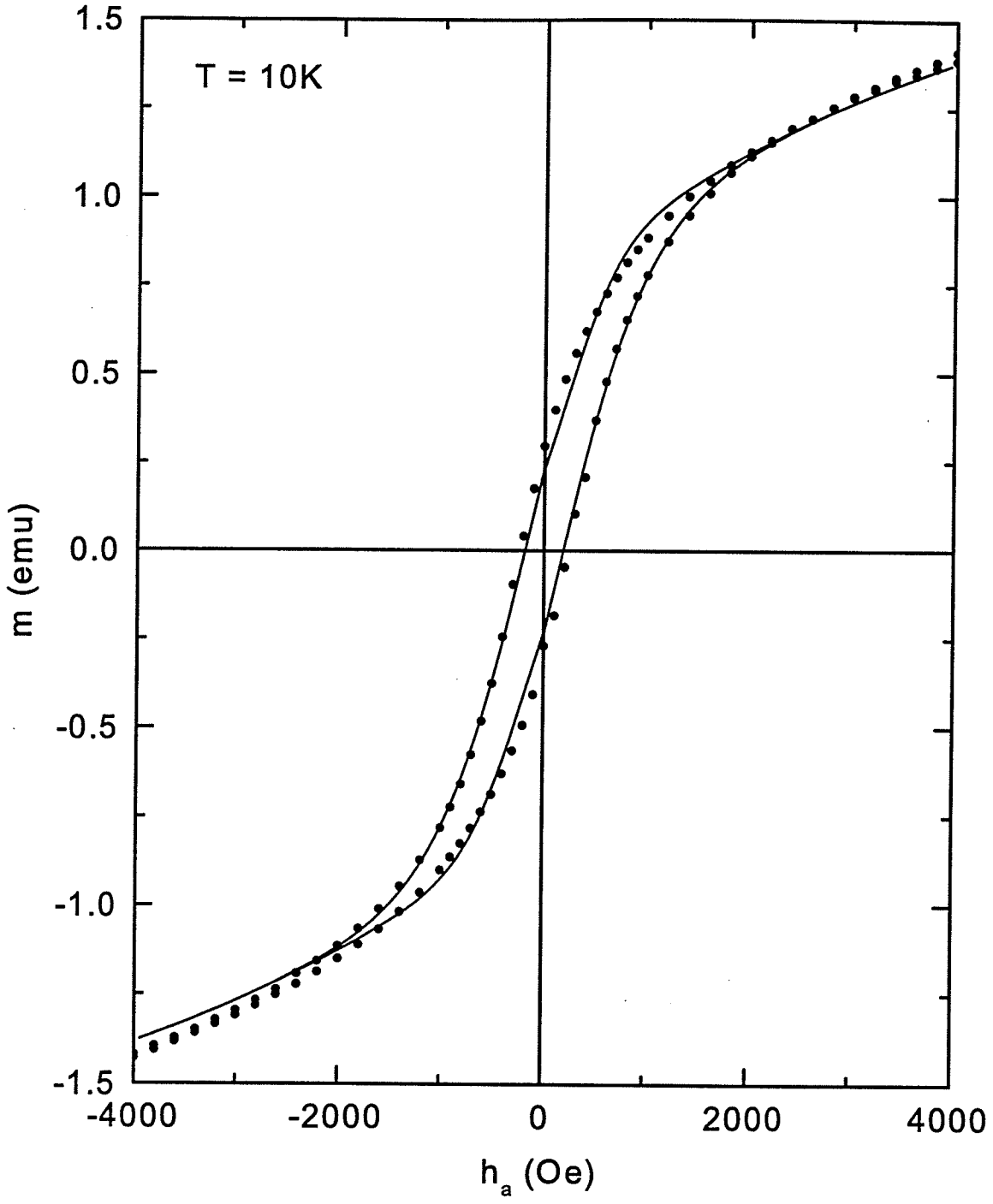

Figure 5.22: *Comparison of Preisach simulations of the major hysteresis loop (solid curves) with the measured major loop of $NiFe_2O_4$ (discrete points) at $T = 10K$.*

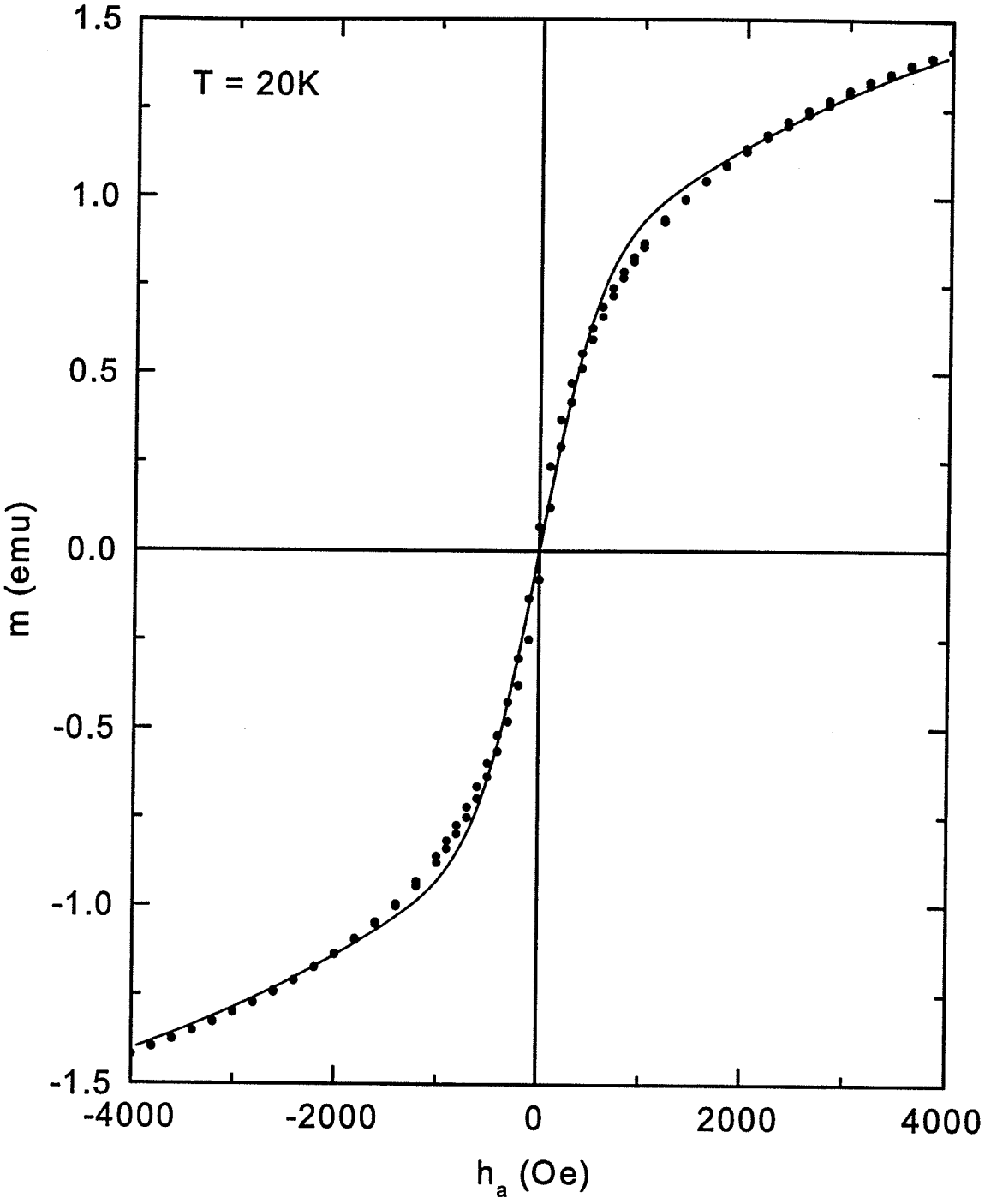

Figure 5.23: *Comparison of Preisach simulations of the major hysteresis loop (solid curves) with the measured major loop of $NiFe_2O_4$ (discrete points) at $T = 20K$.*

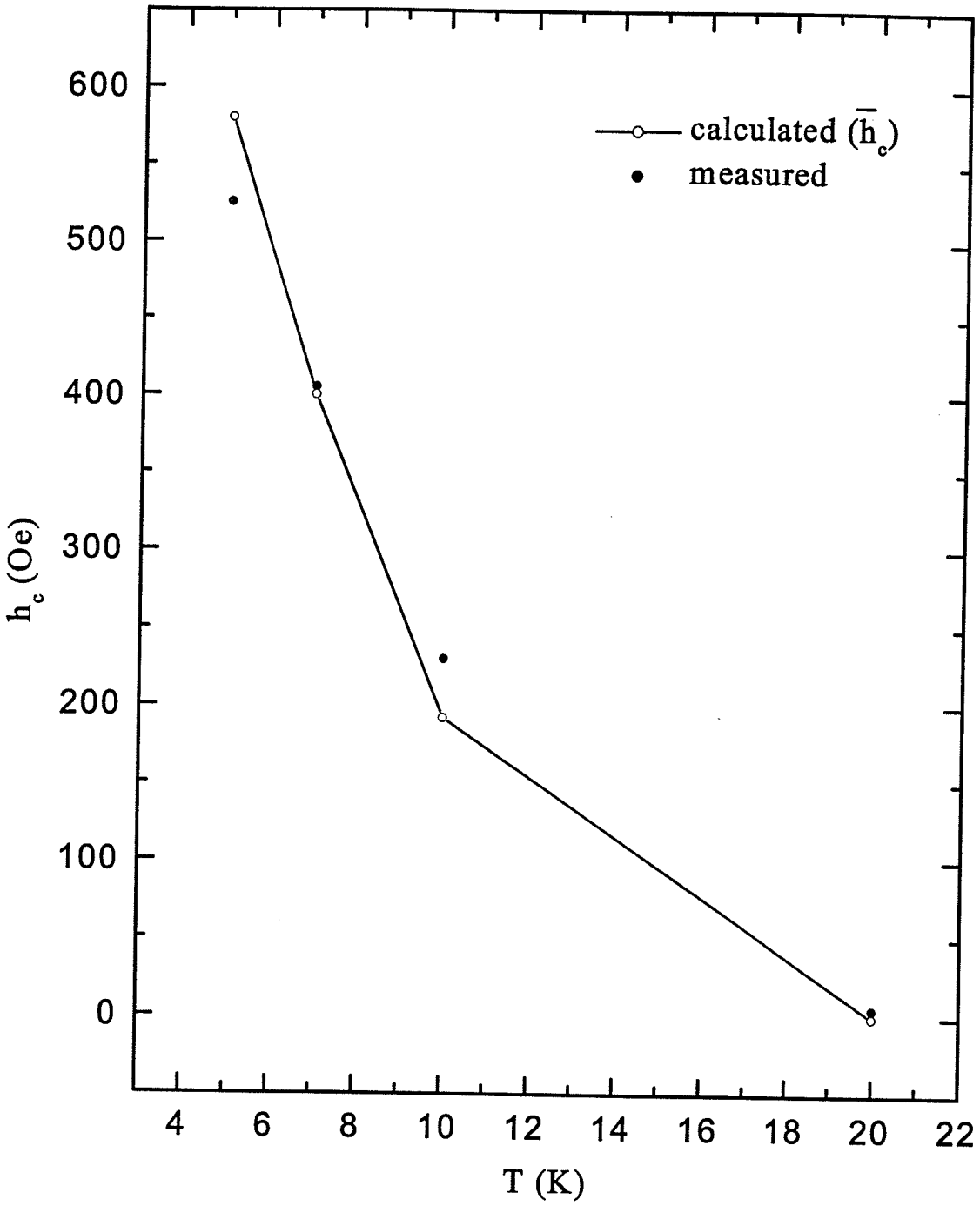

Figure 5.24: *Comparison of the calculated and measured coercive field of* $NeFe_2O_4$.

Table 5.3: Fitting parameters from the ZFC and FC moment of $NiFe_2O_4$ ($T_c = 400K$)

h_a(Oe)	100	200	400	600	1000
$\mu_0(10^{-17}$emu)	8	6	5	4	4
h_{c0}(Oe)	1420	1420	1420	1420	1420
σ_{c0} (Oe)	639	639	639	639	639
σ_{i0} (Oe)	383	426	497	568	639
Γ_m	2.0	2.0	2.0	2.0	2.0
Γ_c	1/3	1/3	1/3	1/3	1/3
Γ_c'	1/3	1/3	1/3	1/3	1/3
Γ_i	1.0	1.0	1.0	1.0	1.0
λ(1/Oe)	0.00018	0.00018	0.00018	0.00018	0.00018
f	0.6	0.6	0.6	0.6	0.6
m_{sat}(emu)	1.85	1.85	1.85	1.85	1.85
$T_b(K)$	120	120	120	120	120
$T_m(K)$	200	200	200	200	200

Table 5.4: Fitting parameters from major hysteresis loops of $NiFe_2O_4$ ($T_c = 400K$)

T (K)	5	7	10	20
$\mu_0(10^{-17}$emu)	5	5	5	5
h_{c0}(Oe)	1420	1420	1420	1420
σ_{c0} (Oe)	639	639	639	639
σ_{i0} (Oe)	497	497	497	497
Γ_c	1/3	1/3	1/3	1/3
Γ_c'	1/3	1/3	1/3	1/3
Γ_i	1.0	1.0	1.0	1.0
λ(1/Oe)	0.0002	0.00022	0.00022	0.00024
f	0.6	0.6	0.6	0.6
m_{sat}(emu)	1.85	1.85	1.85	1.85
$T_b(K)$	120	120	120	120
$T_m(K)$	200	200	200	200

increasing h_a while σ_{i0} increases monotonically with h_a. The change in σ_{i0} reflects a trend towards stronger interaction fields h_i as the system becomes more strongly magnetized. It is reasonable to question whether this behaviour could be replicated by introducing a mean-field-like contribution of the form $\bar{h}_i = km$ into the interaction field distribution $(2\pi\sigma_i^2)^{-1/2}exp[-(h_i - km)^2/2\sigma_i^2]$. A positive value of k would not achieve the desired effect, since it would tend to *amplify* the magnitude of the high field FC and ZFC response, while the increase in σ_{i0} with field acts to suppress it. A negative value of k, on the other hand, is very difficult to justify physically, since it would demand a significant demagnetizing factor, which is inconsistent with the geometry of the sample. It is our contention that the increase in σ_{i0} which emerges from the present analysis, and which represents a shift in the statistical distribution of local interaction fields towards high fields while preserving the inherent randomness of the distribution ($\bar{h}_i = 0$), is in fact compatible with the properties of the dipole field, which admits both positive and negative interaction fields even for *perfectly aligned* moments, depending upon their relative location. Thus a progressive deformation of the width of the interaction field distribution with no change in mean value is physically acceptable.

The decrease in μ_0 was necessary in order to increase the thermal fluctuation field $h_T^* = k_B T \cdot \Omega/\mu$ and hence better replicate the location of the inflection point in the ZFC moment below the maximum. Given that the assumption of a single Barkhausen moment μ is a crude approximation to the real situation, which almost certainly demands a distribution of Barkhausen moments, and hence a *distribution* of *thermal viscosity fields* h_T^*, it is clear that the decrease in μ_0 with increasing field h_a is completely consistent with the fact that at high fields ($h_a \sim \bar{h}_{c0}$), small-moment Barkhausen elements will relax noticeably faster than high-moment Barkhausen elements, and will thus tend to dominate the temperature

dependence of the ZFC response function.

Chapter 6

Analysis of Anisotropy-Dominated Magnetic Systems

6.1 $SrRuO_3$

The $SrRuO_3$ system investigated here is a polycrystalline ferromagnet with a single type of magnetic ion Ru^{4+}, and with a Curie temperature $T_c = 160K$[38]. Figures (6.1) and (6.2) summarize the characteristics of the measured irreversible response of $SrRuO_3$. Figure (6.1) shows the temperature dependence of the moment measured under both field cooled(FC) and zero field cooled(ZFC) conditions, after thermal demagnetization at $T = 180K$, in various applied fields h_a up to the $T = 5K$ coercive field $H_c = 5000$ Oe. Figure (6.2) shows a sequence of major hysteresis isotherms at several representative temperatures which span the ordered phase $T < T_c$.

A comparison of the experimental data in figures (6.1) and (6.2) with the Preisach simulations in figures (3.2) and (3.7) shows that $SrRuO_3$ possesses all the characteristics typical of an *anisotropy-dominated* system. In particular, both the FC and ZFC moments exhibit an extremely rapid variation with temperature over a relatively narrow temperature interval in the vicinity of the critical temperature $T_c = 160K$, which is symptomatic of a system whose magnetic response

is dictated by the growth of the free energy barriers, rather than by thermal fluctuations. Moreover, the temperature dependence of the hysteresis loops in figure (6.2) exhibits a simultaneous collapse in the coercive field, saturation moment, and saturation remanence as $T \rightarrow T_c$ which is once again characteristic of a system whose measured properties are clearly strongly influenced by the critical temperature, and hence are predominantly intrinsic in origin.

The solid curves in figures (6.3), (6.4) and (6.5) are numerical simulations, which are based on a Preisach distribution which is a product of a lognormal coercive field distribution and a Gaussian interaction field distribution:

$$p(h_c, h_i) = (2\pi\sigma_c^2(T)h_c^2)^{-\frac{1}{2}} exp[-(log(h_c/\bar{h}_c(T)))^2/2\sigma_c^2(T)]$$

$$\cdot(2\pi\sigma_i^2(T))^{-\frac{1}{2}} exp[-h_i^2/2\sigma_i^2(T)] \tag{6.1}$$

assuming the following temperature dependences for the Preisach parameters:

$$\left\{ \begin{array}{l} \mu(T) = \mu_0(1 - T/T_c)^{\Gamma} \\ \bar{h}_c(T) = \bar{h}_{c0}[1 - (T/T_c)^{\Gamma_c}] \\ \sigma_c(T) = \sigma_{c0}[1 - (T/T_c)^{\Gamma_c'}] \\ \sigma_i(T) = \sigma_{i0}(1 - T/T_c)^{\Gamma_i} \end{array} \right\} \tag{6.2}$$

Table 6.1 and table 6.2 list the fitting parameters for the FC and ZFC data and the hysteresis loops, respectively. Figure (6.3) shows simulations of the entire sequence of FC and ZFC data in figure (6.1), and figure (6.4) illustrates the quality of the fits for two specific applied fields $h_a = 1000$ Oe and $h_a = 5000$ Oe. Figure (6.5) shows typical fits to two hysteresis loops at extreme ends of the ordered phase.

The model is clearly able to replicate all of the principal structural features, as well as the systematic variations with field and temperature, observed in the magnetic response functions of $SrRuO_3$. Furthermore, the two sets of fitting parameters in table 6.1 and table 6.2 show a remarkably degree of consistency,

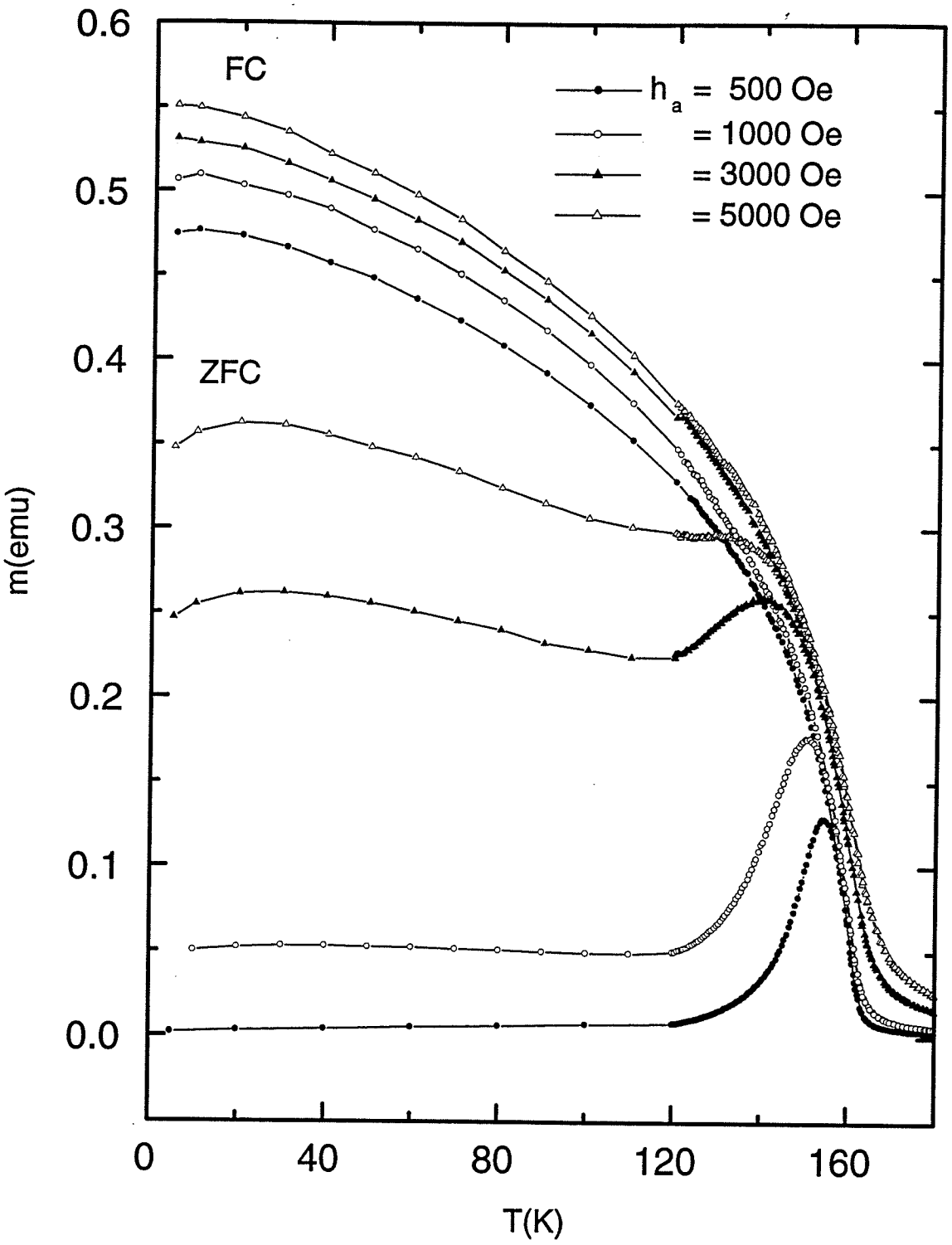

Figure 6.1: *Measurements of the temperature dependence of the field cooled(FC) and zero field cooled(ZFC) moment of $SrRuO_3$ in various applied fields h_a. Solid lines are guides to the eye.*

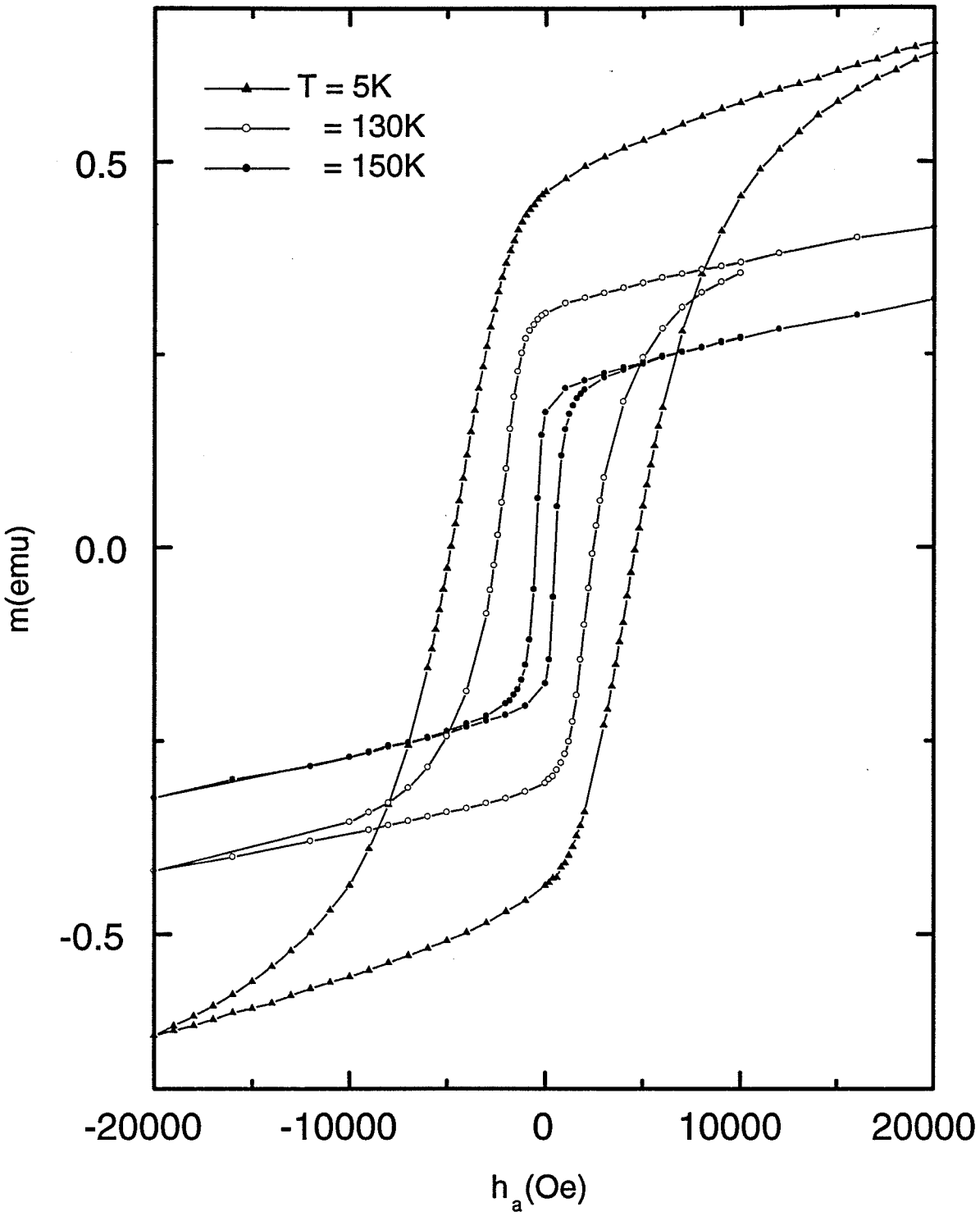

Figure 6.2: *Typical measurements of the major hysteresis loop of $SrRuO_3$ at several representative temperatures which span the ordered phase $T < T_c$. Solid lines are guides to the eye.*

Table 6.1: Fitting parameters from ZFC and FC moment of $SrRuO_3$

h_a(Oe)	200	400	500	1000	3000	5000
$\mu_0(10^{-15}$emu)	2	2	2	2	2	2
h_{c0}(Oe)	5200	5200	5200	5200	5200	5200
σ_{c0}	0.8	0.8	0.8	0.8	0.8	0.8
σ_{i0} (Oe)	104	104	104	104	104	104
Γ	0.3	0.3	0.3	0.3	0.3	0.3
Γ_c	5.0	5.0	5.0	5.0	5.0	5.0
Γ_c'	20.0	20.0	20.0	20.0	20.0	20.0
Γ_i	0.3	0.3	0.3	0.3	0.3	0.3
λ(1/Oe)	0.00004	0.00004	0.00004	0.00004	0.00004	0.00004
f	0.4	0.4	0.4	0.4	0.4	0.4
m_{sat}(emu)	0.8	0.8	0.8	0 8	0.8	0.8
$T_C(K)$	158	158	158	158	158	158

particularly considering the broad spectrum of data which have been replicated here.

The analysis provides a quantitative picture of the spectrum of Baukhausen moments and free energy barriers in $SrRuO_3$, and establishes correlations between individual model parameters and specific structural features of the response. In particular:

1. A comparison of the mean zero temperature anisotropy barrier $\bar{W}_a(0) \equiv \mu_0 \bar{h}_{c0} = 1.0 \times 10^{-11} erg$, with the thermal fluctuation energy at the critical temperature $W_c^* \equiv k_B T_c ln(t_{exp}/\tau_0) = 5.5 \times 10^{-13} erg$ shows that $\bar{W}_a(0) \gg W_c^*$. This confirms our preliminary assessment, namely that $SrRuO_3$ may be classified as an anisotropy-dominated system, in the sense that thermal fluctuations are expected to play a relatively minor role in defining the temperature dependence of the magnetic response functions. This dominance of intrinsic thermal effects over extrinsic thermal fluctuations is clearly apparent in figure 6.6(a), which compares the temperature dependence of the

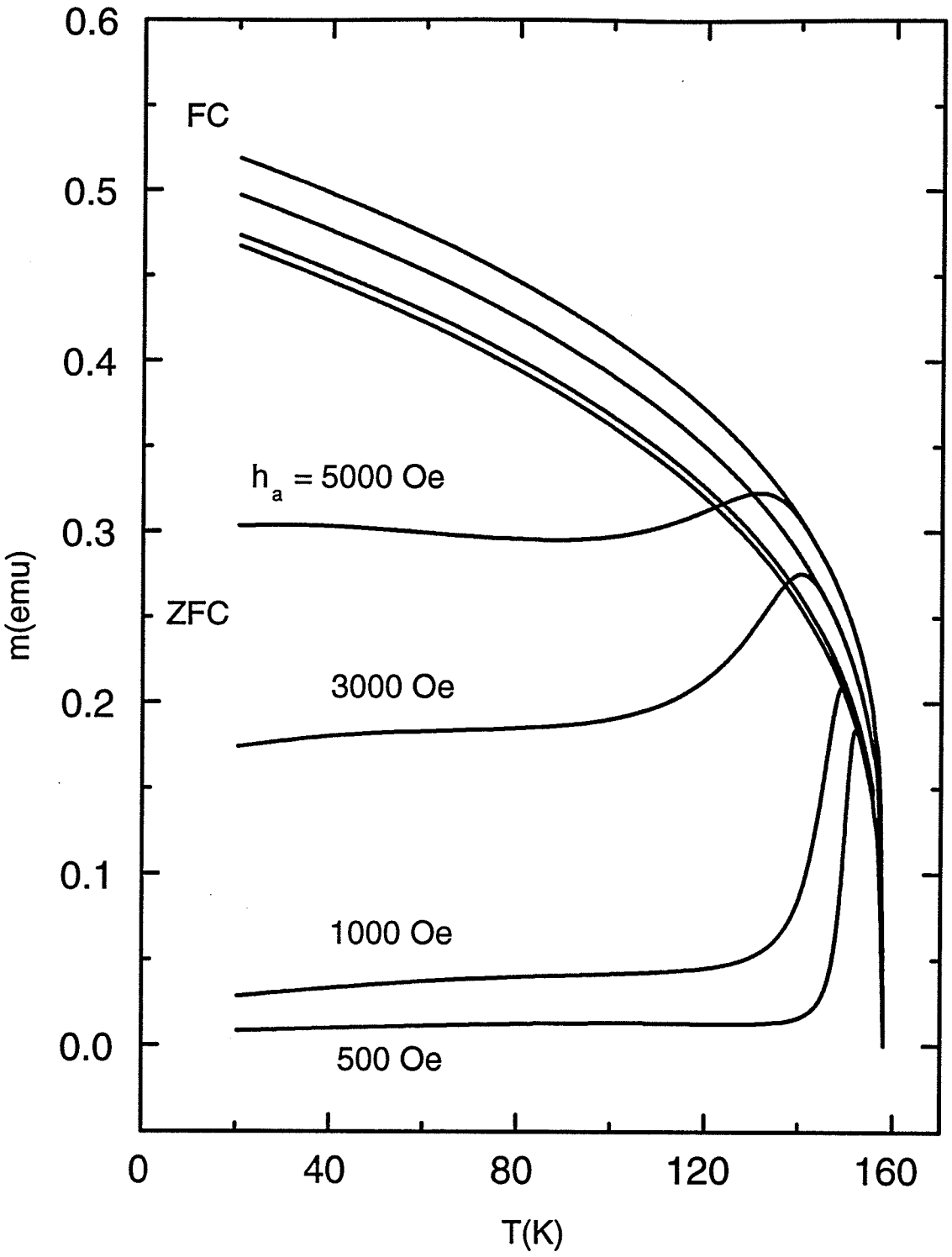

Figure 6.3: *Numerical Preisach simulations of the FC and ZFC data in figure 6.1*

.

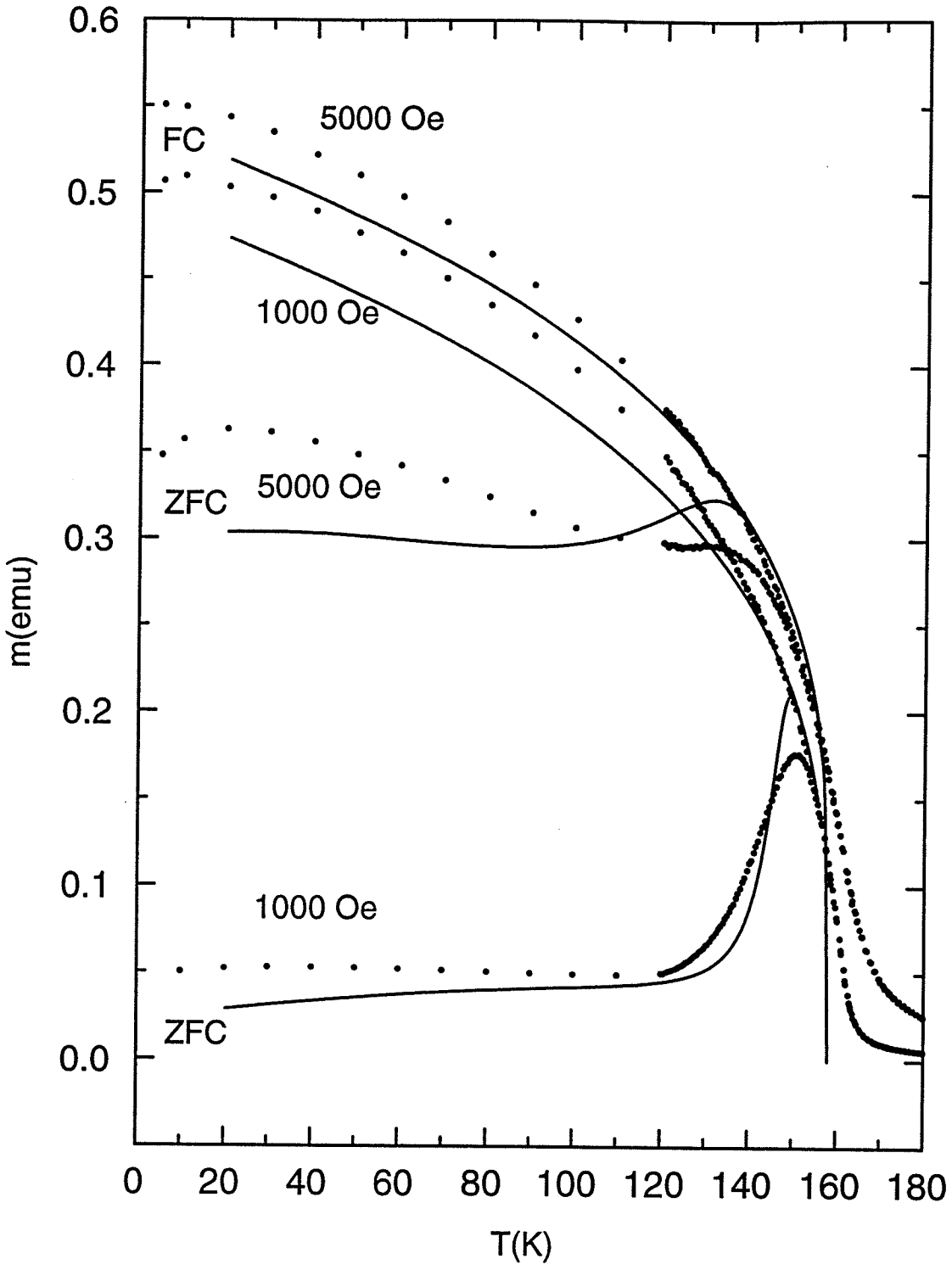

Figure 6.4: *A comparison of the numerical simulations of the FC and ZFC moment (solid curves) with the measured FC and ZFC moment (discrete points) of* $SrRuO_3$ *for* $h_a = 1000$ *Oe and* $h_a = 5000$ *Oe.*

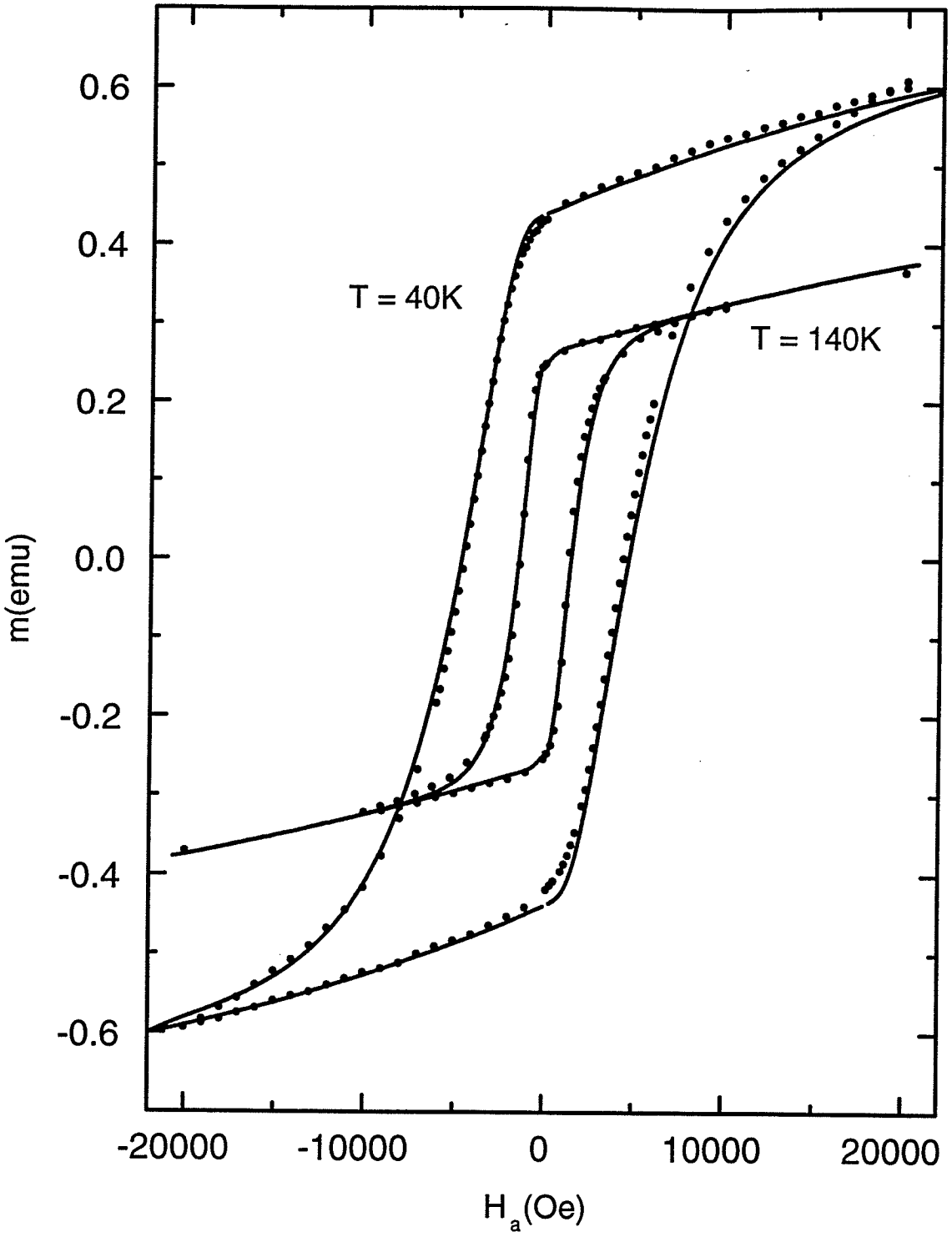

Figure 6.5: *Numerical Preisach simulations(solid curves) of two representative measured hysteresis loops (discrete points) for* $SrRuO_3$.

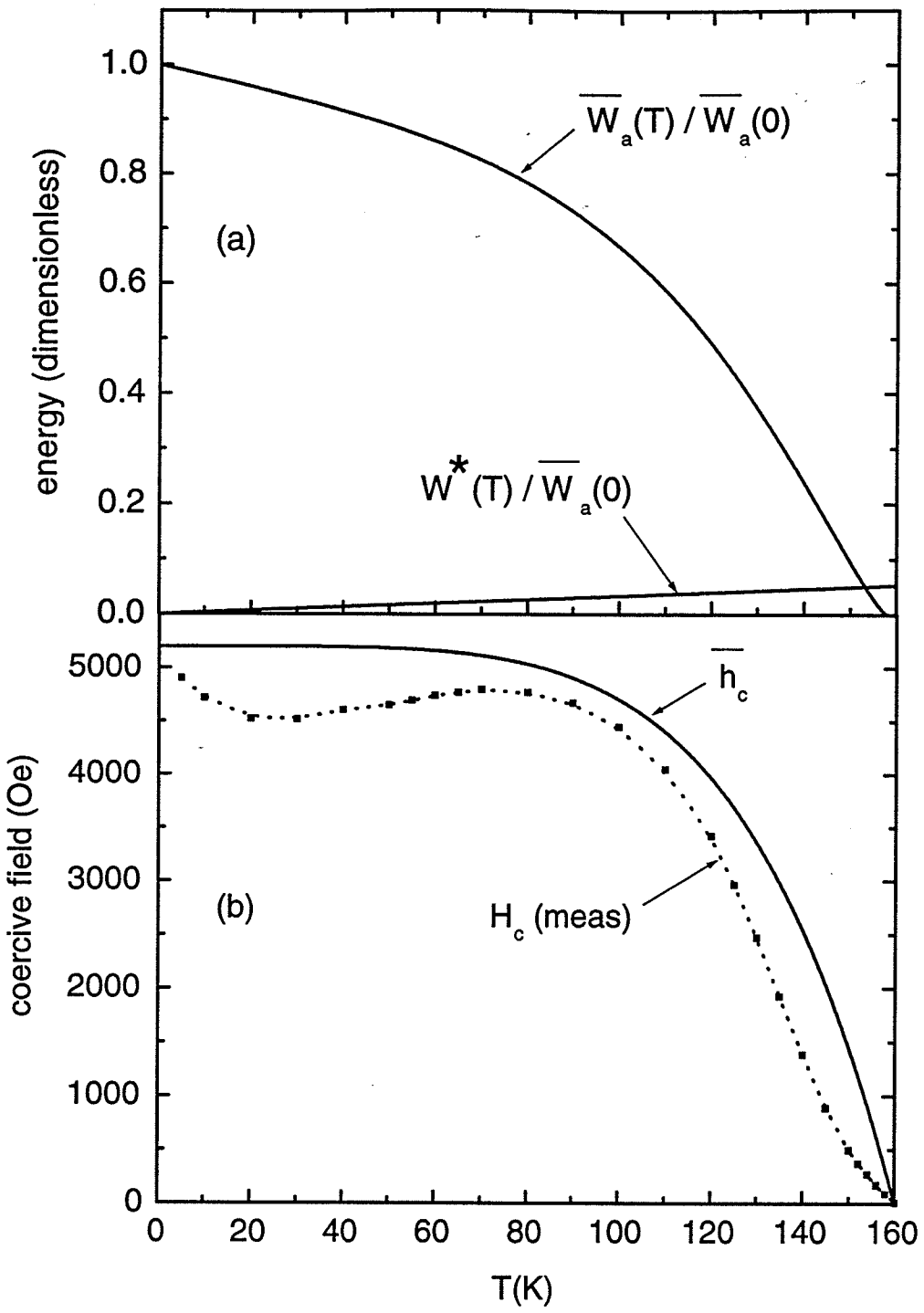

Figure 6.6: *(a) A comparison of the temperature dependence of the mean anisotropy barrier* $\bar{W}_a(T)/\bar{W}_a(0) = [1 - (T/T_c)^{\Gamma_c}](1 - T/T_c)^{\Gamma}$ *in* $SrRuO_3$ *obtained from the numerical simulations, and the thermal fluctuation energy* $W^*(T)/\bar{W}_a(0) = [k_BT/\bar{W}_a(0)]ln(t_{exp}/\tau_0)$. *(b) A comparison of the measured coercive field* H_c *and the model coercive field* $\bar{h}_c$ *from the numerical simulations.*

Table 6.2: Fitting parameters from hysteresis loops of $SrRuO_3$

T (K)	5	40	80	120	130	140	150
$\mu_0(10^{-15}\text{emu})$	2	2	2	2	2	2	2
h_{c0}(Oe)	5200	5200	5200	5200	5200	5200	5200
σ_{c0}	0.6	0.6	0.6	0.6	0.6	0.6	0.6
σ_{i0} (Oe)	104	104	104	104	104	104	104
Γ	0.32	0.30	0.28	0.3	0.26	0.28	0.28
Γ_c	4	4	5	5	4	4	5
Γ_c'	20	20	20	20	20	15	20
Γ_i	0.3	0.3	0.3	0.3	0.3	0.3	0.3
$\lambda(10^{-5}/Oe)$	3.5	3.2	2.6	2.0	2.0	2.2	2.2
f	0.4	0.4	0.4	0.4	0.4	0.4	0.4
m_{sat}(emu)	0.8	0.8	0.8	0.8	0.8	0.8	0.8
$T_C(K)$	158	158	158	158	158	158	158

mean anisotropy barrier obtained from the fits, normalized to $\bar{W}_a(0)$,

$$\bar{W}_a(T)/\bar{W}_a(0) = [1-(T/T_c)^{\Gamma_c}](1-T/T_c)^{\Gamma} \tag{6.3}$$

and the normalized thermal fluctuation energy

$$\bar{W}_a(T)/\bar{W}_a(0) = [k_BT/\bar{W}_a(0)]ln(t_{exp}/\tau_0) \tag{6.4}$$

The intersection of the two curves defines the mean blocking temperature, above which the system is superparamagnetic, and below which the system response is irreversible.

2. The collapse of the major loop coercive field as the system is warmed through the ordered phase towards T_c is almost exclusively intrinsic in origin and is determined primarily by the exponent Γ_c which defines the temperature dependence of the median coercive field $\bar{h}_c(T)$, with only a negligible contribution from thermally activated relaxation. Figure (6.6)(b) shows the relationship between the measured coercive field H_c and the model coercive field $\bar{h}_c$.

3. The structural characteristics of the ZFC branch are almost purely coercive in origin. The peak in the ZFC moment is a consequence of a competition between the collapse of the coercive field distribution as T approaches T_c, which enhances the response, and the collapse of the Barkhausen moment $\mu(T)$, which suppresses the response. The shape of the peak on the low-temperature side is defined by the exponents Γ_c and Γ_c', and the location of the peak is determined jointly by Γ_c and Γ_c' and the zero-temperature spontaneous moment μ_0, which defines the rate at which the thermal viscosity field h_T^* changes with temperature. In fact, this is the single feature of the experimental data which provides the most direct access to the magnitude of the zero temperature spontaneous Barkhausen moment μ_0. Similarly, the field dependence of the ZFC moment at low temperatures is determined by the dispersion σ_{c0} of coercive fields.

4. By contrast, the behaviour of the FC branch is insensitive to the details of the coercive field distribution, and is influenced primarily by the characteristics of the *interaction field distribution*, that is, by σ_{io} and Γ_i, and by the exponent Γ which controls the temperature dependence of the spontaneous moment $\mu(T)$. The zero temperature FC moment $m_{FC}(h_a, T = 0)$ is determined primarily by the ratio h_a/σ_{i0} of the applied field to the dispersion of interaction fields. The weak field dependence of the FC branch observed in $SrRuO_3$ for fields $h_a \geq 500$ Oe is symptomatic of the fact that these fields are much larger than typical interaction fields $\sigma_{i0} = 104$ Oe, and are consequently capable of saturating the FC moment.

5. The pronounced bifurcation of the FC and ZFC branches in low applied fields is a consequence of two inequalities, $\sigma_{i0} \ll h_a$ which ensures that the FC moment is saturated, and $h_a \ll \bar{h}_{c0}$ which ensures that the induced ZFC

response is small.

6.2 $La_{0.5}Sr_{0.5}CoO_3$

The measured response of the $La_{0.5}Sr_{0.5}CoO_3$ system is summarized in figures (6.7) and (6.8). Figure (6.7) shows measurements of the temperature dependence of the FC and ZFC moments performed over a wide range of applied fields $10Oe \leq h_a \leq 1000$ Oe, and figure (6.8) shows measurements of the major hysteresis loop performed over a wide range of temperatures which span the irreversible regime. The system $La_{1-x}Sr_xCoO_3$ has been the subject of extensive previous investigations, some of which have concluded that no true ferromagnetic long-range order exists in this system and, in particular, that the composition investigated here is, in fact, not a ferromagnet but rather a "cluster spin glass"[39]. This identification is based primarily on the significant bifurcation observed between the FC and ZFC branches in figure (6.7), and on the breadth of the maximum which characterizes the temperature dependence of the ZFC moment in this system (in contrast to the behaviour of the low field ZFC moment of $SrRuO_3$ in figure (6.1), which exhibits quite a sharp maximum just below T_c). In our opinion, the rapid variation of the FC and the ZFC moments with temperature in the vicinity of $T \cong 230$K in figure (6.7), and the simultaneous collapse of the coercive field, the saturation remanence, and the saturation moment in figure (6.8), are strongly suggestive of a rapid, thermally localized collapse of the spontaneous moment and of the anisotropy barriers, which is characteristic of a critical transition to long-ranged ferromagnetism, and a preliminary analysis of measurements of the field and temperature dependence of the ac susceptibility performed on this material appear to confirm this assessment[24]. While a Preisach analysis is not able to yield a definitive statement regarding the structure of the magnetically ordered state in $La_{0.5}Sr_{0.5}CoO_3$, it *is* able to show that the ZFC moment in figure (6.7) derives its structure directly from the distribution of anisotropy and pinning bar-

Table 6.3: Preisach fitting parameters from ZFC and FC moments of $La_{0.5}Sr_{0.5}CoO_3$.

$\mu_0(10^{-15}\text{emu})$	6
$\bar{h}_{c0}(\text{Oe})$	2200
σ_{c0}	0.75
$\sigma_{i0}(Oe)$	99
Γ	0.34
Γ_{c1}	6.0
Γ_{c2}	0.2
Γ_i	0.08
$\lambda(1/\text{Oe})$	0.00015
f	0.45
$m_{sat}(\text{emu})$	2.02
$T_c(\text{K})$	230

riers, and that the differences observed between the ZFC response functions of $SrRuO_3$ and $La_{0.5}Sr_{0.5}CoO_3$ are a direct consequence of the very different intrinsic temperature dependences which characterize the collapse of the free energy barriers in these two systems.

The solid curves in figures (6.9) through figures (6.14) are numerical Preisach simulations based on a Preisach distribution of the form

$$p(h_c, h_i) = (2\pi\sigma_c^2(T)h_c^2)^{-\frac{1}{2}} exp[-(log(h_c/\bar{h}_c(T)))^2/2\sigma_c^2(T)]$$

$$\cdot(2\pi\sigma_i^2(T))^{-\frac{1}{2}} exp[-h_i^2/2\sigma_i^2(T)] \tag{6.5}$$

assuming the following temperature dependences for the Preisach parameters:

$$\left\{ \begin{array}{l} \bar{h}_c(T) = \bar{h}_{c0}[0.5(1-T/T_c)^{\Gamma_{c1}} + 0.5(1-T/T_c)^{\Gamma_{c2}}] \\ \sigma_c(T) = \sigma_{c0}[0.5(1-T/T_c)^{\Gamma_{c1}} + 0.5(1-T/T_c)^{\Gamma_{c2}}] \\ \mu(T) = \mu_0(1-T/T_c)^{\Gamma} \\ \sigma_i(T) = \sigma_{i0}(1-T/T_c)^{\Gamma_i} \end{array} \right\} \tag{6.6}$$

The best fit values of the parameters obtained from the FC and ZFC data and the hysteresis loops are listed in tables (6.3) and (6.4), respectively.

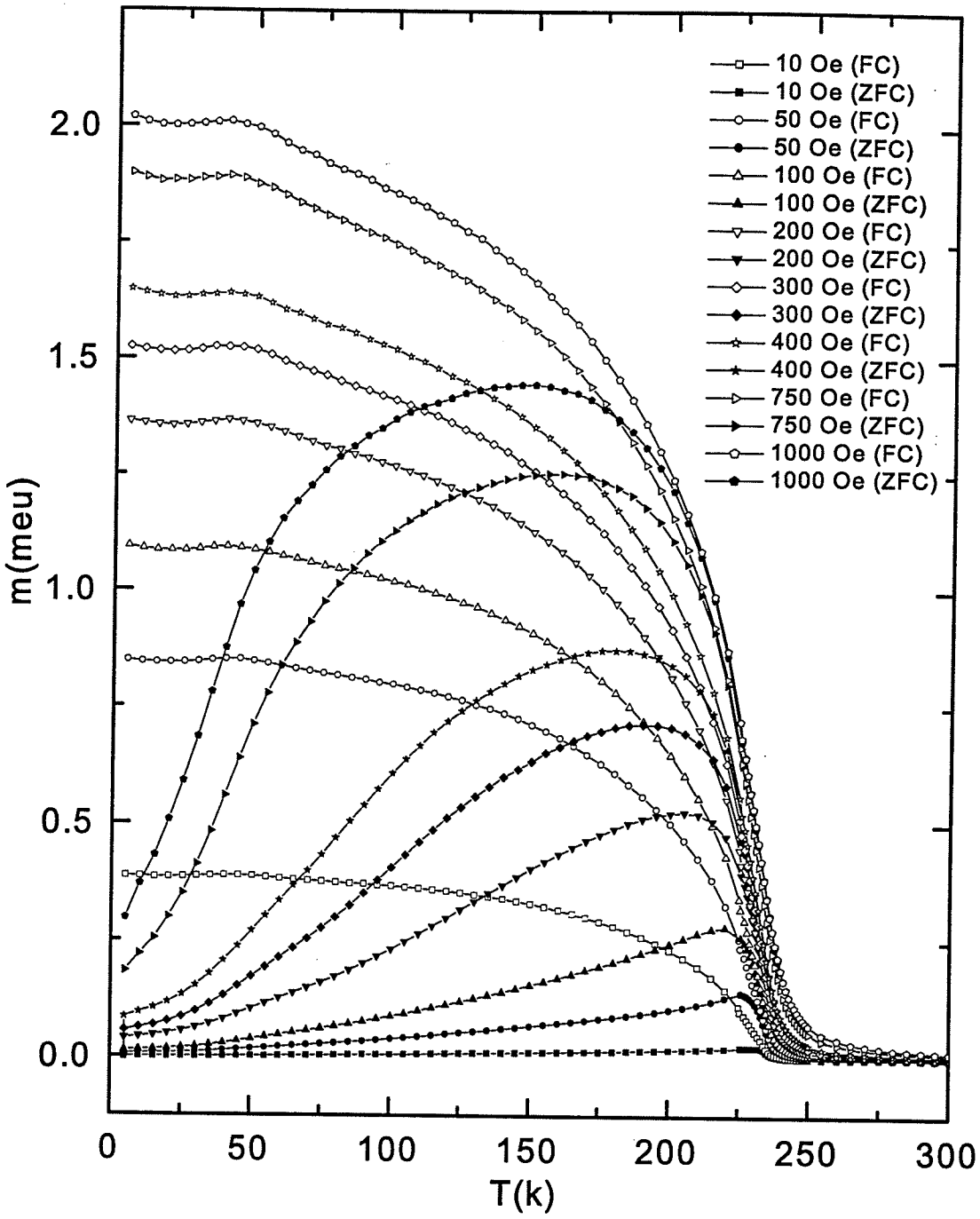

Figure 6.7: *Measurements of the temperature dependence of the field cooled(FC) and zero field cooled(ZFC) moment of* $La_{0.5}Sr_{0.5}CoO_3$ *in various applied fields* h_a.

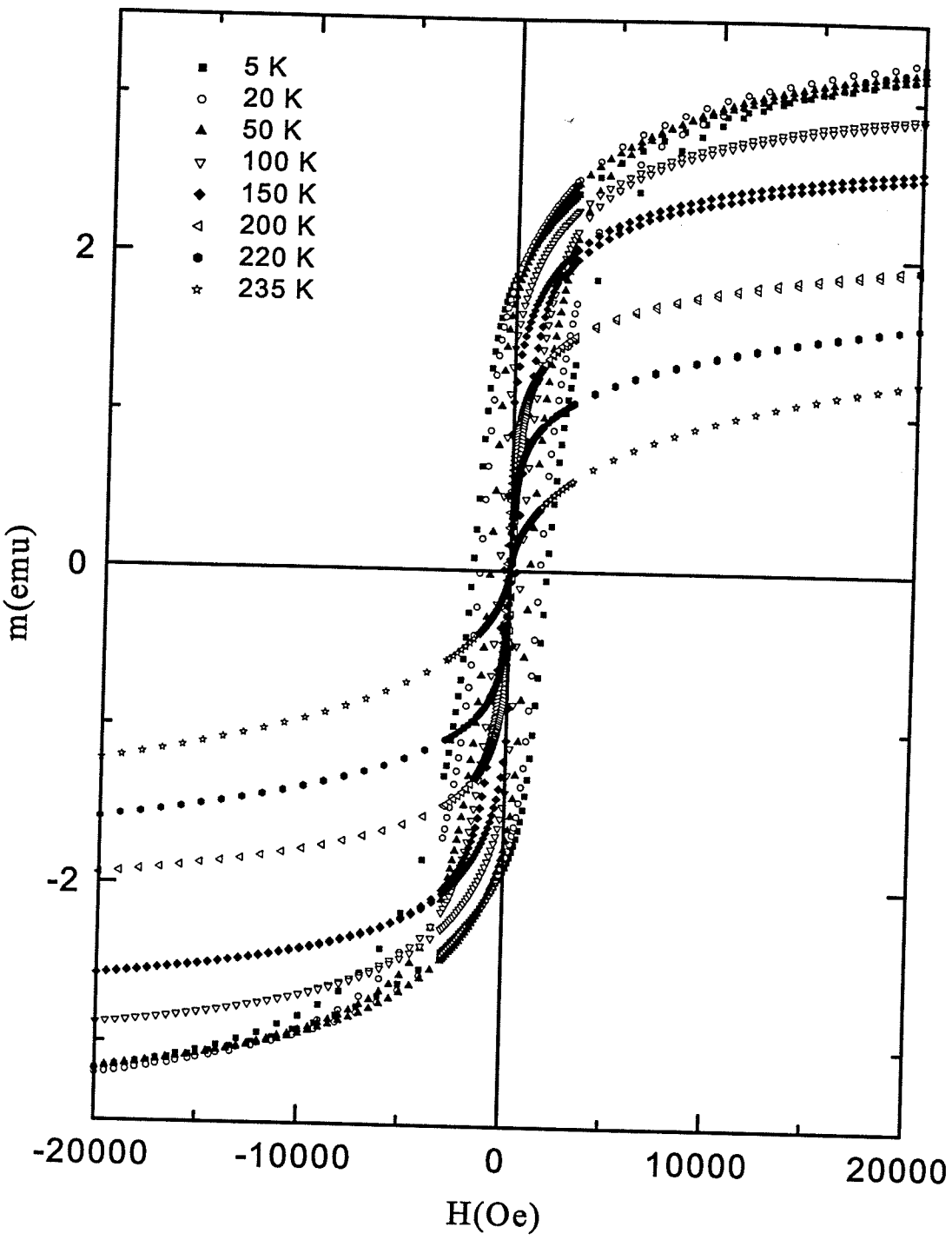

Figure 6.8: *Measurements of major hysteresis loops of $La_{0.5}Sr_{0.5}CoO_3$ at a series of temperatures which span the ordered phase.*

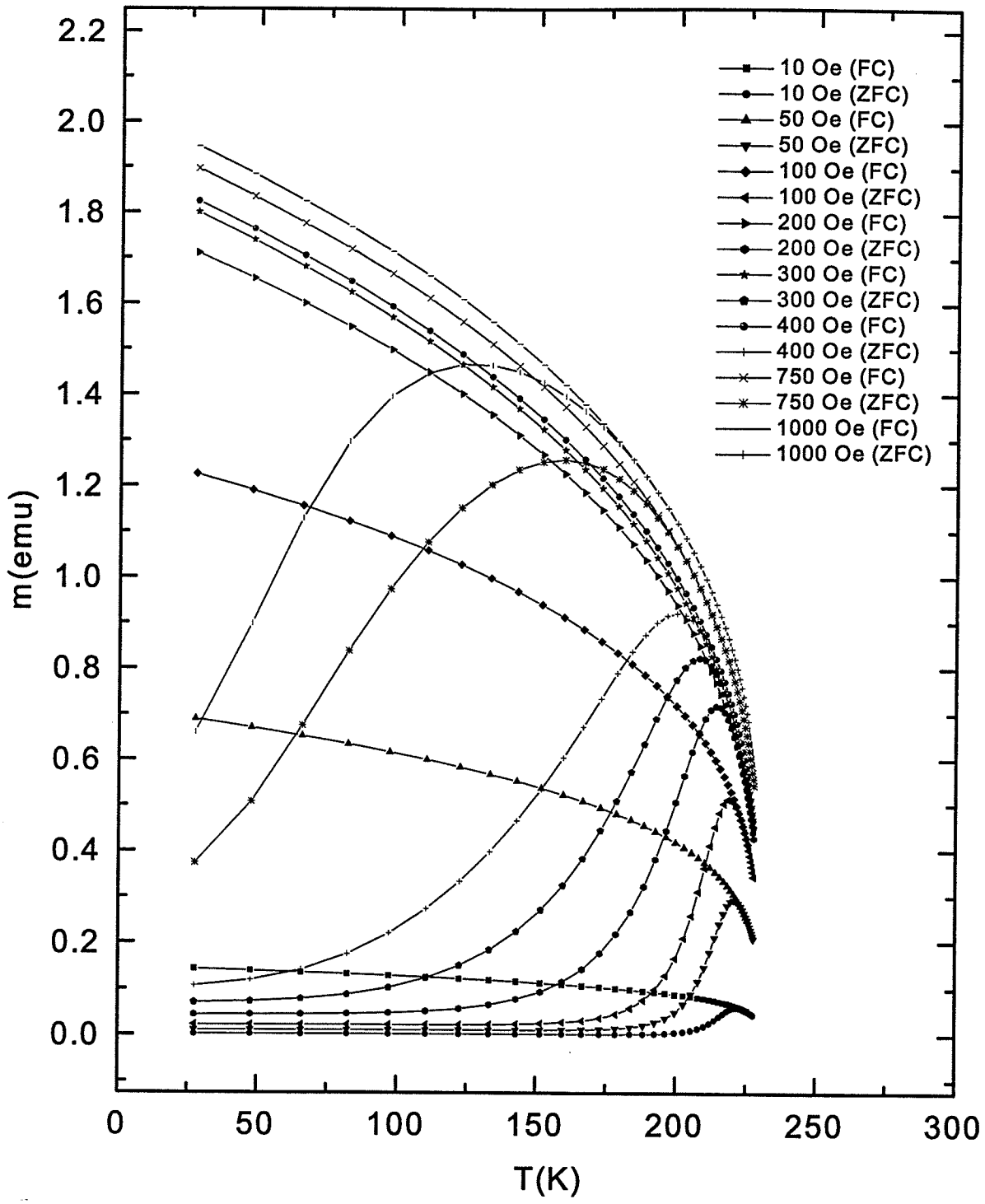

Figure 6.9: *Numerical Preisach simulations of the FC and ZFC data of* $La_{0.5}Sr_{0.5}CoO_3$ *in figure 6.7 .*

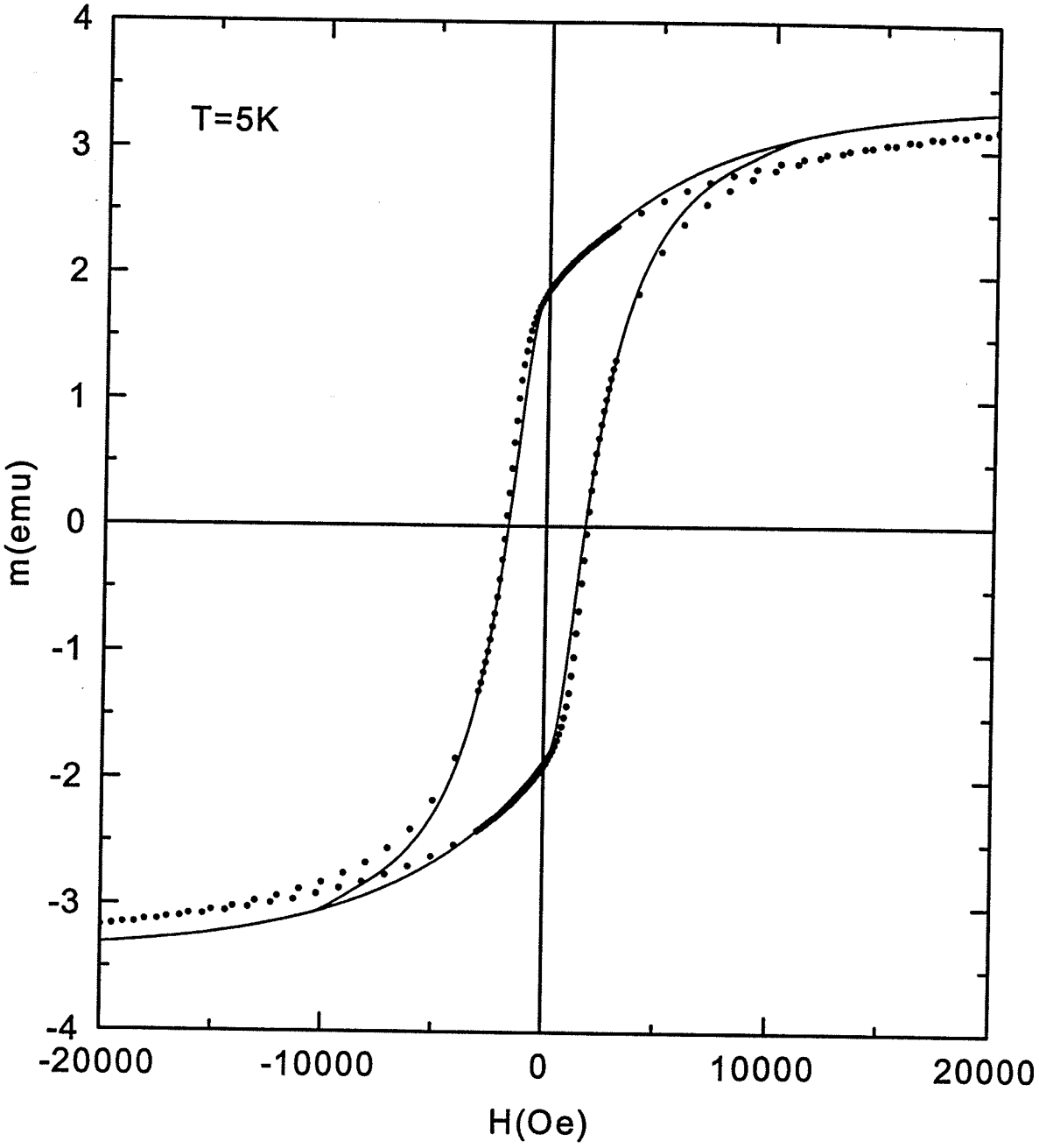

Figure 6.10: *A comparison of the Preisach numerical simulation (solid curve) of the major hysteresis loop of $La_{0.5}Sr_{0.5}CoO_3$ at $T = 5K$ with the measured loop (discrete points).*

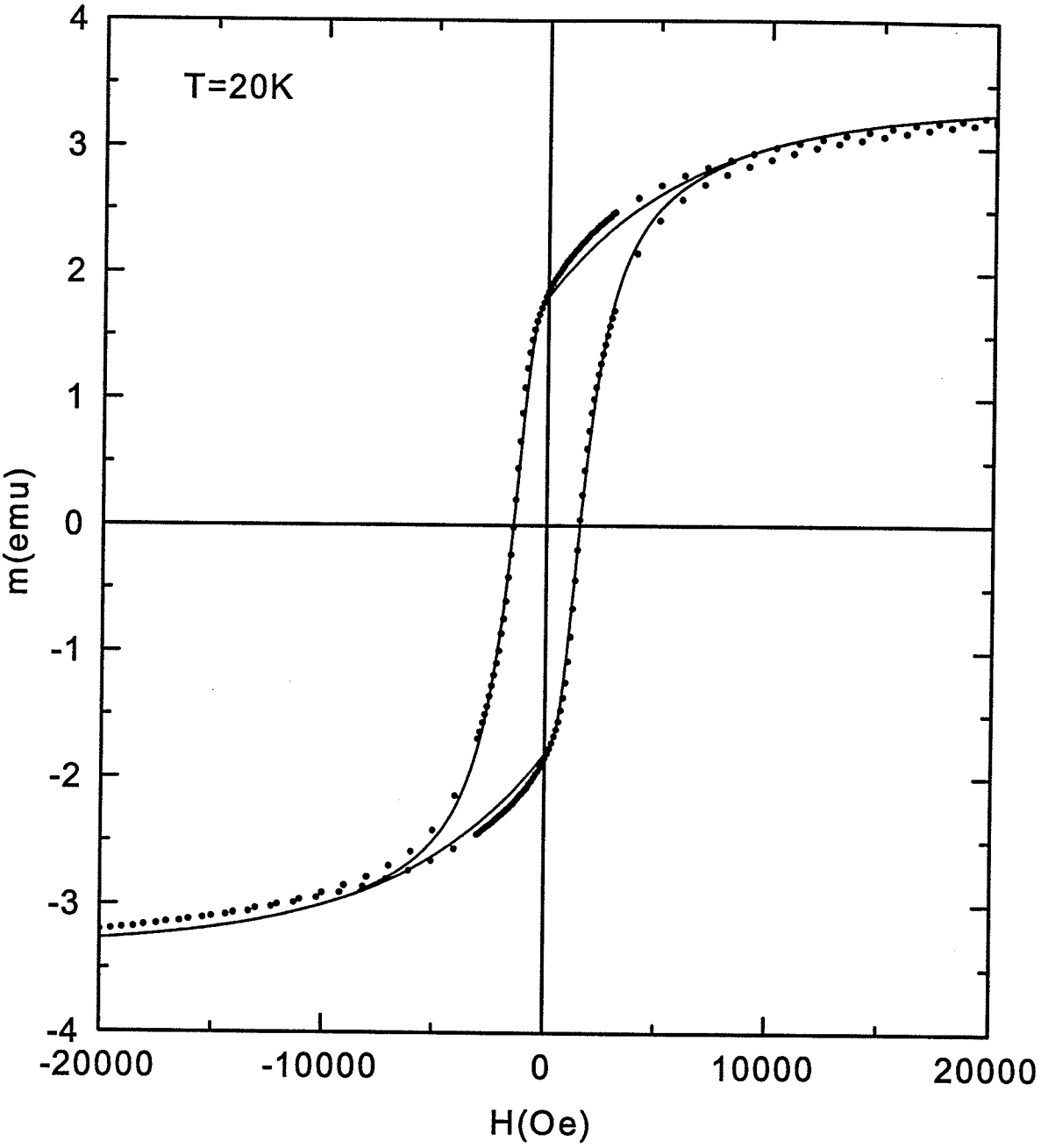

Figure 6.11: *A comparison of the Preisach numerical simulation (solid curve) of the major hysteresis loop of $La_{0.5}Sr_{0.5}CoO_3$ at $T = 20K$ with the measured loop (discrete points).*

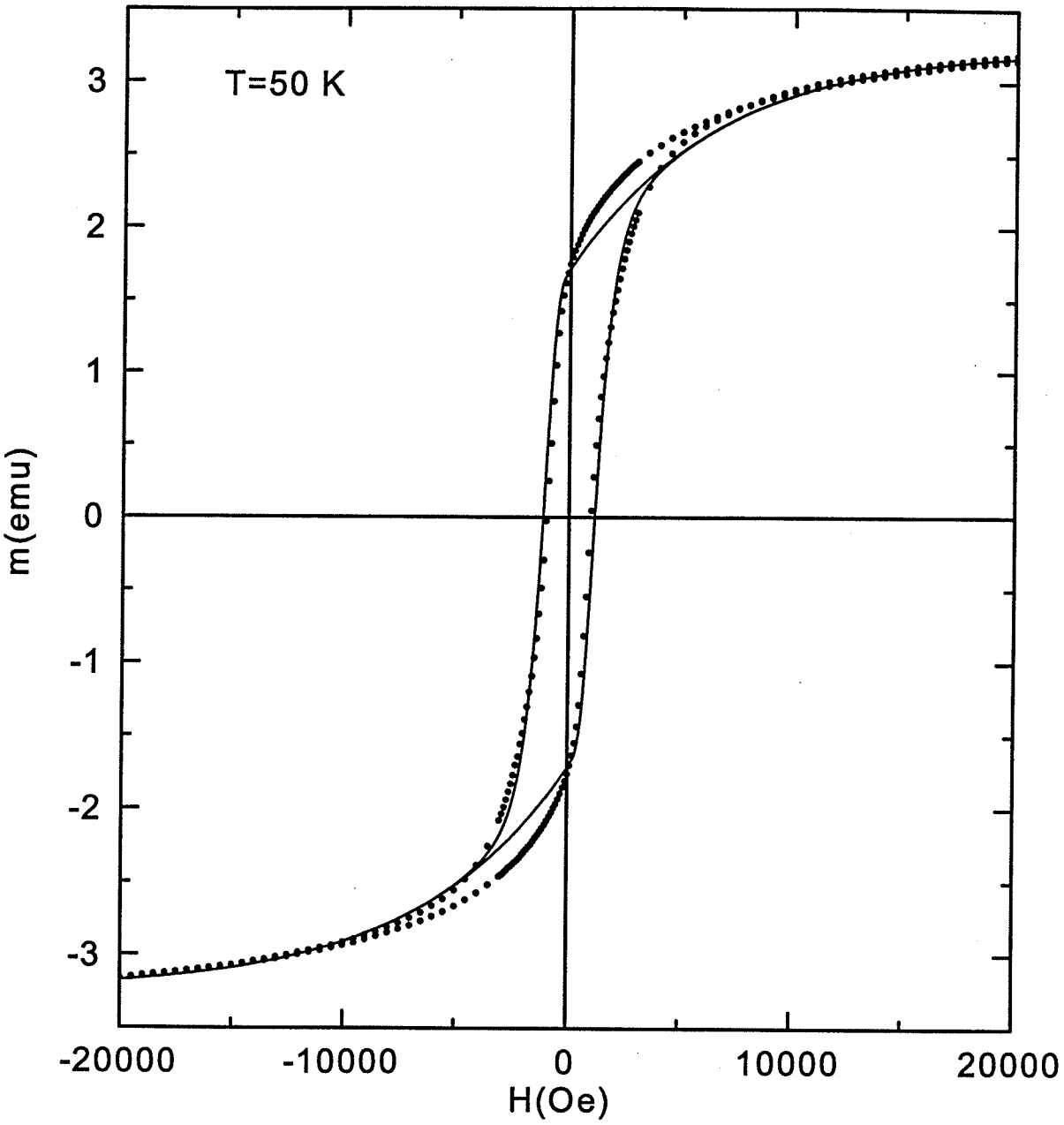

Figure 6.12: *A comparison of the Preisach numerical simulation (solid curve) of the major hysteresis loop of $La_{0.5}Sr_{0.5}CoO_3$ at $T = 50K$ with the measured loop (discrete points).*

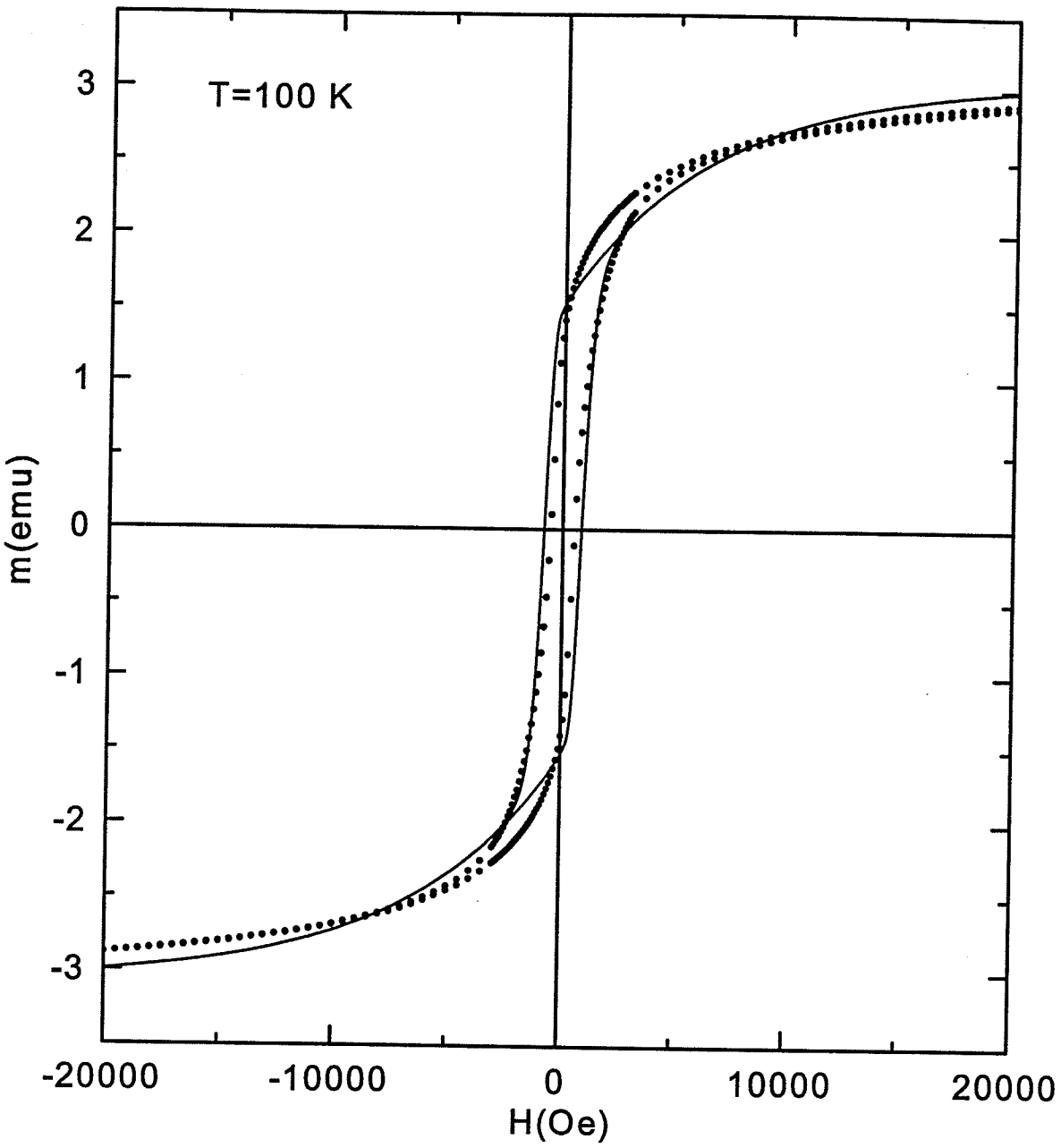

Figure 6.13: *A comparison of the Preisach numerical simulation (solid curve) of the major hysteresis loop of* $La_{0.5}Sr_{0.5}CoO_3$ *at* $T = 100K$ *with the measured loop (discrete points).*

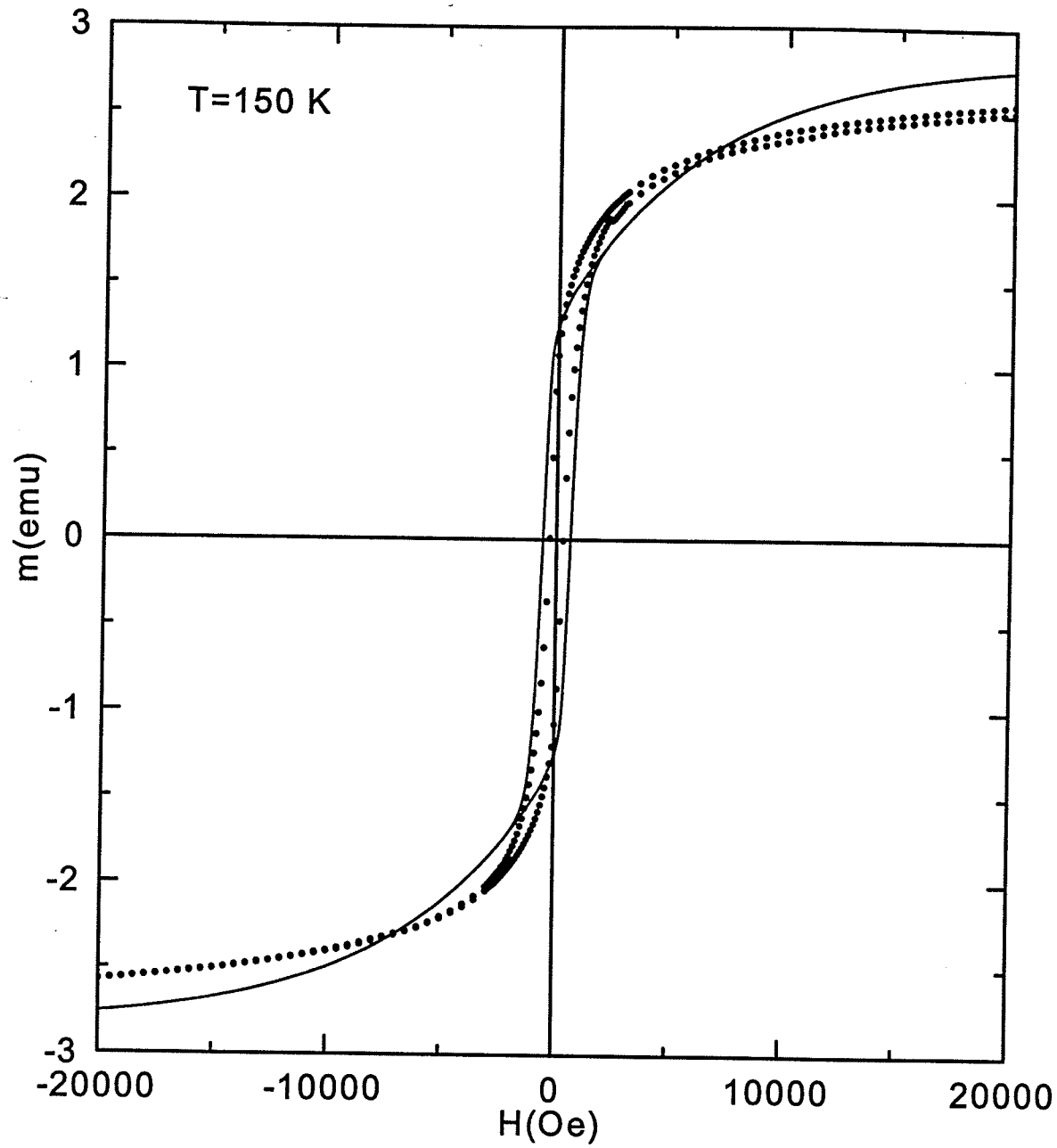

Figure 6.14: *A comparison of the Preisach numerical simulation (solid curve) of the major hysteresis loop of* $La_{0.5}Sr_{0.5}CoO_3$ *at* $T = 150K$ *with the measured loop (discrete points).*

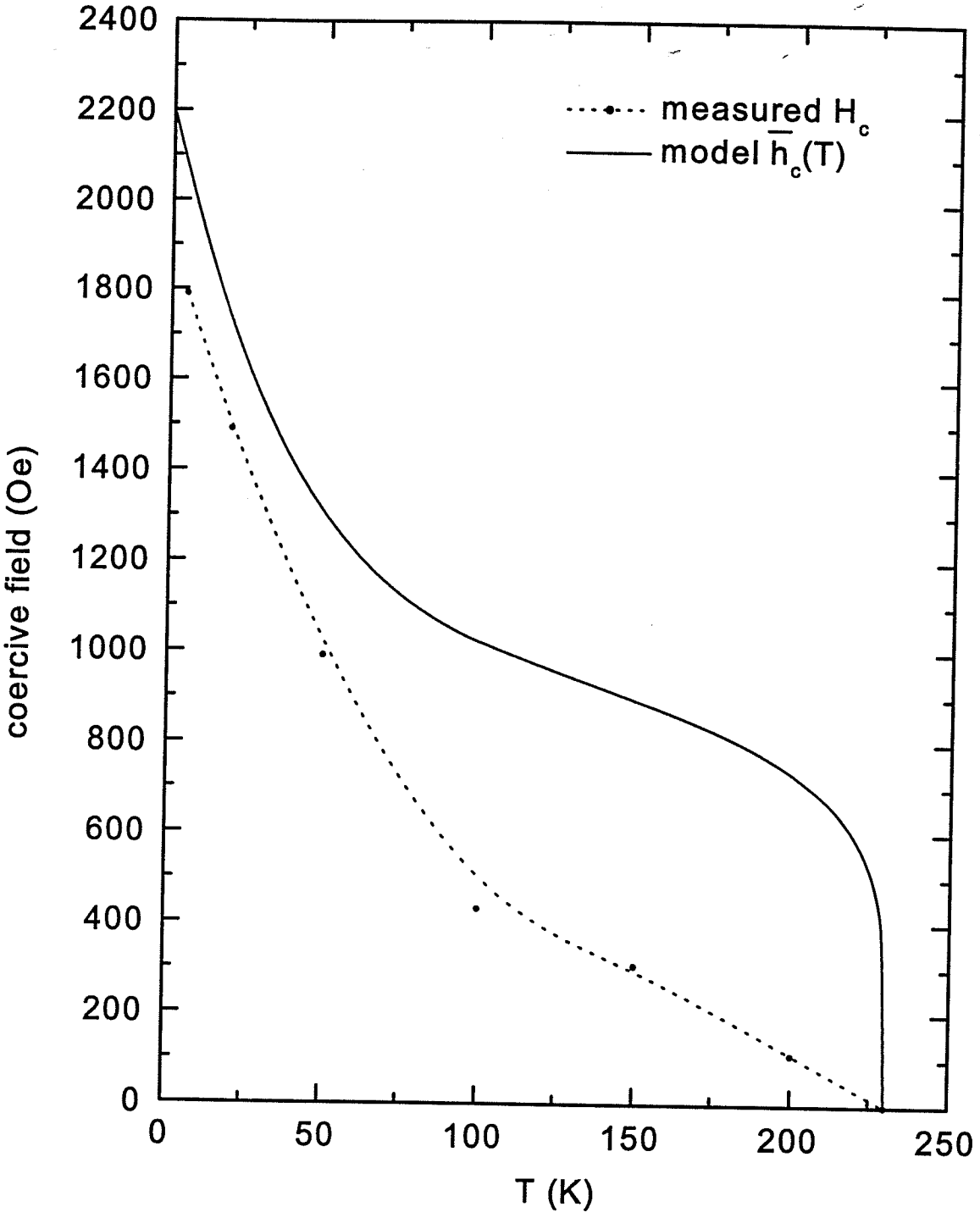

Figure 6.15: *A comparison of the temperature dependence of the measured coercive field H_c and the model coercive field $\bar{h}_c$.*

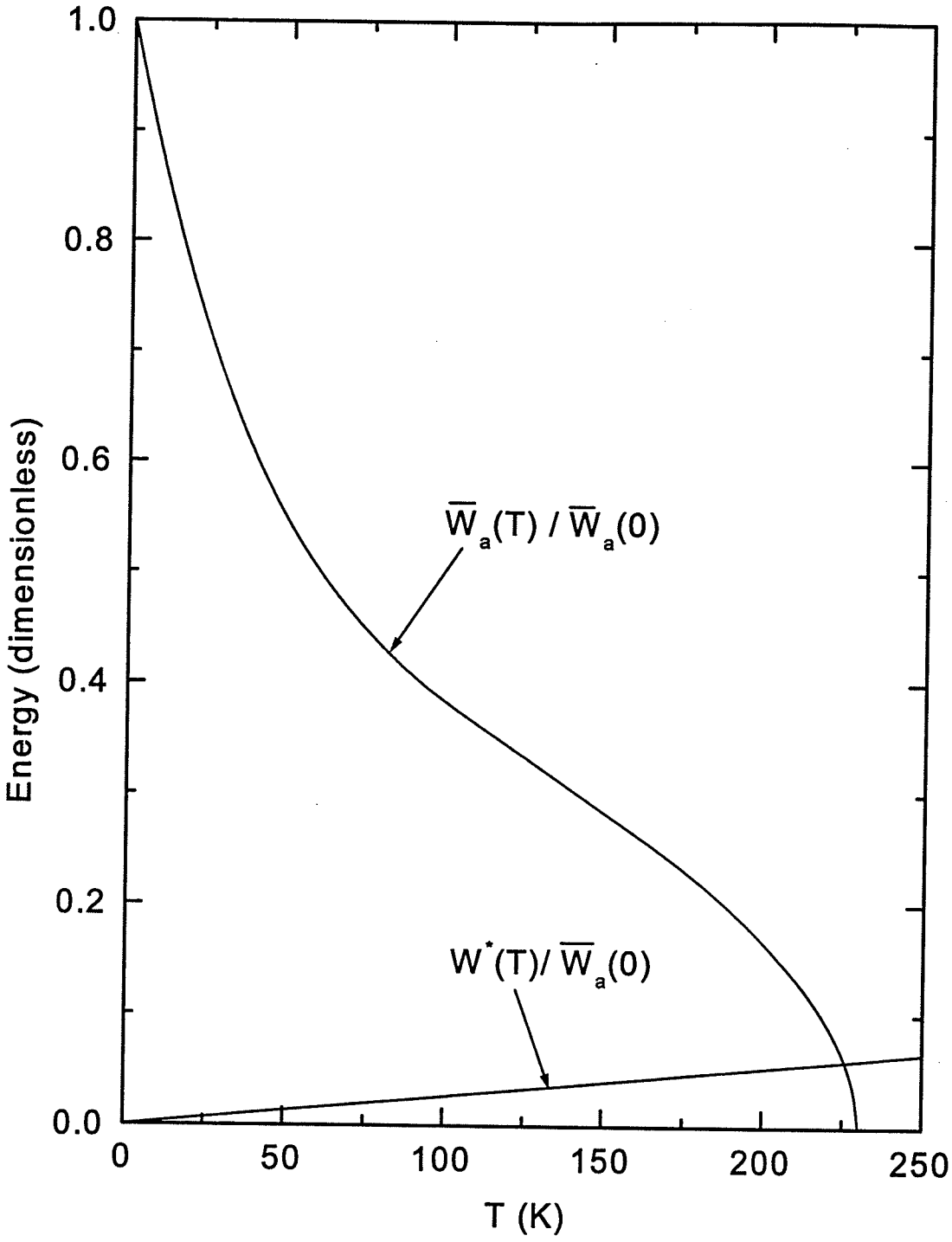

Figure 6.16: *A comparison of the temperature dependence of the mean free energy barrier* $\bar{W}_a(T)/\bar{W}_a(0) = (1 - T/T_c)^{\Gamma}[0.5(1 - T/T_c)^{\Gamma_{c1}} + 0.5(1 - T/T_c)^{\Gamma_{c2}}]$ *and the thermal fluctuation energy* $W^*(T)/\bar{W}_a(0) = k_B T * ln(t_{exp}/\tau_0)/(\mu_0 \bar{h}_{c0})$ *in* $La_{0.5}Sr_{0.5}CoO_3$.

Table 6.4: Preisach fitting parameters from hysteresis loops of $La_{0.5}Sr_{0.5}CoO_3$

T (K)	5	20	50	100	150	200
$\mu_0(10^{-15}\text{emu})$	6	6	6	6	6	6
$h_{c0}(\text{Oe})$	2200	2200	2200	2200	2200	2200
σ_{c0}	0.75	0.75	0.75	0.75	0.75	0.75
$\sigma_{i0}(Oe)$	99	99	99	99	99	99
Γ	0.34	0.34	0.34	0.34	0.34	0.34
Γ_{c1}	6.0	6.0	6.0	6.0	6.0	6.0
Γ_{c2}	0.2	0.2	0.2	0.2	0.2	0.2
Γ_i	0.08	0.08	0.08	0.08	0.08	0.08
$\lambda(10^{-4}/Oe)$	1.6	1.6	1.6	1.6	1.6	1.6
f	0.4	0.4	0.4	0.4	0.4	0.4
$m_{sat}(\text{emu})$	2.02	2.02	2.02	2.02	2.02	2.02
$T_c(\text{K})$	230	230	230	230	230	230

A comparison of figures (6.7) and (6.9) shows that the Preisach model is able to replicate all of the principal structural features of the FC and ZFC response functions, although it tends to overemphasize the sharpness of the response in the low field ($h_a < 300$ Oe) ZFC moment just below T_c. While this latter behaviour is dependent, to a limited extent, on the precise functional form of $\bar{h}_c(T)$ which is used to represent the intrinsic temperature dependence of the free energy barriers, it also tends to be a peculiarity of the lognormal coercive field distribution which vanishes at low fields. For this distribution, the absence of low free energy barriers suppresses thermally activated transitions until the temperature T is close enough to T_c to generate a significant population of these low free energy barriers through the critical collapse of the free energy landscape. The number of thermal activation events then increases dramatically over a relatively narrow temperature interval, leading to a sharp maximum.

Figure (6.15) compares the temperature dependence of the measured coercive field H_c, and the model coercive field $\bar{h}_c$, while figure (6.16) compares the temperature dependence of the mean free energy barrier $\bar{W}_a(T)/\bar{W}_a(0)$ obtained

from the fits with the thermal fluctuation energy $W^*(T)/\bar{W}_a(0)$. The temperature dependence of the free energy barriers in $La_{0.5}Sr_{0.5}CoO_3$ is clearly very different from that of $SrRuO_3$ in figure (6.6), and our analysis shows that these differences are manifested very directly in the ZFC response, which thus provides a highly sensitive probe of the free energy landscape and its variation with temperature.

6.3 $La_{0.7}Sr_{0.3}MnO_3$

The final system investigated here was the substituted perovskite $La_{0.7}Sr_{0.3}MnO_3$. In order to explore in more depth the predictive capabilities of the Preisach formalism, two modifications were introduced into the current analysis: (a) the experimental data set was expanded to include measurements of the field and temperature dependence of the *remanent moment*, and (b) the role of the reversible contribution in the model was altered somewhat.

Figures (6.17) through (6.21) show measurements (discrete points) and Preisach simulations (solid curves) of the temperature dependence in various applied fields of the ZFC moment, the *isothermal remanent magnetization* (IRM) obtained by reducing the field to zero from the ZFC state, the FC moment, and the *thermoremanent moment* (TRM) obtained by reducing the field to zero from the FC state. The FC and ZFC moments exhibit a rapid temperature dependence for $T > 300$K suggestive of ferromagnetic ordering with a critical temperature $T_c \cong 325K$. A critical analysis of the a.c. susceptibility is currently underway to verify this expectation. The FC moment is relatively featureless, and essentially changes in amplitude only with changes in the applied field h_a. The ZFC moment increases gradually with increasing temperature and exhibits a maximum just below T_c which becomes broader and shifts to lower temperatures with increasing h_a. By contrast, the characteristics of the remanence are altered appreciably by changes in the field. At low fields, the TRM and IRM resemble the FC and ZFC moments, respectively. However, as the field increases, the shape of the TRM changes systematically from concave down to concave up at low temperatures so that, at high fields, it bears almost no resemblance to the FC moment. The IRM also undergoes systematic changes such that, at high fields, it exhibits a maximum at low temperatures followed by a "knee" at high temperatures in

the vicinity of 275K. Such measurements of the remanences aid appreciably in defining the characteristics of the reversible component of the response.

Figures (6.22) through (6.25) show measurements (discrete points) and Preisach simulations (solid curves) of the initial magnetizing curve m_i , the magnetizing remanence m_r (identical to the IRM) obtained by reducing the field to zero starting from any given point on the initial magnetizing curve, the descending branch of the major hysteresis loop m_d, and the demagnetizing remanence m_{dr}, obtained by reducing the field to zero starting from any point on the descending branch.

The Preisach analysis assumed that the spectrum of characteristic Barkhausen fields h_c and h_i was described by the product of two Gaussian distributions:

$$p(h_c, h_i) = (2\pi\sigma_c^2)^{-\frac{1}{2}} exp[-(h_c - \bar{h}_c)^2/2\sigma_c^2]$$

$$\cdot(2\pi\sigma_i^2)^{-\frac{1}{2}} exp[-h_i^2/2\sigma_i^2] \tag{6.7}$$

where $\bar{h}_c(T)$, $\sigma_c(T)$ and $\sigma_i(T)$ were allowed to vary with temperature as follows:

$$\left\{ \begin{array}{l} \bar{h}_c(T) = \bar{h}_{c0}[0.6(1 - T/T_c)^{\Gamma_{c1}} + 0.4(1 - T/T_c)^{\Gamma_{c2}}] \\ \sigma_c(T) = \sigma_{c0}[0.6(1 - T/T_c)^{\Gamma'_{c1}} + 0.4(1 - T/T_c)^{\Gamma'_{c2}}] \\ \sigma_i(T) = \sigma_{i0}(1 - T/T_c)^{\Gamma_i} \end{array} \right\} \tag{6.8}$$

In this analysis, each Barkhausen element was assigned a response function consisting of two branches, an upper branch

$$m_+ = (1 - f)\mu(T) \pm f\mu(T)(1 - exp(-\lambda \mid h_a \mid)) \tag{6.9}$$

and a lower branch

$$m_- = -(1 - f)\mu(T) \pm f\mu(T)(1 - exp(-\lambda \mid h_a \mid)) \tag{6.10}$$

where the plus (minus) sign corresponds to positive (negative) h_a. This approach incorporates reversibility clearly into each individual Barkhausen response func-

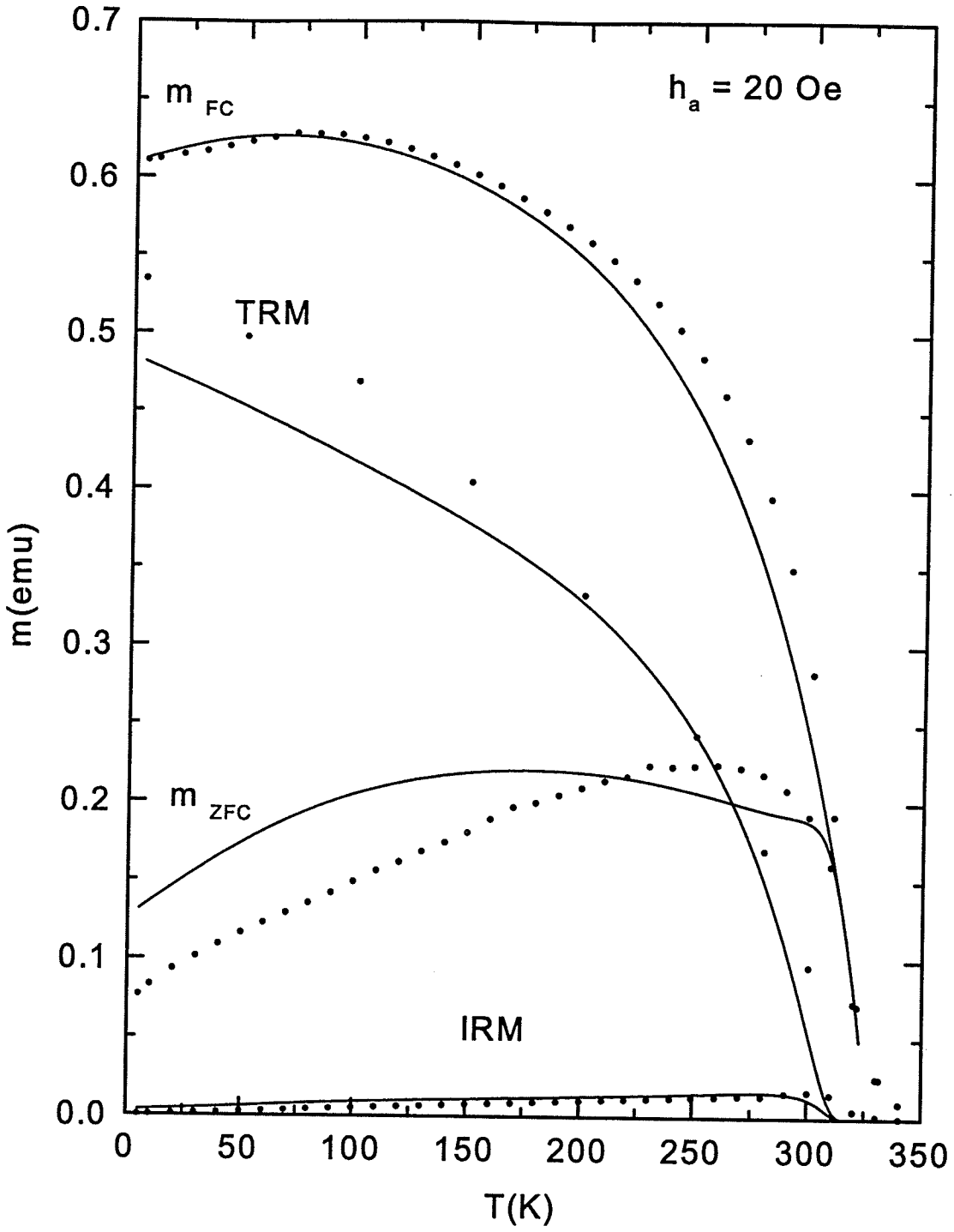

Figure 6.17: *Measurements (discrete points) and Preisach simulations (solid curves) of the temperature dependence of the field cooled (FC) moment, the zero field cooled (ZFC) moment, the thermoremanent moment (TRM), and the isothermal remanent moment (IRM) of* $La_{0.7}Sr_{0.3}MnO_3$ *in an applied field* $h_a = 20$ *Oe.*

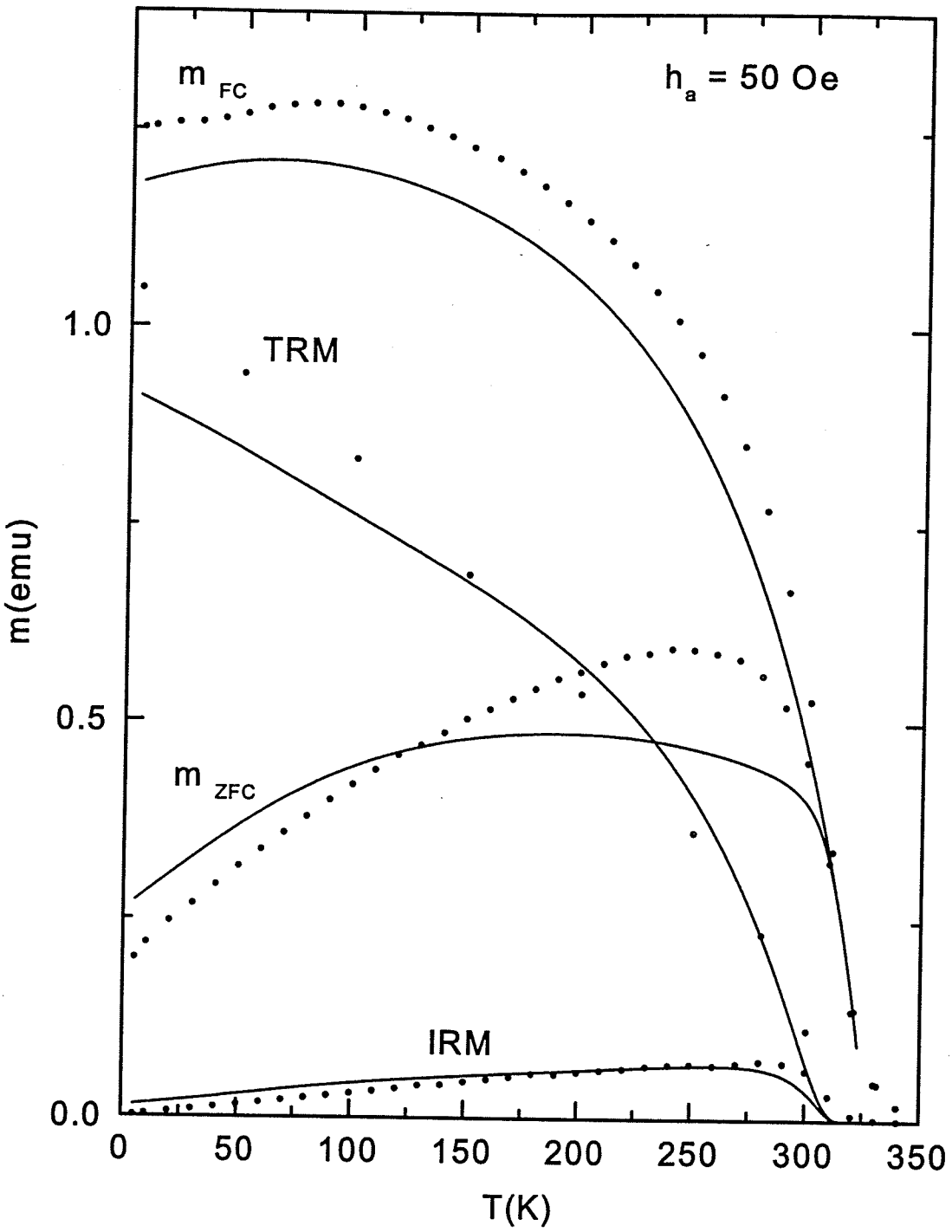

Figure 6.18: *Measurements (discrete points) and Preisach simulations (solid curves) of the temperature dependence of the field cooled (FC) moment, the zero field cooled (ZFC) moment, the thermoremanent moment (TRM), and the isothermal remanent moment (IRM) of* $La_{0.7}Sr_{0.3}MnO_3$ *in an applied field* $h_a = 50$ *Oe.*

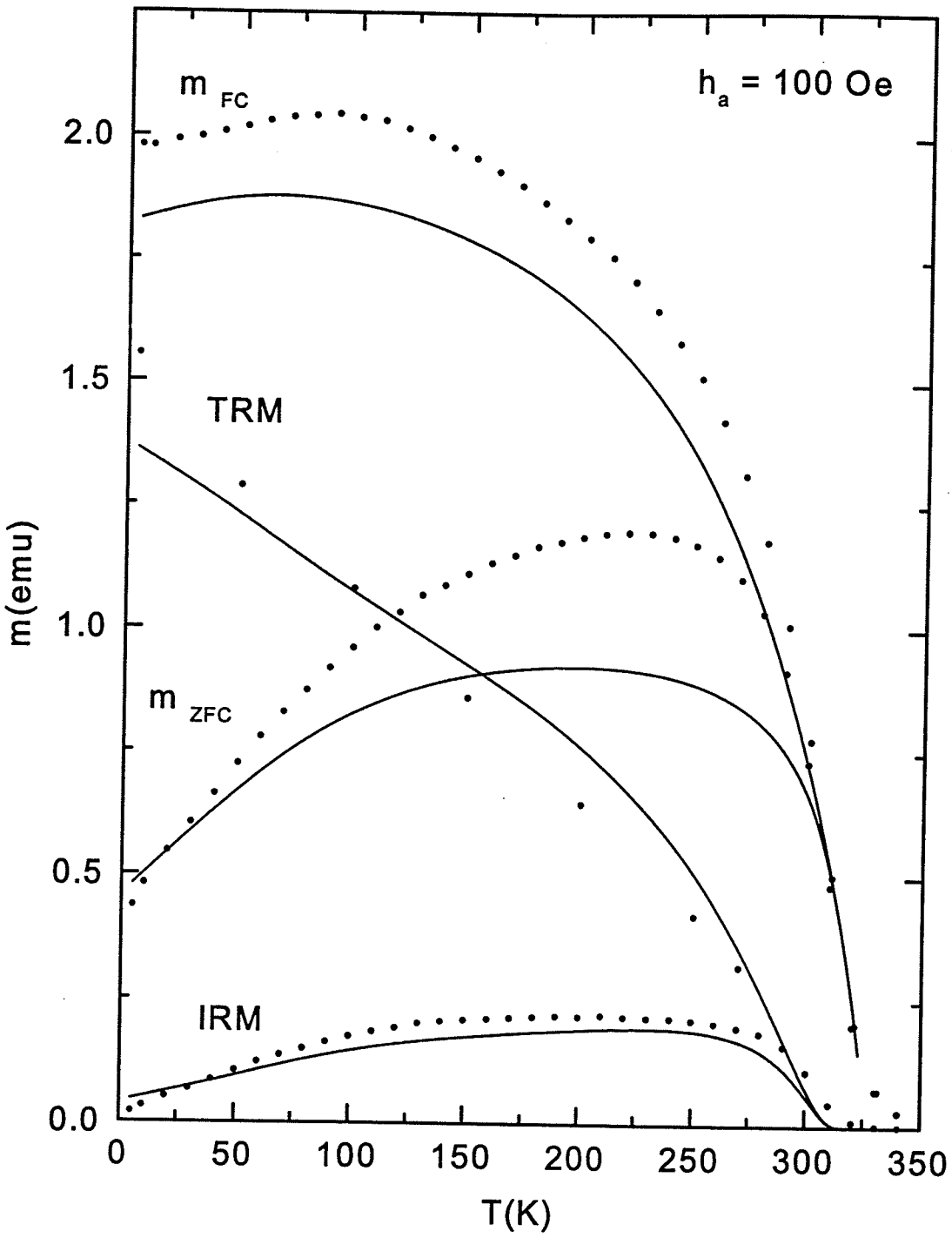

Figure 6.19: *Measurements (discrete points) and Preisach simulations (solid curves) of the temperature dependence of the field cooled (FC) moment, the zero field cooled (ZFC) moment, the thermoremanent moment (TRM), and the isothermal remanent moment (IRM) of* $La_{0.7}Sr_{0.3}MnO_3$ *in an applied field* $h_a = 100$ *Oe.*

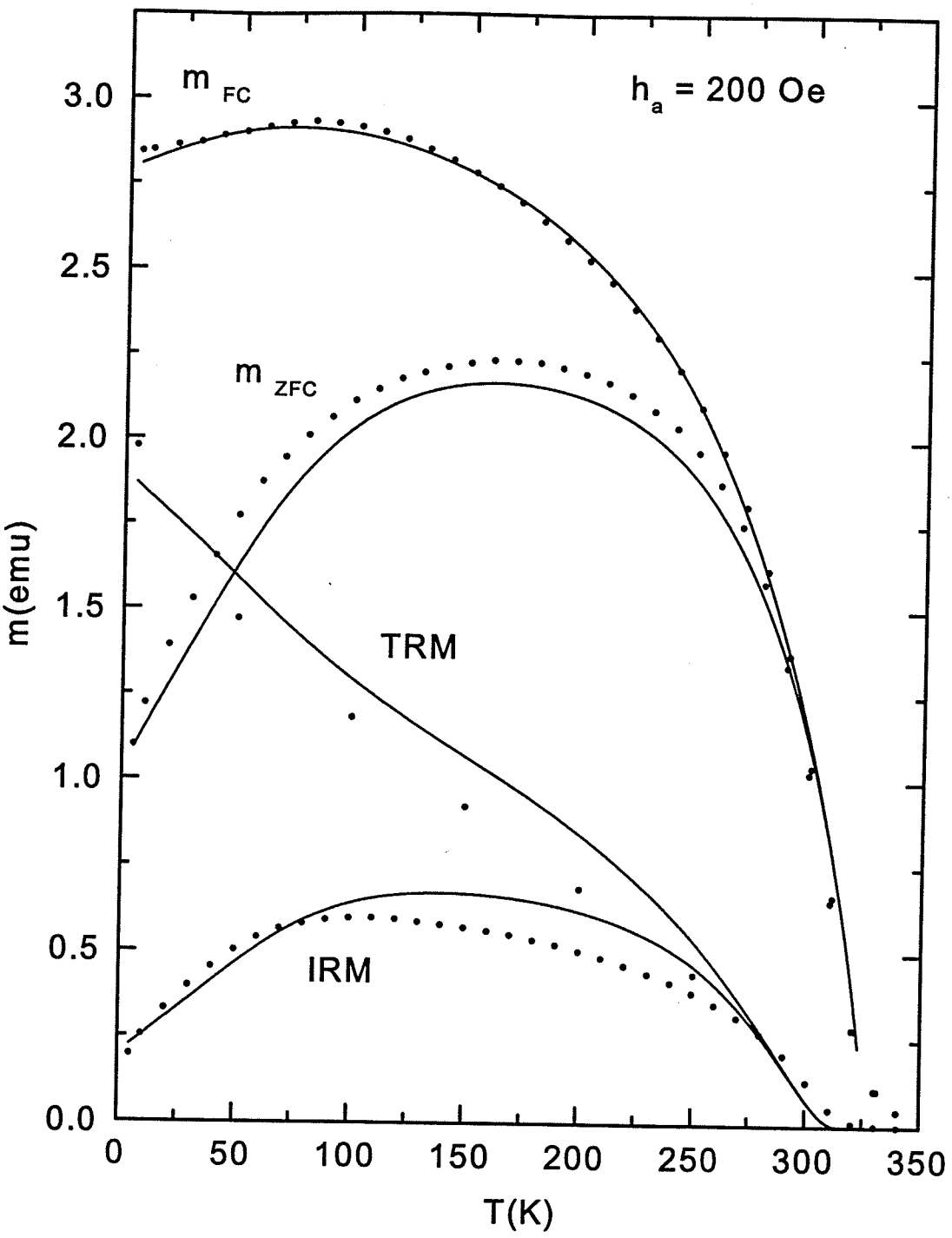

Figure 6.20: *Measurements (discrete points) and Preisach simulations (solid curves) of the temperature dependence of the field cooled (FC) moment, the zero field cooled (ZFC) moment, the thermoremanent moment (TRM), and the isothermal remanent moment (IRM) of* $La_{0.7}Sr_{0.3}MnO_3$ *in an applied field* $h_a = 200$ *Oe.*

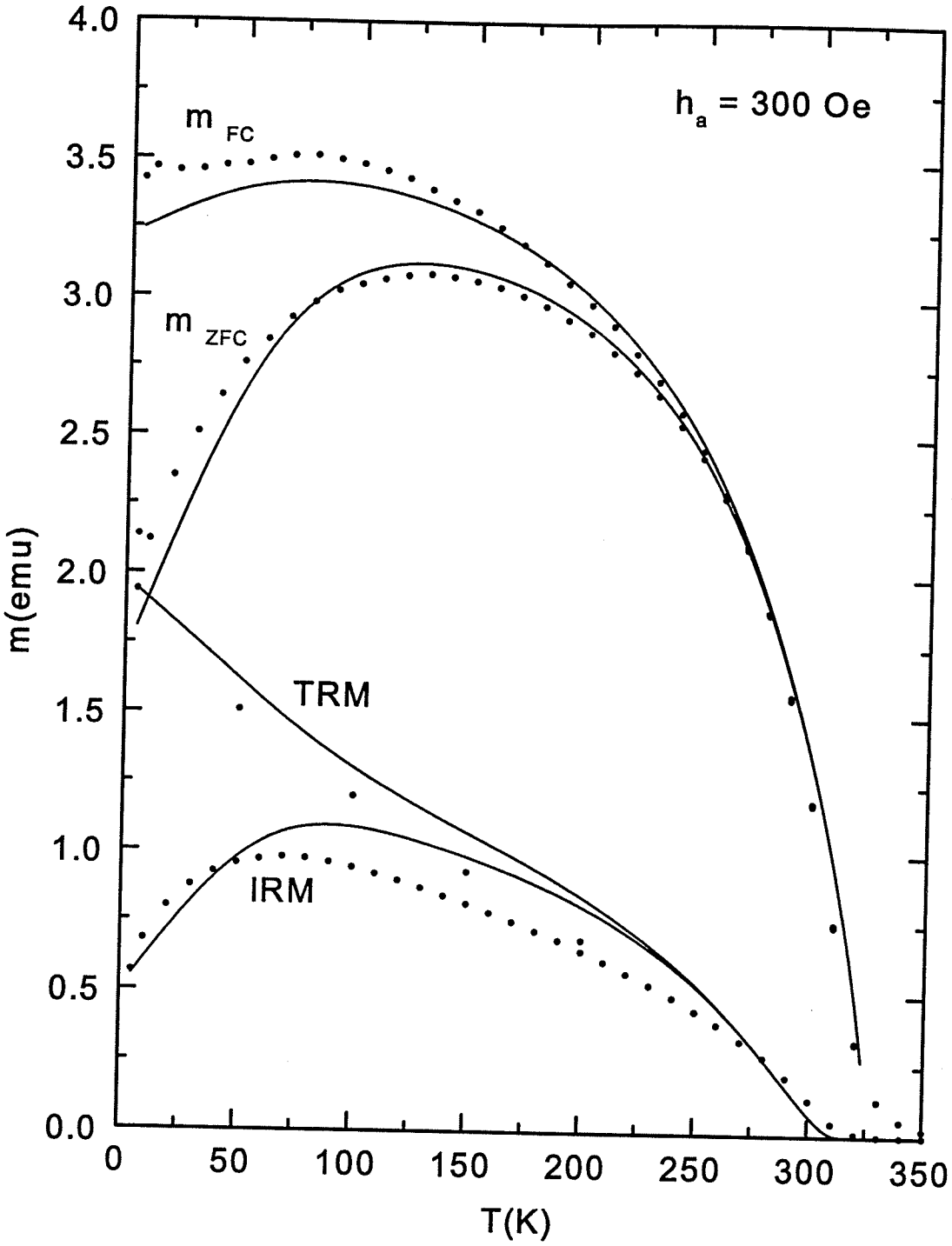

Figure 6.21: *Measurements (discrete points) and Preisach simulations (solid curves) of the temperature dependence of the field cooled (FC) moment, the zero field cooled (ZFC) moment, the thermoremanent moment (TRM), and the isothermal remanent moment (IRM) of* $La_{0.7}Sr_{0.3}MnO_3$ *in an applied field* $h_a = 300$ *Oe.*

tion, and effectively replaces the standard rectangular Preisach hysteresis loop by a Stoner-Wohlfarth-like hysteresis loop with saturation moment $\mu(T)$ and remanence $(1-f)\mu(T)$ but with, in general, asymmetric activation fields (α, β) due to interactions with other Barkhausen subsystems.

In this analysis, the spontaneous moment $\mu(T)$ was allowed to vary with temperature as

$$\mu(T) = \mu_0[0.6(1 - T/T_c)^{\Gamma_1} + 0.4(1 - (T/T_c)^{\Gamma_2})] \tag{6.11}$$

The reversible parameter λ was also allowed to vary with temperature T as

$$\lambda(T) = \lambda_0 + \lambda_1 T + \lambda_2 T^2 + \lambda_3 T^3, \tag{6.12}$$

but the reversible factor f was held constant.

Table (6.5) lists the values of all the fitting parameters. Only *one* set of parameters was used to describe the entire spectrum of experimental data shown in figures (6.17) through (6.25).

Figure (6.26) compares the temperature dependence of the model coercive field $\bar{h}_c(T)$ and the measured coercive field H_c, and figure (6.27) shows the temperature dependence of the reversible parameters $\lambda(T)$ and f(T).

The Preisach model clearly provides an excellent representation of both the moment and remanence data, and the modifications introduced into this analysis, particularly those relating to the remanent moment, allows us to construct a much more detailed physical picture of the thermal activation processes and their relationship to the evolution of the free energy landscape with temperature. In particular, according to the Preisach diagram in figure (2.4), cooling from the critical temperature T_c forces all of the two level Baukhausen subsystems in figure (2.1) into their *lower energy state*, which is $\phi = +\mu(T)$ if $h_i > h_a$ or $\phi = -\mu(T)$ if $h_i < h_a$. Of course the precise configuration of subsystem moments

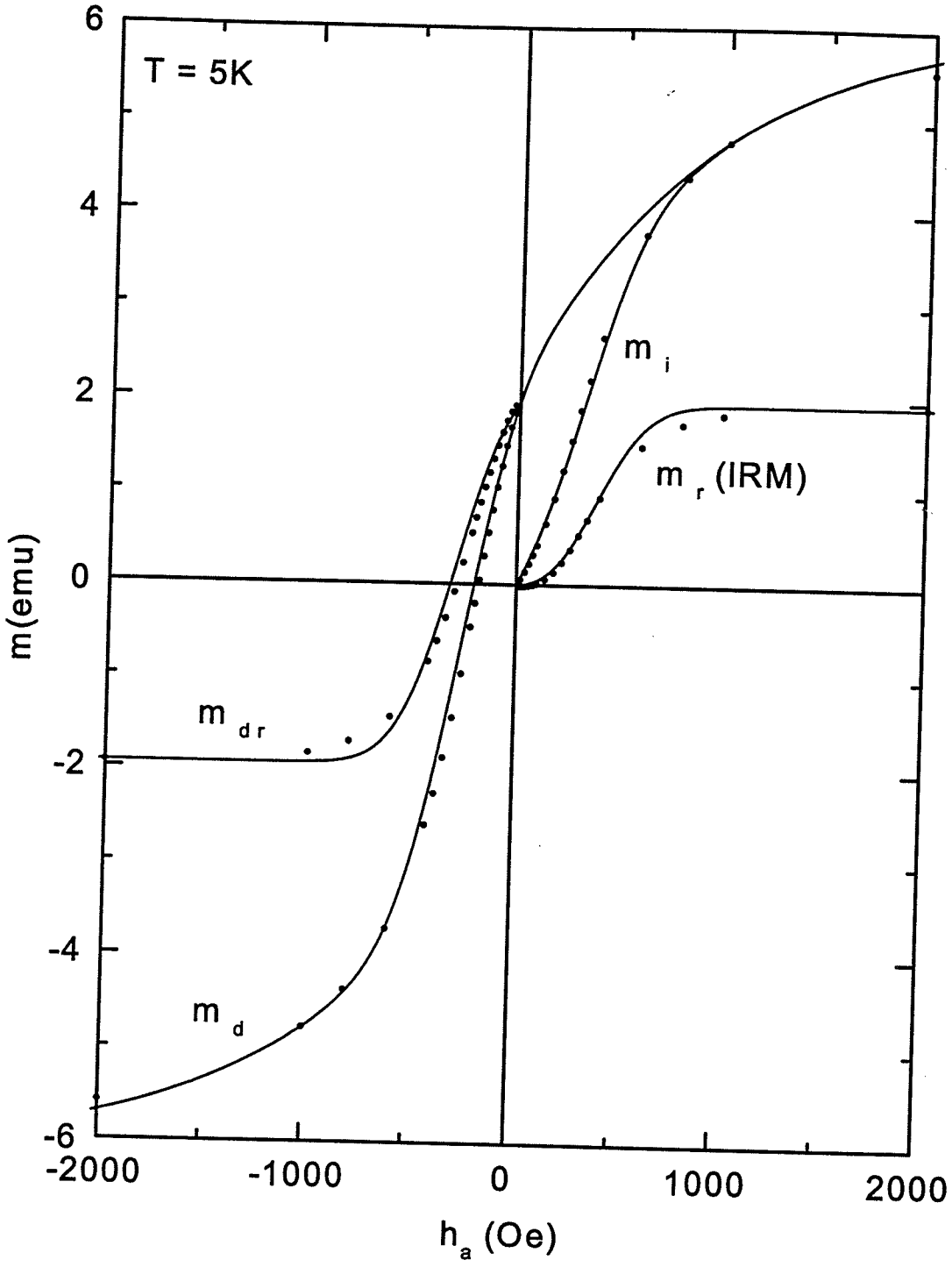

Figure 6.22: *Measurements (discrete points) and Preisach simulations (solid curves) of the initial magnetizing curve m_i, the magnetizing remanence m_r, the descending branch of the major hysteresis loop m_d, and the demagnetizing remanence m_{dr} of $La_{0.7}Sr_{0.3}MnO_3$ at $T = 5K$.*

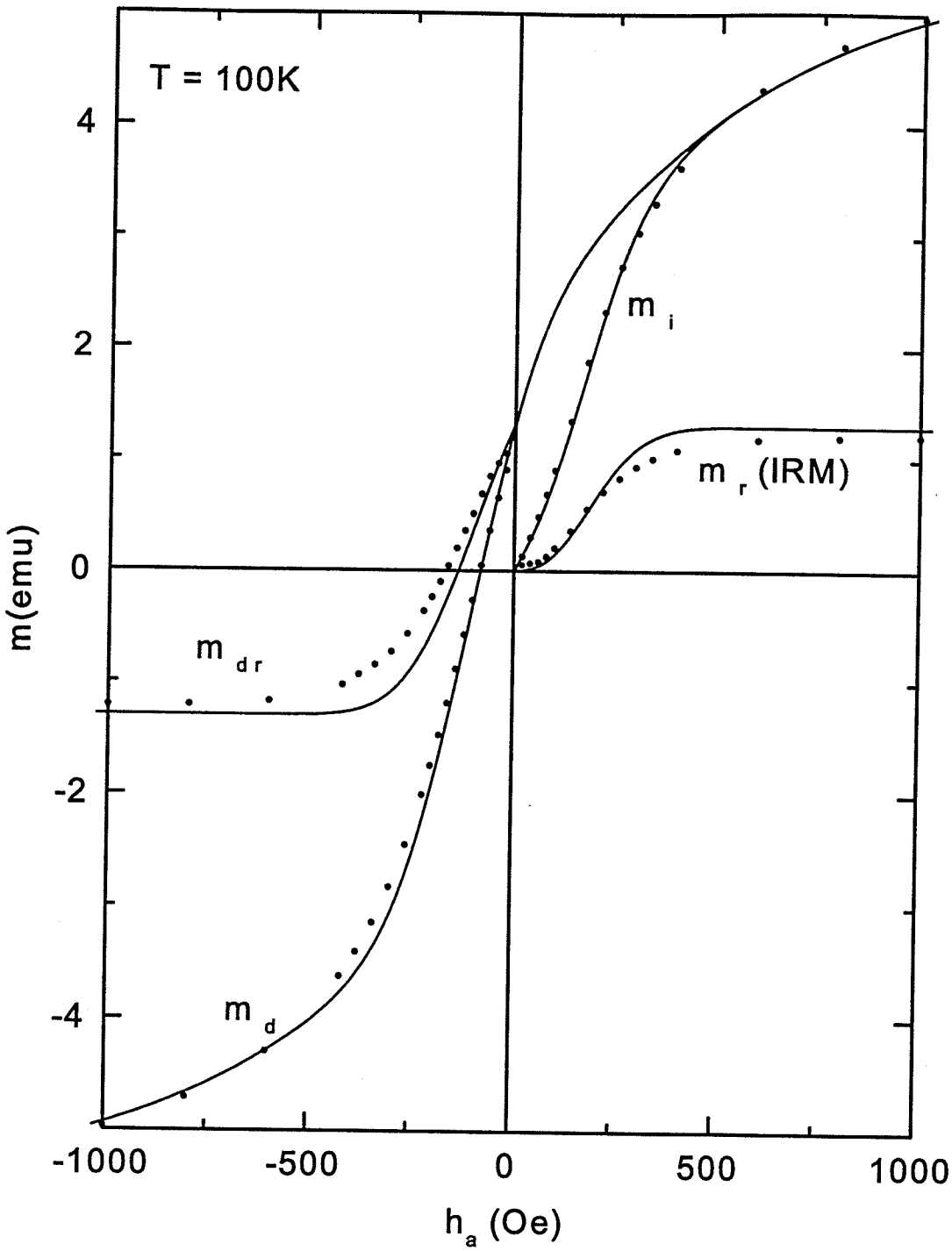

Figure 6.23: *Measurements (discrete points) and Preisach simulations (solid curves) of the initial magnetizing curve m_i, the magnetizing remanence m_r, the descending branch of the major hysteresis loop m_d, and the demagnetizing remanence m_{dr} of $La_{0.7}Sr_{0.3}MnO_3$ at $T = 100K$.*

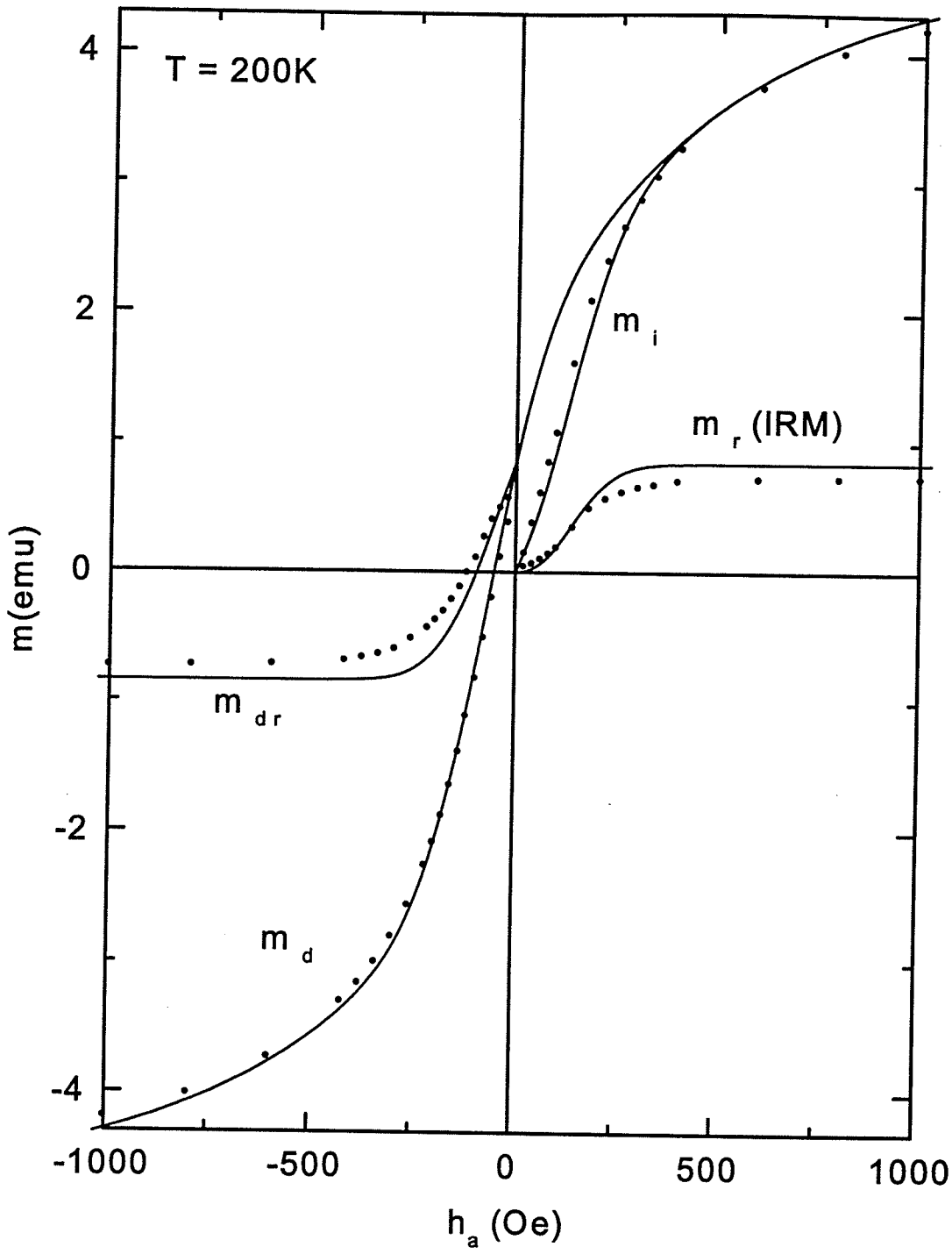

Figure 6.24: *Measurements (discrete points) and Preisach simulations (solid curves) of the initial magnetizing curve m_i, the magnetizing remanence m_r, the descending branch of the major hysteresis loop m_d, and the demagnetizing remanence m_{dr} of $La_{0.7}Sr_{0.3}MnO_3$ at $T = 200K$.*

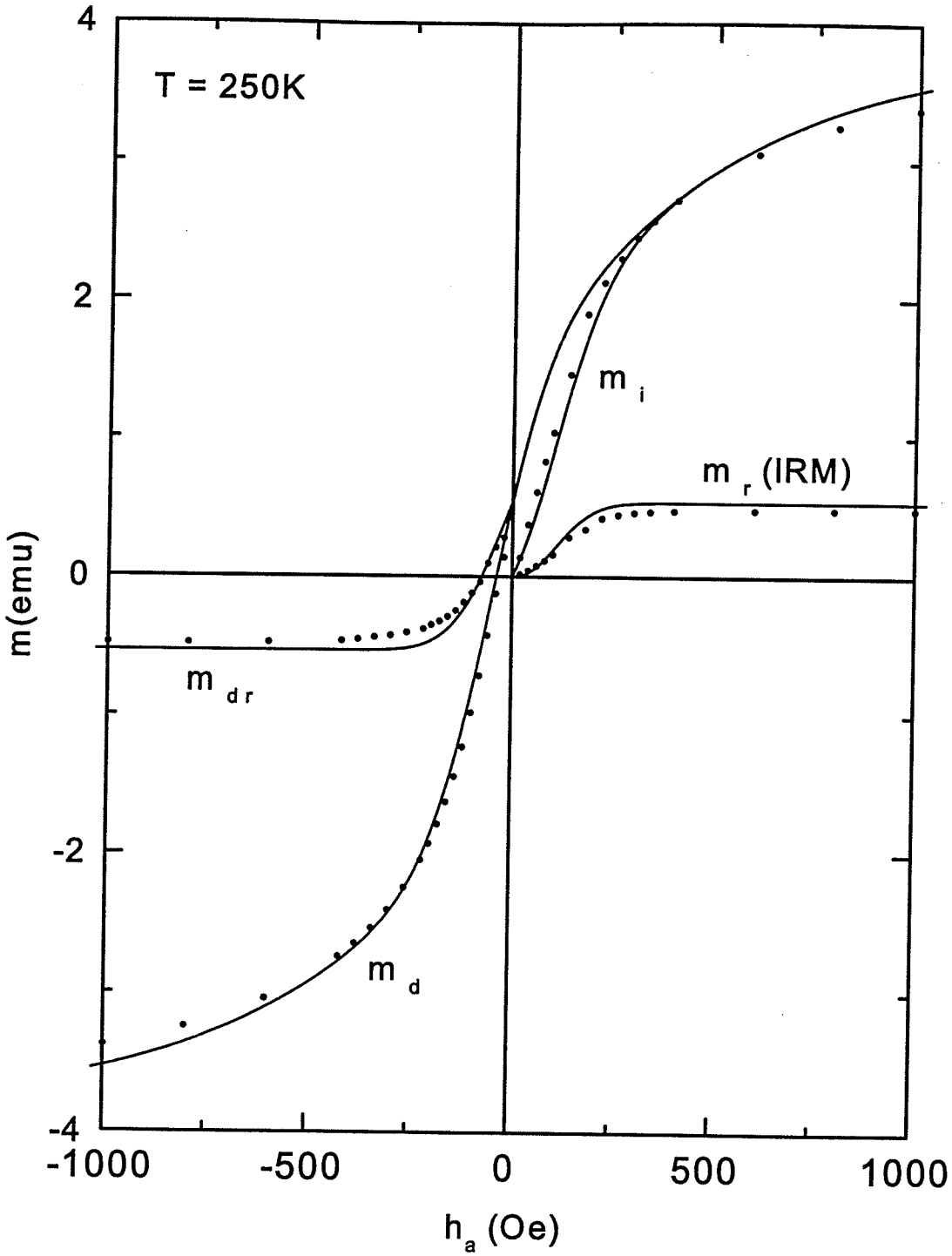

Figure 6.25: *Measurements (discrete points) and Preisach simulations (solid curves) of the initial magnetizing curve m_i, the magnetizing remanence m_r, the descending branch of the major hysteresis loop m_d, and the demagnetizing remanence m_{dr} of $La_{0.7}Sr_{0.3}MnO_3$ at $T = 250K$.*

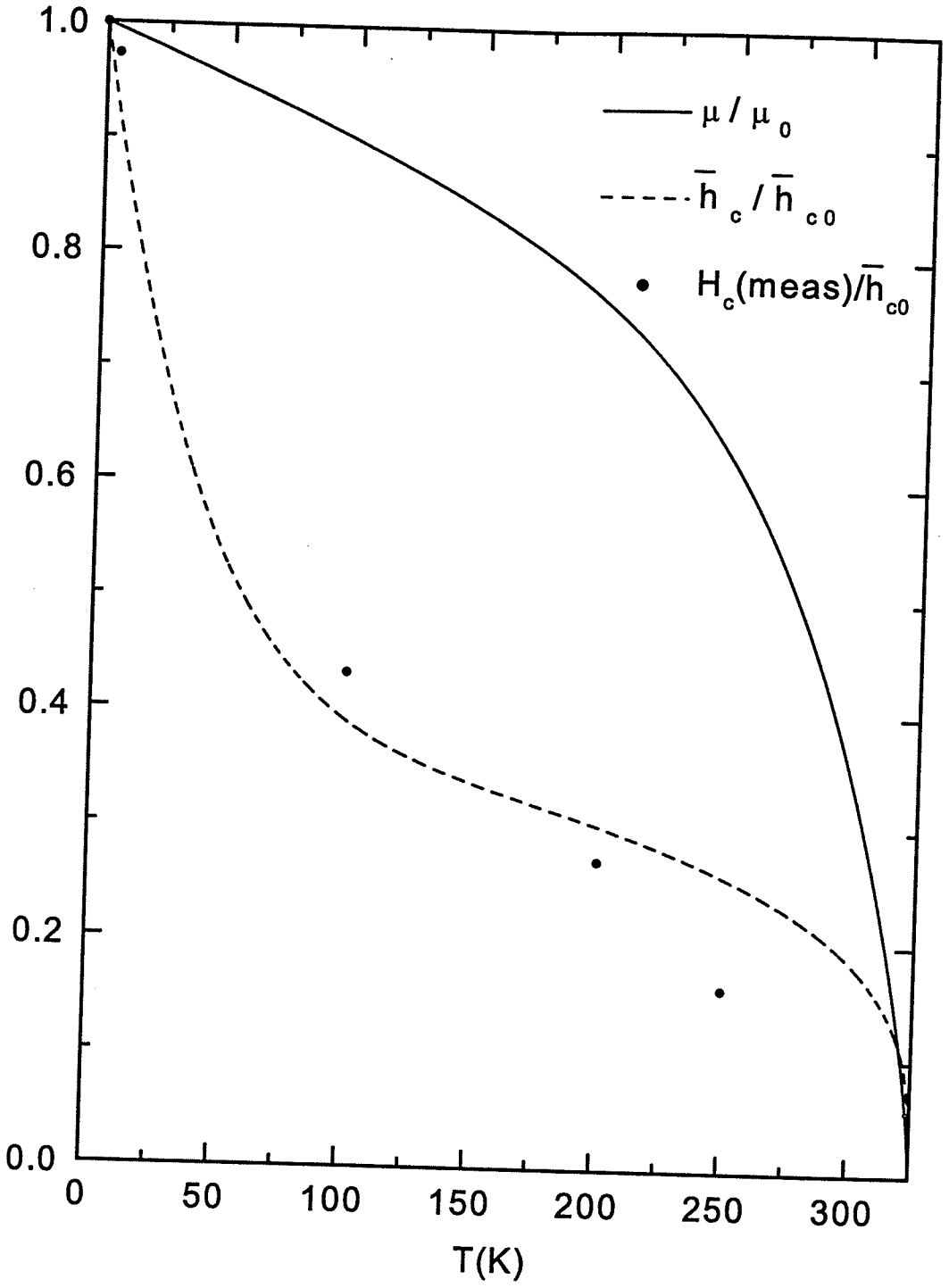

Figure 6.26: *The temperature dependence of the model Barkhausen moment μ/μ_0, the model coercive field $\bar{h}_c/\bar{h}_{c0}$, and the measured coercive field $H_c/\bar{h}_{c0}$ of $La_{0.7}Sr_{0.3}MnO_3$.*

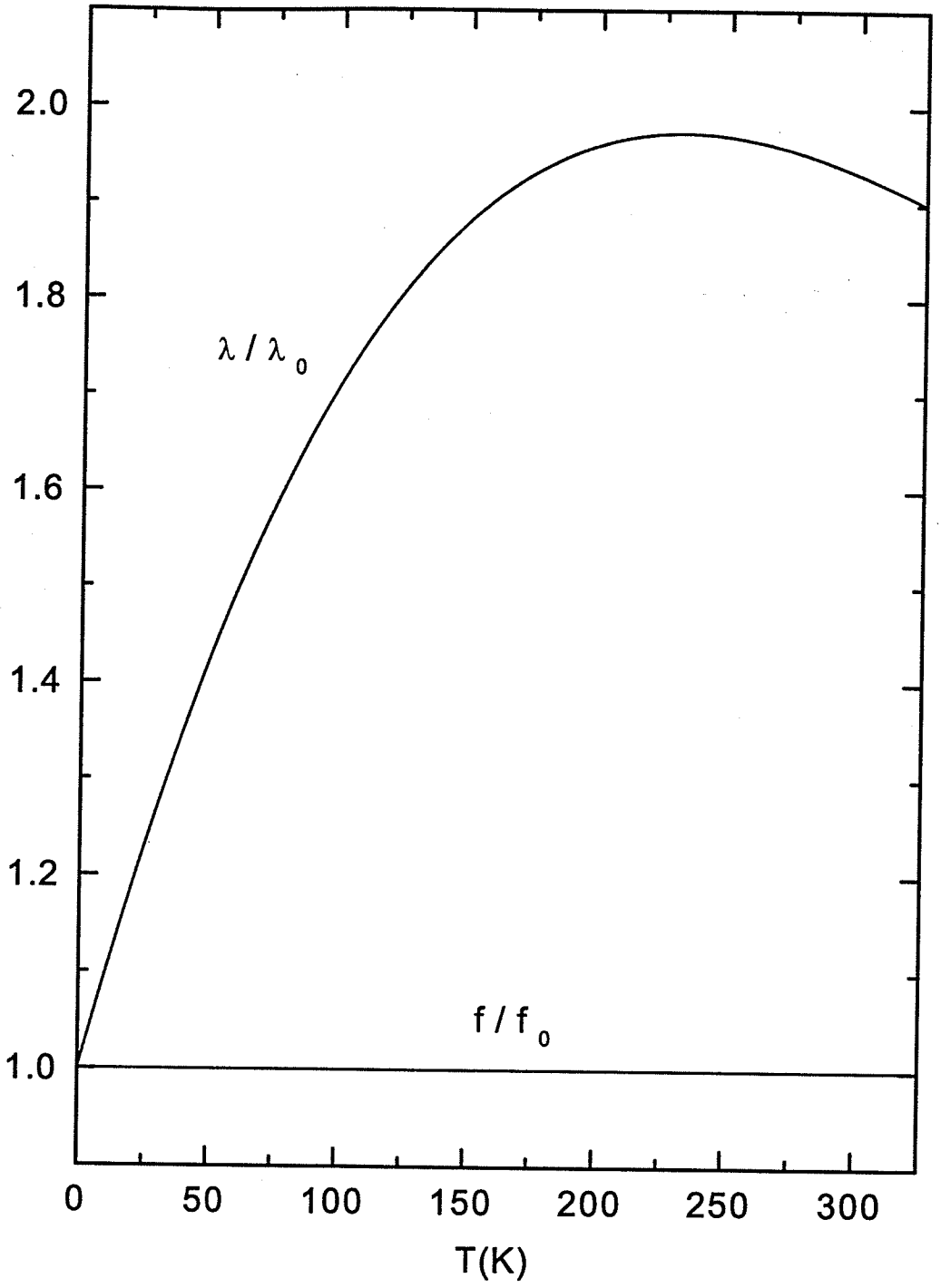

Figure 6.27: *The temperature dependence of the reversible Preisach parameters* λ *and* f *of* $La_{0.7}Sr_{0.3}MnO_3$.

Table 6.5: Preisach fitting parameters for $La_{0.7}Sr_{0.3}MnO_3$.

T_c(K)	325
$\bar{h}_{c0}$(Oe)	300
$\sigma_{c0}(Oe)$	210
$\sigma_{i0}(Oe)$	105
$\mu_0(emu)$	5×10^{-14}
Γ_1	0.5
Γ_2	7.0
Γ_{c1}	8.0
Γ_{c2}	0.3
Γ'_{c1}	8.0
Γ'_{c2}	0.3
Γ_i	0.0
f	0.65
$\lambda_0(Oe^{-1})$	1.0×10^{-3}
$\lambda_1(K^{-1}Oe^{-1})$	1.0×10^{-5}
$\lambda_2(K^{-2}Oe^{-1})$	-3.2×10^{-8}
$\lambda_3(K^{-3}Oe^{-1})$	3.0×10^{-11}
$m_{sat}(emu)$	6.22

$\pm\mu(T)$ at any given temperature depends upon how the energy barriers $W'_{\pm}(T)$ in equation (2.5) and (2.6), and hence the characteristic fields $h_c(T)$ and $h_i(T)$, are growing with temperature, and this is modelled by assuming that all possible fields are in principle represented in the material, and allowing the *distribution* of these fields to evolve with temperature in order to simulate the actual growth. If we focus then on a typical Barkhausen element with coercive field $\bar{h}_c(T)$ which is trapped in either its $+\mu(T)$ or $-\mu(T)$ state in the cooling field h_a, it is clear that this state is very stable with respect to changes in $\bar{h}_c(T)$ with temperature since the trapped state is always the lower energy state. We thus expect that the temperature dependence of the FC moment will be determined primarily by the Barkhausen moment $\mu(T)$ and by the reversible parameter $\lambda(T)$ and will be insensitive to $\bar{h}_c(T)$, and this is indeed confirmed by our fits.

However, the situation may change dramatically when the field h_a is reduced to zero from the field cooled state to form the thermoremanent (TRM) state. In particular, Barkhausen elements with large negative interaction fields $|h_i| \cong \bar{h}_{c0}$, cooled in large positive applied fields $h_a > |h_i|$, will be trapped in an unstable positive state $\phi = +\mu(T)$ state upon removal of the field, and these will be particularly susceptible to thermal activation into the $\phi = -\mu(T)$ state when the temperature is increased from $T = 0$ since the free energy barrier $W_+ = \mu(h_c - |h_i|)$ in figure (2.1) is very small. Moreover, the temperature dependence of these activation processes will be defined primarily by the temperature dependence of $\bar{h}_c(T)$. Thus, if there is a reasonable population of Barkhausen elements with large interaction fields $|h_i| \sim \bar{h}_{c0}$, the TRM measured in large applied fields h_a may provide a sensitive probe of the temperature dependence of the dissipation barriers. By contrast, field cooling in small fields $h_a \ll \bar{h}_{c0}$ will only affect Barkhausen elements with small interaction fields $|h_i| \ll \bar{h}_{c0}$, and these elements will be insensitive to variations in $\bar{h}_c(T)$ except perhaps near T_c. Thus the low field TRM will be determined primarily by $\mu(T)$, with no contribution from $\lambda(T)$ since the reversible component has been removed.

Similar considerations apply to the ZFC moment and the isothermal remanent moment (IRM). Barkhausen elements with large *negative* interaction fields $|h_i| \sim \bar{h}_{c0}$, which are trapped in their stable $\phi = -\mu(T)$ state during zero field cooling, will become unstable when a large positive field is applied at $T = 0$ and will be relatively easy to excite thermally into their $\phi = +\mu(T)$ when the temperature is increased, since their free energy barrier $W_- = \mu(h_c + |h_i| - h_a)$ is small for fields $h_a \sim h_c + |h_i|$. However, these elements will tend to activate *back* to their $\phi = -\mu(T)$ state when h_a is reduced to zero, since now the free energy barrier $W_+ = \mu(h_c - |h_i|)$ will be small, and thus these elements will *not* contribute to the IRM. Instead, it is the Barkhausen elements with low *negative* interaction fields

$|h_i| \ll \bar{h}_{c0}$ which will remain permanently trapped in their $\phi = +\mu(T)$ state when $h_a \rightarrow 0$, and which will be responsible for the IRM. By contrast, in low applied fields, activation will involve elements with low interaction fields and low coercive fields $h_c \ll \bar{h}_{c0}$, and will depend on the growth of the thermal fluctuation energy $W^* \sim k_B T\Omega$, rather than on the collapse of the free energy barriers.

How does $La_{0.7}Sr_{0.3}MnO_3$ fit into the physical picture described above? According to the Preisach simulations, this system does indeed have significant interaction fields since $\sigma_{i0} \sim 0.67\bar{h}_{c0}$. Furthermore, the temperature dependence of the coercive field $\bar{h}_c(T)$ exhibits a pronounced decrease at low temperatures, as shown in figure (6.26). We thus expect to observe a crossover in the behaviour of the TRM and IRM from a low field regime where the TRM is dominated by $\mu(T)$ and the IRM is dominated by W^*, to a high field regime where the TRM exhibits strong curvature reminiscent of $\bar{h}_c(T)$ and the IRM exhibits equally strong, but opposite curvature. This is precisely what is observed experimentally in figures (6.17) to (6.21), and replicated so convincingly by the Preisach formalism.

We conclude this section by plotting the mean anisotropy barrier $\bar{W}_a(T)/\bar{W}_a(0)$ and the thermal fluctuation energy $W^*/\bar{W}_a(0)$ as a function of temperature in figure (6.28) for $La_{0.7}Sr_{0.3}MnO_3$. This figure emphasizes the anisotropy-dominated nature of the irreversible processes in this material.

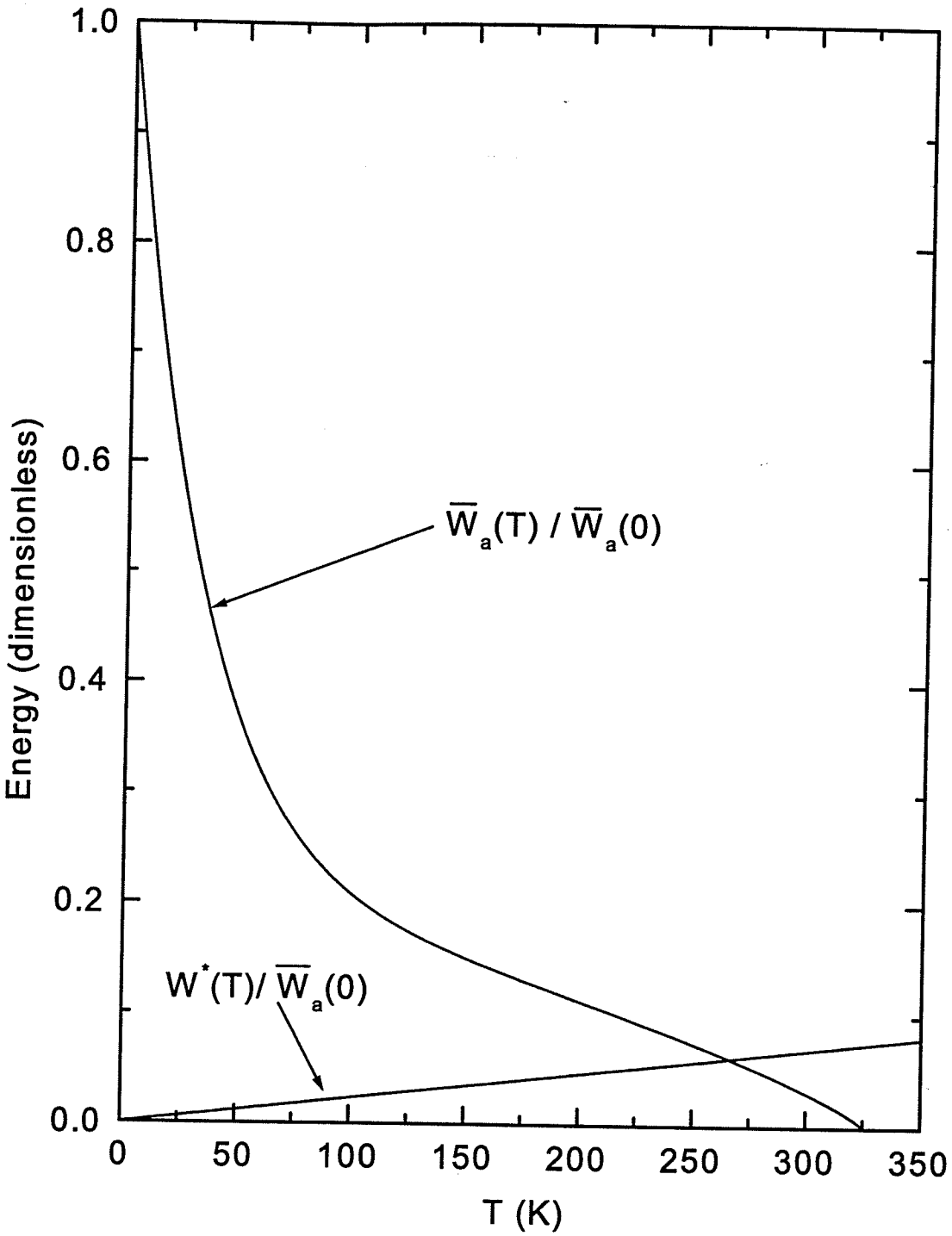

Figure 6.28: *A comparison of the temperature dependence of the mean free energy barrier* $\bar{W}_a(T)/\bar{W}_a(0) = [0.6(1 - T/T_c)^{\Gamma_1} + 0.4(1 - T/T_c)^{\Gamma_2}][0.6(1 - T/T_c)^{\Gamma_{c1}} + 0.4(1 - T/T_c)^{\Gamma_{c2}}]$ *and the thermal fluctuation energy* $W^*(T)/\bar{W}_a(0) = k_B T * ln(t_{exp}/\tau_0)/(\mu_0 \bar{h}_{c0})$ *in* $La_{0.7}Sr_{0.3}MnO_3$.

Chapter 7

Critique and Summary

This thesis represents an attempt to explore and to unlock the potential of the Preisach model as a rigorous physically realistic theoretical framework for describing and interpreting the irreversible response of magnetically ordered materials below their critical ordering temperature T_c. The emphasis here is particularly on replicating the *evolution with temperature* of standard diagnostic response functions like the initial magnetizing curve, the major hysteresis loop, the field cooled moment, and the zero field cooled moment, over a broad range of temperatures, which spans the entire regime of irreversible behaviour. Thus experimental systems have been chosen which reach equilibrium superparamagnetism, or which have a critical temperature T_c which lies, within the experimentally accessible temperature range $2K \leq T \leq 350K$. Furthermore, since no attempt was made to design geometrically simple or symmetric microstructures, the systems studied here are necessarily characterized by substantial structural disorder, and thus are particularly well suited to an analysis which does *not* rely on an intimate knowledge of microstructural details.

In principle, in order for a system to be eligible for a Preisach-based analysis, it must satisfy two criteria: (a) an increment in the applied field from h_{a1} to h_{a2} followed by an *equal reverse* increment must return the system to the original state, and (b) minor loops bounded by the same two reversal fields must be

geometrically congruent. Within experimental accuracy, all of the systems investigated here obey property (a), even for repeating cycling of the field. Attempts to verify property (b) were somewhat less convincing, although at least some of the variation between minor loops could be attributed to lack of reproducibility in the applied field due to the hysteresis in the superconducting magnet.

Perhaps the most common criticism levelled at Preisach-based formulations of hysteresis is their inability to identify the specific physical mechanism which is responsible for the measured irreversible characteristics of a particular material. In fact, the Preisach formalism *does* have the flexibility to accommodate quite specific reversal mechanisms and even symmetries, such as coherent rotation against uniaxial anisotropy, or 180^o degree wall displacement with uniaxial or cubic anisotropy, provided that the generic elementary Preisach loop described in section 6.3 is replaced by the elementary loops appropriate to the specific mechanism, such as those shown in figures (14.3) or (14.8) in Physics of Magnetism by S. Chikazumi[40]. Of course, in highly structurally disordered materials like those studied here, a realistic theoretical description must include some orientational averaging as well as an average over the anisotropy constants or the strength of the pinning sites. However, both of these averages can be conveniently subsumed into a single distribution of coercive fields $f(h_c)$ whose shape is in fact *sensitive to* the details of the individual spectra assumed for both the easy axis orientations as well as the anisotropy constants. For example, if we adopt the Stoner-Wohlfarth model of coherent rotation[41], then $h_c = h_K[(sin\theta)^{2/3} + (cos\theta)^{2/3}]^{-3/2}$, and the distribution of $f(h_c)$ of critical switching fields produced by a distribution $g_1(\theta)$ of orientations and a distribution $g_2(h_K)$ of anisotropy fields is given by

$$f(h_c) = \int_0^{\pi/2} g_1(\theta) g_2(h_K = h_c Z(\theta)) Z(\theta) d\theta \qquad (7.1)$$

where $Z(\theta) = dh_K/dh_c = [(sin\theta)^{2/3} + (cos\theta)^{2/3}]^{3/2}$. Figure 7.1 shows a com-

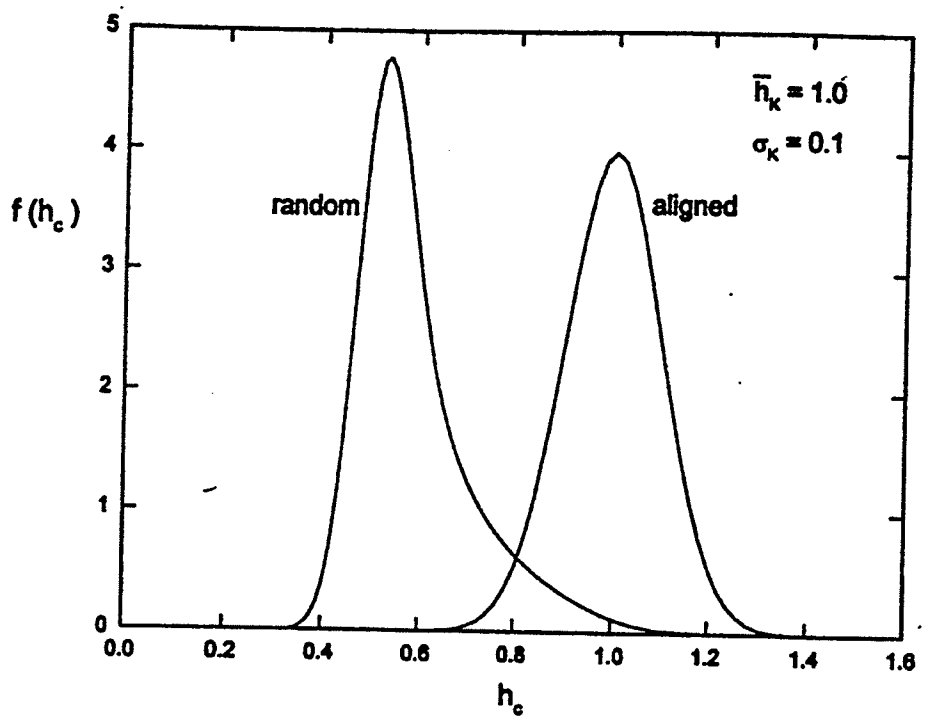

Figure 7.1: *The distribution of coercive fields h_c for a system of aligned particles with a Gaussian distribution of anisotropy fields h_K with mean $\bar{h}_K = 1.0$ and dispersion $\sigma_K = 0.1$, and for the same system but with isotropically oriented easy axes.*

parison of the critical field distributions $f(h_c)$ for a system of perfectly aligned particles $g_1(\theta) = \delta(\theta)$, and for a system of isotropically oriented particles $g_1(\theta) = sin\theta$, both with the *same* Gaussian distribution of anisotropy fields $g_2(h_K) = (2\pi\sigma_K^2)^{-1/2} exp[-(h_K - \bar{h}_K)^2/2\sigma_K^2]$, with $\bar{h}_K = 1$, and $\sigma_K = 0.1$. The effect of randomness is twofold: (1) the most probable critical field $\tilde{h}_c \cong \bar{h}_K/2$ and (2) the distribution $f(h_c)$ develops an *asymmetry* about $\tilde{h}_c$ which is highly reminiscent of the asymmetry which characterizes the *lognormal* distribution of coercive fields used in some of the Preisach analyses in this thesis.

In the current context, where the focus is on simulating and understanding experimental systematics of structural and bond disordered ferromagnets over a broad range of fields and temperatures, rather than replicating the specific

structural features of a single room temperature hysteresis loop, it is our contention that such issues are of secondary importance, and that excessive reliance on specific mechanisms is neither necessary nor physically defensible. Instead, the emphasis here has been on defining the spectrum of free energy Barkhausen barriers $p(W_+, W_-)$ or equivalently $p(h_c, h_i)$ which characterize specific materials, and in particular how its evolution with temperature may be deduced from standard magnetic response functions, and how this evolution is related to the critical ordering temperature T_c. For this purpose, the general formalism described in chapters 2 and 3 is ideal.

According to this formalism, the free energy barriers which impede moment reversal are defined by three elements, a dissipation field h_c which measures energy losses, an asymmetry field h_i which measures energy stored, and the Barkhausen moment μ, all of which are temperature dependent, and all of which are statistically distributed over a spectrum of values. While the most direct source of information about the zero temperature coercive field (h_c) distribution is provided by the lowest temperature ($T = 2K$) initial magnetizing curve and major hysteresis loop, higher temperature hysteresis loops must be interpreted with considerable caution since the collapse of the loop with increasing temperature originates from two sources, thermal fluctuations and intrinsic variations with temperature. To a large extent, the resolution of these effects lies in the ZFC moment, which provides a scan in fixed field of the thermal activation processes as the system is warmed through the irreversible regime, and then the superparamagnetic regime, towards the critical temperature. Assumptions regarding the intrinsic temperature dependences, made within the context of the hysteresis loops, are often incompatible with the thermal profile of the ZFC moment. While this procedure for separating the intrinsic and extrinsic thermal effects is not entirely without ambiguity, in the sense that it is generally possible to identify a *range* of solutions which are

comparably representative of the data, it nevertheless allows us to place each system firmly within a particular *class* of behaviour where thermal fluctuations are either definitely important or definitely negligible. In the latter case, the analysis yields a clear picture of the manner in which the dissipation barriers collapse with temperature.

While the role of the asymmetry (or interaction) field h_i is subtle and often difficult to deduce from an examination of hysteresis isotherms, its impact on the FC moment is particularly profound. To illustrate this point, we show in figure (7.2) Preisach simulations of the FC and ZFC moment of three model anisotropy-dominated systems, ranging from system (a) where $\sigma_{i0} \ll h_a \ll \bar{h}_{c0} = 1.0$ to system (c) where $\bar{h}_{c0} = 1.0 \ll h_a \ll \sigma_{i0}$, with system (b) intermediate between these two. It is clear that the thermal profile of the FC moment depends crucially on the size of σ_{i0} relative to both $\bar{h}_{c0}$ and h_a. To show that this is not a mere mathematical exercise, we show in figure (7.3) measurements of the FC and ZFC moment of four perovskites all measured in roughly the same applied field $h_a = 50$ Oe or 100 Oe, but with very different low temperature coercive fields, which decrease systematically from $H_c = 3600$ Oe for $SrRuO_3$ ($T_c = 161K$) in (a), to $H_c = 320$ Oe for $La_{0.5}Sr_{0.5}CoO_3$ ($T_c = 252K$) in (b), to $H_c = 35$ Oe for $La_{0.7}Ca_{0.3}MnO_3$ ($T_c = 245K$) in (c), to $H_c = 21$ Oe for $Ni_{0.8}Zn_{0.2}Fe_2O_4$ in (d). The simulations in figure (7.2) provide the first *quantitative* explanation for the systematic change in FC and ZFC thermal profiles as one progresses through this sequence of materials. In the two fluctuation-dominated systems studied in this thesis, the temperature dependence of $\sigma_i(T)$ is directly responsible for generating a *maximum* in the temperature dependence of the FC moment. Whether the rapid decrease in σ_i which is responsible for this effect is simply due to the gradual weakening of the static interaction fields as the particles unblock and become superparamagnetic, or is a manifestation of a spin glass-type of ordering

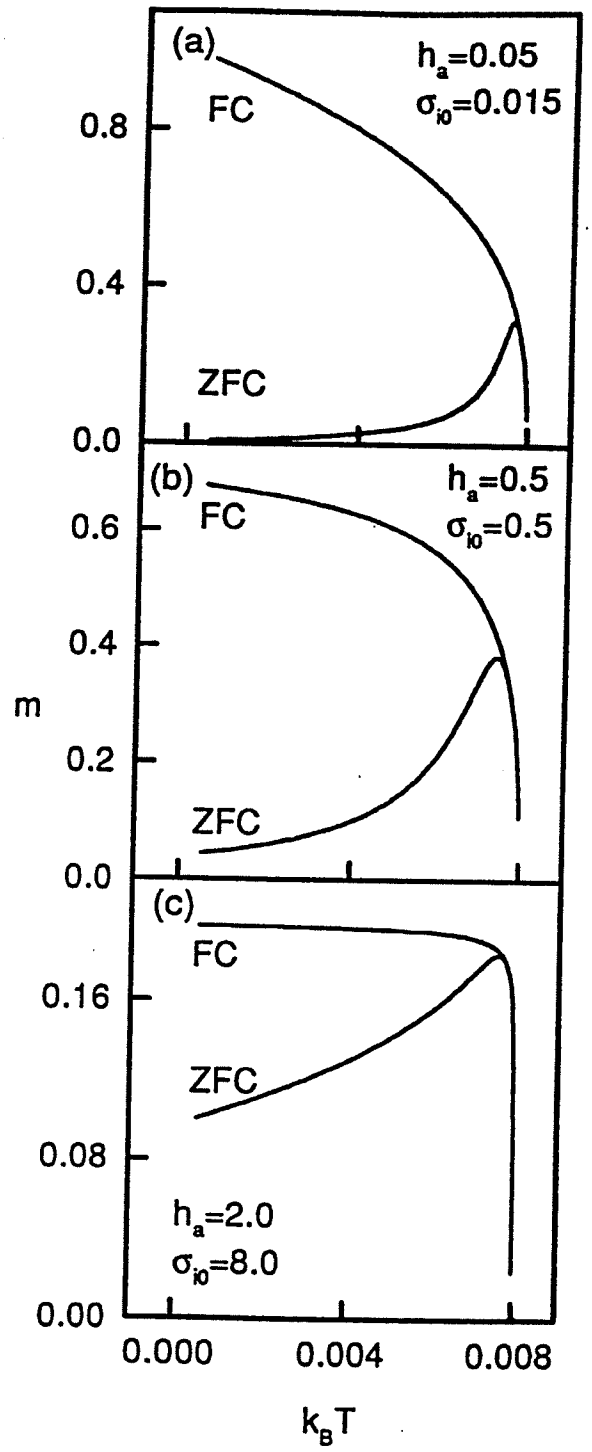

Figure 7.2: *Preisach simulations of the FC and ZFC moment of three model anisotropy-dominated systems, ranging from system (a) where* $\sigma_{i0} \ll h_a \ll \bar{h}_{c0} = 1.0$ *to system (c)* $\bar{h}_{c0} = 1.0 \ll h_a \ll \sigma_{i0}$ *with system (b) intermediate between these two.*

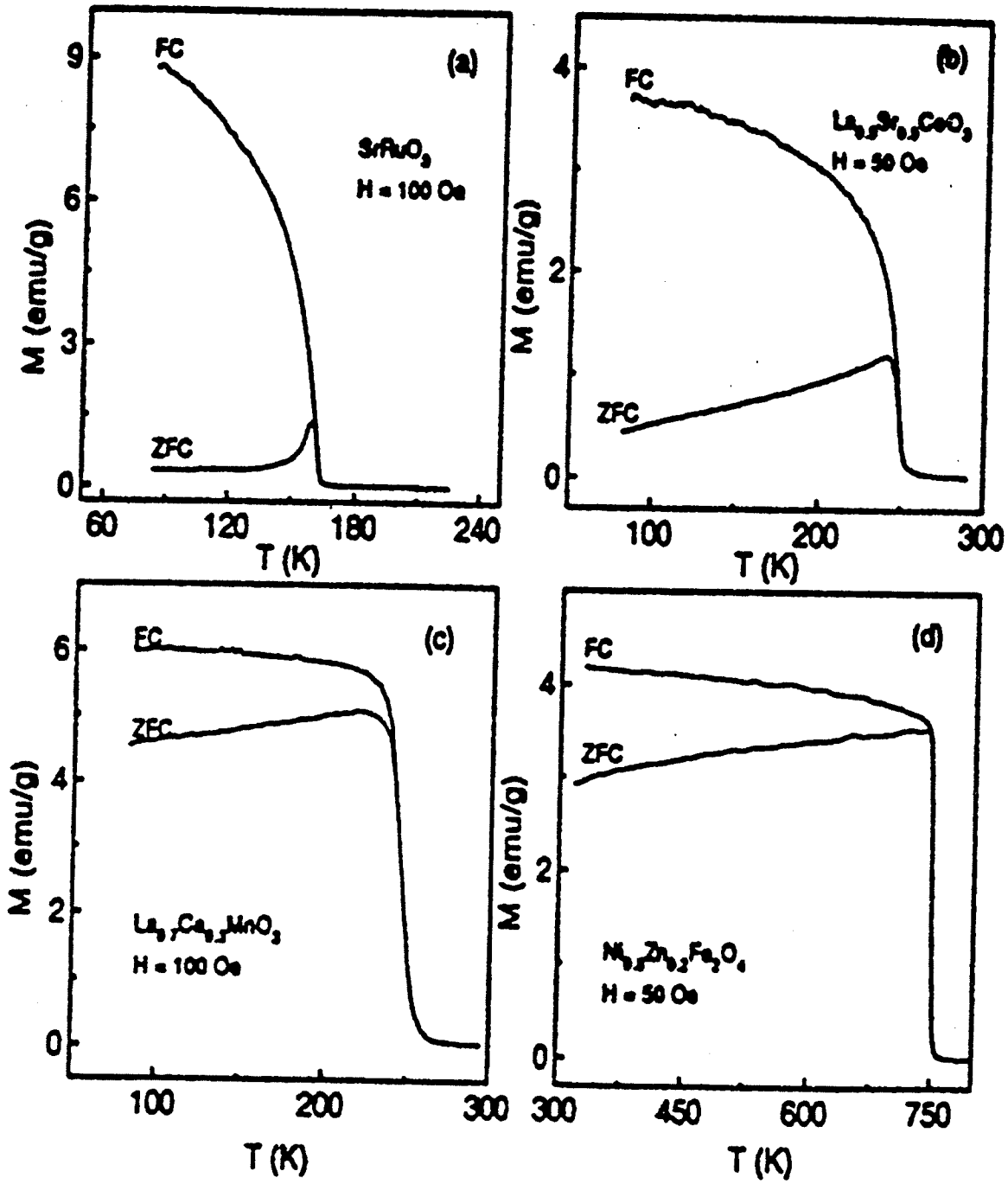

Figure 7.3: *Measurements of the FC and ZFC moment of four perovskites all measured in roughly the same applied field $h_a = 50$ Oe or 100 Oe, but with very different low temperature coercive fields.*

phenomenon is the subject of future investigations.

It is relevant to enquire about the *predictive capabilities* of Preisach models like this one, that is, the extent to which the model is able to predict the field and temperature dependence of the magnetic response functions given some "fundamental" set of characteristic parameters for a given material, in the spirit of micromagnetic models. Ideally, it would be possible *derive* the distribution of Barkhausen characteristic energies (stored and dissipated) from considerations of the topology of the micromagnetic free energy surface, which would depend on specific material parameters and on their temperature dependence, and then implement the Preisach formalism to generate the response functions. Since the basic principles which govern the statistics of the Barkhausen instabilities are not known, this approach is not yet realistic, although at least part of the motivation behind the current work is that Preisach analyses like the ones conducted here may eventually reveal patterns from which these principles could be inferred. At this stage, the Preisach model is an interpretive tool rather than a predictive theory. Nevertheless, as the current analyses show, the generality of the formalism is particularly well suited for establishing *correlations* between specific aspects of the Barkhausen free energy spectrum and specific structural features of the response functions, which would be extremely difficult to recognize from a micromagnetic perspective, and these correlations may ultimately provide the foundation for developing a more rigorous and sophisticated Preisach-based representation of hysteresis, which retains the conceptual simplicity of the double well ensemble, but which relies less on intuitive preconceptions of how the free energy landscape of a given material is configured and how it evolves with temperature.

Bibliography

[1] G. bertotti, "Hysteresis in Magnetism", p33(1998).

[2] B. D. Cullity, "Introduction to Magnetic Materials", p105(1972).

[3] I. Brillouin, "Les Moments de rotation et le Magnetisme dans la Mecanique Ondulatoire", J. de Physique 8, p74-81(1927).

[4] J. L. Dormann, etc, "Magnetic Relaxation in Fine-particle System", p297(1997).

[5] W. Zhong, "Magnetism", p115(1987).

[6] C. Kittel , Rev. Mod. Phys. 21, p541(1949).

[7] E. C. Stoner and E. P. Wohlfarth, "A Mechanism of Magnetic Hysteresis in Heterogeneous Alloys", Phil. Trans. Roy . Soc., A-240, p599-642(1948).

[8] F. Preisach, Z. Phys. 94, p277(1935).

[9] S. H. Charap and A. Kteta, "Vector Preisach Modelling", J. Appl. Phys. 73, p5818-5823(1993).

[10] J. Oti and E. Della, "A Vector Moving Preisach Model of Both Reversible and Irreversible Magnetzing Processes", J. Appl. Phys. 67, p5364-5366(1990).

[11] H. A. J. Cramer, "A Moving Vector Hysteresis Model for Magnetic Recording Media", J. Magn. Magn. Mat. 88, p194-204(1990).

[12] P. D. Mitchler, E. D. Dahlberg, E. E. Wesseling and R. M. Roshko, "Henkel Plots in a Temperature and Time Dependent Preisach Model". IEEE Trans. Magn., vol.32, pp. 3185-3194(1996).

[13] M. L. *Néel*, J. Physique et Rad. 11, p49(1950).

[14] Della Torre E, 1966 IEEE Trans. Audio Electroacoust. 14, p86.

[15] J. Souletie, J.Phys. 44,1095(1983).

[16] L. *Néel*, Philosophical Magzine Suppl. 4, p191(1955).

[17] J. L. Dormann, D. Fiorani and E. Tronc, Adv. Chem. Phys. 98, p283(1987).

[18] P. Prené, E. Tronc, J. P. Jolivet, J. livage, R. Cherkaoui, M.Nogués, J. L. Dormann and D. Fiorani, IEEE Trans. Magnet. 29, p2658(1993).

[19] R. Sappey, E. Vincent, N. Hadacek, F. Chaput, J. P. Boilot and D. Zins, Phys. Rev. B56, p14551(1997).

[20] W. Luo, S. R. Nagel, T. F. Rosenbaum and R. E. RosenWeig, Phys. Rev. Lett. 67, p2721(1991).

[21] J. Tejada, X. X. Zhang, E. Del Barco, J. M. Hernandez and E. M. Chudnovshy, Phys. Rev. Lett. 79, p1754(1997).

[22] B. W. Moskowitz, R. B. Frankel, S. A. Walton, D. P. E. Dickson, K. K. Wong, T. Douglas, and S. Mann, J. Geophys. Research 102, 22, p671(1997).

[23] J. Tejada, X. X. Zhang, and E. M. Chudnovsky, Phys. Rev. B47, p14977(1993).

[24] J. H. Zhao, T. Song, H. P. Kunkel, X. Z. Zhou, R. M. Roshko and G. Williams, "$La_{0.95}Mg_{0.05}MnO_3$: An ideal Ferromagnetic System?", J. Phys.: Condens. Matter 12, 6903-6918(2000).

[25] H. P. Klug and L. P. Alexanda, "X-ray Diffraction Procedures for Polycrystalline and Amorphous Materials ", 2nd edition, Wiley, New York, p618(1974).

[26] L. Tauxe, T. A. T. Mullender, and T. Pick, J. Geophysical Research 101, p571(1996).

[27] J. R. Friedman, U. Voskoboynik, and M. P. Sarachik, Phys. Rev. B56, p10793(1997).

[28] M. Hanson, C. Johnsson, and S. Morup, J. Phys.: Condens. Matter 7, p9263(1995).

[29] J. R. Friedman, M. P. Sarachik, J. Tejada, and R. Ziolo, Phys. Rev. Lett 56, p3830(1996).

[30] P. D. Mitchler, R. M. Roshko, E. Dan Dahlberg, and B. M. Moskowitz, "Interactions and Thermal Effects in Systems of Fine Particles", IEEE Trans. Magnetics 35, p2029(1999).

[31] R. Cherkaoui, M. Nog*acutees*, J. L. Dormann, P. Prene, E. Tronc, J. P. Jolivet, D. Fiorani, "Magnetic Properties of Isolated $\gamma - Fe_2O_3$ Particles", IEEE. Trans. Magn. vol 30, p1098-1100(1994).

[32] L. Spinu, and A. Stancu, "Modelling Magnetic Relaxation Phenomena in Fine Particle Systems with a Preisach-Néel model" , J. Magnetism Magn.Mat., vol.189, p106-114(1998).

[33] A. Stancu, and L. Spinu, "Temperature and Time Dependent Preisach Model for a Stoner-Wohlfarth Particle System," IEEE. Trans. Magn., vol 34, p3867-3875(1998).

[34] J. M. González, Anit K. Giri, C.de Julian, M.P. Morales, "Magnetic viscosity in $FeSiO_2$ granular solids" , J. Magnetism Magn.Mat., vol.140-144, p375-376(1995).

[35] Jen-Hwa Hsu, Yi-Hong Huang,"Size Effect of Magnetic Properties in Al_2O_3 Granular Soldis", J. Magnetism Magn.Mat., vol.140-144, p405-406(1995).

[36] S. Mitani, H. Fujimori, S. Furukawa, S. Ohnuma, "High Electrical Resistivity and Mössbauer Effect of Soft Magnetic $FeSiO_2$ Granular Alloys", J. Magnetism Magn.Mat., vol.140-144, p429-430(1995).

[37] C. L. Chien, S. H. Liou and Xiao, J. Magn. Mater. 54-57, p759(1986).

[38] P. A. Joy, S. K. Date, and P. S. Anil Kumar, Phys. Rev. B 56, p2324(1997).

[39] S. A. Kevelson and V. J. Emery, Cond-Matt/9809082.

[40] S. Chikazumi, Physics of Magnetism, Krieger Publishing Company, p284 and p290(1978).

[41] B. D. Cullity, "Introduction to Magnetic Materials", p389(1972).